الجمهورية الجزائرية الديمقراطية الشعبية

République Algérienne Démocratique et Populaire

Ministère de L'Enseignement Supérieur et de la Recherche Scientifique

Université Ferhat ABBAS Sétif 1

UNIVERSITÉ FERHAT ABBAS - SETIF1

FACULTÉ DE TECHNOLOGIE

THÈSE

Présentée au Département de Génie des Procédés

Pour l'obtention du diplôme de

DOCTORAT

Domaine : Sciences et Technologie

Filière : Génie des Procédés **Option : Génie Chimique**

Par

GUEDIRI MOHAMED KHALIL

THÈME

Optimisation de l'élimination des produits organiques par des procédés intégrés

Soutenue le 23 / 06 / 2022 devant le Jury :

DJERBOUA Ferhat	**Professeur**	**Univ. Sétif 1**	**Président**
CHEBLI Derradji	**Professeur**	**Univ. Sétif 1**	**Directeur de thèse**
BOUGUETTOUCHA Abdallah	**Professeur**	**Univ. Sétif 1**	**Co-Directeur**
NASRALLAH Noreddine	**Professeur**	**USTHB**	**Examinateur**
BOUALLOUCHE née SAADI Rachida	**MCA**	**USTHB**	**Examinateur**
BOURZAMI Riadh	**MCA**	**Univ. Sétif 1**	**Invité**

Acknowledgements

Firstly, I would like to thank God for his undying love, strength, and wisdom to complete this work.

I would like to thank Prof. Derradji Chebli and Abdellah Bouguettoucha for their guidance, encouragement, and support throughout the course of my PhD research.

Prof. Derradji Chebli Prof. Abdallah Bouguettoucha, you have taught me not only enormous knowledge but also how to become a proper researcher with a broader vision in the long run. I have benefited so much from the many discussions with you.

I would like to express my heartfelt gratitude to Dr. Riadh Bourzami. I really appreciated that you spent so much time teaching me even the very little things, patiently revising my manuscripts time after time and kindly sharing your exciting ideas with me.

Words cannot express my deepest gratitude to my parents, from whom I received endless support, encouragement, love, and guidance. Without them, I would never be the man I am today. I would like to thank my brothers, and my sister and her daughters.

Publications

List of publications

Mohamed K. Guediri, Derradji Chebli, Abdallah Bouguettoucha, Riadh Bourzami & Abdeltif Amrane.

Novel Fe_2TiO_5/reduced graphene oxide heterojunction photocatalyst with improved adsorption capacity and visible light photoactivity: experimental and DFT approach.

Environmental Science and Pollution Research **28,** 8507–8519 (2021).

https://doi.org/10.1007/s11356-020-11221-0

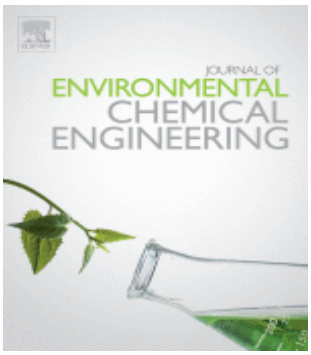

Riadh Bourzami, Mohamed Khalil Guediri, Derradji Chebli, Abdallah Bouguettoucha, Abdeltif Amrane.

Bottom-up construction of reduced-graphene-oxide-anchored spinel magnet $Fe_{2.02}Ni_{1.01}O_{3.22}$, anatase TiO_2 and metallic Ag nanoparticles and their synergy in photocatalytic water reduction.

Journal of Environmental Chemical Engineering,Volume 9, 2021.

https://doi.org/10.1016/j.jece.2021.105307.

Mohamed K. Guediri, Derradji Chebli, Abdallah Bouguettoucha, Riadh Bourzami & Abdeltif Amrane.

Interfacial coupling effects on adsorptive and photocatalytic performances for photoresponsive graphene-wrapped $SrTiO_3$@Ag under UV–visible light: experimental and DFT approach.

Environmental Science and Pollution Research (2022).

https://doi.org/10.1007/s11356-021-17543-x

Conference presentations

International communications

- 2^{éme} workshop international en mécanique des structures et matériaux (IWMSM 2018). Université Mostefa Ben Boulaid -Batna 2, Algérie, le 17 et 18 décembre 2018.

Title: ZnO activation by using activated carbon as a support: Characterization and photoreactivity.

Auteur : Mohamed Khalil Guediri, Derradji chebli, Abdallah Bouguettoucha.

- First International Workshop on Environmental Engineering (IWEE'19). November 16 to 17 – 2019, Ferhat Abbas University -Setif 1, Algeria.

Title: Photocatalytic degradation of Methylene Blue using Type-II CuO/$FeTiO_3$ heterojunctions as novel photocatalyst under visible light irradiation.

Auteurs: Mohamed Khalil Guediri, Derradji chebli, Abdallah Bouguettoucha.

- International Conference on Materials Science (ICMS2018). September 12 to 14 – 2018, Ferhat Abbas University -Setif 1, Algeria.

Title: Synthesis of $FeTiO_3$/rGO composites for remediation of Methylene bleu: kinetics study under different artificial visible light intensity.

Auteurs: Mohamed Khalil Guediri, Derradji chebli, Abdallah Bouguettoucha.

Nationale communication

- Conférence Nationale sur la Chimie des Matériaux. Université M'hamed Bougara - Boumerdes, Algérie, le 02 et 03 juillet 2019.

Title: Enhanced visible light photocatalytic activity of Fe_2TiO_5/rGO nanocomposites for water dye remediation.

Auteurs **:** Mohamed Khalil Guediri, Derradji chebli, Abdallah Bouguettoucha.

List of figures

List of Tables

List of abbreviations

AOPs Advanced Oxidation Processes.

CASTEP Cambridge Serial Total Energy Package.

CB Conduction Band.

CNT Carbon nanotube.

CQDs Carbon quantum dots.

DFT Density Functional Theory.

GGA Generalized Gradient Approximation.

GO Graphene Oxide.

HOMO Highest Occupied Molecular Orbital.

IUPAC International Union of Pure and Applied Chemistry.

JCPDS Joint Committee on Powder Diffraction Standards.

LDA Local-Density Approximation.

LUMO Lowest Unoccupied Molecular Orbital.

MB Methylene Blue.

MOFs Metal-Organic Frameworks.

PEG Polyethylene Glycol.

PFO Pseudo First Order model.

PSO Pseudo Second Order model.

$Pn^{th}O$ Pseudo n^{th} Order.

rGO reduced Graphene Oxide.

ROS Reactive Oxidizing Species.

UV-Vis Ultra-violet visible.

VB valence band.

الملخص

اجتذب التحفيز الضوئي بوساطة أشباه الموصلات اهتمامًا كبيرًا نظرًا لإمكاناته الهائلة لحل قضايا الطاقة والبيئة العالمية. للتغلب على العوائق الكبيرة لإعادة التركيب السريع للشحن والامتصاص المحدود للضوء المرئي للمحفزات الضوئية لأشباه الموصلات ، تم تطوير العديد من الاستراتيجيات في العقود القليلة الماضية, و أكثرها استخدامًا على نطاق واسع هو تطوير الوصلات غير المتجانسة الضوئية. في هذا السياق ، قدمت الخصائص الفيزيائية والكيميائية والبصرية والكهربائية الفريدة للجرافين شبه المعدني أو شبه الموصل حلاً فعالاً لبناء محفزات ضوئية غير متجانسة عالية الكفاءة لقيادة مجموعة متنوعة من تفاعلات الأكسدة والاختزال تحت إشعاع الضوء المناسب. إن العمل الذي تم تنفيذه في هذه الأطروحة مخصص بشكل أساسي لتصميم وصلات غير متجانسة متعددة المكونات تعتمد على أكاسيد أشباه الموصلات ، والجرافين ، والمعدن مع نشاط امتزاز وتحفيزي ضوئي فعال لتطبيقات التنظيف البيئي. تم التحقيق في محورين رئيسيين في كل فصل (الفصل الثالث والرابع والخامس) ، أولهما الدراسة التجريبية عن طريق تخليق أكاسيد شبه موصلة (Fe_2TiO_5, $NiFe_2O_4$-TiO_2, $SrTiO_3$) ودمجها مع أوراق الجرافين (جميع الفصول) وتزيينها باستخدام الجسيمات النانوية للفضّة (الفصلان الرابع والخامس) ثم دراسة خصائصها الإلكترونية والبصرية من أجل تحسين كفاءتها التحفيزية الضوئية. الجزء الثاني يتعامل مع المحاكاة العددية للبنى النانوية الهجينة باستخدام طريقة نظرية الكثافة الوظيفيةDFT ، من أجل تحديد آليات الظواهر الفيزيائية المسؤولة عن تأثيرات التحفيز الضوئي التي تحدث في هذه المواد الهجينة. تم تحديد الخصائص الإلكترونية والبصرية للأنظمة ومقارنتها مع البيانات التجريبية. وبالتالي ، بناءً على المحاكاة الحاسوبية من خلال الطرق الكيميائية الكمومية والأعمال التجريبية التي تم تنفيذها ، تم تمييز ظواهر نقل الشحنة المعنية بهدف فهم نقل الشحنات الكهربائية في المادة الهجينة وتأثير استجابات التحفيز الضوئي.

الكلمات المفتاحية

Fe_2TiO_5، $NiFe_2O_4$، $SrTiO_3$، الجسيمات النانوية للفضّة Ag، الجرافين ، التحفيز الضوئي غير المتجانس ، الامتزاز ، DFT ، التخلص من أزرق الميثيلين.

Résumé

La photocatalyse médiée par les semi-conducteurs a attiré une attention considérable en raison de son énorme potentiel pour résoudre les problèmes énergétiques et environnementaux mondiaux. Pour surmonter les graves inconvénients de la recombinaison rapide des charges et de l'absorption limitée de la lumière visible des photocatalyseurs à semi-conducteurs, plusieurs stratégies ont été développées au cours des dernières décennies, et la plus utilisée consiste à développer des hétérojonctions photocatalytiques. Dans ce contexte, les propriétés physico-chimiques, optiques et électriques uniques du graphène semi-métallique ou semi-conducteur ont offert une solution efficace pour construire des photocatalyseurs à hétérojonction hautement efficaces pour piloter une variété de réactions redox sous irradiation lumineuse appropriée. Les travaux menés dans cette thèse portent principalement sur la conception d'hétérojonctions multicomposants à base d'oxydes semi-conducteurs, de graphène et de métal présentant une activité adsorptive et photocatalytique efficace pour des applications de dépollution environnementale. Deux axes principaux ont été étudiés dans chaque chapitre (chapitre III, IV et V), le premier étant l'étude expérimentale en synthétisant des oxydes semi-conducteurs (Fe_2TiO_5, $NiFe_2O_4$-TiO_2, $SrTiO_3$) et en les combinant avec des feuilles de graphène (tous les chapitres) et en les décorant avec des nanoparticules d'Ag (chapitre IV et V), puis l'étude de leurs propriétés électroniques et optiques afin d'optimiser leurs efficacités photocatalytiques. La deuxième partie traite des simulations numériques des nanostructures hybrides en utilisant l'approche de la méthode DFT, afin de déterminer les mécanismes des phénomènes physiques responsables des effets photocatalytiques se produisant dans ces matériaux hybrides. Les propriétés électroniques et optiques des systèmes ont été déterminées et comparées aux données expérimentales. Ainsi, sur la base de simulations informatiques par des méthodes de chimie quantique et des travaux expérimentaux réalisés, les phénomènes de transfert de charge impliqués ont été caractérisés dans le but de comprendre le transfert de charges électriques dans le matériau hybride et l'effet des réponses photocatalytiques.

Mots clés

Fe_2TiO_5, $NiFe_2O_4$, $SrTiO_3$, Nanoparticules d'Ag, Graphène, Photocatalyse hétérogène, Adsorption, DFT, Élimination du bleu de méthylène.

Abstract

Semiconductor-mediated photocatalysis has attracted considerable attention due to its illustrates enormous potential for resolving global energy and environmental issues. To overcome the serious drawbacks of fast charge recombination and the limited visible-light absorption of semiconductor photocatalysts, several strategies have been developed in the past few decades, and the most widely used one is to develop photocatalytic heterojunctions. In this context, the unique physicochemical, optical, and electrical properties of semi-metallic or semiconducting graphene have offered an efficient solution to construct highly efficient heterojunction photocatalysts for driving a variety of redox reactions under proper light irradiation. The work carried out in this thesis is mainly for the design of multicomponent heterojunctions based on semiconductor oxides, graphene, and metal with efficient adsorptive and photocatalytic activity for environmental cleanup applications. Two main axes have been investigated in each chapter (chapter III, IV, and V), the first of which is the experimental study by synthesizing semiconducting oxides (Fe_2TiO_5, $NiFe_2O_4$-TiO_2, $SrTiO_3$) and combined with graphene sheets (all chapters) and decorated it with Ag nanoparticles (chapter IV and V), and then study of their electronic and optical properties in order to optimize their photocatalytic efficiencies. The second part deals with numerical simulations of hybrid nanostructures using the DFT method approach, in order to determine the mechanisms of physical phenomena responsible for photocatalytic effects occurring in these hybrid materials. The electronic and optical properties of the systems were determined and compared with the experimental data. Thus, based on computer simulations through quantum-chemical methods and the carried out experimental works, the involved charge transfer phenomena were characterized in the aim to understand the transfer of electric charges in the hybrid material and the effect of the photocatalytic responses.

Keywords

Fe_2TiO_5, $NiFe_2O_4$, $SrTiO_3$, Ag nanoparticles, Graphene, Heterogeneous Photocatalysis, Adsorption, DFT, Methylene blue elimination**.**

Thesis structure

The thesis is prepared with a publication-based style, in which a collection of relevant publications is presented as the main body of the thesis. The overall structure of the thesis will be presented as follows:

Chapter 1: Bibliographic review.

Chapter 2: Quantum-chemical calculations and characterization techniques.

Chapter 3: Novel Fe_2TiO_5/reduced graphene oxide heterojunction photocatalyst with improved adsorption capacity and visible light photoactivity: experimental and DFT approach.

Chapter 4: Bottom-up construction of reduced-Graphene-Oxide-anchored spinel magnet $Fe_{2.02}Ni_{1.01}O_{3.22}$, anatase TiO_2, metallic Ag nanoparticles, and their synergy in photocatalytic water reduction.

Chapter 5: Interfacial coupling effects on adsorptive and photocatalytic performances for photoresponsive graphene wrapped- $SrTiO_3$@Ag under visible light: experimental and DFT approach.

Chapter 6: Overall conclusions and recommendations for future work.

Table of Contents

General introduction

The growth of industry is a fundamental technological factor that has a great impact on human civilization. It has been observed that over the past few decades, rapid industrialization have resulted in maximum environmental pollution as a result of large amounts of industrial waste [1], [2]. Therefore, before they are discharged into the environment, the pollutants must be removed or eliminated. Otherwise, water pollution can harm humans, animals, plants and all other biological processes due to its inherent toxicity [3]–[6].

Inorganic micropollutants like metals and a broad array of synthetic organic compounds are prevalent in the industrial waste stream [1]. Organic contaminants in water include dyes (methylene blue, rhodamine B, methyl orange, and fluorescein), which are commonly used in food, textile, paint industries, and furniture [7] [8]. Around 30-40% of these coloring compounds are discharged into waterways as "pigment effluent" (accidentally or without pre-treatment), posing environmental and health risks [9]. A number of these water-soluble pigments limit sunlight from reaching aquatic life and certain other pigments breakdown and produce carcinogenic by products when exposed to sunlight [10], [11].

Scientists are scrambling to find a viable and effective method to purify water and minimize pollution as the degree of pollution rises. Coagulation, microbial decomposition, active carbon adsorption, incineration, filtration, and sedimentation are examples of traditional wastewater treatment processes that have either become economically ineffective or left secondary contaminants [12]–[16]. Adsorption is the most frequently used method for removing coloring agents due to its efficacy and simplicity of use [17]–[20]. However, there are some limitations to the adsorption process, such as the inability to remove certain elements and the production of secondary wastes that require additional treatment [21]. To overcome these constraints, the chemical decomposition process has proven to be a cost-effective method of water purification through decomposition [22]–[24]. Advanced Oxidation Processes (AOPs), a group of established treatment methods including photooxidation using a semiconductor material as a catalyst, ultrasonic cavitation, electron beam irradiation, Fenton reaction, and Interactions [25]–[27]. The use of O_3/H_2O_2, UV/O_3 and UV/H_2O_2 has been found to be effective. The basis of AOP is to generate powerful oxidizing species in situ, such as OH radicals, which triggers a sequence of reactions that

break down the dye molecule into smaller and less hazardous molecules, a process known as mineralization.

Despite good oxidation of organic pollutants (except the photocatalysis technique), the complexity of these technologies (AOPs), high chemical consumption, and relatively high processing costs are significant impediments to large-scale usage [28]. Photocatalysts made of semiconducting materials are projected to supplement and enhance more traditional ways to hazardous chemical waste annihilation and energy production [6], [29], [30]. The development of numerous photocatalytic systems using a range of semiconductor photocatalysts has resulted from research in the field of photocatalytic water splitting into hydrogen and oxygen [4], [5], [27]. Since the major part (about 45%) of sunlight belongs to visible region, it is essential that the efforts to design the semiconducting photocatalysts should be toward the utilization of this part of solar light to ignite photocatalytic reactions [24], [31], [32], [20], [33]. Hence, control of electronic band structure of material by adjusting its elemental compositions was recognized as the effective method to extend light response range. Therefore, various possible strategies to enhance the overall photocatalytic efficiency, including band structure engineering, micro/nano engineering, bionic engineering, co-catalyst engineering, surface and interface engineering, have been widely employed for engineering heterogeneous semiconductors [34]–[38].

A number of novel nanostructured heterogeneous photocatalysts based on graphene nanosheets have been developed in the past several years due to their favorable absorption of solar radiation, efficient separation of charge carriers, high surface areas and exposed reactive sites [39]–[42]. As is known, the overall photocatalytic efficiency is significantly hindered by the fast electron–hole recombination and lowlight utilization, which are governed by all material parameters, including chemical composition, physical dimension, interfacial and electronic properties [43]. Thus, a fundamental understanding and deterministic control of these chemical, interfacial and structural factors will enable the scalable production of graphene nanosheet-based composite photocatalysts with the best photocatalytic behavior, which will be favorable for creating some robust composite systems for practical photocatalytic applications and fundamental insights into low-dimensional physics and chemistry at the single-atom level [44]–[47]. Clearly, the interfaces between graphene and semiconductors play the crucial roles in achieving the significantly boosted photocatalytic efficiency [40]. It is generally regarded that constructing the heterojunction photocatalysts has been extensively shown to be capable of promoting the spatial separation

of photogenerated electron–hole pairs through combining the advantages of integrated functional components, thus fulfilling the higher overall photocatalytic activity [48], [49].

The aim of the presented work is mainly for the design of multicomponent heterojunctions based on semiconductor oxides/ graphene/metal to investigate the influence of the interfacial coupling on the structural, electronic, optical, adsorptive, and photocatalytic properties of all the composites. Adding the graphene with its unique features was proposed as the first element improving the photocatalytic properties of the semiconductors oxides (Fe_2TiO_5, $NiFe_2O_4$-TiO_2, $SrTiO_3$). For this purpose, graphene was synthesized by the reduction of graphene oxide (GO), and this is due to the hydrophilic functional groups including hydroxyl, carboxyl, and epoxide groups on both its edge and surface. In the second phase, Ag nanoparticles were used as electrons sink to facilitate the transfer of the interfacial electron to the composites; as well, the Surface Plasmon Resonance (SPR) effects of the noble metal enhance the light absorbance of the composite and thus improved photocatalytic activity. Then, the structural, electronic, and optical properties of the obtained materials were exhaustively investigated and optimized.

Combining experimental and theoretical methodologies enables a quantitative understanding of the physical mechanisms controlling the photocatalytic characteristics of photoactive semiconducting structures. A number of computer simulations and quantum-chemical calculations were performed in this context in order to deduce the physical mechanisms behind the photocatalytic effects observed in hybrid materials. The structural, electronic, and optical properties of each nanocomposite were calculated separately and jointly using the DFT approach. Additionally, the findings of computer simulations were compared to experimental data in order to confirm the created theoretical models' relevance. Thus, using computer simulations and experimental studies, the associated charge transfer phenomena were defined in order to gain a better understanding of the electric charge transfer in the hybrid material and the effect of photocatalytic responses.

Bibliographic review

1. Bibliographic review

1.1. Introduction

The reduction in freshwater availability is exacerbated by population growth, industrialization, and urbanization, to name a few issues. As a result, water reuse is becoming increasingly important. Similarly, there is an increasing need for the development of water treatment technology capable of entirely eliminating contaminants in water, particularly organic pollutants such as textile dyes and pharmaceuticals, and potentially saving human lives and the environment.

Heterogeneous photocatalysis is part of the advanced oxidation processes, which is a very effective method for the degradation of organic pollutants via photoactivation of non-toxic and environmentally acceptable substances such as some semiconducting oxides. Light can activate these compounds, causing organic contaminants to decompose into small, non-toxic molecules like water and carbon dioxide.

The objective of this chapter is to expose the terminology, the theoretical basis, and the state-of-the-art of dye removal by heterogeneous photocatalysis. Furthermore, this chapter provides details on the different types of pollutants and the conventional water treatment methods for organic dyes. Highlights include adsorption, sophisticated oxidation processes, and details on heterogeneous catalysis, as well as synthetic approaches and strategies that have been used to develop some of the semiconductor photocatalysts.

1.2. Different Types of Pollutants

Water is contaminated by a variety of undesirable foreign substances such as physical substances, chemicals, biological species, domestic, sewage, and industrial wastes [50], [51]. These pollutants degrade the quality of the water, making it unsuitable for its intended uses. Water pollutants can be classified into three types based on their state of existence in water. (Figure. 1.1).

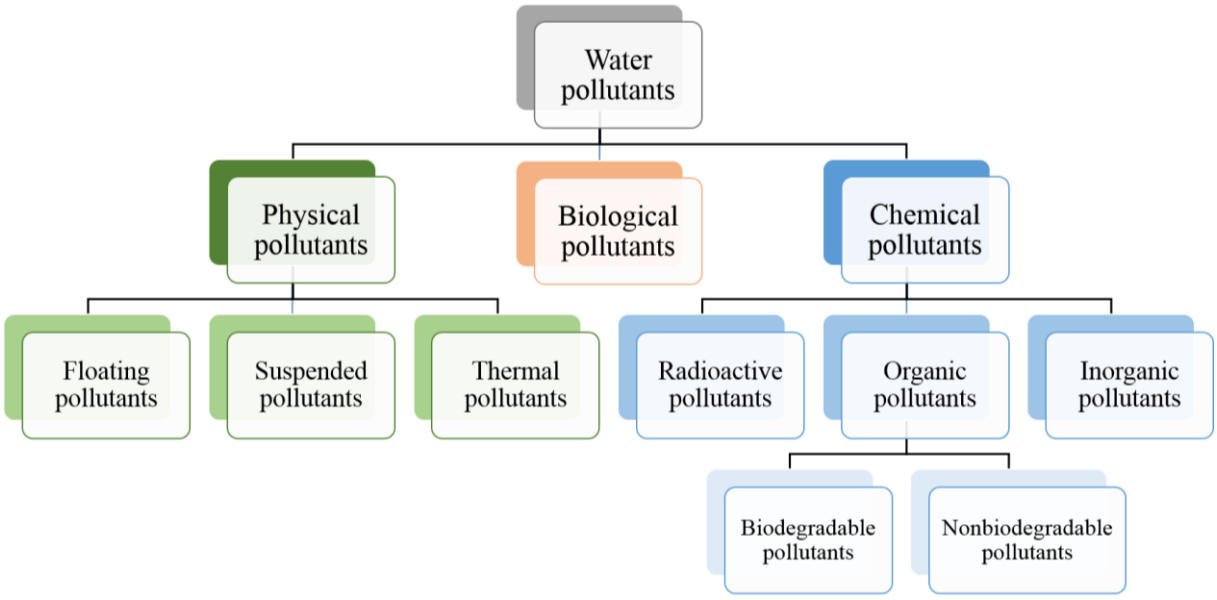

Figure 1.1 *Types of water pollutants*

1.2.1. Organic Dyes in Water

In the past decades, many environmental problems have emerged and need to be resolved, especially polluted wastewater, toxic air pollutants and solid wastes [4], [7], [37]. Among them, organic contaminants in wastewater were particularly concerned. Various trace organic pollutants, such as antibiotics, endocrine disruptors, drug by-products and toxins have been detected in wastewater [52]. The organic pollutants constitute the majority of environmental pollution found in domestic, industrial, and agricultural wastewater sources, which have an adverse influence on aquatic organisms even at low levels of exposure. Many kinds of organic pollutants, such as pharmaceuticals and personal care products, textile, food, beverage, persistent organic pollutants, insecticide, pesticide, oil, fertilizers, and chemical, are included in wastewater [53]. All industries used organic dye as a component in the production of the desired color product. These organic dyes, whether they are natural or synthetic, they are not all environmentally friendly dyes, especially synthetic organic dyes. Most of these organic dyes are very complex molecules, extremely toxic, chemical stability, and slow degradation [54]. Therefore, the discharge of organic dye containing in water is troublesome to the environment, not only bad vision because of their color but also reduction of sunlight transmission. Moreover, these organic dyes also come with a risk substance, for instance, heavy metals (Zn, Pb, Cu, Cd, Co), amines, and aromatic compounds. Therefore, these organic dyes are not only harmful to aquatic life but also mutagenic to humans. The health problems related to organic dyes are skin irritation,

sneezing, sore eyes, carcinogenicity, dysfunction, and mutagenicity, including the brain, liver, kidney, central nervous and reproductive system, and others.

1.3. Conventional water treatment methods for organic dyes

The primary goal of environmental education is to raise public awareness about the importance of environmental protection and conservation, as the indiscriminate release of various contaminants into the environment poses significant health risks. The removal of undesirable chemicals, materials, and biological contaminants from raw water is known as water treatment [55]. Conventional (Physical and Chemical) methods focus on the removal of colloids and bacteria rather than organic pollutants. Such treatments take a long time and are expensive. The disadvantage of such treatments is that they either do not achieve complete mineralization or are ineffective on non-adsorbable or non-volatile pollutants. Furthermore, the major concern is that pollutants are removed from one source only to be disposed of in another. Biological methods require more space, are less responsive to diurnal variation and chemical toxicity, and are less adaptable in design and operation. Although many organic pollutants may be reduced using traditional methods, some are extremely difficult to breakdown due to their difficult chemical construction and simulated organic origin. On the other hand, because they use more chemicals, they generate a large volume of sludge, demanding further treatment. Several physical technologies for wastewater purification, such as membrane filtration and adsorption techniques, are widely available; however, the downside is that they require periodic replacement, which is costly [56].

Many scientists have found and developed methods for treating organic dyes in water, including advanced oxidation processes, adsorption, electro-oxidation, and reverse osmosis [57]–[60]. The photocatalytic process is one of the most intriguing wastewater treatment alternatives because it is non-toxic and has no effect on human life [5], [30]. Photocatalysts for the treatment of organic dyes in water can be homogeneous or heterogeneous catalysts [4]. Despite the fact that photocatalyst suspension in wastewater is the most efficient form for photocatalytic treatment of organic pollutants in water due to high surface contacts between the surface of heterogeneous photocatalysts and organic pollutants in water, the suspension form raises significant concerns about the recovery and reuse of the suspended materials, as well as the photocatalysts' leak potential into the environment. As a result, one of the problems is to develop reuse strategies and leakage precautions for catalysts.

Table 1.1. *Comparison of wastewater treatment methods.*

Methods	Advantages Disadvantages	Disadvantages
Ultrafiltration	• Low driving force • Small space requirement • High packing capacity	• Prone to membrane fouling • Biodegradation of membrane material
Nanofiltration	• Easy operation • Low energy consumption	• Prone to membrane fouling • Expensive
Reverse osmosis	• Efficient rejection rate • Accounts for more than 20% of world desalination capacity	• High power consumption
Adsorption	• Effective • Low cost	• Low reusability capacity
Coagulation-flocculation	• Simple • Applicable to large-scale wastewater treatment • Improved sludge settling	• High chemical consumption • Production of toxic sludge in large quantity • Sludge disposal problem
Ion exchange	• Selective heavy metal removal	• Expensive • Fouling of resin
Chemical precipitation	• Simple to use • Can be adapted to handle large quantity of wastewater	• High chemical requirement • Sludge disposal problem
Chemical oxidation	• Does not increase volume of sludge • Rapid process for removal	• Expensive • Problems in sludge disposal • Formation of by-products
Electrochemical	• Rapid process • Nonchemical requirement	• High cost of electricity • Formation of by-products
Photocatalysis	• Non-toxicity	• Utilization of expensive catalysts

	• No foul smells • No sludge formation	
Biological	• Noninvasive removal of pollutants • Completely mineralizes the toxic pollutants into non-toxic end products without any requirement of rigorous monitoring	• Process takes longer time for the removal of pollutants

1.3.1. Adsorption theory

As a separation process, adsorption is widely applied in our manufacturing economy and in our daily lives. Adsorption is considered an efficient separation process for industrial treatment and domestic effluents [61]. Adsorption methods are universally used for the determination of the specific surface area of fine powders and porous solids, for the separation and purification of fluids in a wide variety of fields, ranging from chemical industries to environmental applications, through agro-industries, pharmaceuticals, and petrochemical industries (separation of hydrocarbons, treatment of air, water, and effluents to remove organic or inorganic pollutants) [62]. In other words more accurate, adsorption is a surface phenomenon that occurs when molecules of a fluid (gas or liquid) called an adsorbate attach themselves to the surface of a solid called an adsorbent. By the surface of the solid, we mean the external and internal surfaces generated by the network of pores and cavities inside the adsorbent [63], [64]. Thus, by contacting fluids with such solids, the desired objective of purification or separation may be achieved. There are two types of adsorption processes: physical adsorption or physisorption, and chemical adsorption or chemisorption.

1.3.1.1. Adsorption equilibrium

Accurate adsorption equilibrium data are essential to the analysis and design of adsorptive separation processes [64]. Broadly speaking, two aspects of adsorption equilibrium deserve our main attention: experimental determination of equilibrium data, and the development of isotherm expressions for equilibrium data representation [65]–[67]. The extent of adsorption of a given situation is reached once equilibrium is established between the adsorbent and its contacting solution. In practice, adsorption performance is also strongly influenced by the mass transfer of the species between the solution and the adsorbent surfaces and the

adsorption reaction rate. Technically, adsorption is, therefore, an equilibrium-diffusion-reaction process.

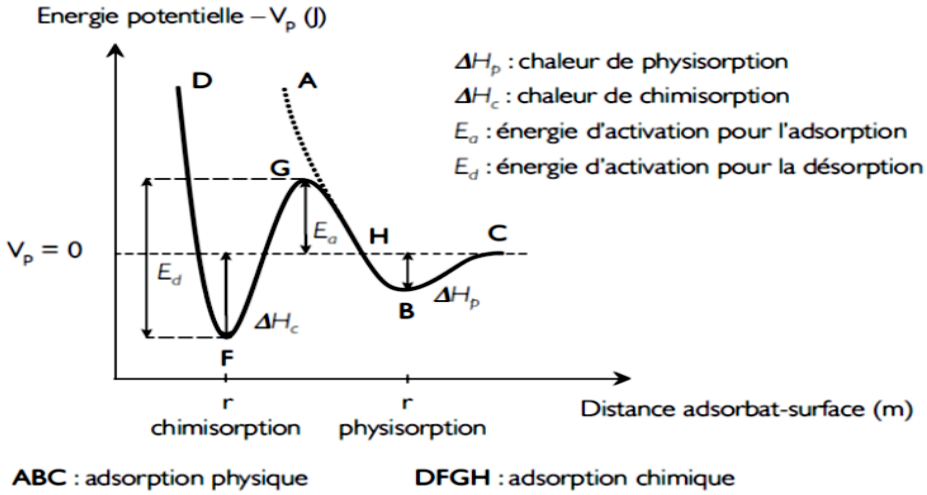

Figure 1.2. *Energy diagram of the adsorption phenomenon.*

1.3.2. Advanced oxidation processes (AOP)

Chemical degradation is one of the most commonly utilized methods for environmental cleanup [68], [69]. It can be accomplished through a variety of methods, including photocatalytic, Fenton method, ozone/UV radiation/H_2O_2 oxidation, sonochemical, electrochemical, supercritical water oxidation, solvated electron reduction, enzymatic treatment, and electron beam irradiation. Only UV light and ozone have disinfecting applications.

The coupled O_3/UV/H_2O_2 technique degrades organic contaminants through oxidation/photolysis processes and the formation of free hydroxyl radicals [70]. However, subsequent treatment for total pollutant neutralization should be carried out using advanced oxidation processes (AOP). AOPs are accomplished through the complete mineralization of matter to H_2O and CO_2 in the presence of highly vivid hydroxyl and superoxide radicals [25]. To create the promoter radicals, one of the effective photodegradation reactions can be advanced utilizing nano-semiconductor and solvated O_2 gas. Photocatalysis is a subclass of AOPs that generates highly reactive and non-selective chemical oxidants (i.e. $\cdot OH$, $\cdot O^{2-}$, O_2) that are highly oxidizing and can breakdown contaminants into benign products such as carbon dioxide and water [71].

1.4. Overview of Photocatalytic Reactions

Photocatalysis defines the speed of chemical reactions or their onset under the influence of UV to IR radiation according to IUPAC definition [72]. The mentioned reaction occurs on a substrate called photocatalyst, which is able to absorb incident radiation. In other way, photocatalysis is a process that utilizes the energy input from incident radiation and the catalytic properties of the surface of a material to carry out and/or accelerate certain chemical reactions [4], [73]. Photocatalysis is known to be able to produce thermodynamically uphill reactions, which otherwise need intense energy inputs in terms of high temperature (or pressure). Understanding the mechanism of photocatalytic reactions is critically important to design and develop new photocatalytic materials [5], [29].

Figure 1.3 [74], shows the reduction and oxidation levels of some of the common photocatalytic reactions with reference to vacuum and the normal hydrogen electrode (NHE). It is noted that these values provide an insight only on the thermodynamic feasibility of the reaction. It is seen that for the reduction reaction, the energy of the (photoexcited) electron should be higher (on the absolute vacuum scale) than the redox level. Therefore, the CB potential of the photocatalyst should be located at a higher energy value than the reduction reaction of interest.

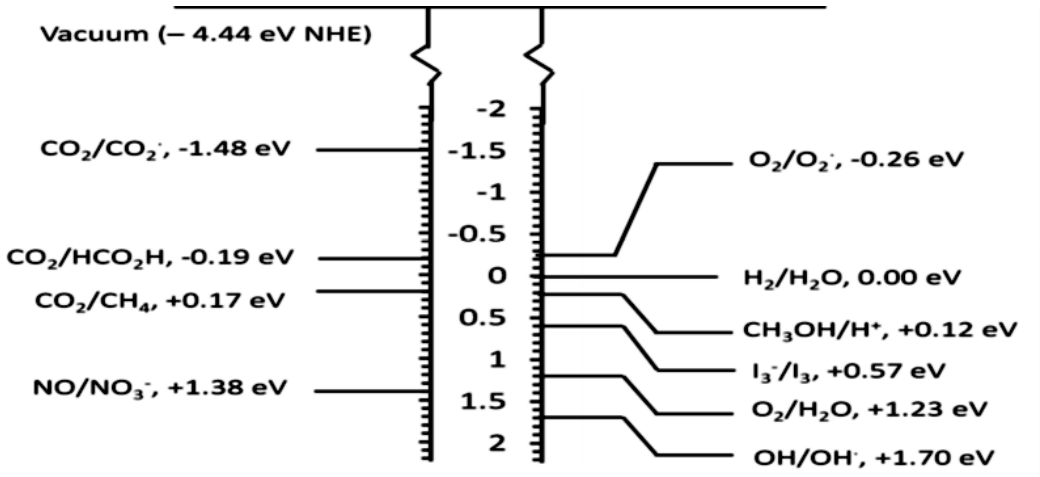

Figure 1.3. *Energy levels of some of the important photocatalytic reactions with respect to NHE at pH = 0*

Based on the relative positions of semiconductor CB levels and redox potentials of specific reactions, some commonly used photocatalysts can be divided into three types: strongly oxidative semiconductors with much higher VB levels for water oxidation reaction, strongly reductive semiconductors with much higher CB levels for CO_2 reduction reaction and H_2

evolution reaction, and semiconductors with moderate oxidation and reduction ability. Figure 1.4, highlights the precise band positions and application areas of some common photocatalysts.

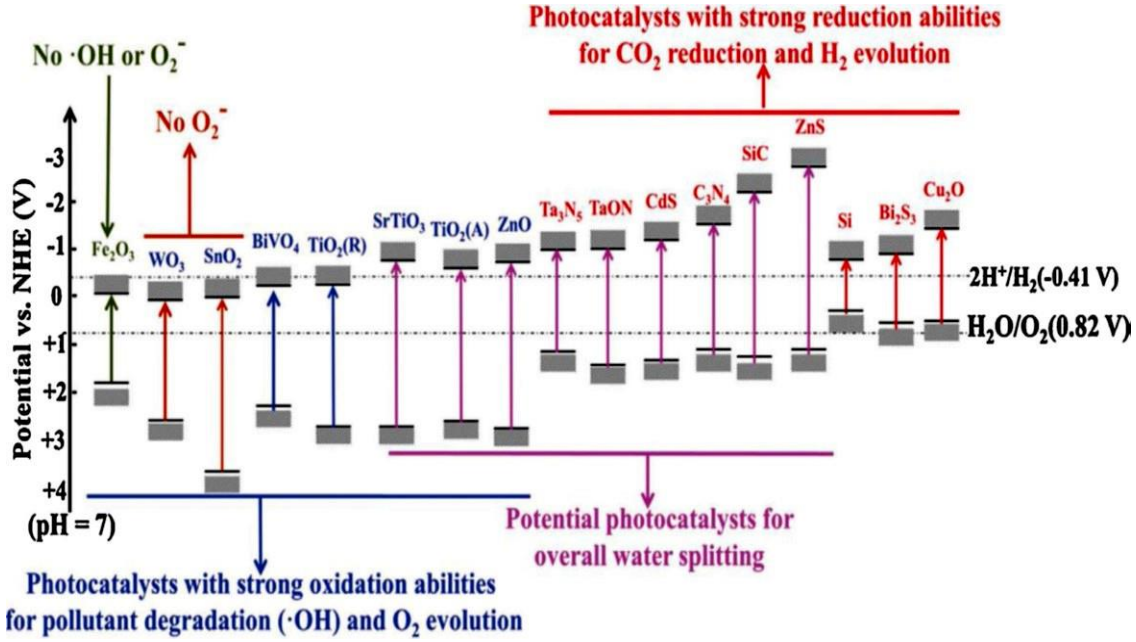

Figure 1.4. *Band positions and potential applications of some typical photocatalysts (at pH = 7 in aqueous solutions) [40]*

1.5. Heterogeneous Photocatalysis

Many years ago, Fujishima and Honda found heterogeneous photocatalysis due to an electrochemical photocatalysis of water at a semiconductor electrode [31], [72]. In heterogeneous photocatalysis, the catalyst is totally separate from the reactants. Based on band gap energy, the differential energy between the valence band (the highest occupied molecular orbital, HOMO) and the conduction band (the lowest unoccupied molecular orbital, LUMO) – the materials are classified into three basic categories (Figure. 1.5).

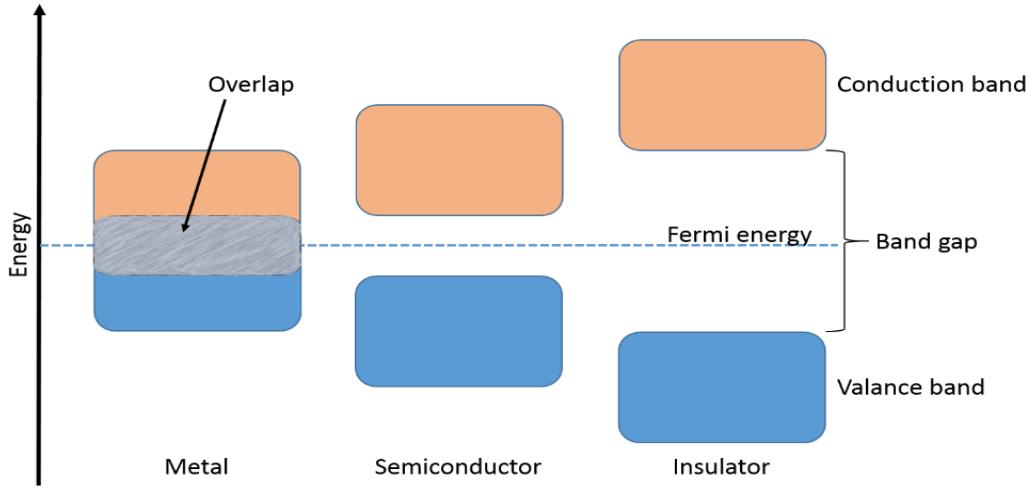

Figure 1.5. *Energy band diagram of a conductor, semiconductor, and Insulator.*

Normally, heterogeneous photocatalysts are semiconductor materials (i.e., metal oxides), because semiconductor can absorb light to activate the movement of electrons, which causes the generation of the reactive species. Heterogeneous photocatalysis is generally carried out by utilization of metal oxides as photocatalysts in the form of suspended phase or immobilized state (on other solid substrates), as heterogeneous photocatalysis occurs with several reactions, e.g., oxidation, dehydrogenation, metal deposition, water detoxification, and gaseous pollutant removals. The illumination of light over the heterogeneous photocatalyst by photons with energy at least equal to its bandgap energy can generate the electron-hole pairs [75], [76]. Eq. (1.1) describes the relationship between the bandgap and the wavelength necessary to excite electrons in the semiconducting material.

$$E = \frac{hc}{\lambda} = \frac{1240}{\lambda} \qquad (1.1)$$

With *h*: Planck constant (h = 6.6256 10^{-34} J.s)

C: speed of light (C = 3.0 10^{8} m.s^{-1})

E: excitement energy (eV).

Figure 1.6 [74], shows how photo-activated electrons migrate from the valence band to the conduction band, leaving positive holes in the valence band. Following that, photo-activated electrons and holes can migrate from the bulk to the photocatalyst surface and react with some adsorbed molecules on the surface to form free radicals. Furthermore, when the migration time of electrons and holes to the surface of the photocatalyst is shorter than the duration of recombination, the photocatalytic process is more efficient. As a result, the lifespan of (h^+, e^-) pairings is critical to photocatalytic efficiency. Organic or biological

molecules adsorbing on the photocatalyst surface can be oxidized if their redox potential is above the semiconductor's valence band. When the redox potential of the substrate falls below the conduction band of the photocatalyst, the reduction process occurs.

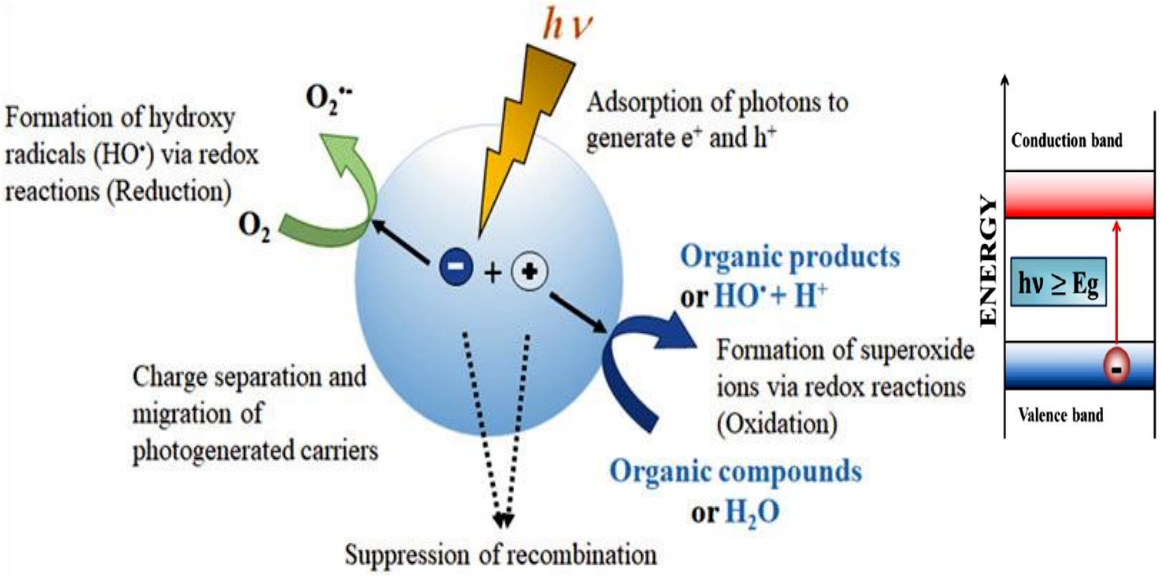

Figure 1.6. *Processes occurring in the semiconductor after absorption of suitable radiation.*

In addition, photoexcited electrons in the conduction band (CB) are responsible for the formation of H_2 and OH when they react with water. However, in order to start producing hydrogen and oxygen, the semiconductor's conduction band level must be more negative than the reduction potential of H_2 ($H+/H_2$) and the valence band level must be more positive than the oxidation potential of O_2 (H_2O/O_2). However, different model contaminants and photocatalysts have a considerable influence on the photocatalytic dye degradation mechanism. Furthermore, the photoactivity and decomposition course would be determined by the different dominating radical species. As a result, the dye degradation mechanism is still poorly understood.

1.5.1. Oxidative Reactions

Typical photocatalysts, i.e., metal oxides (MO), such as oxides of titanium, zinc, and Strontium titanate, can absorb photons to generate the photo-excited electrons and positive holes as expressed in Eq. (1.2) [74], [77], [78]. In the presence of water molecules, hydroxyl radicals (HO•) are produced by a reaction between positive holes and H_2O according to Eq. (1.3). Furthermore, H_2O_2 is possibly formed through the oxidative pathway, leading to the HO• generation from the cleavage of H_2O_2 under photolysis as shown in Eq. (1.4) and (1.5).

$$\text{Photocatalyst} + h\upsilon \longrightarrow \text{Photocatalyst } (e^- (CB) + h^+ (VB)) \quad (1.2)$$

$$H_2O + h^+ \longrightarrow H^+ + HO^\bullet \quad (1.3)$$

$$2\,h^+ + 2H_2O \longrightarrow 2H^+ + H_2O_2 \quad (1.4)$$

$$H_2O_2 + h\upsilon \longrightarrow HO^\bullet + HO^\bullet \quad (1.5)$$

1.5.2. Reductive Reaction

Short-lived free radicals in the form of superoxide anion radicals ($O_2^{-\bullet}$) can be generated by the monovalent reduction of dissolved oxygen molecules adsorbed on the surface of a photocatalyst [74], [77], [78]. Following that, uncharged hydroperoxyl radicals ($HO_2^\bullet$) can be created by protonation of $O_2^{-\bullet}$. Protonation and reduction of $HO_2^\bullet$ may result in the formation of hydrogen peroxide (H_2O_2). Finally, according to Equations (1.6–1.9), homolytic cleavage of H_2O_2 can produce additional hydroxyl radicals ($HO^\bullet$).

$$e^- + O_2 \longrightarrow O_2^{-\bullet} \quad (1.6)$$

$$O_2^{-\bullet} + H^+ \longrightarrow HO_2^\bullet \quad (1.7)$$

$$HO_2^\bullet + e^- + H^+ \longrightarrow H_2O_2 \quad (1.8)$$

$$H_2O_2 + h\upsilon \longrightarrow HO^\bullet + HO^\bullet \quad (1.9)$$

1.6. Mechanism of heterogeneous structure

Significant work has been expended in recent years on the design and manufacture of heterojunctions for enhancing photocatalytic activity [79]. Unique features can be introduced through the mixing of different materials, and thus the operating processes in different systems can be substantially modified. In most situations, however, the ultimate goal of building heterostructured materials is to achieve effective charge separation, smaller bandgaps, and synergistic light absorption [80]. The fundamental idea in this regard is to separate the reduction and oxidation reactions [81], [82]. In general, there are four types of heterojunction photocatalysts [33]: semiconductor–semiconductor (S–S) heterojunction, semiconductor–metal (S–M) heterojunction, semiconductor–carbon group (S–C) heterojunction (carbon group: activated carbon, carbon nanotubes (CNTs), and graphene), and multicomponent heterojunction.

1.6.1. The design principle of S–S heterojunctions

In general, semiconductor heterojunctions can be classified into three types based on their energy bands and Femi levels (Figure 1.7) [33], [40], [83]–[85]: type I, where the valence and conduction bands of one semiconductor completely straddle the bands of the other, type II, where the valence and conduction bands of the two semiconductors are staggered, and type III, where the conduction band minimum of one semiconductor is lower than the

valence band maximum of the other. Because electrons and holes can naturally gather on opposing sides of the interface, type II is the preferred heterojunction among the three band types [31]. Type II heterojunctions can be further classified as n-n junctions, p-n junctions, surface heterojunctions, and phase junctions.

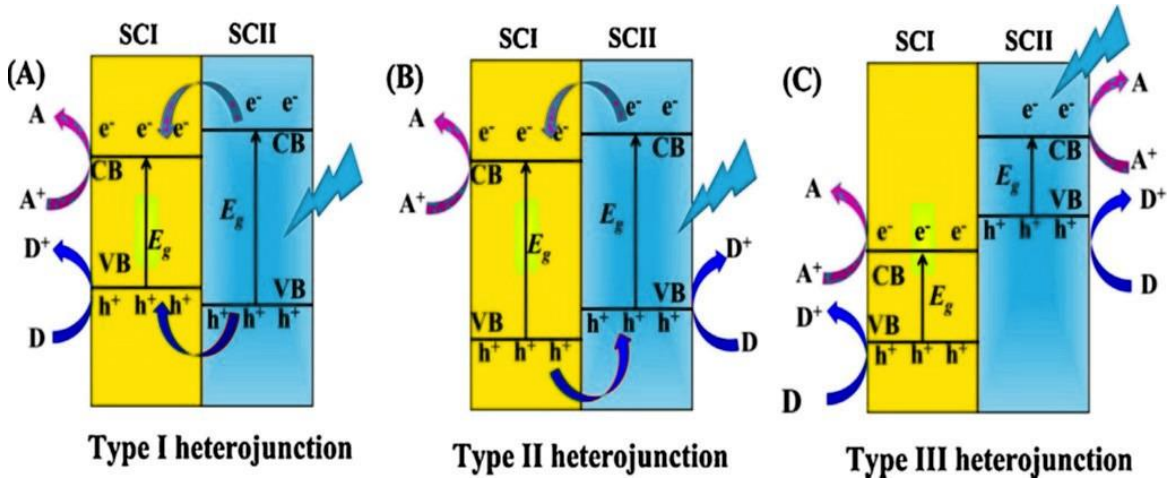

Figure 1.7. *Spatial charge-separation mechanisms for: (A) Type I, (B) Type II, and (C) Type III heterojunctions [40].*

1.6.2. The design principle of S–M heterojunctions

The S–M junction is another effective way to construct a space-charge separation region (also known as the Schottky barrier) [33], [40], [83]–[85]. Electrons flow from one material to the other (from the higher to the lower Fermi level) at the interface of the two materials to align the Fermi energy levels. The most common case is a heterojunction based on an n-type semiconductor and a metal, where the ideal case is that the work function of the metal is greater than that of the n-type semiconductor, and electrons flow from the semiconductor into the metal to adjust the Fermi energy levels (Figure 1.8). The creation of the Schottky barrier results in an excess of negative charges in the metal and an excess of positive charges in the semiconductor [86]–[89]. Furthermore, the Schottky barrier acts as an efficient electron trap, resulting in a high partial electron density near the co-catalysts for photocatalysis and limiting unexpected electron migration from co-catalysts back to the semi-conductor. In general, noble metals with higher work functions were connected with n-type semiconductors to form the Schottky barrier, resulting in better charge separation and photocatalytic activity.

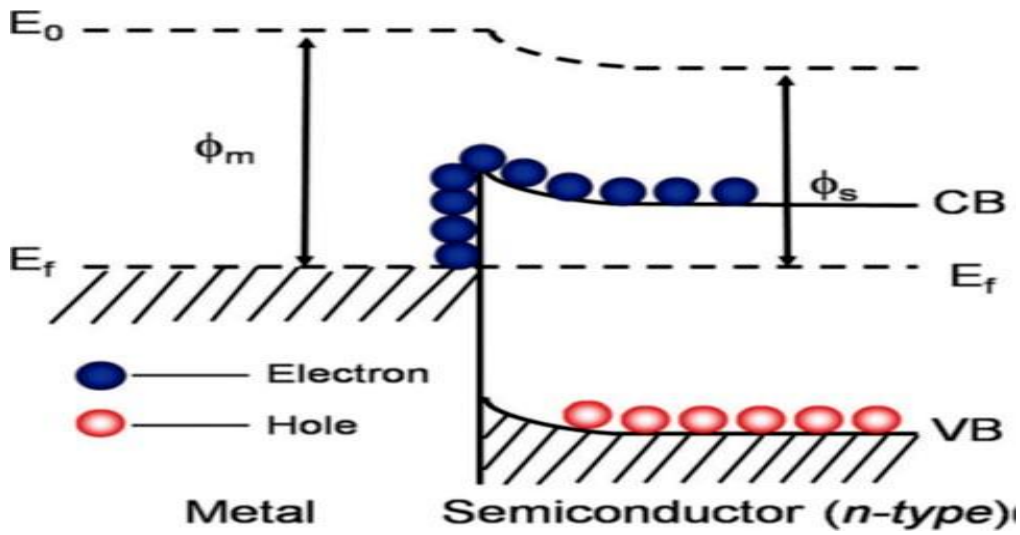

Figure 1.8. *Schematic of the Schottky barrier [33].*

1.6.3. The design principle of S–C heterojunctions

Carbonaceous materials such as graphene (GO/RGO), carbon quantum dots (CQDs), and carbon sphere are being investigated in photocatalysis due to their potential for efficient charge separation, higher charge transfer, extended photo-absorbance, high specific surface area, and strong stability [33], [40], [83]–[85]. As a result, semiconductor-carbon-based composites have been investigated in order to improve the overall photocatalytic performance of the systems.

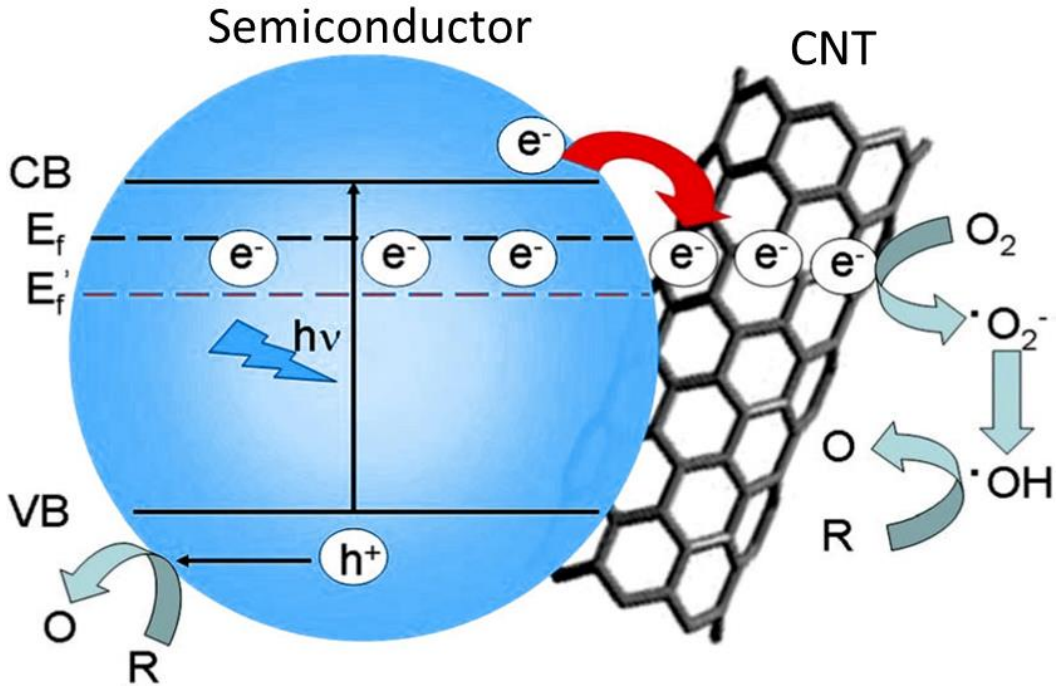

Figure 1.9. *The proposed mechanism for the semiconductor–CNT heterojunction [33].*

1.6.4. Z-scheme heterojunctions

As shown in Figure 1.10, all-solid-state Z-scheme photocatalysts can be classified into indirect Z-scheme and direct Z-scheme systems [33], [40], [83]–[85]. All-solid-state Z-scheme photocatalysts without shuttle redox mediators are often better suited for gas and solid-phase applications . More crucially, all-solid-state Z-scheme photocatalysts may be able to overcome some of the issues that plagued the first generation liquid phase Z-scheme photocatalytic systems, such as obvious backward reactions and competing reactions between mediators and reactants [35], [90]–[92]. As a result, in the photocatalytic areas, all-solid-state Z-scheme photocatalysts have gained increasing attention.

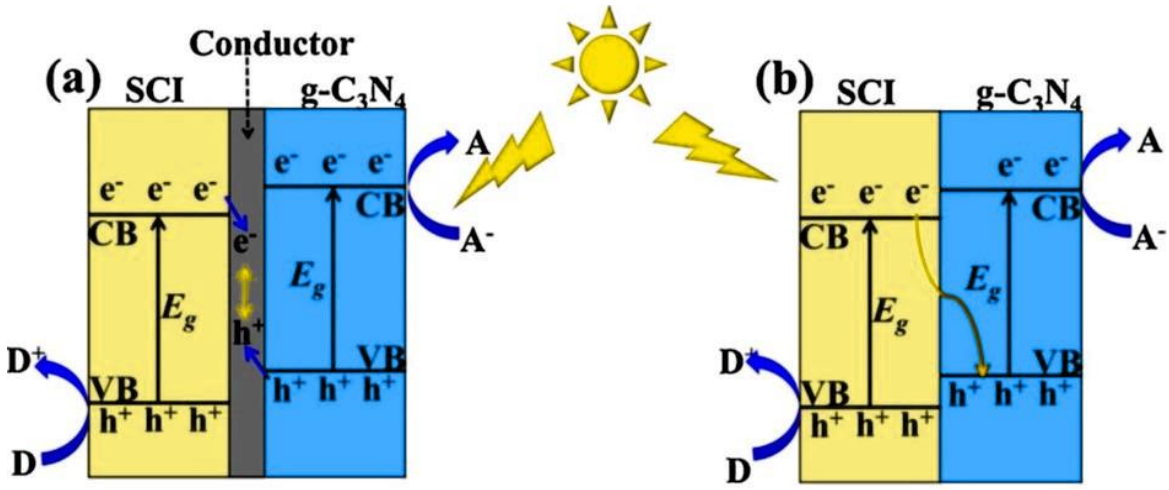

Figure 1.10. *Schematic illustration of spatial charge separation in (a) indirect Z-scheme and (b) direct Z-scheme heterojunctions [40].*

1.6.5. The design and construction of multicomponent heterojunctions

Despite the fact that numerous ways have been established to manufacture various types of heterojonction structures, there are still some limitations, such as the limited region of visible-light photo-response [33], [40], [83]–[85]. To address these issues, multicomponent heterojunction devices with two or more visible-light active components and an electron-transfer system have been developed. Figure 1.11 depicts a typical schematic structure of multicomponent hetero-junction systems. In general, constructing multicomponent heterojunctions could improve visible light utilization, charge carrier separation/transportation, and surface photocatalytic processes all at the same time [93], [94]. The fabrication of distinct interfacial electric fields in multicomponent hetero-junctions, in particular, could synergistically improve charge separation and transfer, resulting in greatly increased photocatalytic efficiency. Typically, a combination of Schottky

junctions with Type-II heterojunctions (or Z-scheme heterojunctions) may enable two-step separation of photo-generated electrons, which might fundamentally prolong the lifespan of photo-generated electrons, leading to widespread photocatalytic applications.

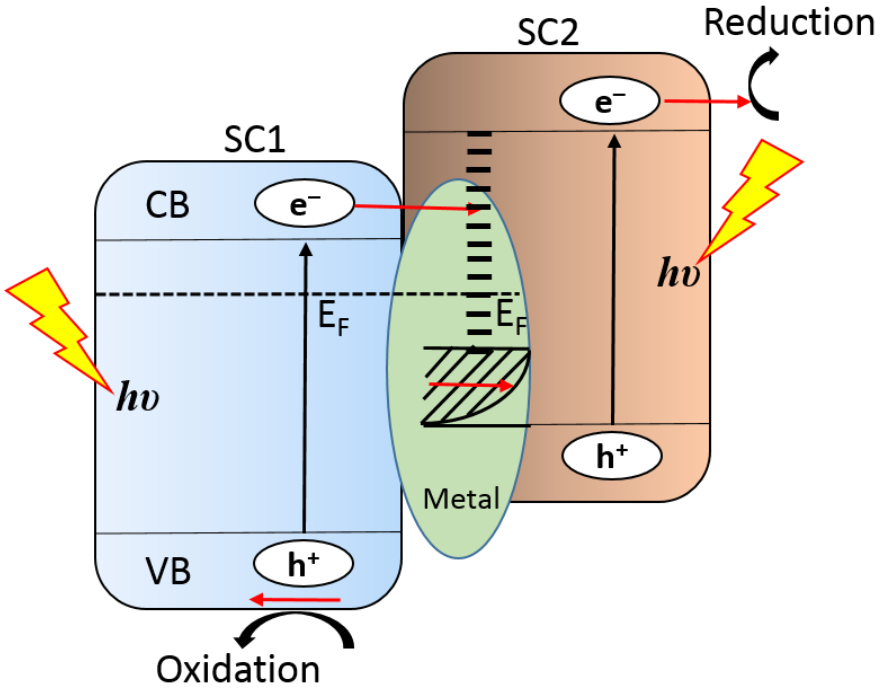

Figure 1.11. *Schematic structure of multicomponent heterojunction systems.*

1.7. Photocatalysis process improvement strategies

Doping with transition metals, surface modification, nanoparticle coupling, and other activities are being tried to broaden the spectrum reactivity of metal oxides to visible light [95]–[97]. A variety of photocatalysts with acceptable band gaps for visible light adsorption have been found; nevertheless, the quick recombination of photogenerated charge carriers, which reduces photocatalytic activity, may be a restriction for most of them. As a result, greater effort must be expended in designing smart photocatalysts with enhanced photocatalytic properties. Furthermore, inhibiting factors such as passivation and contamination of the photocatalytic system can significantly affect the rate of organic compound degradation and must therefore be taken into account in the process's design and operation; a number of improvement strategies must be implemented to improve the photocatalytic degradation process [98]–[100].

The overall photocatalytic performance is greatly influenced by the thermodynamic and kinetic balance of all the processes in all steps, which is strongly influenced by the surface/bulk features and electronic structures of a specific photocatalyst [40]. Because of the increasing availability of visible light semiconductors, activities in the bulk and surface

phases are more important for boosting overall photocatalytic efficiency than photoexcitation in the unit cell. Various surface and interface modification strategies have been developed to improve both charge carrier dynamics and slow surface reaction kinetics (Figure 1.12), resulting in highly active, selective, and stable solar-to-chemical energy conversion.

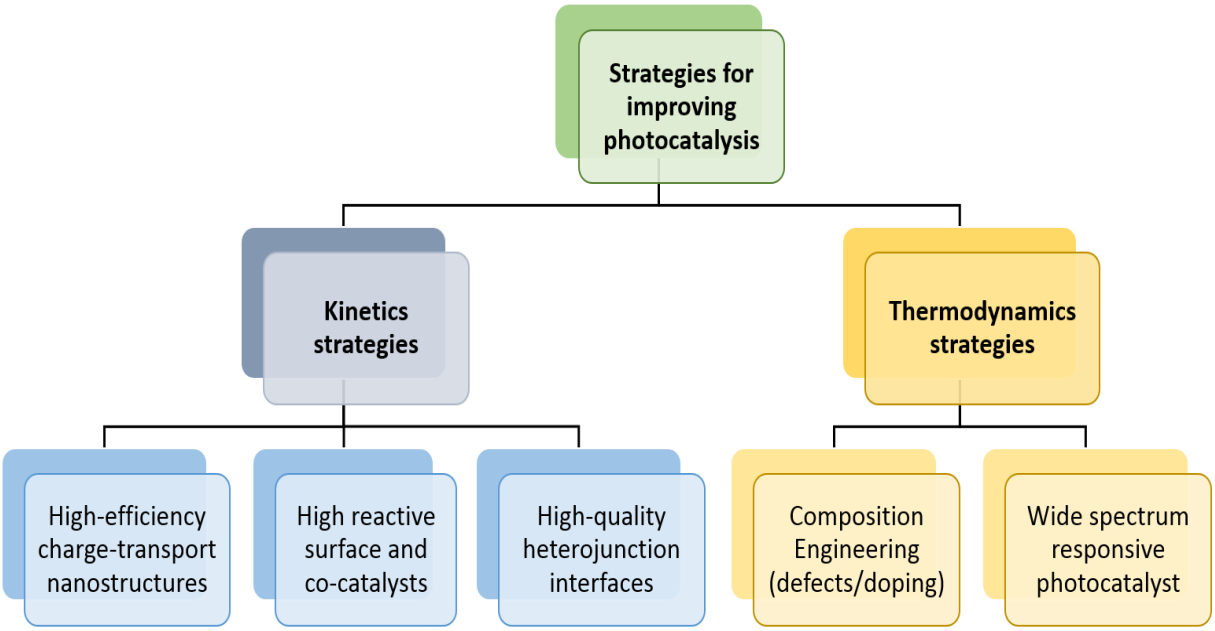

Figure 1.12. *Thermodynamic and kinetics strategies for improving photocatalysis.*

1.8. Design of efficient Photocatalysts

Heterogeneous catalysts have attracted a lot of interest in materials science, photochemistry, electrochemistry, photophysics, and other fields [101], [102]. General criteria are necessary to prepare an effective photocatalyst. Hence, several parameters should be considered at various stages of photocatalytic technology, including before, during, and after the catalyst is used [31], [103]. In addition to high activity, selectivity, lifetime, and durability, the following criteria should be addressed when constructing photocatalysts (Figure 1.13).

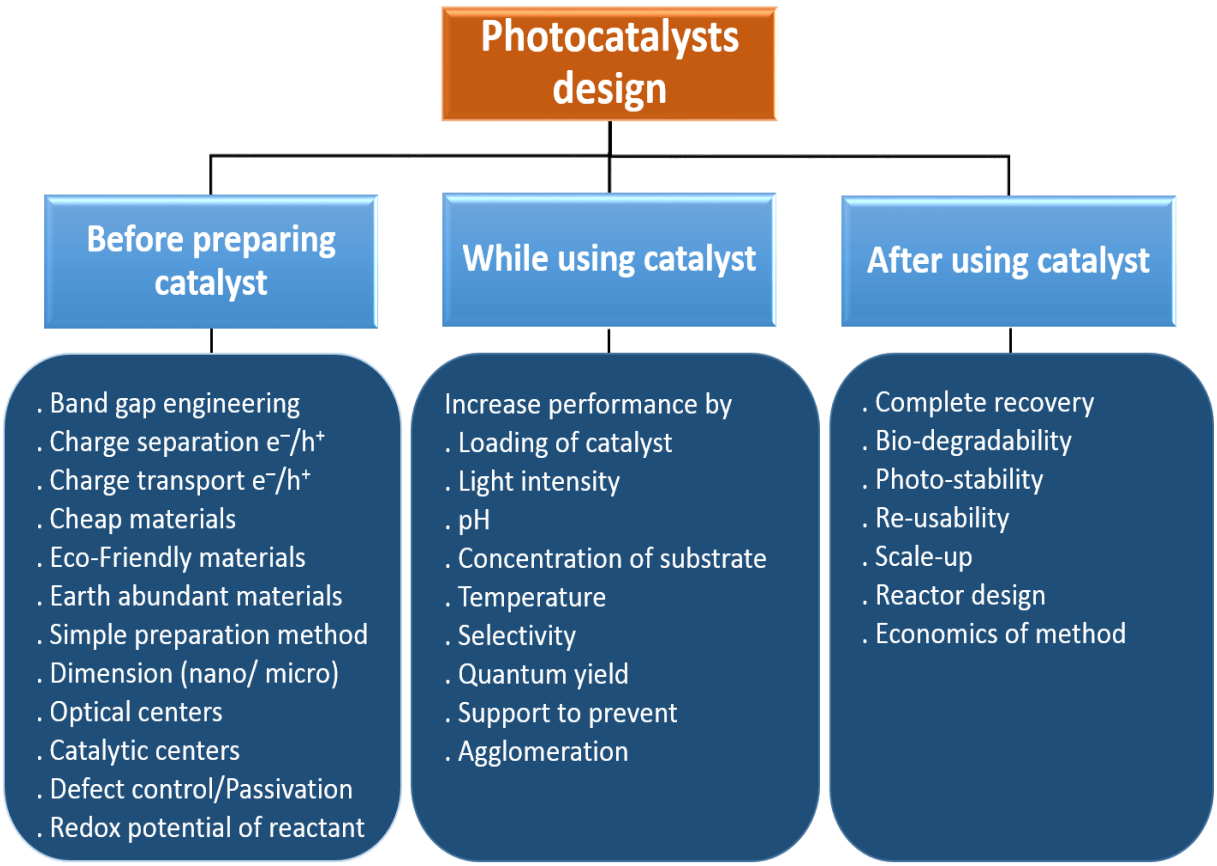

Figure 1.13. *Design consideration of a photocatalyst.*

1.9. Photoactive semiconducting oxides

Because of their excellent physicochemical features, metal oxides are extensively utilized in photocatalytic processes. Metal oxides have great technological relevance in environmental cleanup and electronics due to their capacity to create charge carriers when stimulated with the appropriate amount of energy [6], [72], [104]. The bulk of metal oxides have been used as photocatalysts due to their favorable electronic structure, light absorption capabilities, and charge transport characteristics. Aside from photoactivity, nontoxic nature, chemical stability, and environmental friendliness are significant characteristics for photocatalysts to be used in environmentally friendly applications [105], [106].

1.10. Overview and fundamentals of perovskite

Perovskite-type oxide materials are one of the most important classes of functional materials [107], exhibiting a wide range of physical properties such as ferroelectric, piezoelectric, dielectric, ferromagnetic, magnetoresistant, and multiferroic properties that have been extensively researched over the last century [103], [108], [109]. The chemical formula ABO_3 is derived from the prototype $CaTiO_3$ crystalline perovskite, where A and B are two distinct metal ions with highly different ionic sizes, and O anions are bonded to them. Because the

majority of the metal elements in the periodic table may be employed to build perovskite oxides by logically combining different metal ions at A and B-sites, the perovskite structure is characterized by structural simplicity and flexibility. Many desirable features of perovskite oxides can be adjusted via appropriate chemical substitutions at the A and/or B sites [110]. These perovskite materials have a unique structural property that promotes photocatalytic activity [111]. More research is needed to understand the relationship between electronic structure and photocatalytic activity in order to create innovative perovskites with effective photocatalytic activity.

1.10.1. Perovskite material-based photocatalysts

Third-generation photocatalysts have been produced, which are unique binary metal oxides with the chemical formula $A_xB_yO_z$. These include perovskites ($A^{3+}B^{3+}O_3$, $A^{2+}B^{4+}O_3$), perovskite-related materials, $A^{3+}B^{5+}O_4$ compounds such as tungstate, molybdate, or vanadate, and iron spinals (AB_2O_4) [112], [113]. They have stable structures and can form solid solutions with a variety of metal ions, which can aid in bandgap engineering and lead to more photocatalytic applications. Perovskite photoactivity has lately been widely documented, owing to the benefits of perovskite photocatalysts such as comparable and basic structures, well-characterized structure and surface characteristics, changeable valences, stoichiometry, and vacancies [88], [111], [114], [115]. The unique features of perovskite materials, together with specific structural modifications, make them an appealing choice for water splitting and hydrogen production by photocatalysis. Figure 1.14, shows an overview of various perovskite groups based on structural classification by lattice distortion, including ABO_3, A, and B site substituted perovskite groups, solid perovskite solutions, nitrogen induced perovskites, and layered perovskite.

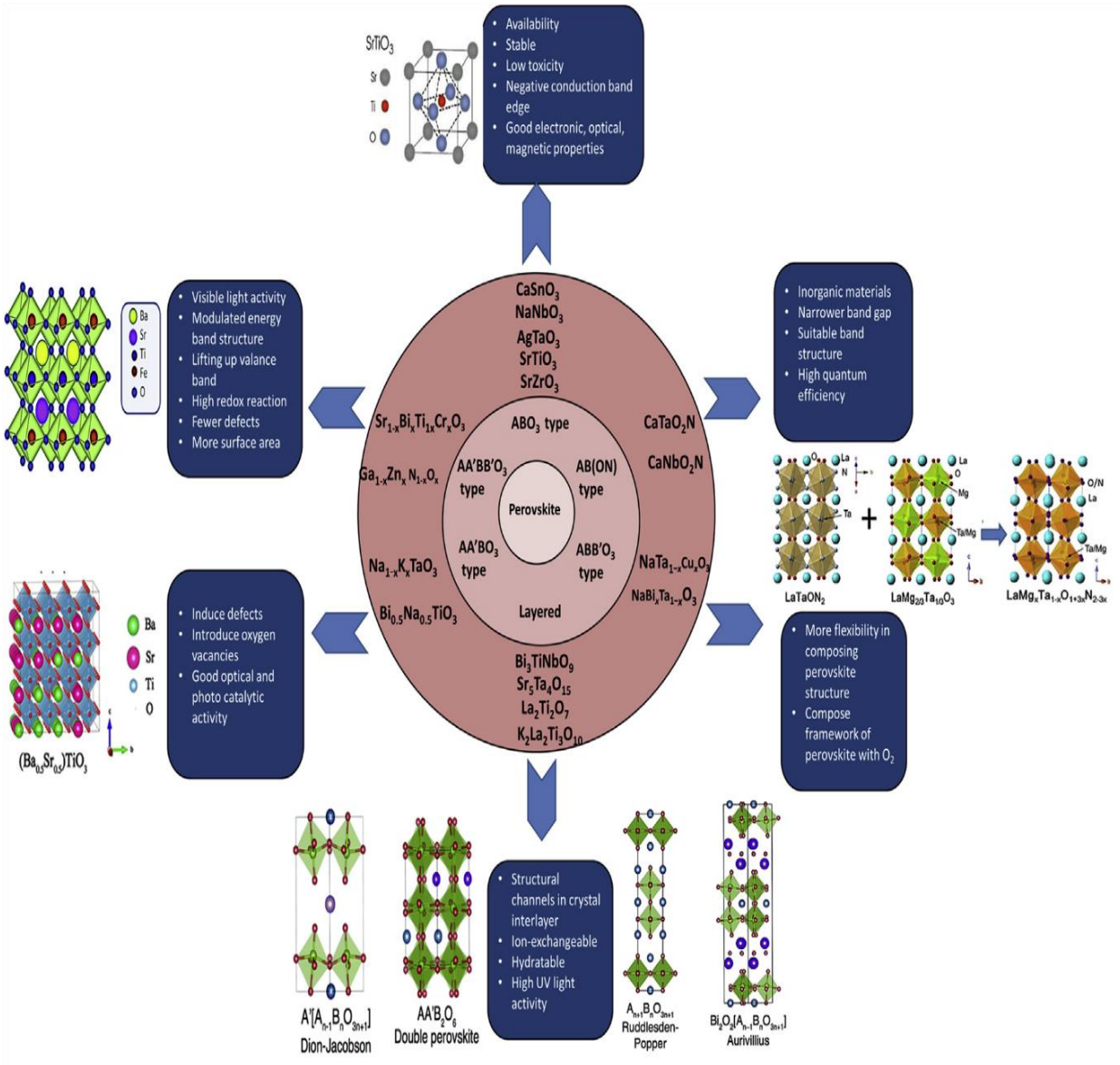

Figure 1.14. *Overview of perovskite and related groups with examples and properties for photocatalysis [112].*

1.10.2. Synthesis of perovskite

Much progress has been made in the manufacturing of nanoscale perovskite oxide materials over the last few decades. For perovskite synthesis, many conventional and non-conventional routes are used, including the solid-state method, hydrothermal method, sol-gel method, co-precipitation, and spray-freeze drying; microwave-assisted, spray pyrolysis, low-temperature combustion, pulse laser deposition, and wet chemical method [112], [107]. The synthesis processes have a strong influence on the performance of perovskites [116]. According to various research, the same perovskite behaves variably depending on its synthesis technique under the same operating parameters for photocatalytic reaction.

Furthermore, each approach produces perovskite with a unique microstructure, which influences the ionic and electrical characteristics of the catalyst [117]. All of the methods described for perovskite photocatalyst synthesis have advantages and disadvantages. The synthesis process, which provides perovskite with efficient light absorption, charge transfer, and greater surface area, is critical for efficient photocatalytic water splitting [109], [111], [118], [119]. Some of the most commonly used techniques are reviewed below. The simplified flow chart of various perovskite preparation methods is shown in Figure 1.15.

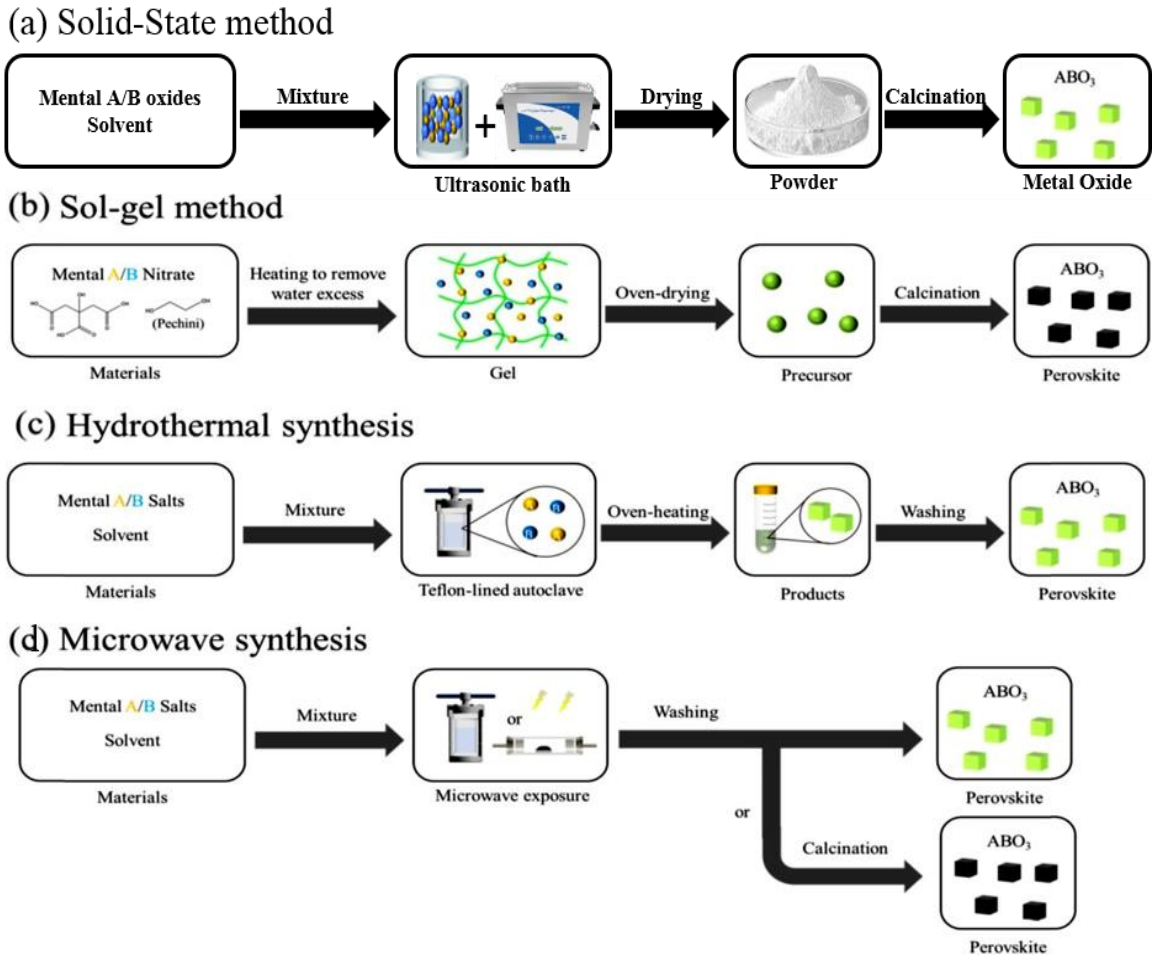

Figure 1.15. *Schematic representations of representative synthesis methods for perovskite oxide catalysts. (a) Solid-State method. (b) Sol-gel method. (c) Hydrothermal synthesis. (d) Microwave synthesis.*

1.10.2.1. Solid-State Reaction Route

One of the most widely used methods for producing perovskite oxide nano-powders is the solid-state reaction method [120], [121]. Weighting the starting materials (the appropriate oxides or carbonates), mixing, grinding, and finally calcining at high temperatures to produce the perovskite phase are all parts of this process.

1.10.2.2. Soli-gel Reaction Route

Due to the reason that the reacting species are homogenized at the atomic level in a sol-gel process, diffusion rates are significantly reduced when compared to a solid-state reaction. As a result, the sol-gel technique allows for the production of final products at much lower temperatures [165],[166]. To produce perovskite nanoparticles with regulated grain size, shape, and crystallinity without further sintering, improved sol-gel methods such as the Pechini method, polymer complex solution, and glycol-gel reaction were developed.

1.10.2.3. Hydrothermal Routes

a) Hydrothermal Process

The hydrothermal method entails heating an aqueous suspension of insoluble salts in an autoclave at a moderate temperature and pressure to generate the appropriate phase structure [112], [122], [123]. Due to the obvious synergetic effects of solvent, temperature, and pressure, it is frequently employed for the preparation of perovskite nanoparticles, which can offer stable final products and prevent the production of impure phases.

b) Solvothermal Process

In comparison to the hydrothermal process, solvothermal synthesis is typically carried out in a nonaqueous solution (e.g., NH_3, methanol, ethanol, and n-propanol), which has the following advantages: the reaction occurs under mild conditions and yields cubic-phase perovskite powder, and the powders have particle sizes on the nanometer scale, with low agglomeration and a narrow particle-size distribution due to the differences between the solvents [112], [122], [123].

1.10.2.4. Microwave routes

Microwave synthesis is a relatively new chemical synthesis process that has evolved in recent years [112], [124]. In the process of perovskite synthesis, microwave radiation can efficiently substitute the heat source. In comparison to previous ways of perovskite synthesis, this method saves a significant amount of time and energy.

1.11. Physical features of semiconductors photocatalysts

1.11.1. Fe_2TiO_5 semiconductor photocatalyst

Among the numerous studied materials, Fe_2TiO_5 is projected to be a fine replacement for TiO_2 in a wide range of possible applications, including water oxidation and photo-degradation [125]. It is composed of earth-abundant elements, has a strong chemical surface stability, paramagnetic properties at ambient temperature, is an n-type semiconductor with

anisotropic uniaxial spin-freezing ability, and a relatively narrow bandgap (E_{gap} = 2.1 eV) [126]. These extremely promising properties can help overcome the limitations of low carrier mobility and poor solar absorptivity that hematite (Fe_2O_3) and anatase TiO_2 suffer from, respectively. In comparison to these last two semiconductors, Fe_2TiO_5 exhibits intermediate behavior with a good optical band gap and electrical transport.

Fe_2TiO_5 pseudobrookite crystallizes with an orthorhombic structure (space group 63 Cmcm or similar), Z=4, and the cations are placed in two distinct octahedral positions, M1 and M2. (Figure 1.16) [127]–[130].

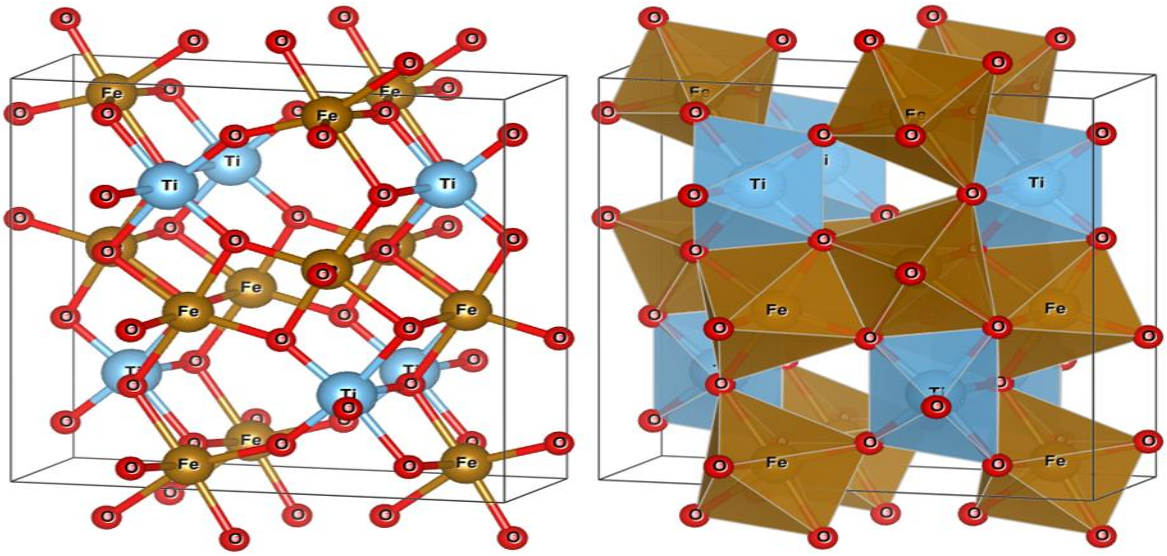

***Figure 1.16**. Crystal structures of pseudobrookite Fe_2TiO_5.*

1.11.2. $SrTiO_3$ semiconductor Photocatalyst

$SrTiO_3$ has aroused the interest of many researchers due to its remarkable physicochemical features, such as a large number of active sites, superior chemical, and thermal stability, and environmentally benign nature [114], [118], [131]. Strontium titanate ($SrTiO_3$) nanoparticles are one of the best and least costly perovskites utilized as a photocatalyst [132]–[135]. $SrTiO_3$ has a bandgap energy of 3.2 eV, and when compared to TiO_2, the $SrTiO_3$ band edge for the conduction band (CB) is approximately 200 mV more negative [136], [137].

As shown in Figure 1.17, $SrTiO_3$ has a perovskite ABO_3 structure with perfect cubic possessing the space group of the Pm % 3m and a lattice constant of 3.905 Å. The valence band (VB) of $SrTiO_3$ is dominated by O *2p* orbitals, with a modest contribution from Ti *3d* orbitals, whereas the CB is dominated by Ti *3d* orbitals and Sr *3d* orbitals at high energies [138]–[140].

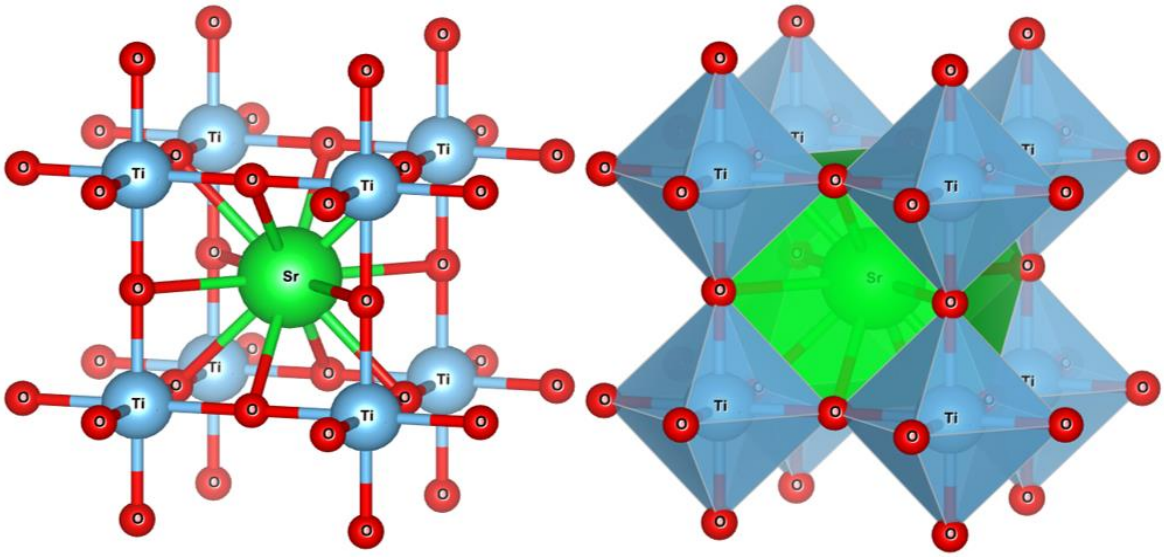

Figure 1.17 *Cubic unit cell of $SrTiO_3$.*

1.11.3. $NiFe_2O_4$ semiconducteur photocatalysis

One of the most important ferrite materials, nickel ferrite powders, has been explored for a variety of applications, including ferro-fluids, catalysts, microwave devices, gas sensors, and magnetic materials [141]–[143]. Nickel ferrite ($NiFe_2O_4$) is an inverse spinel in which ferric ions occupy the tetrahedral or A-sites and ferric and nick el ions occupy the octahedral or B-sites. Thus, the compound is represented by the formula (Fe^{3+}) [Ni^{2+}, Fe^{3+}] O^{4+}, where the round and square brackets represent the A and B sites, respectively (Figure 1.18) [144]–[146].

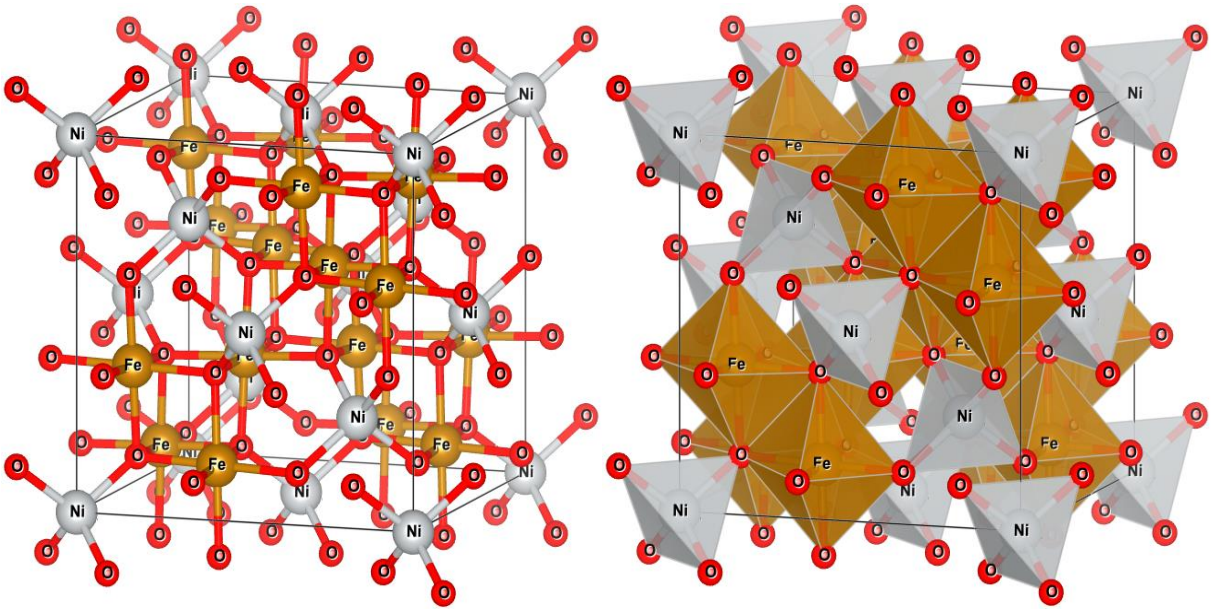

Figure 1.18*. Crystal structures of Nickel ferrite $NiFe_2O_4$.*

1.12. Fundamental properties of graphene

Graphene, the contemporary marvel of nanoscience, has emerged as a remarkable material with multifunctional capabilities [42], [147]. The discovery of graphene is a watershed moment in the fields of optoelectronics, absorption materials, sensing, and catalysis, and it will play a significant role in modern science and technology. Graphene's extraordinary qualities are due to its distinctive structure. It is composed of a monolayer of covalently bonded sp2 hybridized carbon atoms structured into a regular hexagonal packing. The planar density is 0.77 mg/m^2 and the hexagonal carbon ring area is 0.052 nm^2 [148]. Graphene has a high carrier mobility due to conduction band interactions with the valence band at two points in the Brillouin zone [149]–[151]. Furthermore, in pristine undoped graphene, its antibonding π^* orbitals (which make up its conduction band) and bonding orbitals π (which make up its valence band) degenerate and touch at Brillouin zone corners, transforming graphene into a zero bandgap semi-metallic material, as shown on the left of Figure 1.18 [40]. Chemical doping by the addition of foreign atoms, on the other hand, can break lattice symmetry and open a bandgap, transforming semi-metallic graphene into a semiconductor due to the establishment of a gap between the π and π^* bands, as seen on the right of Figure 1.18. Because of these unique features, graphene can be used to construct hybrid materials with enhanced photoresponsive functionality [41], [147]. These features could be employed to improve the optical performance of conventional polymers, organic and inorganic materials. The solubility and processibility of graphene-based materials is a major issue that can be mitigated by the use of graphene oxide (GO). Because GO has hydrophilic functional groups including hydroxyl, carboxyl, and epoxide groups on both its edge and surface, it is also amenable to further chemical modifications [39], [152].

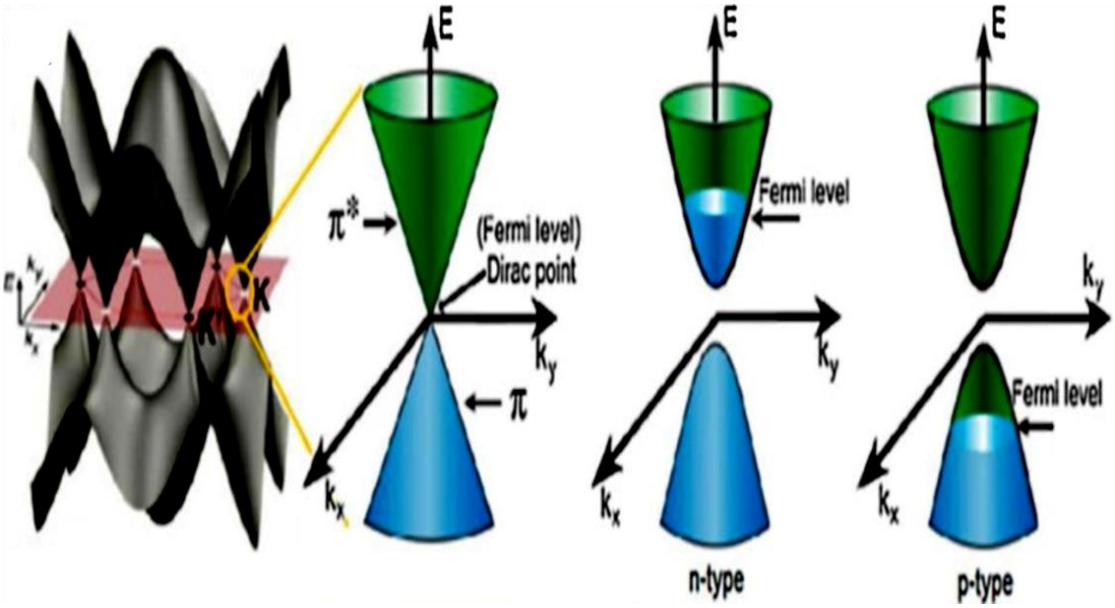

Figure 1.18. *Left: the dispersed band gaps of semimetallic pristine graphene in the Brillouin zone. Right: the energy bands at the Dirac point and the position of Fermi level of semiconducting graphene by suitable heteroatom doping* [40].

1.13. Classification and comparison of graphene-based heterojunctions

Heterojunctions in graphene-based composite photocatalysts can be classified into four types based on the nature of graphene (Figure 1.19): Schottky junctions, Type II heterojunctions, Z-scheme heterojunctions, and multicomponent heterojunctions are all examples of heterojunctions [39]–[41]. Metallic graphene could clearly be used to create Schottky junctions and indirect all-solid-state Z-scheme heterojunctions, whereas semiconducting graphene could be used to create Type-II (containing n-n and p-n junctions) and direct Z-scheme heterojunctions [90],[134],[153]–[155]. More intriguingly, the multicomponent heterojunctions could be created using both semi-metallic and semi-conducting graphene [156]–[158]. The built-in electric fields could be mainly achieved for all four types of graphene-based heterojunctions, which could significantly facilitate the spatial transfer and separation of photoinduced charge carries in graphene-based composite photocatalysts, thus fulfilling the fundamentally enhanced photocatalytic efficiency.

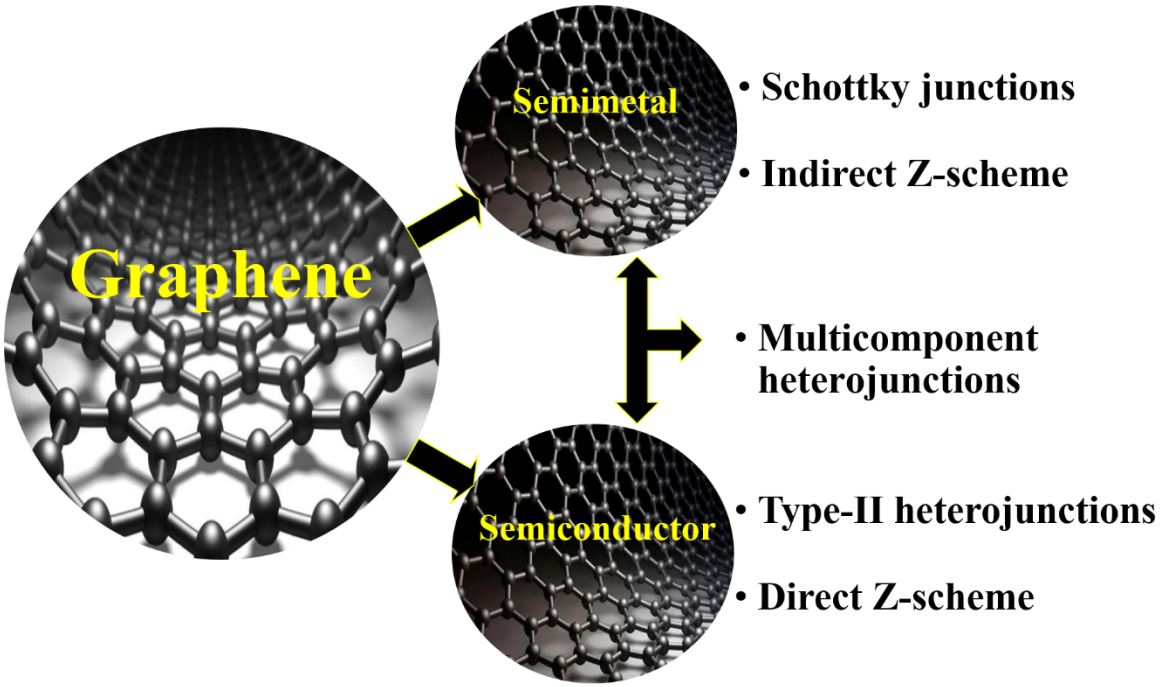

Figure 1.19. *The classification of graphene-based heterojunctions.*

1.14. Advantages of graphene-based heterojunctions in photocatalysis

Graphene in heterojunctions has a number of advantages over other heterojunction photocatalysts, including low cost, readily adjustable band structures, and various structures (i.e., morphology, dimensionality) for producing nanoscale-architecture graphene-based composites [40], [159], [160]. For starters, semi-metallic graphene is a far lower-cost co-catalyst than noble metal co-catalysts. Second, unlike other standard inorganic semiconductors, the semiconductoring graphene process has customizable band gaps and simple fabrication processes for generating diverse graphene-based heterojunctions [34], [48], [161], [162]. Furthermore, when compared to organic semiconductors like g-C3N4 and metal-organic frameworks (MOFs), semiconductoring graphene is obviously far more stable, and its band structures can be easily modified thanks to GO's broad wet chemistry processability [163]. Furthermore, the structural diversity of graphene materials (for example, 0D graphene quantum dots, 1D graphene nanoribbons, 2D graphene nanosheets, and porous 3D graphene networks) provides infinite possibilities for constructing diverse heterojunctions for heterogeneous photocatalysis [164], making graphene a more promising carbon than its other carbon allotropes in designing advanced heterojunction photocatalysts. In a nutshell, graphene's multiple benefits make it the shining star material for building advanced and multi-functional heterojunctions for photocatalytic applications.

Aim and objectives

This project aims to develop a series of multicomponent heterogeneous photocatalysts based on semiconductor oxides, graphene, and metal for an efficient adsorptive and photocatalytic activity for environmental cleanup applications.

Three main multicomponent heterogeneous photocatalysts were synthesized:

- ✓ The Fe_2TiO_5/rGO composites were prepared by hosting several amounts of reduced graphene oxide (rGO) into pseudobrookite nanocrystals (Fe_2TiO_5).
- ✓ A mixture of semiconductors ($NiFe_2O_4$-TiO_2) was employed as a substrate to deposit reduced graphene oxide (rGO) sheets, followed by surface decoration with Ag nanoparticles.
- ✓ Semiconductors with perovskite structure ($SrTiO_3$) deposited on reduced graphene oxide (rGO) with various graphene contents, followed by decorating the surface with Ag nanoparticles.

The key objectives of this project are to:

➢ Investigate the synthesis both of pseudobrookite nanocrystals (Fe_2TiO_5) via a solid-state reaction, paramagnet spinel with titanium dioxide ($NiFe_2O_4$-TiO_2) and strontium titanate ($SrTiO_3$) via a simple hydrothermal method, and reduced graphene oxide via Hummers modified method.

➢ constructing multicomponent heterogeneous photocatalysts composites based on semiconductor oxides, graphene, and metal.

➢ Study the structures and physicochemical properties of the composites.

➢ Evaluate the capabilities of the composites for the adsorptive and photocatalytic activity for environmental cleanup applications.

➢ Determine the mechanisms of physical phenomena responsible for photocatalytic effects by numerical simulations of hybrid nanostructures using the DFT method approach.

References

[1] M. I. Ahamed, A. M. Asiri, and E. Lichtfouse, *Nanophotocatalysis and Environmental Applications*. Springer, 2019.

[2] Inamuddin, M. I. Ahamed, A. M. Asiri, and E. Lichtfouse, *Nanophotocatalysis and environmental applications: energy conversion and chemical transformations*. 2019.

[3] M. I. Fadlalla, P. Senthil Kumar, V. Selvam, and S. Ganesh Babu, "Recent Advances in Nanomaterials for Wastewater Treatment," in *Advanced Nanostructured Materials for Environmental Remediation*, vol. 25, Mu. Naushad, S. Rajendran, and F. Gracia, Eds. Cham: Springer International Publishing, 2019, pp. 21–58. doi: 10.1007/978-3-030-04477-0_2.

[4] M. Umar and H. Abdul, "Photocatalytic Degradation of Organic Pollutants in Water," in *Organic Pollutants - Monitoring, Risk and Treatment*, M. N. Rashed, Ed. InTech, 2013. doi: 10.5772/53699.

[5] P. Pichat, *Photocatalysis and Water Purification: From Fundamentals to Recent Applications*. John Wiley & Sons, 2013.

[6] S. Balakumar, V. Keller, and M. V. Shankar, Eds., *Nanostructured Materials for Environmental Applications*. Cham: Springer International Publishing, 2021. doi: 10.1007/978-3-030-72076-6.

[7] Z. Carmen and S. Daniel, "Textile Organic Dyes – Characteristics, Polluting Effects and Separation/Elimination Procedures from Industrial Effluents – A Critical Overview," in *Organic Pollutants Ten Years After the Stockholm Convention - Environmental and Analytical Update*, T. Puzyn, Ed. InTech, 2012. doi: 10.5772/32373.

[8] "Catalysts | Free Full-Text | Mechanistic Insights into Photodegradation of Organic Dyes Using Heterostructure Photocatalysts." https://www.mdpi.com/2073-4344/9/5/430 (accessed Feb. 05, 2022).

[9] I. K. Kapdan, F. Kargi, G. McMullan, and R. Marchant, "Biological Decolorization of Textile Dyestuff by Coriolus Versicolor in a Packed Column Reactor," *Environmental Technology*, vol. 21, no. 2, pp. 231–236, Feb. 2000, doi: 10.1080/09593330.2000.9618905.

[10] S. Khan and A. Malik, "Environmental and Health Effects of Textile Industry Wastewater," in *Environmental Deterioration and Human Health: Natural and anthropogenic determinants*, A. Malik, E. Grohmann, and R. Akhtar, Eds. Dordrecht: Springer Netherlands, 2014, pp. 55–71. doi: 10.1007/978-94-007-7890-0_4.

[11] "Potentials and applications of algal pigments in biology and industry in: Acta Botanica Hungarica Volume 49 Issue 1-2 (2007)." https://akjournals.com/configurable/content/journals$002f034$002f49$002f1-2$002farticle-p131.xml?t:ac=journals%24002f034%24002f49%24002f1-2%24002farticle-p131.xml (accessed Feb. 06, 2022).

[12] A. Saravanan *et al.*, "Effective water/wastewater treatment methodologies for toxic pollutants removal: Processes and applications towards sustainable development," *Chemosphere*, vol. 280, p. 130595, Oct. 2021, doi: 10.1016/j.chemosphere.2021.130595.

[13] H. Asakura and T. Matsuto, "Experimental study of behavior of endocrine-disrupting chemicals in leachate treatment process and evaluation of removal efficiency," *Waste Management*, vol. 29, no. 6, pp. 1852–1859, Jun. 2009, doi: 10.1016/j.wasman.2008.11.030.

[14] F. Renault, B. Sancey, P.-M. Badot, and G. Crini, "Chitosan for coagulation/flocculation processes – An eco-friendly approach," *European Polymer Journal*, vol. 45, no. 5, pp. 1337–1348, May 2009, doi: 10.1016/j.eurpolymj.2008.12.027.

[15] V. Homem and L. Santos, "Degradation and removal methods of antibiotics from aqueous matrices – A review," *Journal of Environmental Management*, vol. 92, no. 10, pp. 2304–2347, Oct. 2011, doi: 10.1016/j.jenvman.2011.05.023.

[16] P. Chelme-Ayala *et al.*, "Physico-Chemical Processes," *Water Environment Research*, vol. 81, no. 10, pp. 1056–1126, 2009, Accessed: Feb. 06, 2022. [Online]. Available: https://www.jstor.org/stable/29763348

[17] V. K. Gupta, R. Kumar, A. Nayak, T. A. Saleh, and M. A. Barakat, "Adsorptive removal of dyes from aqueous solution onto carbon nanotubes: A review," *Advances in Colloid and Interface Science*, vol. 193–194, pp. 24–34, Jun. 2013, doi: 10.1016/j.cis.2013.03.003.

[18] A. Mittal, D. Kaur, A. Malviya, J. Mittal, and V. K. Gupta, "Adsorption studies on the removal of coloring agent phenol red from wastewater using waste materials as adsorbents," *Journal of Colloid and Interface Science*, vol. 337, no. 2, pp. 345–354, Sep. 2009, doi: 10.1016/j.jcis.2009.05.016.

[19] Y. Zhou, J. Lu, Y. Zhou, and Y. Liu, "Recent advances for dyes removal using novel adsorbents: A review," *Environmental Pollution*, vol. 252, pp. 352–365, Sep. 2019, doi: 10.1016/j.envpol.2019.05.072.

[20] S. Natarajan, H. C. Bajaj, and R. J. Tayade, "Recent advances based on the synergetic effect of adsorption for removal of dyes from waste water using photocatalytic process," *Journal of Environmental Sciences*, vol. 65, pp. 201–222, Mar. 2018, doi: 10.1016/j.jes.2017.03.011.

[21] M. K. Guediri, D. Chebli, A. Bouguettoucha, R. Bourzami, and A. Amrane, "Novel Fe2TiO5/reduced graphene oxide heterojunction photocatalyst with improved adsorption capacity and visible light photoactivity: experimental and DFT approach," *Environmental Science and Pollution Research*, Oct. 2020, doi: 10.1007/s11356-020-11221-0.

[22] B.-C. Huang, J. Jiang, G.-X. Huang, and H.-Q. Yu, "Sludge biochar-based catalysts for improved pollutant degradation by activating peroxymonosulfate," *J. Mater. Chem. A*, vol. 6, no. 19, pp. 8978–8985, May 2018, doi: 10.1039/C8TA02282H.

[23] R. Saravanan, E. Thirumal, V. K. Gupta, V. Narayanan, and A. Stephen, "The photocatalytic activity of ZnO prepared by simple thermal decomposition method at various temperatures," *Journal of Molecular Liquids*, vol. 177, pp. 394–401, Jan. 2013, doi: 10.1016/j.molliq.2012.10.018.

[24] F. Tavasol, T. Tabatabaie, B. Ramavandi, and F. Amiri, "Photocatalyst production from wasted sediment and quality improvement with titanium dioxide to remove cephalexin in the presence of hydrogen peroxide and ultrasonic waves: A cost-effective technique," *Chemosphere*, vol. 284, p. 131337, Dec. 2021, doi: 10.1016/j.chemosphere.2021.131337.

[25] Y. Deng and R. Zhao, "Advanced Oxidation Processes (AOPs) in Wastewater Treatment," *Curr Pollution Rep*, vol. 1, no. 3, pp. 167–176, Sep. 2015, doi: 10.1007/s40726-015-0015-z.

[26] A. Stasinakis, "22. Stasinakis A.S. (2008) Use of selected advanced oxidation processes (AOPs) for wastewater treatment – A mini review.," *Global Nest Journal*, vol. 10, pp. 376–385, Nov. 2008.

[27] T. Oppenländer, *Photochemical Purification of Water and Air: Advanced Oxidation Processes (AOPs) - Principles, Reaction Mechanisms, Reactor Concepts*. John Wiley & Sons, 2007.

[28] R. Dewil, D. Mantzavinos, I. Poulios, and M. A. Rodrigo, "New perspectives for Advanced Oxidation Processes," *Journal of Environmental Management*, vol. 195, pp. 93–99, Jun. 2017, doi: 10.1016/j.jenvman.2017.04.010.

[29] J. Schneider, D. Bahnemann, J. Ye, G. Li Puma, and D. D. Dionysiou, Eds., *Photocatalysis - fundamentals and perspectives*. Cambridge: Royal Society of Chemistry, 2016.

[30] "Photocatalysis | Principles and Applications | Rakshit Ameta, Suresh C." https://www.taylorfrancis.com/books/mono/10.1201/9781315372396/photocatalysis-rakshit-ameta-suresh-ameta (accessed Feb. 05, 2022).

[31] J. N. Jebaranjitham and B. G. Kumar, "Heterogeneous Type-I and Type-II Catalysts for the Degradation of Pollutants," in *Green Photocatalysts*, vol. 34, Mu. Naushad, S. Rajendran, and E. Lichtfouse, Eds. Cham: Springer International Publishing, 2020, pp. 209–234. doi: 10.1007/978-3-030-15608-4_9.

[32] W. Hu, "INTRINSIC PHOTODYNAMIC STUDY ON PHOTOCATALYTIC MATERIALS," p. 24.

[33] H. Wang *et al.*, "Semiconductor heterojunction photocatalysts: design, construction, and photocatalytic performances," *Chemical Society Reviews*, vol. 43, no. 15, p. 5234, Jul. 2014, doi: 10.1039/C4CS00126E.

[34] N. H. Mohd Kaus, A. F. Rithwan, R. Adnan, M. L. Ibrahim, S. Thongmee, and S. F. Mohd Yusoff, "Effective Strategies, Mechanisms, and Photocatalytic Efficiency of Semiconductor Nanomaterials Incorporating rGO for Environmental Contaminant Degradation," *Catalysts*, vol. 11, no. 3, Art. no. 3, Mar. 2021, doi: 10.3390/catal11030302.

[35] J. Yan, H. Wu, H. Chen, Y. Zhang, F. Zhang, and S. F. Liu, "Fabrication of TiO2/C3N4 heterostructure for enhanced photocatalytic Z-scheme overall water splitting," *Applied Catalysis B: Environmental*, vol. 191, pp. 130–137, Aug. 2016, doi: 10.1016/j.apcatb.2016.03.026.

[36] Y. Li and S. C. E. Tsang, "Recent progress and strategies for enhancing photocatalytic water splitting," *Materials Today Sustainability*, vol. 9, p. 100032, Sep. 2020, doi: 10.1016/j.mtsust.2020.100032.

[37] P. A. K. Reddy, P. V. L. Reddy, E. Kwon, K.-H. Kim, T. Akter, and S. Kalagara, "Recent advances in photocatalytic treatment of pollutants in aqueous media," *Environment International*, vol. 91, pp. 94–103, May 2016, doi: 10.1016/j.envint.2016.02.012.

[38] F. Chen, X. Liu, W. Zhou, F. Li, C. Yu, and H. Ji, "The distinct role of non-noble metal Cu NPs deposition in boosting the overall photocatalytic performance over a ternary Zn-based photocatalyst system," *Journal of Alloys and Compounds*, vol. 875, p. 160068, Sep. 2021, doi: 10.1016/j.jallcom.2021.160068.

[39] X. Li, J. Yu, S. Wageh, A. A. Al-Ghamdi, and J. Xie, "Graphene in Photocatalysis: A Review," *Small*, vol. 12, no. 48, pp. 6640–6696, 2016, doi: 10.1002/smll.201600382.

[40] X. Li, R. Shen, S. Ma, X. Chen, and J. Xie, "Graphene-based heterojunction photocatalysts," *Applied Surface Science*, vol. 430, pp. 53–107, Feb. 2018, doi: 10.1016/j.apsusc.2017.08.194.

[41] N. M. Julkapli and S. Bagheri, "Graphene supported heterogeneous catalysts: An overview," *International Journal of Hydrogen Energy*, vol. 40, no. 2, pp. 948–979, Jan. 2015, doi: 10.1016/j.ijhydene.2014.10.129.

[42] G. Xie, K. Zhang, B. Guo, Q. Liu, L. Fang, and J. R. Gong, "Graphene-Based Materials for Hydrogen Generation from Light-Driven Water Splitting," *Advanced Materials*, vol. 25, no. 28, pp. 3820–3839, Jul. 2013, doi: 10.1002/adma.201301207.

[43] W. S. Koe, J. W. Lee, W. C. Chong, Y. L. Pang, and L. C. Sim, "An overview of photocatalytic degradation: photocatalysts, mechanisms, and development of photocatalytic membrane," *Environ Sci Pollut Res*, vol. 27, no. 3, pp. 2522–2565, Jan. 2020, doi: 10.1007/s11356-019-07193-5.

[44] Y. K. Jo, J. M. Lee, S. Son, and S.-J. Hwang, "2D inorganic nanosheet-based hybrid photocatalysts: Design, applications, and perspectives," *Journal of Photochemistry and Photobiology C: Photochemistry Reviews*, vol. 40, pp. 150–190, Sep. 2019, doi: 10.1016/j.jphotochemrev.2018.03.002.

[45] S. Morales-Torres, L. M. Pastrana-Martínez, J. L. Figueiredo, J. L. Faria, and A. M. T. Silva, "Design of graphene-based TiO2 photocatalysts—a review," *Environ Sci Pollut Res*, vol. 19, no. 9, pp. 3676–3687, Nov. 2012, doi: 10.1007/s11356-012-0939-4.

[46] J. Low, J. Yu, and W. Ho, "Graphene-Based Photocatalysts for CO2 Reduction to Solar Fuel," *J. Phys. Chem. Lett.*, vol. 6, no. 21, pp. 4244–4251, Nov. 2015, doi: 10.1021/acs.jpclett.5b01610.

[47] S. Zhang *et al.*, "Recent developments of two-dimensional graphene-based composites in visible-light photocatalysis for eliminating persistent organic pollutants from wastewater," *Chemical Engineering Journal*, vol. 390, p. 124642, Jun. 2020, doi: 10.1016/j.cej.2020.124642.

[48] A. Mondal, A. Prabhakaran, S. Gupta, and V. R. Subramanian, "Boosting Photocatalytic Activity Using Reduced Graphene Oxide (RGO)/Semiconductor Nanocomposites: Issues and Future Scope," *ACS Omega*, vol. 6, no. 13, pp. 8734–8743, Apr. 2021, doi: 10.1021/acsomega.0c06045.

[49] M.-Q. Yang, C. Han, N. Zhang, and Y.-J. Xu, "Precursor chemistry matters in boosting photoredox activity of graphene/semiconductor composites," *Nanoscale*, vol. 7, no. 43, pp. 18062–18070, Oct. 2015, doi: 10.1039/C5NR05143F.

[50] "Recent developments in physical, biological, chemical, and hybrid treatment techniques for removing emerging contaminants from wastewater," *Journal of Hazardous Materials*, vol. 416, p. 125912, Aug. 2021, doi: 10.1016/j.jhazmat.2021.125912.

[51] M. M. Ghangrekar and P. Chatterjee, "Water Pollutants Classification and Its Effects on Environment," in *Carbon Nanotubes for Clean Water*, R. Das, Ed. Cham: Springer International Publishing, 2018, pp. 11–26. doi: 10.1007/978-3-319-95603-9_2.

[52] S. Weber, S. Khan, and J. Hollender, "Human risk assessment of organic contaminants in reclaimed wastewater used for irrigation," *Desalination*, vol. 187, no. 1, pp. 53–64, Feb. 2006, doi: 10.1016/j.desal.2005.04.067.

[53] A. Ahamad, S. Madhav, A. K. Singh, A. Kumar, and P. Singh, "Types of Water Pollutants: Conventional and Emerging," in *Sensors in Water Pollutants Monitoring: Role of Material*, D. Pooja, P. Kumar, P. Singh, and S. Patil, Eds. Singapore: Springer, 2020, pp. 21–41. doi: 10.1007/978-981-15-0671-0_3.

[54] A. Tkaczyk, K. Mitrowska, and A. Posyniak, "Synthetic organic dyes as contaminants of the aquatic environment and their implications for ecosystems: A review," *Science of The Total Environment*, vol. 717, p. 137222, May 2020, doi: 10.1016/j.scitotenv.2020.137222.

[55] G. Crini and E. Lichtfouse, "Advantages and disadvantages of techniques used for wastewater treatment," *Environ Chem Lett*, vol. 17, no. 1, pp. 145–155, Mar. 2019, doi: 10.1007/s10311-018-0785-9.

[56] G. Crini, E. Lichtfouse, L. D. Wilson, and N. Morin-Crini, "Conventional and non-conventional adsorbents for wastewater treatment," *Environ Chem Lett*, vol. 17, no. 1, pp. 195–213, Mar. 2019, doi: 10.1007/s10311-018-0786-8.

[57] C. Trellu *et al.*, "Electro-oxidation of organic pollutants by reactive electrochemical membranes," *Chemosphere*, vol. 208, pp. 159–175, Oct. 2018, doi: 10.1016/j.chemosphere.2018.05.026.

[58] R. Liang, A. Hu, M. Hatat-Fraile, and N. Zhou, "Fundamentals on Adsorption, Membrane Filtration, and Advanced Oxidation Processes for Water Treatment," in *Nanotechnology for Water Treatment and Purification*, A. Hu and A. Apblett, Eds. Cham: Springer International Publishing, 2014, pp. 1–45. doi: 10.1007/978-3-319-06578-6_1.

[59] Z. Pan *et al.*, "Membrane technology coupled with electrochemical advanced oxidation processes for organic wastewater treatment: Recent advances and future prospects," *Chemical Engineering Journal*, vol. 376, p. 120909, Nov. 2019, doi: 10.1016/j.cej.2019.01.188.

[60] J. Wang, T. Zhang, Y. Mei, and B. Pan, "Treatment of reverse-osmosis concentrate of printing and dyeing wastewater by electro-oxidation process with controlled oxidation-reduction potential (ORP)," *Chemosphere*, vol. 201, pp. 621–626, Jun. 2018, doi: 10.1016/j.chemosphere.2018.03.051.

[61] J. Toth, *Adsorption*. CRC Press, 2002.

[62] D. M. Ruthven, "Past Progress and Future Challenges in Adsorption Research," *Ind. Eng. Chem. Res.*, vol. 39, no. 7, pp. 2127–2131, Jul. 2000, doi: 10.1021/ie000060d.

[63] V. Ponec, Z. Knor, and S. Cerny, *Adsorption on Solids*. Butterworth, 2018. Accessed: Feb. 06, 2022. [Online]. Available: https://modps71.lib.kmutt.ac.th/xmlui//handle/123456789/300

[64] W. J. T. FEng and B. Crittenden, *Adsorption Technology and Design*. Butterworth-Heinemann, 1998.

[65] A. Guediri, A. Bouguettoucha, D. Chebli, N. Chafai, and A. Amrane, "Molecular dynamic simulation and DFT computational studies on the adsorption performances of

methylene blue in aqueous solutions by orange peel-modified phosphoric acid," *Journal of Molecular Structure*, vol. 1202, p. 127290, Feb. 2020, doi: 10.1016/j.molstruc.2019.127290.

[66] D. Chebli, A. Bouguettoucha, T. Mekhalef, S. Nacef, and A. Amrane, "Valorization of an agricultural waste, Stipa tenassicima fibers, by biosorption of an anionic azo dye, Congo red," *Desalination and Water Treatment*, vol. 54, no. 1, pp. 245–254, 2015.

[67] A. Bouguettoucha, A. Reffas, D. Chebli, T. Mekhalif, and A. Amrane, "Novel activated carbon prepared from an agricultural waste, Stipa tenacissima, based on ZnCl2 activation—characterization and application to the removal of methylene blue," *Desalination and Water Treatment*, vol. 57, no. 50, pp. 24056–24069, 2016.

[68] S. Chaturvedi and P. N. Dave, "Environmental Application of Photocatalysis," *Materials Science Forum*, vol. 734, pp. 273–294, 2013, doi: 10.4028/www.scientific.net/MSF.734.273.

[69] P. G. Tratnyek and R. L. Johnson, "Nanotechnologies for environmental cleanup," *Nano Today*, vol. 1, no. 2, pp. 44–48, May 2006, doi: 10.1016/S1748-0132(06)70048-2.

[70] A. Abou Dalle, "Couplage d'un procédé électrochimique d'oxydation avancée, électro-Fenton, et d'un traitement biologique avancé pour l'élimination d'un composé pharmaceutique, le Métronidazole, en milieux aqueux," These de doctorat, Rennes, Ecole nationale supérieure de chimie, 2017. Accessed: Feb. 05, 2022. [Online]. Available: https://www.theses.fr/2017ENCR0043

[71] A. Kumar, *Advanced Ceramics for Energy and Environmental Applications*, 1st ed. Boca Raton: CRC Press, 2021. doi: 10.1201/9781003005155.

[72] K. Ordon, "Functionalized semiconducting oxides based on bismuth vanadate with anchored organic dye molecules for photoactive applications," These de doctorat, Le Mans, 2018. Accessed: Feb. 06, 2022. [Online]. Available: https://www.theses.fr/2018LEMA1006

[73] T. Xian, H. Yang, L. Di, J. Ma, H. Zhang, and J. Dai, "Photocatalytic reduction synthesis of SrTiO3-graphene nanocomposites and their enhanced photocatalytic activity," *Nanoscale Res Lett*, vol. 9, no. 1, p. 327, Dec. 2014, doi: 10.1186/1556-276X-9-327.

[74] M. I. Ahamed and E. Lichtfouse, *Water pollution and remediation: Photocatalysis*. Springer, 2021.

[75] D. Tian *et al.*, "Heterogeneous photocatalyst-driven persulfate activation process under visible light irradiation: From basic catalyst design principles to novel enhancement strategies," *Chemical Engineering Journal*, vol. 428, p. 131166, Jan. 2022, doi: 10.1016/j.cej.2021.131166.

[76] A. Kudo and Y. Miseki, "Heterogeneous photocatalyst materials for water splitting," *Chemical Society Reviews*, vol. 38, no. 1, pp. 253–278, 2009, doi: 10.1039/B800489G.

[77] R. P. S. Suri, J. Liu, D. W. Hand, J. C. Crittenden, D. L. Perram, and M. E. Mullins, "Heterogeneous photocatalytic oxidation of hazardous organic contaminants in water," *Water Environment Research*, vol. 65, no. 5, pp. 665–673, 1993, doi: 10.2175/WER.65.5.9.

[78] M. Kumarasamy, *Studies on Water Management Issues*. BoD – Books on Demand, 2012.

[79] C. K. Y. Park, "Semiconductor Interfaces and Solid Solutions for Enhanced Photocatalysis," p. 156.

[80] M. Kitano and M. Hara, "Heterogeneous photocatalytic cleavage of water," *J. Mater. Chem.*, vol. 20, no. 4, pp. 627–641, Jan. 2010, doi: 10.1039/B910180B.

[81] D. Friedmann, A. Hakki, H. Kim, W. Choi, and D. Bahnemann, "Heterogeneous photocatalytic organic synthesis: state-of-the-art and future perspectives," *Green Chemistry*, vol. 18, no. 20, pp. 5391–5411, 2016, doi: 10.1039/C6GC01582D.

[82] J. Kou, C. Lu, J. Wang, Y. Chen, Z. Xu, and R. S. Varma, "Selectivity Enhancement in Heterogeneous Photocatalytic Transformations," *Chem. Rev.*, vol. 117, no. 3, pp. 1445–1514, Feb. 2017, doi: 10.1021/acs.chemrev.6b00396.

[83] S. Bera, D.-I. Won, S. B. Rawal, H. J. Kang, and W. I. Lee, "Design of visible-light photocatalysts by coupling of inorganic semiconductors," *Catalysis Today*, vol. 335, pp. 3–19, Sep. 2019, doi: 10.1016/j.cattod.2018.11.001.

[84] L. Zhang and M. Jaroniec, "Toward designing semiconductor-semiconductor heterojunctions for photocatalytic applications," *Applied Surface Science*, vol. 430, pp. 2–17, Feb. 2018, doi: 10.1016/j.apsusc.2017.07.192.

[85] O. A. Arotiba, B. O. Orimolade, and B. A. Koiki, "Visible light–driven photoelectrocatalytic semiconductor heterojunction anodes for water treatment applications," *Current Opinion in Electrochemistry*, vol. 22, pp. 25–34, Aug. 2020, doi: 10.1016/j.coelec.2020.03.018.

[86] Y. Wu and T. He, "Ag loading induced visible light photocatalytic activity for pervoskite SrTiO 3 nanofibers," *Spectrochimica Acta Part A: Molecular and Biomolecular Spectroscopy*, vol. 199, pp. 283–289, Jun. 2018, doi: 10.1016/j.saa.2018.03.078.

[87] P. M. Nithya and L. G. Devi, "Effect of surface Ag metallization on the photocatalytic properties of BaTiO3: Surface plasmon effect and variation in the Schottky barrier height," *Surfaces and Interfaces*, Mar. 2019, doi: 10.1016/j.surfin.2019.03.005.

[88] S. Saris, A. Loiudice, M. Mensi, and R. Buonsanti, "Exploring Energy Transfer in a Metal/Perovskite Nanocrystal Antenna to Drive Photocatalysis," *The Journal of Physical Chemistry Letters*, vol. 10, no. 24, pp. 7797–7803, Dec. 2019, doi: 10.1021/acs.jpclett.9b03164.

[89] S. Wan, M. Chen, M. Ou, and Q. Zhong, "Plasmonic Ag nanoparticles decorated SrTiO3 nanocubes for enhanced photocatalytic CO2 reduction and H2 evolution under visible light irradiation," *Journal of CO2 Utilization*, vol. 33, pp. 357–364, Oct. 2019, doi: 10.1016/j.jcou.2019.06.024.

[90] Y. Li *et al.*, "Graphene-induced formation of visible-light-responsive SnO2-Zn2SnO4 Z-scheme photocatalyst with surface vacancy for the enhanced photoreactivity towards NO and acetone oxidation," *Chemical Engineering Journal*, vol. 336, pp. 200–210, Mar. 2018, doi: 10.1016/j.cej.2017.11.045.

[91] M. Humayun *et al.*, "Experimental and DFT Studies of Au Deposition Over WO3/g-C3N4 Z-Scheme Heterojunction," *Nano-Micro Letters*, vol. 12, no. 1, Jan. 2020, doi: 10.1007/s40820-019-0345-2.

[92] C. Du *et al.*, "Construction of Z-scheme g-C3N4 / MnO2 /GO ternary photocatalyst with enhanced photodegradation ability of tetracycline hydrochloride under visible light radiation," *Environmental Research*, vol. 200, p. 111427, Sep. 2021, doi: 10.1016/j.envres.2021.111427.

[93] H. Xu *et al.*, "Construction of Ag/AgCl-CN heterojunctions with enhanced photocatalytic activities for degrading contaminants in wastewater," *Journal of Colloid and Interface Science*, vol. 543, pp. 25–33, May 2019, doi: 10.1016/j.jcis.2019.01.133.

[94] K. Wei *et al.*, "One-step fabrication of g-C3N4 nanosheets/TiO2 hollow microspheres heterojunctions with atomic level hybridization and their application in the multi-component synergistic photocatalytic systems," *Applied Catalysis B: Environmental*, vol. 222, pp. 88–98, Mar. 2018, doi: 10.1016/j.apcatb.2017.09.070.

[95] R. Ebrahimi *et al.*, "Effects of doping zinc oxide nanoparticles with transition metals (Ag, Cu, Mn) on photocatalytic degradation of Direct Blue 15 dye under UV and visible light irradiation," *J Environ Health Sci Engineer*, vol. 17, no. 1, pp. 479–492, Jun. 2019, doi: 10.1007/s40201-019-00366-x.

[96] Y. Gao, M. Hu, and B. Mi, "Membrane surface modification with TiO2–graphene oxide for enhanced photocatalytic performance," *Journal of Membrane Science*, vol. 455, pp. 349–356, Apr. 2014, doi: 10.1016/j.memsci.2014.01.011.

[97] K. Lee, H. Yoon, C. Ahn, J. Park, and S. Jeon, "Strategies to improve the photocatalytic activity of TiO2: 3D nanostructuring and heterostructuring with graphitic carbon nanomaterials," *Nanoscale*, vol. 11, no. 15, pp. 7025–7040, Apr. 2019, doi: 10.1039/C9NR01260E.

[98] N. Fajrina and M. Tahir, "A critical review in strategies to improve photocatalytic water splitting towards hydrogen production," *International Journal of Hydrogen Energy*, vol. 44, no. 2, pp. 540–577, Jan. 2019, doi: 10.1016/j.ijhydene.2018.10.200.

[99] D. S. M. Constantino, M. M. Dias, A. M. T. Silva, J. L. Faria, and C. G. Silva, "Intensification strategies for improving the performance of photocatalytic processes: A review," *Journal of Cleaner Production*, p. 130800, Feb. 2022, doi: 10.1016/j.jclepro.2022.130800.

[100] R. Marschall, "Semiconductor Composites: Strategies for Enhancing Charge Carrier Separation to Improve Photocatalytic Activity," *Advanced Functional Materials*, vol. 24, no. 17, pp. 2421–2440, 2014, doi: 10.1002/adfm.201303214.

[101] W.-D. Oh and T.-T. Lim, "Design and application of heterogeneous catalysts as peroxydisulfate activator for organics removal: An overview," *Chemical Engineering Journal*, vol. 358, pp. 110–133, Feb. 2019, doi: 10.1016/j.cej.2018.09.203.

[102] S. Rahim Pouran, A. A. Abdul Raman, and W. M. A. Wan Daud, "Review on the application of modified iron oxides as heterogeneous catalysts in Fenton reactions," *Journal of Cleaner Production*, vol. 64, pp. 24–35, Feb. 2014, doi: 10.1016/j.jclepro.2013.09.013.

[103] Y. Huang *et al.*, "The application of perovskite materials in solar water splitting," *Journal of Semiconductors*, vol. 41, no. 1, p. 011701, Jan. 2020, doi: 10.1088/1674-4926/41/1/011701.

[104] M. M. Khan, S. F. Adil, and A. Al-Mayouf, "Metal oxides as photocatalysts," *Journal of Saudi Chemical Society*, vol. 19, no. 5, pp. 462–464, Sep. 2015, doi: 10.1016/j.jscs.2015.04.003.

[105] K. Kannan, D. Radhika, K. K. Sadasivuni, K. R. Reddy, and A. V. Raghu, "Nanostructured metal oxides and its hybrids for photocatalytic and biomedical

applications," *Advances in Colloid and Interface Science*, vol. 281, p. 102178, Jul. 2020, doi: 10.1016/j.cis.2020.102178.

[106] C. Karthikeyan, P. Arunachalam, K. Ramachandran, A. M. Al-Mayouf, and S. Karuppuchamy, "Recent advances in semiconductor metal oxides with enhanced methods for solar photocatalytic applications," *Journal of Alloys and Compounds*, vol. 828, p. 154281, Jul. 2020, doi: 10.1016/j.jallcom.2020.154281.

[107] N. S. Arul and V. D. Nithya, *Revolution of Perovskite*. Springer, 2020.

[108] S. Bhattacharjee, S. P. Chaudhary, and S. Bhattacharyya, "Lead-Free Metal Halide Perovskite Nanocrystals for Photocatalysis in Water," p. 27.

[109] A. Kumar, S. Kumar, and V. Krishnan, "Perovskite-Based Materials for Photocatalytic Environmental Remediation," in *Nanophotocatalysis and Environmental Applications*, vol. 29, Inamuddin, G. Sharma, A. Kumar, E. Lichtfouse, and A. M. Asiri, Eds. Cham: Springer International Publishing, 2019, pp. 139–165. doi: 10.1007/978-3-030-10609-6_5.

[110] S. Banerjee, A. Debnath, B. K. Allam, and N. Musa, "Adsorptive and photocatalytic performance of perovskite material for the removal of food dye in an aqueous solution," *Environmental Challenges*, vol. 5, p. 100240, Dec. 2021, doi: 10.1016/j.envc.2021.100240.

[111] P. Kanhere and Z. Chen, "A Review on Visible Light Active Perovskite-Based Photocatalysts," *Molecules*, vol. 19, no. 12, pp. 19995–20022, Dec. 2014, doi: 10.3390/molecules191219995.

[112] S. Tasleem and M. Tahir, "Recent progress in structural development and band engineering of perovskites materials for photocatalytic solar hydrogen production: A review," *International Journal of Hydrogen Energy*, vol. 45, no. 38, pp. 19078–19111, Jul. 2020, doi: 10.1016/j.ijhydene.2020.05.090.

[113] T. Ofoegbuna, P. Darapaneni, S. Sahu, C. Plaisance, and J. A. Dorman, "Stabilizing the B-site oxidation state in ABO_3 perovskite nanoparticles," *Nanoscale*, vol. 11, no. 30, pp. 14303–14311, 2019, doi: 10.1039/C9NR04155A.

[114] B. Kayaalp, "Design strategies towards SrTiO3 based perovskite nanostructures for environmental catalysis," 2019.

[115] Y. Hu *et al.*, "Layered perovskite oxides and their derivative nanosheets adopting different modification strategies towards better photocatalytic performance of water splitting," *Renewable and Sustainable Energy Reviews*, vol. 119, p. 109527, Mar. 2020, doi: 10.1016/j.rser.2019.109527.

[116] I. A. Abdel-Latif, A. A. Ismail, M. Faisal, A. M. Ali, A. E. Al-Salmi, and A. Al-Hajry, "Impact of the annealing temperature on perovskite strontium doped neodymium manganites nanocomposites and their photocatalytic performances," *Journal of the Taiwan Institute of Chemical Engineers*, vol. 75, pp. 174–182, Jun. 2017, doi: 10.1016/j.jtice.2017.03.030.

[117] H. Wang, Q. Zhang, M. Qiu, and B. Hu, "Synthesis and application of perovskite-based photocatalysts in environmental remediation: A review," *Journal of Molecular Liquids*, vol. 334, p. 116029, Jul. 2021, doi: 10.1016/j.molliq.2021.116029.

[118] I. A. Abdel-Latif, "Perovskite Strontium Doped Rare Earth Manganites Nanocomposites and Their Photocatalytic Performances," in *Nanocomposites - Recent Evolutions*, S. Sivasankaran, Ed. IntechOpen, 2019. doi: 10.5772/intechopen.79479.

[119] B. Bajorowicz *et al.*, "Perovskite-type KTaO3–reduced graphene oxide hybrid with improved visible light photocatalytic activity," *RSC Adv.*, vol. 5, no. 111, pp. 91315–91325, Oct. 2015, doi: 10.1039/C5RA18124K.

[120] B. Wang *et al.*, "Large-Scale Synthesis of Highly Luminescent Perovskite Nanocrystals by Template-Assisted Solid-State Reaction at 800 °C," *Chem. Mater.*, vol. 32, no. 1, pp. 308–314, Jan. 2020, doi: 10.1021/acs.chemmater.9b03804.

[121] R. E. Schaak and T. E. Mallouk, "Perovskites by Design: A Toolbox of Solid-State Reactions," *Chem. Mater.*, vol. 14, no. 4, pp. 1455–1471, Apr. 2002, doi: 10.1021/cm010689m.

[122] R. I. Walton, "Perovskite Oxides Prepared by Hydrothermal and Solvothermal Synthesis: A Review of Crystallisation, Chemistry, and Compositions," *Chemistry – A European Journal*, vol. 26, no. 42, pp. 9041–9069, 2020, doi: 10.1002/chem.202000707.

[123] S. Ananthakumar and S. Moorthy Babu, "Progress on synthesis and applications of hybrid perovskite semiconductor nanomaterials—A review," *Synthetic Metals*, vol. 246, pp. 64–95, Dec. 2018, doi: 10.1016/j.synthmet.2018.10.003.

[124] J. Ding, X. Lü, H. Shu, J. Xie, and H. Zhang, "Microwave-assisted synthesis of perovskite ReFeO3 (Re: La, Sm, Eu, Gd) photocatalyst," *Materials Science and Engineering: B*, vol. 171, no. 1, pp. 31–34, Jul. 2010, doi: 10.1016/j.mseb.2010.03.050.

[125] X. An, H. Lan, R. Liu, H. Liu, and J. Qu, "Light absorption modulation of novel Fe2TiO5 inverse opals for photoelectrochemical water splitting," *New J. Chem.*, vol. 41, no. 16, pp. 7966–7971, Aug. 2017, doi: 10.1039/C7NJ00294G.

[126] G. Seitz, N. Penin, L. Decoux, A. Wattiaux, M. Duttine, and M. Gaudon, "Near the Ferric Pseudobrookite Composition (Fe_2TiO_5)," *Inorg. Chem.*, vol. 55, no. 5, pp. 2499–2507, Mar. 2016, doi: 10.1021/acs.inorgchem.5b02847.

[127] H. D. Ngo *et al.*, "Structure and optical properties of sputter deposited pseudobrookite Fe_2TiO_5 thin films," *CrystEngComm*, vol. 21, no. 1, pp. 34–40, 2019, doi: 10.1039/C8CE01475B.

[128] M. Enhessari, M. K. Razi, L. Etemad, A. Parviz, and M. Sakhaei, "Structural, optical and magnetic properties of the Fe2TiO5 nanopowders," *Journal of Experimental Nanoscience*, vol. 9, no. 2, pp. 167–176, Feb. 2014, doi: 10.1080/17458080.2011.649432.

[129] J. L. Tholence, Y. Yeshurun, J. K. Kjems, and B. Wanklyn, "Spin dynamics and low temperature properties of the anisotropic spin glass Fe2TiO5," *Journal of Magnetism and Magnetic Materials*, vol. 54–57, pp. 203–204, Feb. 1986, doi: 10.1016/0304-8853(86)90551-2.

[130] W. Q. Guo, S. Malus, D. H. Ryan, and Z. Altounian, "Crystal structure and cation distributions in the FeTi2O5-Fe2TiO5 solid solution series," *Journal of Physics: Condensed Matter*, vol. 11, no. 33, p. 6337, 1999.

[131] B. L. Phoon, C. W. Lai, J. C. Juan, P.-L. Show, and G.-T. Pan, "Recent developments of strontium titanate for photocatalytic water splitting application," *International Journal of*

Hydrogen Energy, vol. 44, no. 28, pp. 14316–14340, May 2019, doi: 10.1016/j.ijhydene.2019.01.166.

[132] M. Guo and G. Ma, "Alteration of onset potentials of Rh-doped SrTiO3 electrodes for photoelectrochemical water splitting," *Journal of Catalysis*, vol. 391, pp. 241–246, Nov. 2020, doi: 10.1016/j.jcat.2020.08.029.

[133] M. A. Ferreira *et al.*, "Fabrication of SrTiO3/g-C3N4 heterostructures for visible light-induced photocatalysis," *Materials Science in Semiconductor Processing*, vol. 108, p. 104887, Mar. 2020, doi: 10.1016/j.mssp.2019.104887.

[134] C.-W. Chang and C. Hu, "Graphene oxide-derived carbon-doped SrTiO3 for highly efficient photocatalytic degradation of organic pollutants under visible light irradiation," *Chemical Engineering Journal*, vol. 383, p. 123116, Mar. 2020, doi: 10.1016/j.cej.2019.123116.

[135] S.-T. Huang, W. W. Lee, J.-L. Chang, W.-S. Huang, S.-Y. Chou, and C.-C. Chen, "Hydrothermal synthesis of SrTiO3 nanocubes: Characterization, photocatalytic activities, and degradation pathway," *Journal of the Taiwan Institute of Chemical Engineers*, vol. 45, no. 4, pp. 1927–1936, Jul. 2014, doi: 10.1016/j.jtice.2014.02.003.

[136] "A review of synthesis and morphology of SrTiO3 for energy and other applications - Phoon - 2019 - International Journal of Energy Research - Wiley Online Library." https://onlinelibrary.wiley.com/doi/abs/10.1002/er.4505 (accessed Feb. 07, 2022).

[137] F. Sultanov *et al.*, "Influence of Metal Oxide Particles on Bandgap of 1D Photocatalysts Based on SrTiO3/PAN Fibers," *Nanomaterials*, vol. 10, no. 9, Art. no. 9, Sep. 2020, doi: 10.3390/nano10091734.

[138] H. Sudrajat, M. M. Fadlallah, S. Tao, M. Kitta, N. Ichikuni, and H. Onishi, "Dopant site in indium-doped SrTiO3 photocatalysts," *Phys. Chem. Chem. Phys.*, vol. 22, no. 34, pp. 19178–19187, Sep. 2020, doi: 10.1039/D0CP02822C.

[139] A. Chen, S. V. Nair, B. Miljkovic, C. Souza, H. E. Ruda, and Z. Ji, "Electronic structure of bulk and two-dimensional SrTiO3: DFT calculation with GGA + U methods," *Journal of Nanoparticle Research*, vol. 22, no. 9, Sep. 2020, doi: 10.1007/s11051-020-04994-5.

[140] Y.-C. Yang, L. Xu, W.-Q. Huang, C.-Y. Luo, G.-F. Huang, and P. Peng, "Electronic structures and photocatalytic responses of SrTiO3 (100) surface interfaced with graphene, reduced graphene oxide, and graphane: surface termination effect," *The Journal of Physical Chemistry C*, vol. 119, no. 33, pp. 19095–19104, 2015.

[141] J. Qu, T. Che, L. Shi, Q. Lu, and S. Qi, "A novel magnetic silica supported spinel ferrites NiFe2O4 catalyst for heterogeneous Fenton-like oxidation of rhodamine B," *Chinese Chemical Letters*, 2019.

[142] J. L. Gunjakar, A. M. More, K. V. Gurav, and C. D. Lokhande, "Chemical synthesis of spinel nickel ferrite (NiFe2O4) nano-sheets," *Applied Surface Science*, vol. 254, no. 18, pp. 5844–5848, Jul. 2008, doi: 10.1016/j.apsusc.2008.03.065.

[143] A. Vasanthakumar, G. G. Redhi, and R. M. Gengan, "Efficient catalytic activity of ionic liquid-supported NiFe2O4 magnetic nanoparticle doped Titanium Dioxide nano-composite," Dec. 2016, doi: 10.18178/ijcea.2016.7.6.618.

[144] A. Alarifi, N. M. Deraz, and S. Shaban, "Structural, morphological and magnetic properties of NiFe2O4 nano-particles," *Journal of Alloys and Compounds*, vol. 486, no. 1–2, pp. 501–506, Nov. 2009, doi: 10.1016/j.jallcom.2009.06.192.

[145] B. Vara Prasad, K. V. Ramesh, and A. Srinivas, "Structural and magnetic studies of nano-crystalline ferrites MFe2O4 (M= Zn, Ni, Cu, and Co) synthesized via citrate gel autocombustion method," *Journal of superconductivity and Novel magnetism*, vol. 30, no. 12, pp. 3523–3535, 2017.

[146] Q.-C. Sun *et al.*, "Optical band gap hierarchy in a magnetic oxide: Electronic structure of NiFe$\{\}_\{2\}$O$\{\}_\{4\}$," *Phys. Rev. B*, vol. 86, no. 20, p. 205106, Nov. 2012, doi: 10.1103/PhysRevB.86.205106.

[147] S. Fatima, S. I. Ali, D. Younas, A. Islam, D. Akinwande, and S. Rizwan, "Graphene nanohybrids for enhanced catalytic activity and large surface area," *MRS Communications*, pp. 1–10, undefined/ed, doi: 10.1557/mrc.2018.194.

[148] Z. Zhen and H. Zhu, "1 - Structure and Properties of Graphene," in *Graphene*, H. Zhu, Z. Xu, D. Xie, and Y. Fang, Eds. Academic Press, 2018, pp. 1–12. doi: 10.1016/B978-0-12-812651-6.00001-X.

[149] N. M. R. Peres, "Colloquium: The transport properties of graphene: An introduction," *Rev. Mod. Phys.*, vol. 82, no. 3, pp. 2673–2700, Sep. 2010, doi: 10.1103/RevModPhys.82.2673.

[150] R. Ma *et al.*, "Multidimensional graphene structures and beyond: Unique properties, syntheses and applications," *Progress in Materials Science*, vol. 113, p. 100665, Aug. 2020, doi: 10.1016/j.pmatsci.2020.100665.

[151] L. De Marchi, C. Pretti, B. Gabriel, P. A. A. P. Marques, R. Freitas, and V. Neto, "An overview of graphene materials: Properties, applications and toxicity on aquatic environments," *Science of The Total Environment*, vol. 631–632, pp. 1440–1456, Aug. 2018, doi: 10.1016/j.scitotenv.2018.03.132.

[152] Y. Zhu *et al.*, "Graphene and Graphene Oxide: Synthesis, Properties, and Applications," *Advanced Materials*, vol. 22, no. 35, pp. 3906–3924, Sep. 2010, doi: 10.1002/adma.201001068.

[153] C. Wang and D. Astruc, "Recent developments of metallic nanoparticle-graphene nanocatalysts," *Progress in Materials Science*, vol. 94, pp. 306–383, May 2018, doi: 10.1016/j.pmatsci.2018.01.003.

[154] M. K. Ahmed, M. E. El-Naggar, A. Aldalbahi, M. H. El-Newehy, and A. A. Menazea, "Methylene blue degradation under visible light of metallic nanoparticles scattered into graphene oxide using laser ablation technique in aqueous solutions," *Journal of Molecular Liquids*, vol. 315, p. 113794, Oct. 2020, doi: 10.1016/j.molliq.2020.113794.

[155] Y. Fu, H. Chen, X. Sun, and X. Wang, "Graphene-supported nickel ferrite: A magnetically separable photocatalyst with high activity under visible light," *AIChE Journal*, vol. 58, no. 11, pp. 3298–3305, 2012.

[156] H. Yao, X. Guo, A. Bao, H. Mao, Y. Ma, and X. Li, "Graphene-based heterojunction for enhanced photodetectors," *Chinese Phys. B*, 2021, doi: 10.1088/1674-1056/ac1b8b.

[157] S. Singh, M. Faraz, and N. Khare, "Recent Advances in Semiconductor–Graphene and Semiconductor–Ferroelectric/Ferromagnetic Nanoheterostructures for Efficient

Hydrogen Generation and Environmental Remediation," *ACS Omega*, vol. 5, no. 21, pp. 11874–11882, Jun. 2020, doi: 10.1021/acsomega.9b03913.

[158] X. Cui, L. Tian, X. Xian, H. Tang, and X. Yang, "Solar photocatalytic water oxidation over Ag3PO4/g-C3N4 composite materials mediated by metallic Ag and graphene," *Applied Surface Science*, vol. 430, pp. 108–115, Feb. 2018, doi: 10.1016/j.apsusc.2017.07.290.

[159] A. T. Kuvarega, R. Selvaraj, and B. B. Mamba, "Graphene-Based Photocatalytic Materials: An Overview," in *Nanostructured Materials for Environmental Applications*, S. Balakumar, V. Keller, and M. V. Shankar, Eds. Cham: Springer International Publishing, 2021, pp. 433–454. doi: 10.1007/978-3-030-72076-6_17.

[160] M. S. Sajna, S. M. Simon, N. V. Unnikrishnan, and K. K. Sadasivuni, "An Overview of Graphene-Based 2D/3D Nanostructures for Photocatalytic Applications," *Top Catal*, Jan. 2022, doi: 10.1007/s11244-021-01539-5.

[161] Z. Mengting *et al.*, "Applicability of BaTiO3/graphene oxide (GO) composite for enhanced photodegradation of methylene blue (MB) in synthetic wastewater under UV–vis irradiation," *Environmental Pollution*, vol. 255, p. 113182, Dec. 2019, doi: 10.1016/j.envpol.2019.113182.

[162] Y. Wang, H. Wu, Z. Liu, H. Zhao, H. Liu, and Y. Zhang, "Bottom-up construction of reduced-graphene-oxide-anchored MnO with an nitrogen-doped carbon coating for synergistically improving lithium-ion storage," *Inorganic chemistry*, vol. 57, no. 21, pp. 13693–13701, 2018.

[163] A. Hazra and S. Basu, "Graphene Nanoribbon as Potential On-Chip Interconnect Material—A Review," *C*, vol. 4, no. 3, Art. no. 3, Sep. 2018, doi: 10.3390/c4030049.

[164] A. Garg, S. Basu, N. P. Shetti, and K. R. Reddy, "2D materials and its heterostructured photocatalysts: Synthesis, properties, functionalization and applications in environmental remediation," *Journal of Environmental Chemical Engineering*, vol. 9, no. 6, p. 106408, Dec. 2021, doi: 10.1016/j.jece.2021.106408.

[165] S. Tasleem and M. Tahir, "Recent progress in structural development and band engineering of perovskites materials for photocatalytic solar hydrogen production: A review," International Journal of Hydrogen Energy, vol. 45, no. 38, pp. 19078–19111, Jul. 2020, doi: 10.1016/j.ijhydene.2020.05.090.

[166] N. S. Arul and V. D. Nithya, Revolution of Perovskite. Springer, 2020.

Quantum-chemical calculations and characterization techniques

2. Quantum-chemical calculations and characterization techniques

2.1. Quantum-chemical calculations

The purpose of the computational work was to investigate the electronic structure of each catalyst independently as well as their composite multilayered structures. Computational results were also used to better understand of the energy associated with interfaces and mixing.

Several breakthroughs in quantum chemistry and mathematics have paved the way for novel techniques to solving the Schrödinger equation for many-body systems [1], [2]. Hohenburg and Kohn decreased the complexity of the many-body problem by focusing on electron density rather than electron wavefunctions [3], [4]. The work of Hohenburg and Kohn laid the groundwork for Kohn and Sham, who made major advances by demonstrating that multiple interacting electrons in an effective potential can be mapped to a set of non-interacting electrons. These discoveries resulted in the creation of exchange and correlation functional, which may be used to correlate energy to the electron density function [5]. Density functional theory evolved as an accurate and computationally less demanding way for studying the behavior of chemical systems by viewing the system's energy as a functional of the electron density [6].

2.1.1. Hartree-Fock and hybrid methods

The Hartree-Fock approach evolved from a separate set of approximations. The Hartree-Fock approach is based on the assumption that the wavefunction of a system of many electrons can be expressed as a Slater determinant. In these computations, electron correlation energy is neglected, but exchange energy is exact [7]–[9].

Density functional theory is a ground-state theory, which means that it models a many-body system in its lowest-energy state [10], [11]. Because of the imprecise nature of the Kohn-Sham potential, DFT is known to underestimate band gaps (exchange-correlation energy) [12], [13]. While DFT frequently underestimates bandgap energy, the Hartree-Fock approach frequently overestimates bandgap energies. To address this issue, hybrid functionals have been shown to provide accurate bandgap values for a variety of materials. B3LYP, which stands for Becke 3-parameter Lee-Yang-Parr, is a well-known hybrid exchange-correlation energy functional that combines Hartree-Fock and DFT energies [14].

2.1.2. Density Functional Theory (DFT)

Density Functional Theory (DFT) is now one of the most extensively utilized methods in quantum computations of matter's electronic structure (atoms, molecules, solids), as well as in condensed matter physics and quantum chemistry [4], [10], [15], [16]. Hohenberg, Kohn, and Sham developed this technology in two stages, in 1964 and 1965. It entails reducing a problem with several bodies to a problem with only one body in an effective field while accounting for all system interactions. The concept is that the precise features of the ground state of a system composed of nuclei and electrons are functional (function of a function) of electron density.

2.1.2.1.Calculation codes

There are numerous DFT-based calculation codes, such as Dmol3, VASP, ABINIT, CRYSTAL, and BigDFT [17]. All of the calculations described in this paper were carried out using the numerical modeling code CASTEP (Cambridge Serial Total Energy Package), which was created by Payne et al. in 1988 [18], [19]. This is an ab-initio calculation code that is part of Accelrys' Material Studio suite of digital simulation software. This code is based on Density Functional Theory (DFT) and employs the pseudo-potentials method and a wavebase to simulate the properties of solids, interfaces, and surfaces for a wide range of material classes [20]–[22]. CASTEP simplifies the number and type of atoms in order to solve Schrödinger's equation and calculates characteristics such as lattice constants, molecular geometry, structural properties, band structures, densities of states, charge densities, wave function, and optical properties [23], [24]. Parallel versions of the code are also available for simulating huge systems with hundreds of atoms. The CASTEP code involves the entry of the space group, mesh parameter, pseudo-potentials, and functional type (LDA, GGA...).

2.2. Characterization techniques

2.2.1. X-ray diffraction (XRD)

The technique of X-ray diffraction is used to determine the crystallinity, phase structure lattice characteristics, structural identification, and texture of a sample [25]–[27]. During the analysis, X-rays are emitted using a cathode ray tube, which is then filtered to produce monochromatic radiation, which is then collimated and directed towards the sample (Figure 2.1) [28]. When the sample interacts with the light rays, constructive interference and diffraction occur in accordance with Bragg's Law:

$$2d_{hkl} \sin\theta = n\lambda \qquad (2.1)$$

$$d_{hkl} = \frac{1}{\sqrt{\frac{h^2}{a^2}+\frac{k^2}{b^2}+\frac{l^2}{c^2}}} \quad (2.2)$$

Where, n is an integer, λ is the wavelength of the X-rays measured in angstrom, and d is the interplanar spacing that generates the diffraction in angstrom and θ is the angle of diffraction.

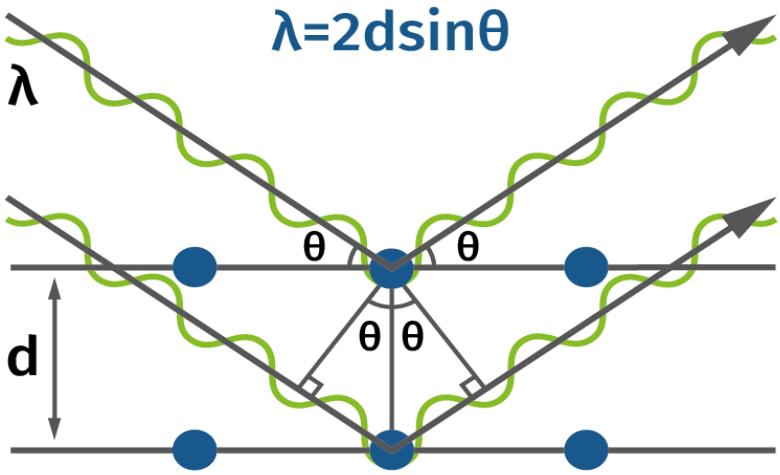

Figure. 2.1. *Representation diagram of incident and diffraction rays [28].*

In a crystalline sample, it is a relationship between the wavelength of electromagnetic radiation and the diffraction angle and lattice spacing . The diffracted X-rays are then transmitted to the detector for processing and counting. The crystalline size and microstrain of the samples can also be obtained using the XRD. Profile widths also provide determine the average grain seizes (D), microconstraint (ξ%) and dislocation density (δ) according to the Debye-Scherrer relation, equations (2.3) (2.4), and (2.5)

$$D = \frac{K\lambda}{\beta \cos\theta} \quad (2.3)$$

$$\xi\% = \frac{\beta}{4 \tan\theta} \quad (2.4)$$

$$\delta = \frac{1}{D^2} \quad (2.5)$$

D is the crystalline size

λ is the wavelength of the x-rays

K is the dimensionless constant,

θ is the Bragg angle

β is the full width at half-maximum (FWHM) of the peak in radians corrected for instrumental broadening and is equal to 0.154059 nm.

X-ray diffraction was used to identify the crystallographic phases with a Siemens D5000 diffractometer, a Bragg-Brentano-geometry and vertical 2-theta goniometer and operated at 45 kV using Cu Kα1 radiation. Diffractograms were carried out in a 2-theta range from 4 ° to 85 ° with an angular step of 0.0167° and an accumulation time of 6.985 s per step.

2.2.2. X-ray fluorescence analysis (XRF)

XRF is an analytical technique used to determine the chemical composition of a variety of materials (solids, liquids, powders, and so on); it is also used to determine the thickness and composition of layers and coatings [29], [30]. The technique is also a useful analysis technique in research and pharmaceuticals. The precision and reproducibility of XRF analysis are extremely good. When good standard specimens are available, very accurate results can be obtained, but they can even be obtained in cases where no specific standards can be established.

The sample is irradiated with X-rays produced by a source in XRF. The source is usually an X-ray tube, although it could also be a synchrotron or a radioactive material in some situations [31]. The elements present in the sample will emit fluorescent X-ray radiation with distinct energies (corresponding to optical light hues) that are unique to these elements. Distinct energy corresponds to a distinct color. It is possible to detect which elements are present by measuring the energy (or colors) of the radiation emitted by the sample. This is the qualitative analysis step. The amount of each element present in the sample may be determined by measuring the intensities of the emitted energy (colors). This is known as quantitative analysis.

2.2.3. Scanning Electron Microscopy (SEM)

Scanning Electron Microscopy (SEM) is a type of electron microscopy used to determine a material's surface [32], [33]. The sample is positioned in a raster pattern using an electron beam. The SEM has an electron gun, which generates a beam of electrons in a column and onto a series of electromagnetic lenses that are tuned wrapped in coils referred as solenoids. The coils can be adjusted to focus the electron beam on the sample, causing voltage variations that can increase or decrease the speed at which the electrons interact with the material surface. When the instrument's electrons interact with the electrons in the sample, electrons are emitted in the form of a signal from the sample's surface conveying information about the sample's surface, shape, texture, and composition, and an image is formed (figure 2.2) [28], [34].

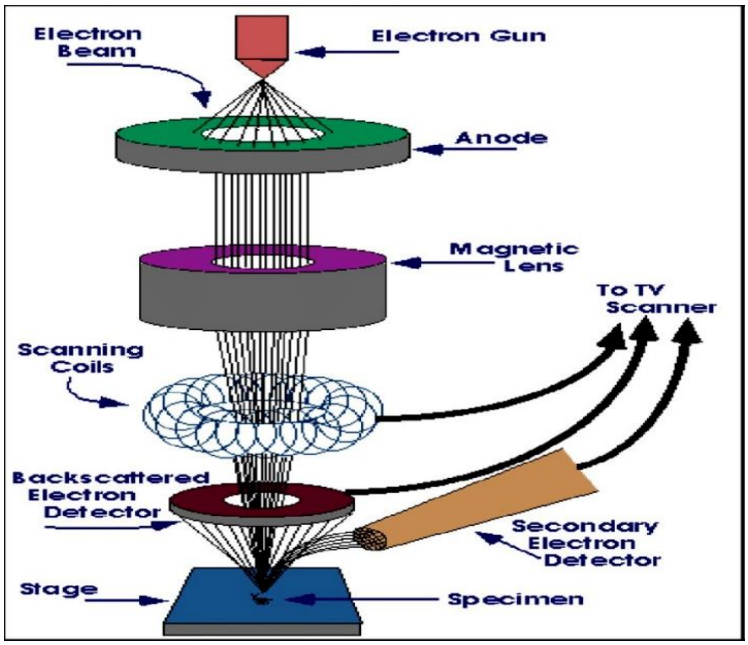

Figure 2.2. *Schematic diagram of scanning electron Microscopy [28].*

The surface morphology and elemental composition of all nanocomposites was investigated with FEI QUANTA 250 FEG scanning electron microscopy (SEM; FEI, Hillsboro, OR, USA), with 10 KV as acceleration voltage.

2.2.4. Energy dispersive X-ray spectrometry (EDX)

Energy dispersive X-ray spectroscopy (EDS) is a technique for quantitative and qualitative material analysis that is often used as an attachment to SEM and TEM [28], [34]. It provides information about the elemental surface composition of the materials.

2.2.5. Dynamic light scattering (DLS)

Dynamic light scattering (DLS) is a typical technique for determining particle size in colloidal dispersions that involves illuminating a suspension of particles or droplets with a coherent and monochromatic light, such as a laser beam [35]–[37]. When light is scattered off particles in suspension, Brownian motion creates time-dependent fluctuations in the local concentration of the particles, resulting in fluctuations in the intensity of the scattered light (figure 2.3) [38], [39].

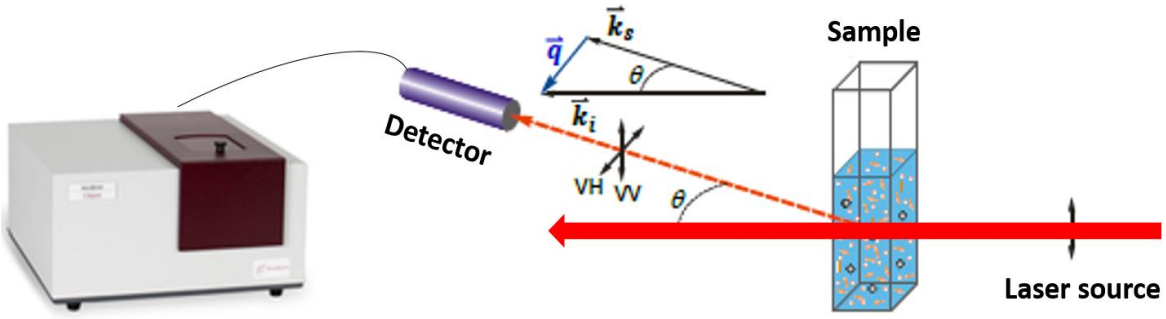

Figure 2.3. *Schematic diagram of dynamic light scattering*

2.2.6. UV-visible Spectrophotometry

One of the earliest instrumental techniques in chemical analysis is ultraviolet-visible (UV-Vis) spectroscopy. The phenomenon of electromagnetic radiation absorption by matter has a wide range of applications, including particle structure studies and qualitative and quantitative chemical analysis [40], [41]. The absorption of visible light and ultraviolet radiation is determined by the molecule's and compound's structures. The absorption of specified radiation leads electrons to move from ground states to higher energy levels, known as excited states.

Generally in a UV-Vis, a beam of light with wavelength in the range of 200-1000 nm passes through the moochromator, which then passes through a cuvette carrying the sample. The samples absorbs the ultra violet or visible light irradiation. The amount of light the sample absorbs depends on the concentration, the path length of light passing through the sample and how well the sample absorbs the light with certain wavelength. The amount of absorption by the samples is related to the concentration of the samples and is given by the relation Lambert-Beer's law equation (2.9) [3], [28]. Figure 2.4 shows the schematic diagram of UV-Vis.

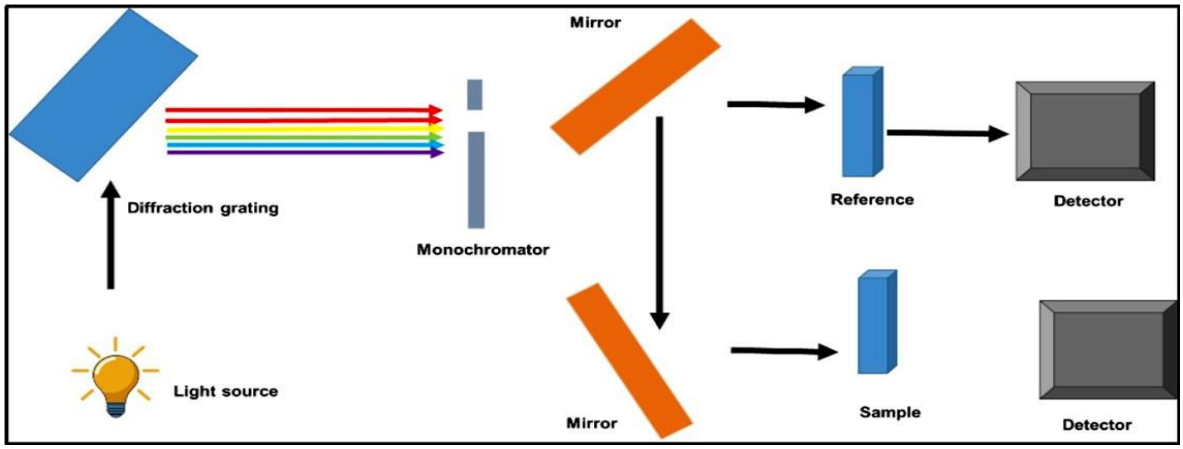

Figure 2.4. *Schematic diagram of UV-Vis.*

In a practical application, when electromagnetic radiation crosses a matter, it can be absorbed, reflected or dispersed. The intensity of the incident beam is given by [28]:

$$I_0 = I_a + I_t + I_r \qquad (2.6)$$

where I_a is intensity of radiation absorbed by the material, the I_t and I_r are related respectively to the transmitted and reflected as well as diffused light.

Since radiation absorption measurements are usually made in relation to the reference solution which composition should be similar to that of the sample and they should be in identical cuvettes, the reflected and diffused radiation I_r in both cases is identical and may be omitted. One may assume that the reference solution under the measurement conditions does not absorb radiation and the intensity of the radiation beam passing through the reference solution is equal to the intensity of the incident beam on the sample.

The ratio of the intensity of the radiation passing through the sample I_t to the intensity of radiation incident on the sample I_a (equal to the intensity of the radiation passing through the reference), is called transmittance or permeability and is denoted as [3], [28]:

$$T = \frac{I_t}{I_0} \qquad (2.7)$$

The intensity of absorbed radiation depends on the concentration of the solution *c* and on the thickness of the absorbing layer *l* (2.9) and is described by the Lambert-Beer law, which takes the logarithmic form [3], [28]:

$$A = \log \frac{I_0}{I_t} = kcl \qquad (2.8)$$

Where *k* is a proportionality constant (radiation absorption coefficient, often called the absorption coefficient). The decimal logarithm of the intensity ratio of the radiation beam incident on the sample I_0 to the intensity of the radiation beam passing through the sample I_t is called absorbance. I_t takes values from zero to infinity.

When the concentration of the solution *c* is expressed in mol/dm^3 and the thickness of the layer *l* is expressed in cm, the proportionality coefficient *k* is called the molar absorption coefficient ε. In consequence, the Eq. (2.9) takes the form [3], [28]:

$$A = \varepsilon lc \qquad (2.9)$$

This is the basic law of absorption spectrophotometry. The relationship between absorbance and transmittance is expressed by the relation [3], [28]:

$$A = \log \frac{1}{T} \qquad (2.10)$$

For the photocatalytic tests, the concentrations of the samples were measured before and after adsorption using a UV-visible spectrophotometer (Shimadzu 1700 UV-vis Spectrophotometer) at λ_{max} = 664 nm of methylene blue (MB).

2.2.7. Diffuse Reflectance Spectroscopy (DRS)

DRS spectroscopy is a spectroscopic technique based on the reflection of light by a powdered sample in the ultraviolet (UV), visible (VIS), and near infrared (NIR) regions. The ratio of light scattered from an infinitely thick layer to light scattered from an ideal non-absorbing reference sample is measured as a function of wavelength in a DRS spectrum. Incident radiation illumination of powdered samples results in diffuse illumination of the samples [42], [43]. The incident light is absorbed in part and scattered in part. The scattered radiation emitted by the sample is collected and detected in an integration sphere. Figure 2.5, shows a simplified representation of this.

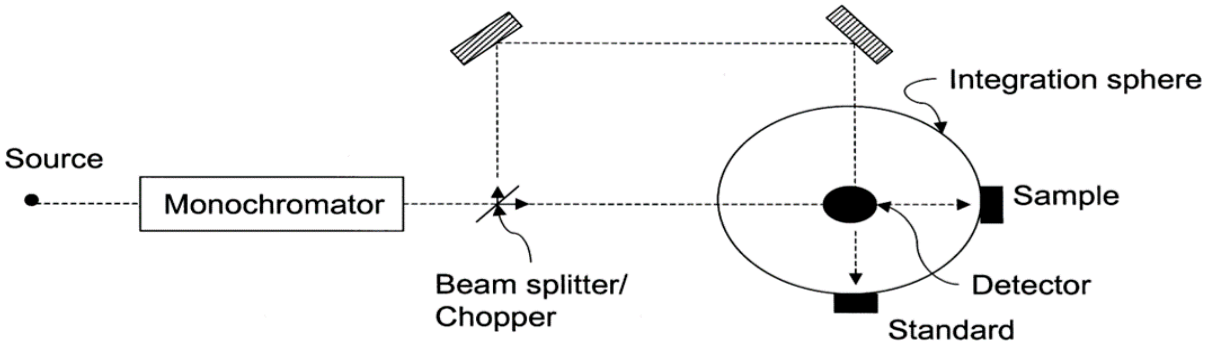

Figure. 2.5. *Schematic overview of a diffuse reflectance spectrophotometer with integration sphere [43].*

The basic equation for the phenomenological description of diffuse reflection is the radiation transfer equation [44], [45]:

$$\frac{-\mathrm{d}I}{\kappa\rho\mathrm{d}S} = I - \frac{j}{\kappa} \qquad (2.11)$$

Where *I* is the incident light intensity of a given wavelength; d*I*/d*S* the change of the intensity with the path length d*S*; ρ the density of the medium; κ an attenuation coefficient corresponding with the total radiation loss due to absorption and scattering; *j* is the scattering function.

Equation (2.11) can be solved by incorporating simplifications relating to easily achievable experimental conditions. The Schuster–Kubelka–Munk (S–K–M) theory simplifies the

solution of the radiative transfer Equation (2.11), which was first proposed by Schuster and later developed by Kubelka and Munk. The incident and scattered light fluxes are approximated in this theory by two fluxes *I* and *j* that are perpendicular to the surface of the powdered sample but in the opposite direction. This is depicted in Figure 2.6. *I* represents the flow of monochromatic diffuse illumination, while *j* represents the flux of diffusively dispersed light. If the sample is infinitely thick, the diffuse reflection (R_∞) is connected to an apparent absorption (K) and an apparent scattering coefficient (S) by using the Schuster–Kubelka–Munk (S–K–M) or Kubelka–Munk (K–M) function [44], [45]:

$$F(R_\infty) = \frac{(1-R_\infty)^2}{2R_\infty} = \frac{K}{S} \qquad (2.12)$$

The incident and remitted light fluxes are approximated by two opposite fluxes, perpendicular to the surface of the infinitely thick sample layer.

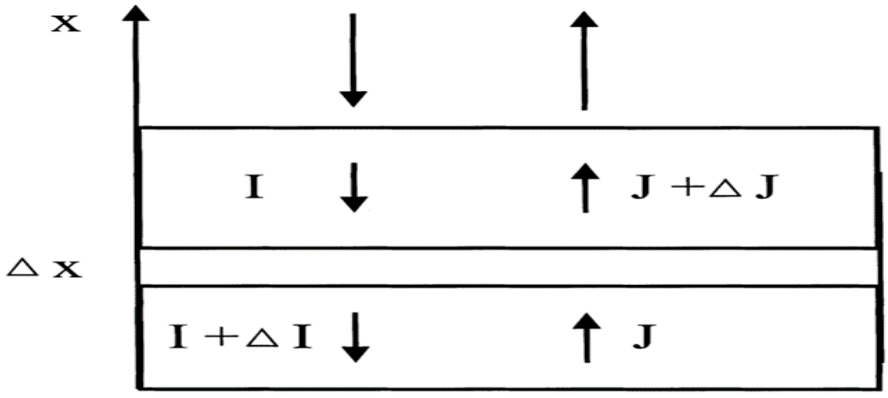

Figure. 2.6. *The Schuster–Kubelka–Munk approximation in diffuse reflectance spectroscopy.*

To quantify E_g, the absorption coefficients '$F(R_\infty)$' must be deduced from the reflectance curves 'R', according to the Kubelka-Munk formula.

According to the Davis-Mott relationship for which the values of α are above 104 cm^{-1} the data follows the Tauc equation (2.13):

$$\alpha hv = A(hv - Eg)^n \qquad (2.13)$$

The absorbance (A) depends on the transition probability, α is the absorption coefficient, *Eg* is the optical band gap and n is the number with transition processes and the values of 2, 2/3, 1/2 or 1/3 can be either direct (allowed), direct (forbidden), indirect (allowed) and indirect (forbidden) respectively.

The band gap 'E_g' is estimated through Tauc plot on the linear part of $(\alpha.h\upsilon)^n \propto (h\upsilon - E_g)$,

Another characteristic parameters, which can be evaluated and discussed through the UV-Vis-DRS is the Urbach energy 'E_U' [46], [47]. This energy characterizes the variation in the electronic band structure caused by different origins (vacant or interstitial sites, lattice strain, dislocation…); it characterizes additional states within the band gap near HOMO and LUMO levels, and can be seen as tails of conduction and valence bands. E_U is roughly equal to the average width of tails.

The Urbach energy E_U is evaluated using the relation (2.14) [43]:

$$F(R) = \alpha_0 \, exp\left(\frac{h\nu - E_0}{E_u}\right) \qquad (2.14)$$

Where, α_0 and E_0 are constants relative to the studied compounds.

'E_U' is estimated through the plot of $\ln[F(R_\infty)] \propto h\upsilon$ and it is evaluated from the slope of the linear part: $\ln[F(R_\infty)] \propto (h\upsilon - E_0)$.

Optical transmission and absorption spectra were performed in Ultraviolet-Visible Diffuse Reflection Spectroscopy (UV-Vis-DRS) spectrometer, Shimadzu UV-3600 spectrophotometer with a Harrick Praying Mantis accessory, in the range of 200-to1000 nm.

2.2.8. Fourier Transform Infra-Red

The Fourier transform-infrared spectroscopy (FTIR) is a technique for determining the structure and functional groups of materials [48]–[50]. A typical FTIR consists of two independent beams from the IR-source that travel through the sample and reference chambers (Figure. 2.7) [28]. The optical chopper focuses the reference and sample beams. For analytical comparison of transmitted photon wave front information, one beam passes through the sample and the second beam travels through a reference sample. After the incident radiation passes through the sample, a wave front of radiation is dispersed into the instrument frequencies by gratings and slits. Varied slit sizes have different effects on the results. Narrow slits provide higher resolution and the ability to discriminate between the separated frequencies of radiation, but broader slits allow more light to flow through the sample and reach the detector, resulting in good system sensitivity. The emitted wave front beam strikes the detector, generating an electrical signal as a response, which is then processed by the computer using a mathematical algorithm to produce the final spectrum.

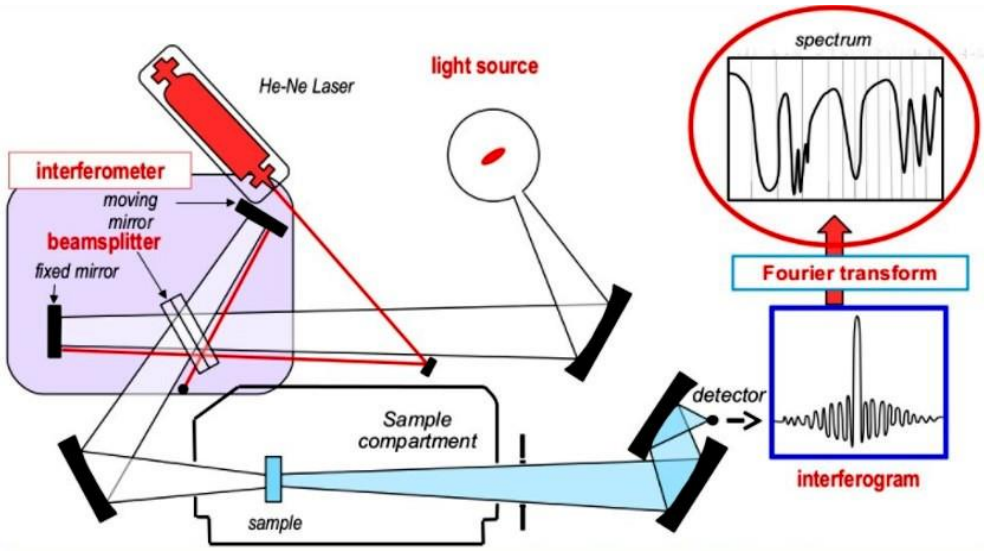

Figure 2.7. *Schematic diagram of FTIR.*

The Infrared spectra were carried out on an Agilent Technologies Fourier Transform Spectrophotometer (FTIR) driven by a microcomputer and the infrared spectra are performed in the spectral domain between 4500 and 400 cm^{-1}.

2.2.9. Raman spectroscopy

Raman spectroscopy is based on the measurements of radiation scattered from vibrational modes of the investigated substance [51], [52]. The symmetry of the molecules or the crystalline structure dictates which vibrations are active in the Raman spectrum. This criterion is expressed by the selection procedures that determine the likelihood of seeing the intensity of a certain band. According to the Raman spectroscopy selection rules, only vibrations in which the molecule polarization is modified are seen.

Polarization has a tensor form and can be represented as a polarization ellipsoid. The polarization of a sample is isotropic when the electrical field interaction is similar in all directions. Polarization is anisotropic when the polarizability is dependent on the spatial orientation. The intensity of the Raman spectra is related to the network's polarization and can be characterized by the function [3], [4]:

$$I = f(v^4) \qquad (2.15)$$

where I (intensity of diffused radiation) is proportional to the fourth power of a radiation frequency υ. The intensity of the radiation I exiting the sample in the Raman spectra is a linear function of the molar concentration and thickness of the layer, whereas in the IR spectrum this relationship is exponential. Figure 2.8, illustrates the various types of bands detected in Raman spectra.

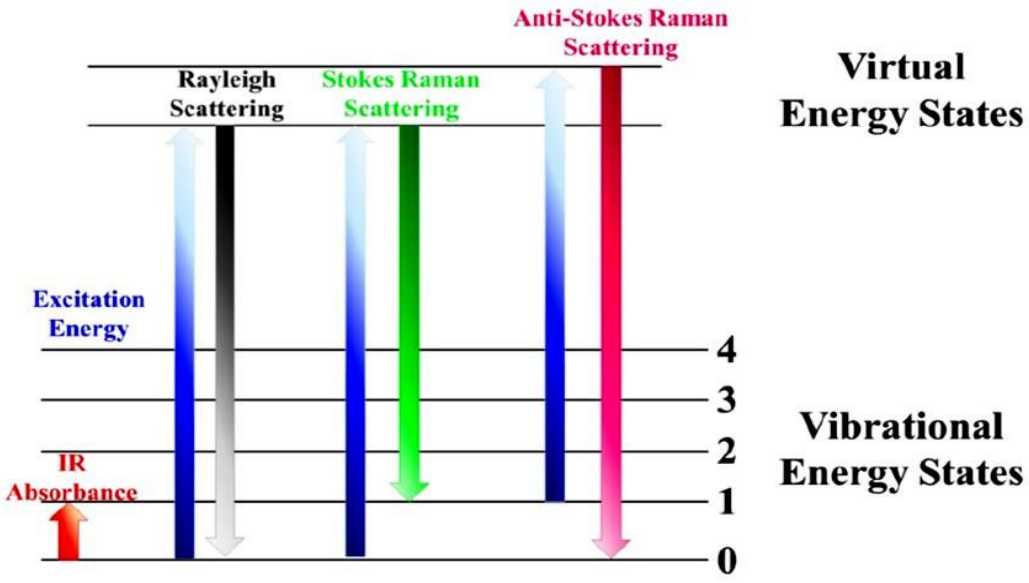

Figure 2.8. *Diagram of energy presenting different types of scattering [3].*

In the present work, the vibrational properties are investigated by Raman spectroscopy (LabRAM HR Evolution - HORIBA Jobin Yvon, OLYMPUS BX41) supplied by a laser source operating at 473 nm wavelength at room temperature.

2.2.10. Kinetics of adsorption

The adsorption kinetics represent an important step in the study of an adsorption process, allowing to determine the time needed to obtain the adsorption equilibrium [53]–[55]. The procedure was carried out in the dark and at room temperature as follows: a specific amount of photocatalyst [50 mg/l of Fe_2TiO_5/rGO_x (x = 0, 5, 10 and 15%), 50 mg $NiFe_2O_4$-TiO_2/rGO_x (x = 0, 5, 10, 15 and 20%), and 100 mg of $SrTiO_3$ and $SrTiO_3$/rGO_x (x = 5, 10, 15 and 20 %)] were dispersed in a 200 ml solution of MB with a concentration of 10 mg/L, the mixture was rigorously stirred. To follow the evolution of the adsorbed quantity (Q_{ads}), samples were taken at time intervals of 10 min until equilibrium was obtained. The yield was calculated according to Eq. (2.16):

$$R(\%) = \frac{(C_0 - C_e)}{C_0} \times 100 \qquad (2.16)$$

Where R is the percentage of MB fixed on the adsorbent, C_0 is the initial concentration of the MB solution (mg/L) and Ce is the residual concentration of the MB solution at equilibrium (mg/L).

2.2.11. Equilibrium modeling

The study of adsorption dynamics describes solute adsorption rate. This rate controls the residence time of adsorbed molecules on the solid–solution interface. Several kinetic models were applied to fit experimental data. In this work, three models were used: pseudo-first-order, pseudo-second order and pseudo n^{th} order [53]–[55]. The conformity of the experimental results with those of the modeling was estimated by the correlation coefficients R^2.

2.2.11.1. Pseudo First Order model (PFO)

The PFO kinetic model can be related to the adsorption at the solid/liquid interface; this model is based on the adsorption capacity [53]–[55] and managed by the Eq. (2.17):

$$\frac{dQ_t}{dt} = k_1 (Q_e - Q_t) \qquad (2.17)$$

Where Q_e (mg/g) and Q_t (mg/g) refer to the quantity of dye adsorbed at equilibrium and at t (min) respectively, k_1 (min^{-1}) is the constant of equilibrium rate.

The solution of the differential equation Eq. (2.17) which took into consideration the boundary conditions t = 0 to t = t and Q_t = 0 to Q_t gives Eq. (2.18):

$$Q_t = Q_e(1 - e^{-K_1 t}) \qquad (2.18)$$

2.2.11.2. Pseudo Second Order model (PSO)

The PSO model is applicable to a wider time interval, usually the entire adsorption process [53]–[55], this model is governed by Eq. (2.19):

$$Q_t = \left(\frac{k_2 {Q_e}^2 t}{k_2 Q_e t + 1}\right) \qquad (2.19)$$

Where k_2 ($g.mg^{-1}\ min^{-1}$) is the equilibrium rate constant of PSO model.

2.2.11.3. Pseudo n^{th} Order ($Pn^{th}O$)

The general rate law equation without pre-set order to a fixed value can be written as Eq.5 [53]–[55]:

$$\frac{dQ_t}{dt} = K_n(Q_e - Q_t)^n \qquad (2.20)$$

The solution of the differential equation Eq. (2.20) which took into consideration of boundary conditions gives Eq. (2.21):

$$Q_t = Q_e\left(1 - \frac{1}{\left[1+(n-1)K_n t {Q_e}^{(n-1)}\right]^{\frac{1}{n-1}}}\right) \qquad (2.21)$$

2.2.12. Adsorption mechanism

2.2.12.1. Boyd and Webber model (pore-diffusion model)

Currently, the models of Boyd and Webber are widely used to study the adsorption mechanism [56], [57]. Boyd's model determines if the primary resistance to mass transfer is in the thin film (boundary layer) surrounding the adsorbent particle or in the diffusion resistance within the pores. This model is described by the following relation:

$$F = \frac{Q_t}{Q_e} = 1 - \frac{6}{\pi^2}\sum_{n=1}^{\infty}\frac{1}{n^2}exp(-n^2 Bt) \qquad (2.22)$$

Where F is a fractional equilibrium at different times, t, and Bt is a function of F.

It is not possible to calculate B values for each adsorbed fraction from Eq. 2.22. The following approximations were obtained by implementing the Fourier transformation and then integration:

for F > 0.85 $$Bt = -0{,}4977 - Ln(1-F) \qquad (2.23)$$

for F < 0.85 $$Bt = \left(\sqrt{\pi} - \sqrt{\pi - \left(\frac{\pi^2 F}{3}\right)}\right)^2 \qquad (2.24)$$

They could be used to forecast the mechanism of adsorption using Eq. 2.23 and Eq. 2.24. This can be accomplished by plotting Bt against time. If the plot is linear and goes through the origin, then the rate of mass transfer is governed by the pore diffusion [58]. If the plot is nonlinear or linear but does not pass through the origin, the adsorption rate is controlled by film-diffusion or chemical reaction.

On the other hand, the pore-diffusion model of Webber was obtained from the second law of diffusion of Fick. The parameter for pore diffusion, k_i (mg/g $min^{0.5}$) is described by:

$$Q_t = k_i . t^{0,5} \qquad (2.25)$$

Where Q_t is the adsorbed quantity (mg/g) at a given time t. From Eq 12, if pore-diffusion is the rate-limiting step, then a Q_t plot against $t^{0.5}$ must offer a straight line with a slope equal to k_i and an intercept equivalent to zero.

2.2.13. Photocatalytic tests

Photocatalytic tests were performed at room temperature using a batch photo-reactor, an open-air double-walled beaker of 200 mL with a cooling water jacket, which keeps the temperature at (25 ± 2) °C equipped with a visible LED spotlight (LED Projector 50W Ultra-fin SMD - IP66) with luminous flow = 4000 lm (chapter III), and Xenon lamp 150W (chapter IV and V), positioned above 30 mm of light-exposed surface 32.17 cm^2 (figure 2.9). The operating parameters used were the same as in the adsorption kinetic. To establish the adsorption desorption balance, the solution was agitated in the dark until equilibrium was reached before the light was turned on; each 20 minutes, 1 mL of the suspension was removed, diluted five times, and immediately centrifuged to separate the catalyst from the solution, the solution was then analysed using UV-Vis spectroscopy. To assure photocatalyst photostability, all photocatalytic experiments were duplicated.

Photocatalytic experiments were monitored using Shimadzu 1700 UV-Vis. spectrophotometer. The spectra were recorded between 200 and 800 nm and the kinetic curves were traced for the absorbance at λ_{max} = 664 nm of the MB.

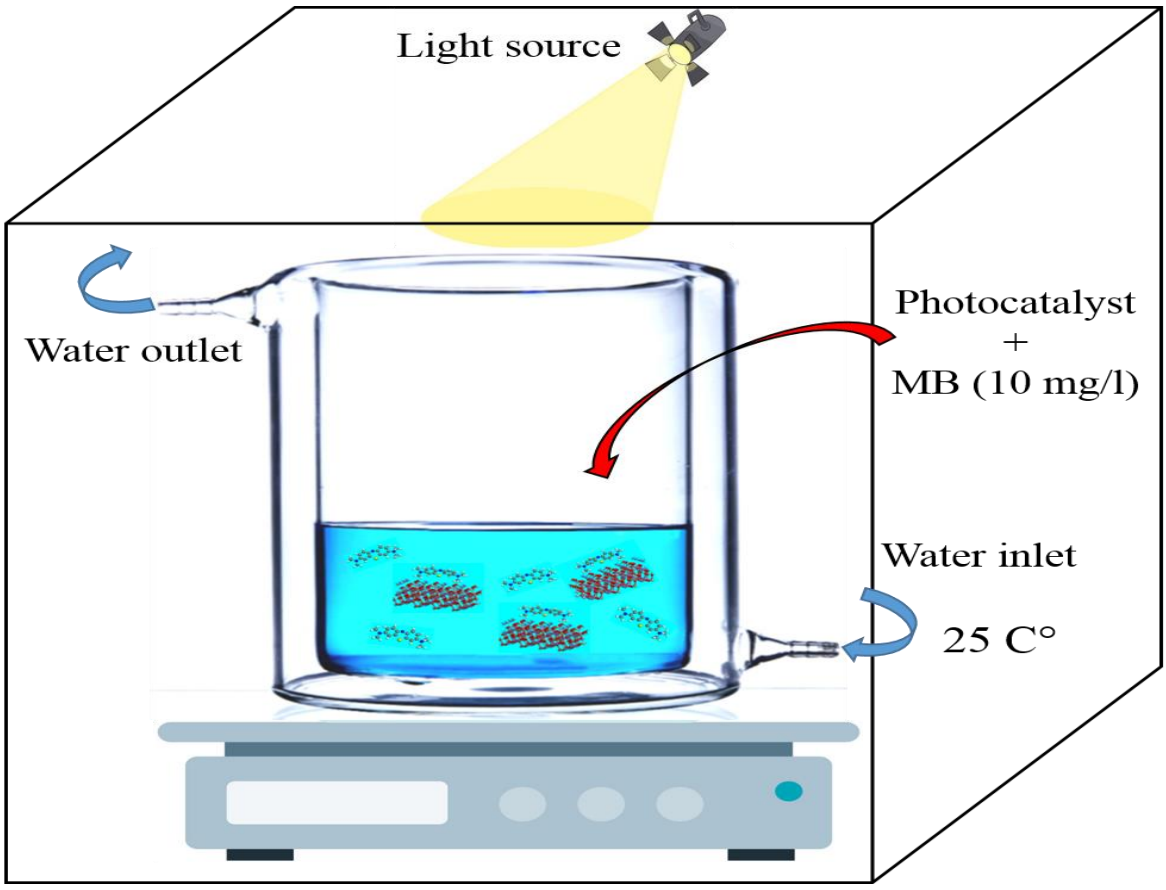

Figure 2.9. *Batch photocatalytic reactor for MB degradation.*

References

[1] W. Lucha and F. F. Schöberl, "Solving the schrödinger equation for bound states with mathematica 3.0," *Int. J. Mod. Phys. C*, vol. 10, no. 04, pp. 607–619, Jun. 1999, doi: 10.1142/S0129183199000450.

[2] I. W. Sudiarta and D. J. W. Geldart, "Solving the Schrödinger equation using the finite difference time domain method," *J. Phys. A: Math. Theor.*, vol. 40, no. 8, pp. 1885–1896, Feb. 2007, doi: 10.1088/1751-8113/40/8/013.

[3] K. Ordon, "Functionalized semiconducting oxides based on bismuth vanadate with anchored organic dye molecules for photoactive applications," These de doctorat, Le Mans, 2018. Accessed: Feb. 06, 2022. [Online]. Available: https://www.theses.fr/2018LEMA1006

[4] C. K. Y. Park, "Semiconductor Interfaces and Solid Solutions for Enhanced Photocatalysis," 2019.

[5] T. Tsuneda, *Density Functional Theory in Quantum Chemistry*. Springer Science & Business Media, 2014.

[6] "The Density Functional Theory and Beyond: Example and Applications | IntechOpen." https://www.intechopen.com/chapters/79549 (accessed Feb. 08, 2022).

[7] "Effect of Hartree–Fock pseudopotentials on local density functional theory calculations - Physical Chemistry Chemical Physics (RSC Publishing)." https://pubs.rsc.org/en/content/articlelanding/2018/cp/c8cp00990b/unauth (accessed Feb. 08, 2022).

[8] R. I. Eglitis, J. Purans, and R. Jia, "Comparative Hybrid Hartree-Fock-DFT Calculations of WO2-Terminated Cubic WO3 as Well as SrTiO3, BaTiO3, PbTiO3 and CaTiO3 (001) Surfaces," *Crystals*, vol. 11, no. 4, Art. no. 4, Apr. 2021, doi: 10.3390/cryst11040455.

[9] Y. Chen, L. Zhang, H. Wang, and W. E, "Ground State Energy Functional with Hartree–Fock Efficiency and Chemical Accuracy," *J. Phys. Chem. A*, vol. 124, no. 35, pp. 7155–7165, Sep. 2020, doi: 10.1021/acs.jpca.0c03886.

[10] W. Kohn, A. D. Becke, and R. G. Parr, "Density Functional Theory of Electronic Structure," *J. Phys. Chem.*, vol. 100, no. 31, pp. 12974–12980, Jan. 1996, doi: 10.1021/jp960669l.

[11] D. Sholl and J. A. Steckel, *Density Functional Theory: A Practical Introduction*. John Wiley & Sons, 2011.

[12] "Density-inversion method for the Kohn–Sham potential: Role of the screening density: The Journal of Chemical Physics: Vol 152, No 16." https://aip.scitation.org/doi/abs/10.1063/5.0005781 (accessed Feb. 08, 2022).

[13] Y. Shi and A. Wasserman, "Inverse Kohn–Sham Density Functional Theory: Progress and Challenges," *J. Phys. Chem. Lett.*, vol. 12, no. 22, pp. 5308–5318, Jun. 2021, doi: 10.1021/acs.jpclett.1c00752.

[14] "Systematic beyond-DFT study of binary transition metal oxides | npj Computational Materials." https://www.nature.com/articles/s41524-019-0251-7 (accessed Feb. 08, 2022).

[15] "Density functional theory across chemistry, physics and biology | Philosophical Transactions of the Royal Society A: Mathematical, Physical and Engineering Sciences." https://royalsocietypublishing.org/doi/full/10.1098/rsta.2012.0488 (accessed Feb. 08, 2022).

[16] E. Runge and E. K. U. Gross, "Density-Functional Theory for Time-Dependent Systems," *Phys. Rev. Lett.*, vol. 52, no. 12, pp. 997–1000, Mar. 1984, doi: 10.1103/PhysRevLett.52.997.

[17] P. Makkar and N. Nath Ghosh, "A review on the use of DFT for the prediction of the properties of nanomaterials," *RSC Advances*, vol. 11, no. 45, pp. 27897–27924, 2021, doi: 10.1039/D1RA04876G.

[18] M. Rizwan, Hajra, I. Zeba, M. Shakil, S. S. A. Gillani, and Z. Usman, "Electronic, structural and optical properties of BaTiO3 doped with lanthanum (La): Insight from DFT calculation," *Optik*, vol. 211, p. 164611, Jun. 2020, doi: 10.1016/j.ijleo.2020.164611.

[19] R. Ashraf *et al.*, "DFT based investigations of BAWO4: Electronic and optical properties," *Physica B: Condensed Matter*, vol. 621, p. 413309, Nov. 2021, doi: 10.1016/j.physb.2021.413309.

[20] A. Louafi, Y. Chaouche, and A. El Hassasna, "A DFT study on the structural, elastic and phonons properties of YP1−xSbx alloys," *Appl. Phys. A*, vol. 127, no. 7, p. 506, Jun. 2021, doi: 10.1007/s00339-021-04645-z.

[21] S. Berri, "First principle analysis of structural, electronic, optical, and thermoelectric characteristics of Ba3CaTa2O9 complex perovskite," *emergent mater.*, Jan. 2022, doi: 10.1007/s42247-021-00331-1.

[22] M. U. Salma and Md. Atikur Rahman, "Study of structural, elastic, electronic, mechanical, optical and thermodynamic properties of NdPb3 intermetallic compound: DFT based calculations," *Computational Condensed Matter*, vol. 15, pp. 42–47, Jun. 2018, doi: 10.1016/j.cocom.2018.04.001.

[23] S. J. Clark *et al.*, "First principles methods using CASTEP," *Zeitschrift für Kristallographie - Crystalline Materials*, vol. 220, no. 5/6, Jan. 2005, doi: 10.1524/zkri.220.5.567.65075.

[24] M. D. Segall *et al.*, "First-principles simulation: ideas, illustrations and the CASTEP code," *J. Phys.: Condens. Matter*, vol. 14, no. 11, pp. 2717–2744, Mar. 2002, doi: 10.1088/0953-8984/14/11/301.

[25] H. Stanjek and W. Häusler, "Basics of X-ray Diffraction," *Hyperfine Interactions*, vol. 154, no. 1, pp. 107–119, Jun. 2004, doi: 10.1023/B:HYPE.0000032028.60546.38.

[26] V. S. Ramachandran and J. J. Beaudoin, *Handbook of Analytical Techniques in Concrete Science and Technology: Principles, Techniques and Applications*. Elsevier, 2000.

[27] A. A. Bunaciu, E. gabriela Udriştioiu, and H. Y. Aboul-Enein, "X-Ray Diffraction: Instrumentation and Applications," *Critical Reviews in Analytical Chemistry*, vol. 45, no. 4, pp. 289–299, Oct. 2015, doi: 10.1080/10408347.2014.949616.

[28] M. P. Sithole, "Chalcogenide semiconductor photocatalysis for the photocatalytic degradation of organic pollutants in water," Jan. 2020, Accessed: Feb. 08, 2022. [Online]. Available: https://uir.unisa.ac.za/handle/10500/27359

[29] M. S. Shackley, "An Introduction to X-Ray Fluorescence (XRF) Analysis in Archaeology," in *X-Ray Fluorescence Spectrometry (XRF) in Geoarchaeology*, M. S. Shackley, Ed. New York, NY: Springer, 2011, pp. 7–44. doi: 10.1007/978-1-4419-6886-9_2.

[30] G. Kortüm, *Reflectance Spectroscopy: Principles, Methods, Applications*. Springer Science & Business Media, 2012.

[31] P. Brouwer, “Getting acquainted with the principles,” p. 62.

[32] A. Mohammed and A. Abdullah, “SCANNING ELECTRON MICROSCOPY (SEM): A REVIEW,” p. 9.

[33] W. Zhou and Z. L. Wang, *Scanning Microscopy for Nanotechnology: Techniques and Applications*. Springer Science & Business Media, 2007.

[34] M. Abd Mutalib, M. A. Rahman, M. H. D. Othman, A. F. Ismail, and J. Jaafar, “Chapter 9 - Scanning Electron Microscopy (SEM) and Energy-Dispersive X-Ray (EDX) Spectroscopy,” in *Membrane Characterization*, N. Hilal, A. F. Ismail, T. Matsuura, and D. Oatley-Radcliffe, Eds. Elsevier, 2017, pp. 161–179. doi: 10.1016/B978-0-444-63776-5.00009-7.

[35] F. Babick, “Chapter 3.2.1 - Dynamic light scattering (DLS),” in *Characterization of Nanoparticles*, V.-D. Hodoroaba, W. E. S. Unger, and A. G. Shard, Eds. Elsevier, 2020, pp. 137–172. doi: 10.1016/B978-0-12-814182-3.00010-9.

[36] M. Kaszuba, D. McKnight, M. T. Connah, F. K. McNeil-Watson, and U. Nobbmann, “Measuring sub nanometre sizes using dynamic light scattering,” *J Nanopart Res*, vol. 10, no. 5, pp. 823–829, May 2008, doi: 10.1007/s11051-007-9317-4.

[37] Ö. Topel, B. A. Çakır, L. Budama, and N. Hoda, “Determination of critical micelle concentration of polybutadiene-block-poly(ethyleneoxide) diblock copolymer by fluorescence spectroscopy and dynamic light scattering,” *Journal of Molecular Liquids*, vol. 177, pp. 40–43, Jan. 2013, doi: 10.1016/j.molliq.2012.10.013.

[38] Y. Li, V. Lubchenko, and P. G. Vekilov, “The use of dynamic light scattering and Brownian microscopy to characterize protein aggregation,” *Review of Scientific Instruments*, vol. 82, no. 5, p. 053106, May 2011, doi: 10.1063/1.3592581.

[39] A. Hawe, W. L. Hulse, W. Jiskoot, and R. T. Forbes, “Taylor Dispersion Analysis Compared to Dynamic Light Scattering for the Size Analysis of Therapeutic Peptides and Proteins and Their Aggregates,” *Pharm Res*, vol. 28, no. 9, pp. 2302–2310, Sep. 2011, doi: 10.1007/s11095-011-0460-3.

[40] M. H. Penner, “Basic Principles of Spectroscopy,” in *Food Analysis*, S. S. Nielsen, Ed. Cham: Springer International Publishing, 2017, pp. 79–88. doi: 10.1007/978-3-319-45776-5_6.

[41] S. Behera, “UV-Visible Spectrophotometric Method Development and Validation of Assay of Paracetamol Tablet Formulation,” *J Anal Bioanal Techniques*, vol. 03, no. 06, 2012, doi: 10.4172/2155-9872.1000151.

[42] M. L.C. Passos and M. L. M.F.S. Saraiva, “Detection in UV-visible spectrophotometry: Detectors, detection systems, and detection strategies,” *Measurement*, vol. 135, pp. 896–904, Mar. 2019, doi: 10.1016/j.measurement.2018.12.045.

[43] B. M. Weckhuysen and R. A. Schoonheydt, “Recent progress in diffuse re¯ectance spectroscopy of supported metal oxide catalysts,” *Catalysis Today*, p. 11, 1999.

[44] V. Mishra *et al.*, “Diffuse reflectance spectroscopy: An effective tool to probe the defect states in wide band gap semiconducting materials,” *Materials Science in Semiconductor Processing*, vol. 86, pp. 151–156, Nov. 2018, doi: 10.1016/j.mssp.2018.06.025.

[45] P. Makuła, M. Pacia, and W. Macyk, "How To Correctly Determine the Band Gap Energy of Modified Semiconductor Photocatalysts Based on UV–Vis Spectra," *J. Phys. Chem. Lett.*, vol. 9, no. 23, pp. 6814–6817, Dec. 2018, doi: 10.1021/acs.jpclett.8b02892.

[46] O. V. Rambadey, A. Kumar, A. Sati, and P. R. Sagdeo, "Exploring the Interrelation between Urbach Energy and Dielectric Constant in Hf-Substituted BaTiO3," *ACS Omega*, vol. 6, no. 47, pp. 32231–32238, Nov. 2021, doi: 10.1021/acsomega.1c05057.

[47] Neha Sharma, K. Prabakar, S. Ilango, S. Dash, and A. K. Tyagi, "Optical band-gap and associated Urbach energy tails in defected AlN thin films grown by ion beam sputter deposition: Effect of assisted ion energy," *Advanced Materials Proceedings*, vol. 2, no. 5, pp. 342–346, Dec. 2021, doi: 10.5185/amp.2017/511.

[48] N. Jaggi and D. R. Vij, "FOURIER TRANSFORM INFRARED SPECTROSCOPY," in *Handbook of Applied Solid State Spectroscopy*, D. R. Vij, Ed. Boston, MA: Springer US, 2006, pp. 411–450. doi: 10.1007/0-387-37590-2_9.

[49] B. C. Smith, *Fundamentals of Fourier Transform Infrared Spectroscopy*. CRC Press, 2011.

[50] A. Dutta, "Chapter 4 - Fourier Transform Infrared Spectroscopy," in *Spectroscopic Methods for Nanomaterials Characterization*, S. Thomas, R. Thomas, A. K. Zachariah, and R. K. Mishra, Eds. Elsevier, 2017, pp. 73–93. doi: 10.1016/B978-0-323-46140-5.00004-2.

[51] "Introductory Raman Spectroscopy - John R. Ferraro - Google Livres." https://books.google.dz/books?hl=fr&lr=&id=9_s-XBnLcMcC&oi=fnd&pg=PP1&dq=Raman+spectroscopy+&ots=quU7Gq2qva&sig=yu1XWxqGnUDDrl48jZS4DbfhC4w&redir_esc=y#v=onepage&q=Raman%20spectroscopy&f=false (accessed Feb. 08, 2022).

[52] "Raman Spectroscopy for Chemical Analysis - Richard L. McCreery - Google Livres." https://books.google.dz/books?hl=fr&lr=&id=qY4MI0Zln1YC&oi=fnd&pg=PR5&dq=Raman+spectroscopy+&ots=ne1dAQ-V1M&sig=T1dvSnRI5QOTkWbfRdeBrgIogOE&redir_esc=y#v=onepage&q=Raman%20spectroscopy&f=false (accessed Feb. 08, 2022).

[53] A. Guediri, A. Bouguettoucha, D. Chebli, N. Chafai, and A. Amrane, "Molecular dynamic simulation and DFT computational studies on the adsorption performances of methylene blue in aqueous solutions by orange peel-modified phosphoric acid," *Journal of Molecular Structure*, vol. 1202, p. 127290, Feb. 2020, doi: 10.1016/j.molstruc.2019.127290.

[54] A. Bouguettoucha, A. Reffas, D. Chebli, T. Mekhalif, and A. Amrane, "Novel activated carbon prepared from an agricultural waste, Stipa tenacissima, based on ZnCl2 activation—characterization and application to the removal of methylene blue," *Desalination and Water Treatment*, vol. 57, no. 50, pp. 24056–24069, 2016.

[55] D. Chebli, A. Bouguettoucha, T. Mekhalef, S. Nacef, and A. Amrane, "Valorization of an agricultural waste, Stipa tenassicima fibers, by biosorption of an anionic azo dye, Congo red," *Desalination and Water Treatment*, vol. 54, no. 1, pp. 245–254, 2015.

[56] R. M. C. Viegas, M. Campinas, H. Costa, and M. J. Rosa, "How do the HSDM and Boyd's model compare for estimating intraparticle diffusion coefficients in adsorption processes," *Adsorption*, vol. 20, no. 5–6, pp. 737–746, Aug. 2014, doi: 10.1007/s10450-014-9617-9.

[57] B. H. Hameed and M. I. El-Khaiary, “Malachite green adsorption by rattan sawdust: Isotherm, kinetic and mechanism modeling,” *Journal of Hazardous Materials*, vol. 159, no. 2–3, pp. 574–579, 2008.

[58] M. U. Dural, L. Cavas, S. K. Papageorgiou, and F. K. Katsaros, “Methylene blue adsorption on activated carbon prepared from Posidonia oceanica (L.) dead leaves: Kinetics and equilibrium studies,” *Chemical Engineering Journal*, vol. 168, no. 1, pp. 77–85, Mar. 2011, doi: 10.1016/j.cej.2010.12.038.

Novel Fe_2TiO_5/reduced graphene oxide heterojunction photocatalyst with improved adsorption capacity and visible light photoactivity: experimental and DFT approach

3. Novel Fe_2TiO_5/reduced graphene oxide heterojunction photocatalyst with improved adsorption capacity and visible light photoactivity: experimental and DFT approach

3.1. Abstract

The design of high efficiency materials is a major challenge for the degradation of organic pollutants. In this work, type II p-n heterojunction photocatalyst Fe_2TiO_5/rGO, with enhanced performance, was successfully prepared through simple process. The Fe_2TiO_5/rGO composites were prepared by hosting several amounts of reduced Graphene Oxide (rGO) into pseudobrookite nanocrystals (Fe_2TiO_5) which were priorly synthesized by a solid-state reaction. The morphology and the properties of the as-prepared composites were characterized trough different techniques. The fixation of rGO sheets on Fe_2TiO_5 was proved using the X-Ray Diffraction analysis (XRD). The results for the Scanning Electron Microscope (SEM) analysis showed a good mixing of rGO with Fe_2TiO_5. The X-Ray Fluorescence (XRF) confirmed the purity of the pristine Fe_2TiO_5. The Dynamic Light Scattering (DLS) illustrated a strong tendency to aggregation. Ultraviolet-Visible Diffuse Reflectance Spectroscopy (UV-Vis DRS) analysis was performed to characterize the electronic aspect as the gap and the Urbach energies. Finally, computational Density Functional Theory DFT calculations were carried out to confirm the experimental results. The adsorptive and photoactivity of Fe_2TiO_5/rGO heterojunction photocatalysts were evaluated by methylene blue (MB) degradation under visible light irradiation. The highest MB degradation rate was achieved for $Fe_2TiO_5/rGO_{10\%}$ photocatalyst with the highest value of the elimination rate.

3.2. Introduction

Water pollution is caused by various categories of toxic chemical and biological materials, such as organic dyes which are recognized as common pollutants that threaten human health and the environment [1]. Often, several techniques are used to treat several types of pollutants on the same chain; depending on the quality of water, each method requires a distinct reuse or disposal action plan. Biological, chemical and physical techniques of water remediation are frequently implemented [2]. The adsorption is the most applied method for the elimination of coloring agents due to its efficiency and ease of use. However, the adsorption process has certain limitations, such as the inability to remove certain elements and the production of secondary wastes which require an additional treatment [3]. To avoid these drawbacks, the

advanced oxidation processes (AOP) have been rapidly expanded and widely considered. Photocatalysis is one of the most effective AOPs in the degradation of organic compounds, the reduction of metal cations or the mixture of the two, which is characterized by low consumption of energy, moderate cost, and strong efficiency of pollutant degradation and mineralization [4]. Adsorption accompanied with the photocatalytic process seems therefore the most appropriate technique for the treatment of water, air and soil [5], [6]. The photocatalysis is based on the production of non-selective Reactive Oxidizing Species (ROS) such as hydroxyl $OH^{\bullet}$, superoxide $O_2^{\bullet-}$ and H_2O_2, that allow the oxidation of many organic pollutants. The implementation of Semiconductor materials is of great interest in this process. When the semiconductor is activated by photons, electron-hole pairs are generated by exciting the electrons from the Valence Band (VB) to the Conductive Band (CB), and the migration of the photogenerated electron-holes to the semiconductor surface produces ROS through redox water reactions [7]. However, the rapid recombination of the photogenerated electron-hole pairs limits the applications of photocatalysis systems in industry, and improving the life time are the major deals of the scientific research [8]. Moreover, for implementation in industry, a photocatalyst must fulfill the following conditions: wide absorption in the visible solar spectrum, high charge transport properties; it should also exhibits a high surface/volume ratio, a structural stability (thermal and aqueous) and should be nontoxic, abundant, and cheap [9].

The pseudobrookite Fe_2TiO_5 material is an n-type semiconductor [9], [10] and has attracted a growing interest owing to its notable many prospective applications [11]. It has an atomic structure matching that of TiO_2 and a band gap energy of about 2.0 to 2.2 eV (depending on the synthesis method). Moreover, the minimal energy of CB of Fe_2TiO_5 is around −0.7 eV and that of TiO_2 is around −0.5 eV; those values lead to a quick charge transfer under light illumination [10]. So, it was investigated as a photocatalyst for use in the visible domain [11]–[13]. In parallel, Fe_2TiO_5 also drew attentions due to its unique magnetic properties [14], anisotropic spin-glass behavior at low temperature [15] and conductive properties [16]. Thus, an alternative potential approach for enhancement of water oxidation consists to develop heterojunctions. In this way, heterojunction between Fe_2TiO_5 and other semiconductor was studied previously [10], [17], [18].

In concrete terms, graphene is used thermodynamically in the building of heterojunction photocatalysts susceptible to wide spectrum or in the doping of wide bandgap semiconductors [8], [19], [20]. Owing to high efficiency charge transfer and high-quality heterojunction interfaces and extremely reactive catalyst surfaces [20], graphene is also used kinetically to enhance the efficiency of photocatalysis owing to the high adsorption capacity of organic / inorganic contaminants [21]. For those arguments, the combination of graphene with various semiconductors was suggested as a promising research route. For example, the formation of p-n heterojunctions between $KTaO_3$ nanocubes and rGO (reduced Graphene Oxide) sheets leads to $KTaO_3$/rGO composites, which have shown a significant improvement in the photocatalytic performance of phenol degradation under visible light irradiation that can be attributed to the role of graphene photosensitizer [22]. A second example can be given by $LaFeO_3$/rGO nanocomposites, which showed to be an effective photocatalyst for the degradation of methyl orange dye under visible light irradiation [23].

This research work aims at synthesizing a new heterojunction Fe_2TiO_5/rGO nanocomposite photocatalyst. The composite structure and morphology, electronic, and absorption properties were systematically studied and further linked with the photocatalytic studies by investigated in the Methylene Blue (MB) degradation as a model organic pollutant. As far as we know, the bulk of the literature works focuses only on the experimental or the theoretical study search separately. Hence, aspects related to the mechanism of reactions remain unclear. For this, the aim, several experimental characterizations, and theoretical computational based on density functional theory (DFT) were employed to achieve a clearer picture.

3.3. Experimental

3.3.1. Preparation methods

3.3.1.1. Preparation of Graphene Oxide (GO)

Graphene Oxide (GO) was synthesized according to the modified Hummers method [24], [25]. In a typical synthesis, 5 g of powder graphite and 2.5 g of potassium nitrate $K(NO_3)$ were added to 115 mL of 98% sulfuric acid H_2SO_4 and mixed with constant stirring; the mixture temperature was kept below 10 °C using an ice bath. 15 g of potassium permanganate $KMnO_4$ was then slowly added to the suspension and the stirring persisted for 2 hours. At the end, the temperature was increased to 35 °C and

the mixture was kept at this temperature for another 45 minutes. Additionally, 230 mL of distilled water was added to the paste, the temperature was increased to 98 °C and the reaction was retained for 45 minutes. Finally, the resulted suspension was further diluted with addition of 350 mL of warm distilled water, and then treated with 15 mL of H_2O_2 (30%) solution to reduce the residual permanganate; the addition of H_2O_2 resulted in yellow color, indicating high level of oxidation and the manganese dioxide swing to colorless soluble manganese sulfate. The suspension was washed five times with 5% HCl aqueous solution using a centrifuge (6000 rpm for 5 minutes) until the complete removal of SO_4^{-2}. The removal of SO_4^{-2} was detected by addition of barium chloride, where the presence of sulfate ion induced a white precipitate when barium chloride was added to the supernatant [26]. The mixture was then repeatedly centrifuged and washed with de-ionized water until the supernatant's pH was neutral. The material was finally dried for 72 hours at 40 °C giving brown-black sample.

3.3.1.2. Preparation of Fe_2TiO_5 nanocrystal using solid state reaction

Equimolar quantities of Fe_2O_3 and TiO_2 were placed as a lubricant in 50 ml of acetone. The solution was put for 1 h in an ultrasonic bath. The powder was dried at 80 °C and placed in a crucible and air-heated at 900 °C for 24 hours [27].

3.3.1.3. Preparation of Fe_2TiO_5/rGO_x photocatalysts

The preparation of Fe_2TiO_5/rGO_x photocatalysts with different weight ratios 5, 10 and 15 wt.% of rGO to Fe_2TiO_5 were prepared via hydrothermal method [28]. 200 mg of Fe_2TiO_5 powder and appropriate mass percent of GO were dispersed in solution of H_2O (40 mL) and ethanol (20 mL); the obtained mixture was treated for 2 hours in an ultrasonic bath and stirred for another 2 hours to obtain homogeneous suspension. The suspension was transferred to Teflon sealed autoclave and kept for 12 hours at 120 °C. The resulting product was washed four times with distilled water and ethanol using a centrifuge (6000 rpm for 5 minutes) and dried in an oven at 60 °C for 24 hours.

3.3.2. Computational Details

The aim of the DFT calculation was to explore the impact of electronic corrections on the electronic structure characteristics of the pseudobrookite Fe_2TiO_5, and then compare the theoretical results with the experimental ones. The calculations are performed within the framework of the local density approximation (GGA) and (LDA+U) by using the Cambridge Serial Total Energy Package (CASTEP) based on

the plane-wave pseudopotential DFT methods with the Perdew-Burke-Ernzerhof (PBE) approximation for the exchange correlation functional. A previous paper used the local spin density approximation Hubbard U (LSDA++U (U = 4)) approach with the CA-PZ [29]. In this work, the same parameters were also considered for the GGA method: plane wave-based cut-off energy was set at 1000 eV and k-points grid sampling were set at 7*7*3 for the Brillouin zone. For the parameters of convergence, maximum force tolerance was set at 0.03 eV/nm, maximum stress component was set at 0.05 GPa and total energy tolerance at 1.0*10-5 eV/atom.

3.4. Results and discussion

3.4.1. Structural analysis

Figure 3.1 shows the XRD patterns of Fe_2TiO_5/rGO_x (x = 0, 5, 10 and 15%). Several diffraction peaks are observed at angular positions: 2θ = 18.14°, 25.57°, 32.57°, 36.61°, 37.37°, 40.58°, 41.09°, 46.01°, 48.83°, 55.22°, 56.15°, and 59.68°; these peaks are identified according to the JCPDS card (96-200-2303) as respectively (0 2 0), (1 1 0), (0 2 3), (1 3 0), (1 1 3), (0 2 4), (0 4 2), (0 4 3), (2 0 0), (0 0 6), (1 5 2) and (1 5 3) Bragg's planes of the Fe_2TiO_5 pseudobrookite structure, in an orthorhombic system. It can be seen that more x is important more the pattern appears noisy, indicating the presence of amorphous phase in the rGO sheets. Moreover, no new peak is observed for $Fe_2TiO_5/rGO_{5\%}$ in comparison with Fe_2TiO_5, proving that for small ratio of graphene the crystalline structure is conserved. Above x = 5%, some new peaks appear and are more intense when x increases, showing a partial transition of the pseudobrokite crystalline phase; these new peaks are related to the reduction of Fe_2TiO_5 during the fixation of rGO sheets, leading to precursors of Fe_2O_3 and TiO_2. Furthermore, the diffraction peaks shift to the small angles when x increases, which means that the crystal is stressed when the rGO sheets are inserted on the surface of Fe_2TiO_5. The characteristic crystalline parameters (a, b and c), and the average grain seize (D), micro-constraint (ε%) and dislocation density (δ) are illustrated in Table 3.1.

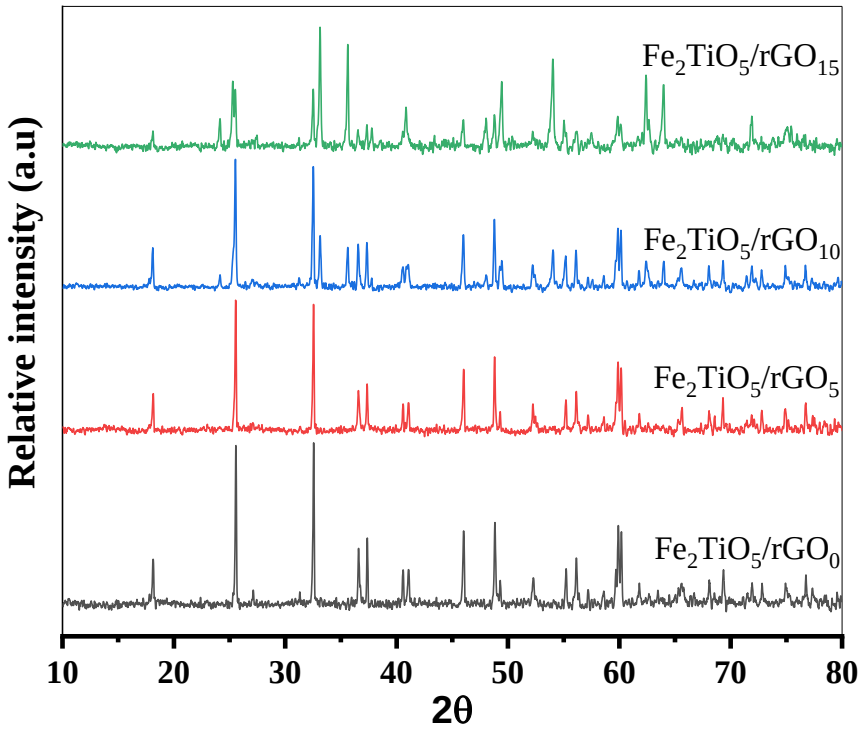

Figure 3.1: *XRD patterns of Fe_2TiO_5/rGO$_x$ (x = 0, 5, 10 and 15%), normalized by the highest intensity to 1*

Table 3.1: *Lattice parameters, grain seizes, microconstraints and dislocation densities of Fe_2TiO_5/rGO$_x$ (x = 0, 5, 10 and 15%)*

Fe_2TiO_5/rGO$_x$			0%	5%	10%	15%
a (Å)	experimental		3.726	3.729	3.730	3.730
	theoretical	LSDA	3.715			
		GGA	3.737			
b (Å)	experimental		9.767	9.780	9.799	9.797
	theoretical	LSDA	9. 797			
		GGA	9.992			
c (Å)	experimental		9.968	9.978	9.985	9.999
	theoretical	LSDA	9.879			
		GGA	10.125			
D (Å)			984.28	818.84	654.65	542.97
ε %			0.126	0.157	0.206	0.235
δ (nm)$^{-2}10^{-3}$			0.103	0.149	0.233	0.339

It is clearly seen that the fixation of graphene sheets on Fe_2TiO_5 at the microscopic scale increases the lattice parameters, evidently accompanied with an increase of the micro-constraints and at the macroscopic scale reduces significantly the grain seize and induces strong structural defects estimated by an increase of the dislocation density. In comparison with XRD results, for a high ratio x, the defects reduce partially the crystalline structure of Fe_2TiO_5.

3.4.2. XRF analysis

In view of confirming the purity of the synthetized Fe_2TiO_5, optical spectroscopy was investigated; XRF analysis proves the presence of O, Fe and Ti elements with different weight percent 37.95%, 43.2% and 18.85% (wt.%), respectively (Figure 3.2). These results are close to the theoretical weight percent given by an ideal unit cell of pseudobrokite Fe_2TiO_5, O (33.40 %), Fe (46.62 %) and Ti (19.98%), confirming the high purity of the compound. The empiric formula can be written as $Fe_{1.85}Ti_{0.95}O_{5.66}$, and is considered thereafter.

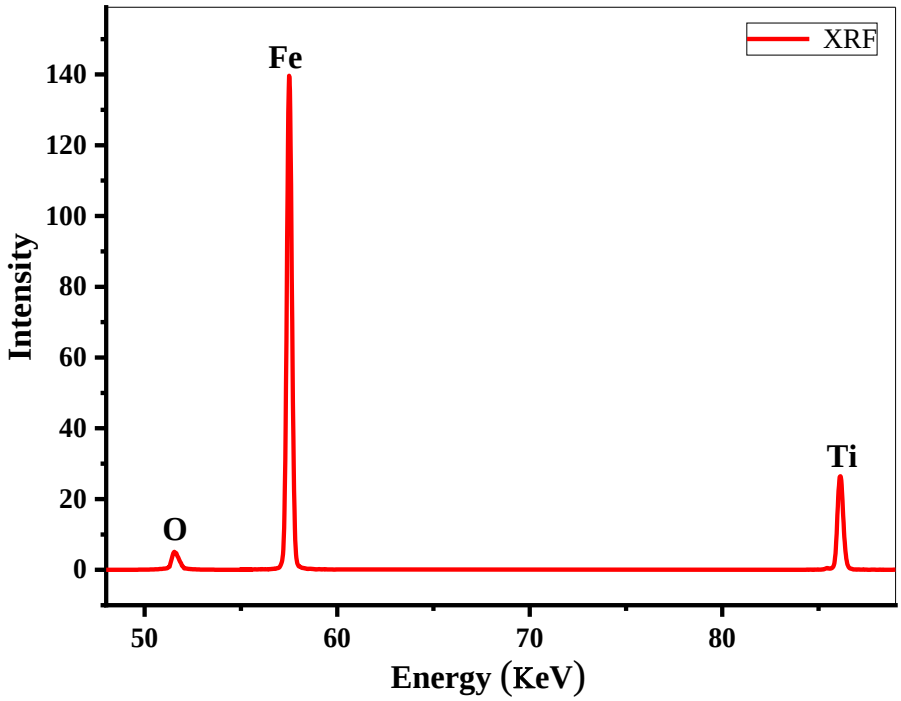

Figure 3.2: *The XRF spectrum of FTO obtained using solid-state reaction.*

3.4.3. SEM images

Figure 3.3 shows SEM images of Fe_2TiO_5/rGO_x composite; the top images are captured at strong zoom (x20000) and illustrate that the nanocrystals have different

sizes with elongated rhombohedric forms. Bottom images are carried out with weak zoom (x500) and prove that the Fe_2TiO_5 nanocrystals are uniformly scattered on the graphene sheets. These observations confirm the formation of the heterojunction of Fe_2TiO_5/rGO_x.

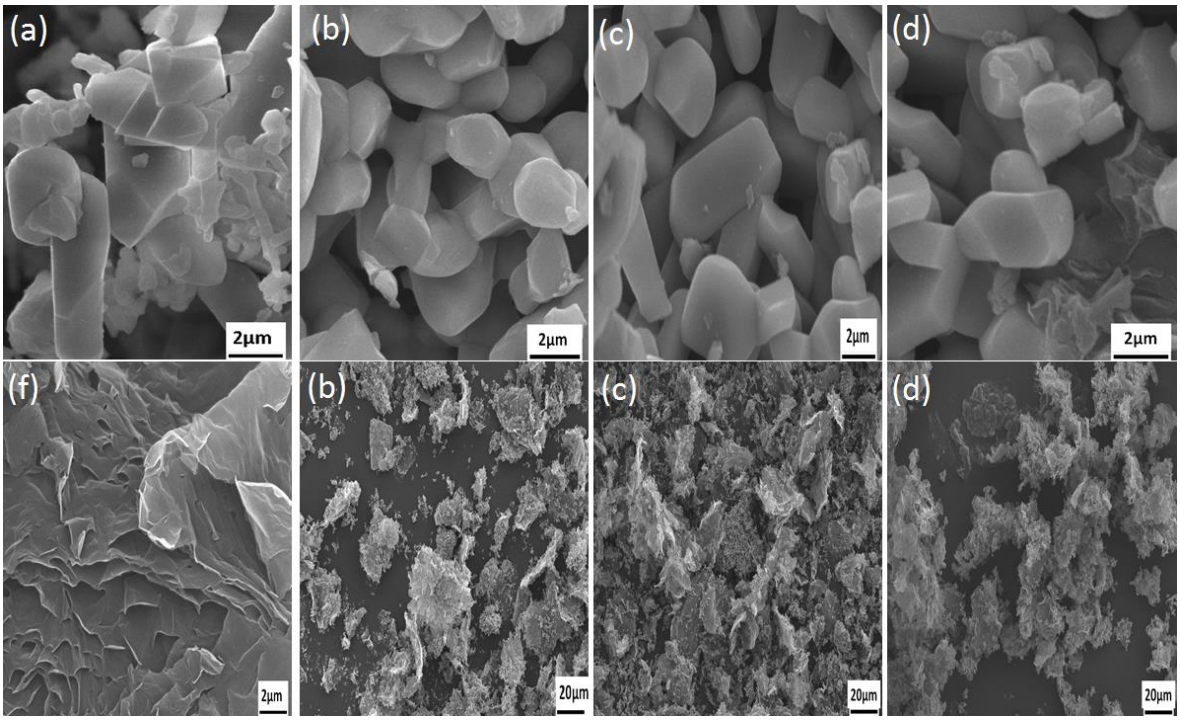

Figure 3.3: *SEM images, top images strong zoom x20000 and bottom images weak zoom x500 of (a) x = 0, (b) x = 5, (c) x = 10 and (d) x = 15%) (f) rGO.*

3.4.4. DLS analysis

The adsorption and the photocatalytic activities are influenced by the external surface of the nanoparticules and their surface state; and the effective surface exposed to the external medium is the surface of the aggregated particles. Furthermore, the aggregation of transition metal oxides in aqueous solution is well known and well-studied [33], [34]. For this purpose, the sample Fe_2TiO_5 was characterized by DLS. Figure 3.4 shows the hydrodynamic diameter of the aggregated nanoparticles in distilled water suspension, and the experimental data was fitted with a Gaussian function.

The fitted curve indicates the formation of different size of aggregated particles; the average seize value of hydrodynamic diameter is about 752.4 µm and the width at half height of the fitted curve is about 333.4 µm, showing a strong tendency to aggregate

of the Fe_2TiO_5 particles. The experimental data also shows a shoulder at low values of the hydrodynamic diameter, which can be related to unaggregated particles.

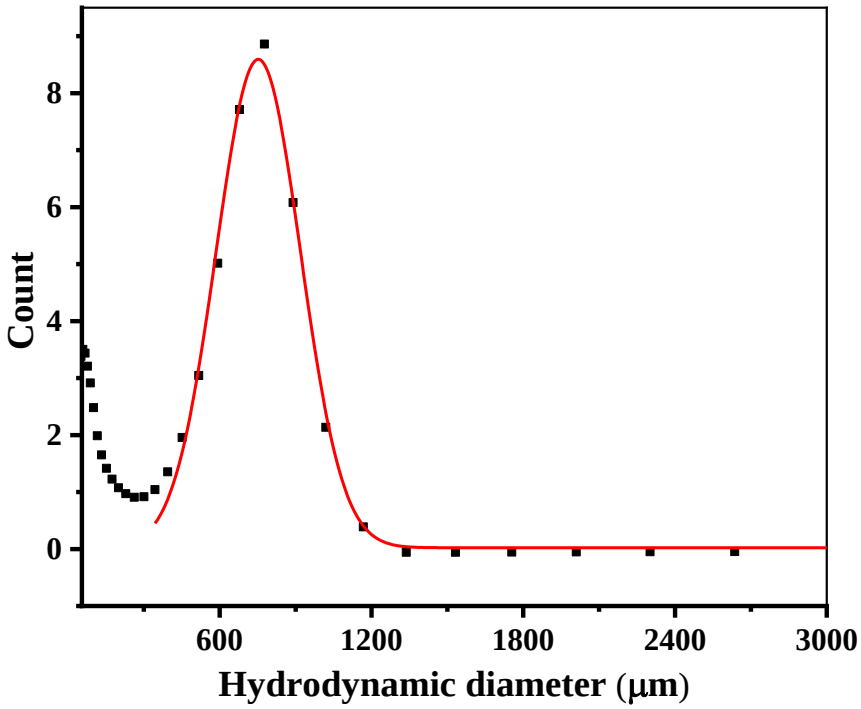

Figure 3.4: *Hydrodynamic diameter of Fe_2TiO_5 in H_2O suspension.*

3.4.5. Electronic structure and optical properties

3.4.5.1. Band structure

For the theoretical calculation of the band structure, both LSDA and GGA were used and the results of the band gaps are compared to the experimental values (Table 3.2). The figure 3.5 shows the band structures calculated by GGA of the Fe_2TiO_5 compounds at the equilibrium lattice parameters along the highest symmetry direction in the Brillouin zone. The separation of the bands exists, and the Fermi level can be located at the band gap, which indicates the semi-conductivity character of Fe_2TiO_5. The maximum VB and minimum CB are not located at the same Brillouin area point, indicating that the gap is indirect. Moreover, the Fe_2TiO_5 compound with pseudobrookite crystalline phase is a paramagnet semiconductor; its magnetic moment is principally centered on the Fe (III) ions, with less contribution of the Ti and O ions that are magnetized via super-exchange interactions. The effective magnetic moment of Fe_2TiO_5 is determined and found to be 3.80 μ_B/Fe [29]. This magnetic moment of the semiconductor split the levels of the band structure, forming two possible band structures (i) alpha electronic stat channel and (ii) beta electronic

stat channel. The value of the band gap for the alpha channel calculated by LSDA (U = 4) is about 1.81eV [29]; while the gap value calculated by GGA is about 1.88 eV, which is the closest to the experimental value.

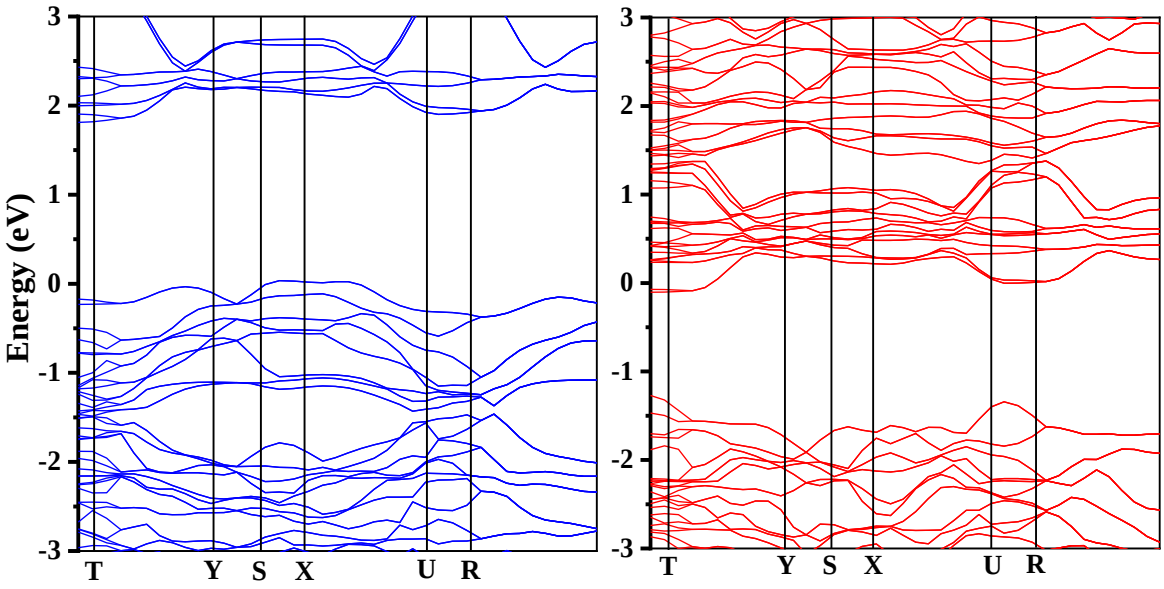

Figure 3.5: *Energy band structures of alpha (blue line) and beta spin channel (red line) of Fe_2TiO_5 along the high symmetry direction in the Brillouin zone.*

3.4.5.2. UV-Vis-DRS

For the experimental quantification of the electronic properties, namely the gap energy and the Urbach energy, UV-Vis-DRS spectroscopy is a suitable tool. The spectra shown in Figure 3.6 (b) correspond to Fe_2TiO_5/rGO_x (x = 0, 5, 10 and 15%). The lines prove that the composites are transparent in the visible range beyond the wavelength λ = 600 nm, and show also a strong and large absorption band in the UV and in the visible near the UV regions, most likely due to transitions from the VB to the CB. This band is confirmed by the theoretical calculation using GGA calculation and the obtained theoretical spectrum is shown in Figure 3.6 (a).

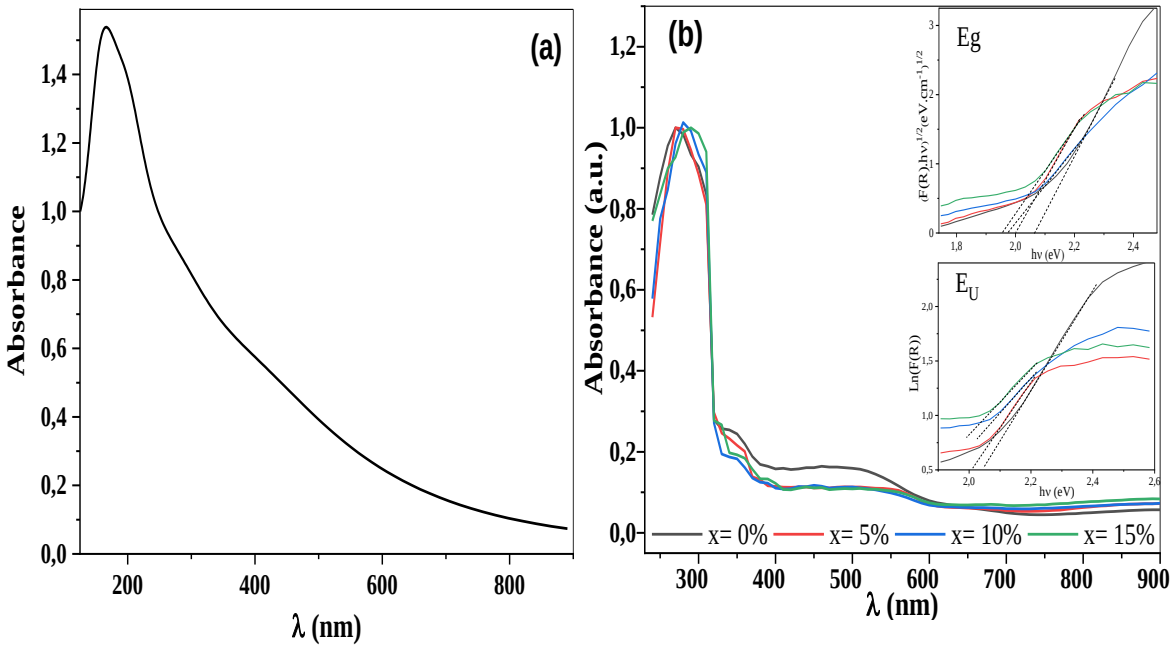

Figure 3.6: *UV-Visible spectra of Fe_2TiO_5/rGO$_x$ (x=0, 5, 10 and 15%). The insert figure: variation of the band gap E_g according to Kubelka-Munk method and variation of Urbach energy E_U. All spectra are normalized to 1 by the maximum of absorbance.*

The bump around 550 nm can be attributed to the spin-flip d-d transition [35], [36]; this weak band is observed as a shoulder on the theoretical spectrum.

The band gap 'E_g' is estimated through Tauc plot on the linear part of $(\alpha.h\upsilon)^n \propto (h\upsilon - E_g)$, where n = 1/2 for indirect band gap (insert of Figure 3.6), and n = 2 for direct gap; these optical transitions are respectively due to transitions from O2p to Fe3d orbitals and from O2p to Ti3d orbitals. The evaluated band gap energies are summarized in Table 3.2.

Table 3.2: *Indirect and direct band gap energies and Urbach energy of Fe_2TiO_5/rGO$_x$ (x = 0, 5, 10 and 15%)*

Fe_2TiO_5/rGO$_x$	x = 0%			x = 5%	x = 10%	x = 15%
	Exp	LSDA	GGA			
Indirect band gap energy (eV)	2.06	1.81	188	2.00	1.97	1.95
Direct band gap energy (eV)	2.26	198	207	2.07	2.05	2.02
Urbach energy (meV)		216		239	313	333

'E_U' is estimated through the plot of $\ln[F(R)] \propto h\upsilon$ and it is evaluated from the slope of the linear part: $\ln[F(R)] \propto (h\upsilon - E_0)$ (insert of Figure 3.6). Table 3.2 sums up the values.

E_U characterizes the change in the electronic band structure caused by different origins (vacant or interstitial sites, lattice strain, dislocation…). These various origins generate additional states within the band gap close to HOMO and LUMO levels, and can be seen as tails of CB and VB, E_U is roughly equal to the average width of tails [41]. From the Table 3.2, the deposit of rGO sheets on Fe_2TiO_5 induces an increase of the Urbach energy. Both XRD and UV-Vis-DRS analyses confirm therefore that the deposit of rGO induces stress and defects within the Fe_2TiO_5 nanocrystals.

Moreover, the decrease of E_g by adding rGO sheets shifts the Fermi level. The shift of Fermi level strengthens the migration of photogenerated electrons and represses the electron-hole recombination, which let expect an amelioration of the photocatalytic activity.

3.4.6. Kinetic of adsorption

Figure 3.7 shows time-courses of experimental and fitted kinetic curves of MB adsorption. It is well seen that the equilibrium time was about 120 minutes. Furthermore, due to the high specific surface area of rGO sheets, the adsorption of MB was significantly improved (from Q_{ads}= 2.68 mg/g to Q_{ads}= 16.26 mg/g) for increasing values of x.

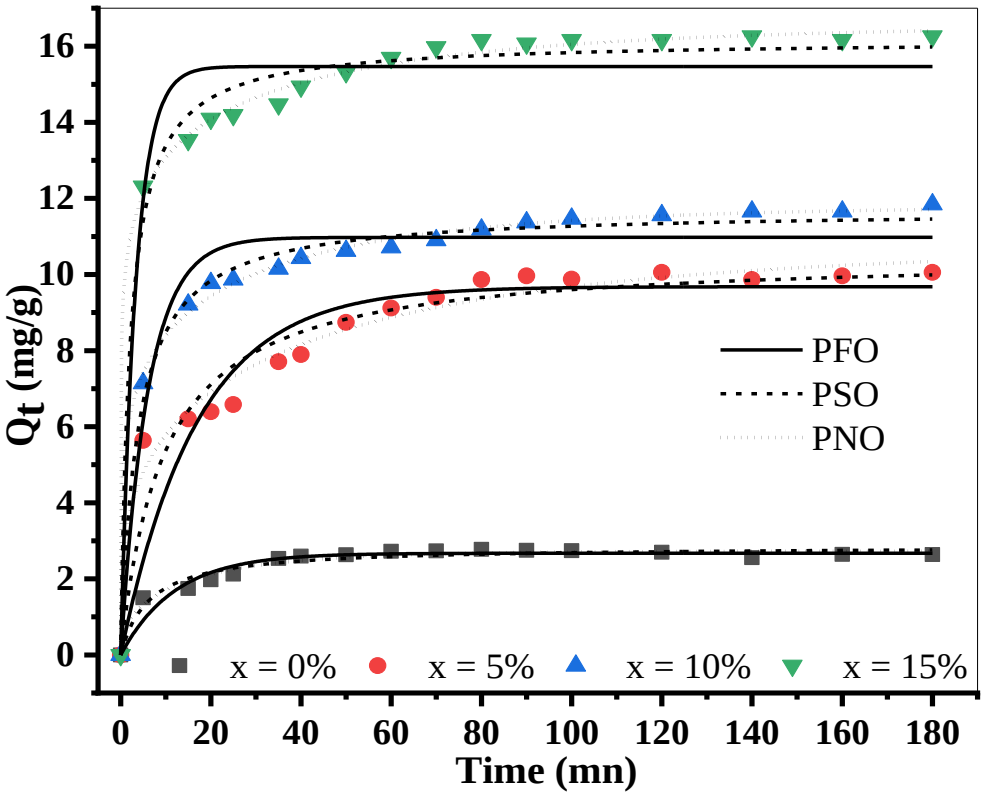

Figure 3.7: *Adsorption kinetic curves of BM on Fe_2TiO_5/rGO$_x$ composites ($C_{catalyst}$ = 50 mg/l ,C_{MB} = 10 mg/l, and $Vol_{solution}$ = 200 ml).*

The constant rate K, the theoretical maximum adsorbed quantities Q_e and the correlation coefficients R^2 of fit, given by modeling using PFO, PSO and $Pn^{th}O$ models are included in the Table 3.3.

Table 3.3: *Modeling results of adsorption kinetics of BM on Fe_2TiO_5/rGO$_x$*

Fe_2TiO_5 /rGO$_x$	Q_e exp. (mg/g)	Model									
		PFO			PSO			$Pn^{th}O$			
		K_1 (min^{-1})	Q_e (mg/g)	R^2	K_2 (min^{-1})	Q_e (mg/g)	R^2	K_n (min^{-1})	Q_e (mg/g)	n	R^2
0	2.63	0.133	2.67	0.93	0.056	2.85	0.957	0.040	2.72	0.425	0.973
5	10.06	0.059	9.68	0.87	0.010	10.52	0.935	0.012	10.69	0.284	0.976
10	11.84	0.176	10.97	0.94	0.022	11.69	0.991	0.019	11.78	0.193	0.998
15	16.26	0.301	15.46	0.95	0.030	16.16	0.985	0.015	16.55	0.119	0.997

From Table 3.3, the adsorbed quantities Q_{ads} calculated by the Pseudo-First Order (PFO) model were fairly far from the experimental values; while the Pseudo-Second Order (PSO) model led to closer Q_{ads} values. To assess for the accuracy of the fit, the correlation coefficients R^2 is the most appropriate factor; it was found between [0.875-0.959] and [0.935-0.990] for PFO, PSO models; while the $Pn^{th}O$ model led to better results, with R^2 values in the range [0.973-0.998], and the order for this last model was between 0.119 and 0.425.

In an attempt to determine the rate controlling step involved in the adsorption of MB on the synthesized composites, the kinetic data were further analyzed using the Boyd and Webber models. Figure 3.8 (a) Shows Boyd plots for the first 70 min for MB adsorption. The plots indicate a linear section, which do not cross the origin at the beginning of adsorption. This implies that adsorption does not follow Eq. 2.23 and Eq. 2.24 and therefore does not regulates the adsorption rate during the initial period. This demonstrates that during this period, chemical reaction or film diffusion regulates the adsorption rate.

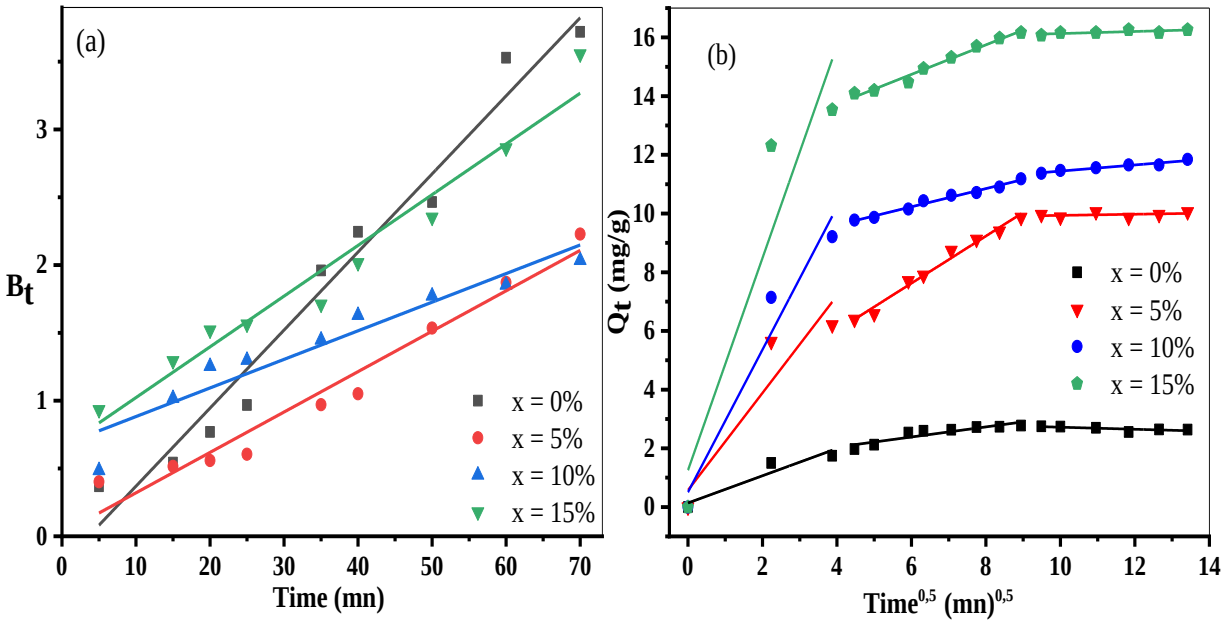

Figure 3.8: *Adsorption of MB on Fe_2TiO_5/rGO_x (x = 0, 5, 10 and 15%) (a) Boyd plots (b) pore-diffusion plots.*

Figure 3.8 (b) shows a pore diffusion plots of MB adsorption obtained by the Webber model. It is evidently seen that the plots are multi-linear, having at least three linear sections. The regression findings are seen in Table 3.4.

For various multilinear plots in Figure 3.8 (b), the regression results of the first linear section give intercept values that differ significantly from zero. These intercept values corroborate the conclusion from the Boyd plots that pore diffusion at this early point does not control the adsorption. It is therefore verified that the first linear segment represents film-diffusion (or chemical reaction).

Table 3.4: *Boyd and Webber (pore-diffusion) plots fit parameters*

	Model					
	Webber model				Boyd plot	
Fe_2TiO_5	k_ID_1	R^2	k_ID_1	R^2	Intercept	R^2
x = 0%	0.464	0.909	0.172	0.833	-0.206	0.970
x = 5%	1.656	0.881	0.804	0.984	0.022	0.959
x = 10%	2.426	0.953	0.310	0.983	0.672	0.913
x = 15%	3.613	0.881	0.503	0.982	0.649	0.959

3.4.7. Photocatalytic activity study

The overall elimination of BM is shown in figure 3.9. We see that BM elimination increases with increasing rGO content for Fe_2TiO_5/rGO_x composite (with x = 0, 5, 10 and 15 wt.%) by weight with a yield of R = 31.39% to 42.19% respectively. This elimination is due to the strong adsorption of BM by the rGO following the increase of the interfacial surface developed by the increase of the rGO content in the composite Fe_2TiO_5/rGO_x.

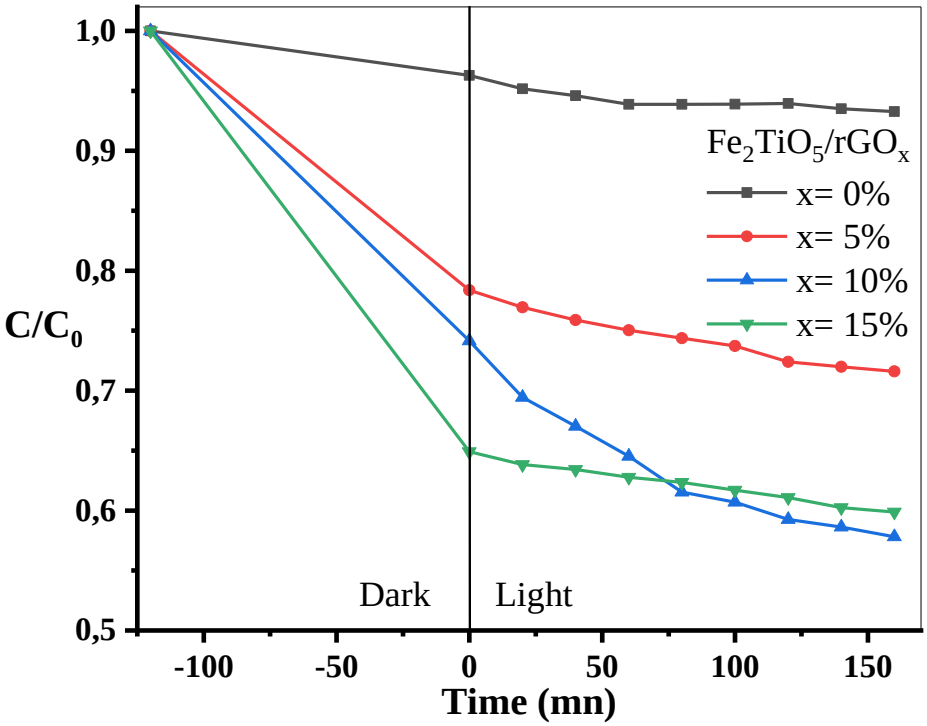

Figure 3.9: *Photodegradation of BM dye ($C_{catalyst}$ = 50 mg/l, C_{MB} = 10 mg/l, and $Vol_{solution}$ = 200 ml)*

This can be clarified in two ways: (i) in dark, by the adsorption phenomena principally of MB on rGO sheets due to its height specific surface, (ii) after saturation of adsorption and under visible light, electron-hole pairs generated within Fe_2TiO_5 can oxidize MB via photocatalysis and also, tend to be transferred to graphene sheets and works as the receiver, extending the lifetime of the charge carrier. It is worth noting that the concentration of MB shows no noticeable difference in the absence of Fe_2TiO_5/rGOx, indicating that MB cannot be degraded by photolysis. Therefore, any change in the MB concentration can be attributed to the photocatalytic process. The photocatalytic part of the kinetic curves was fitted with an exponential function, leading to the following values of the rate constants $K*10^{-4}$ = 1.61, 5.61, 15.10, and 4.91 min^{-1} for the Fe_2TiO_5/rGO_x composite (with x = 0, 5, 10 and 15 wt.%) respectively. The heterojunction composite having the ratio x = 10% presents a weak modification of the crystalline structure and it has the highest value of the rate constant. This result can be explained by lower access to the photocatalytic sites of Fe_2TiO_5 owing to the over-crowding of rGO sheets when the composite heterojunction has more than 10% of x [24]. In addition, other factors are also known as the fundamental operating parameters in heterogeneous photocatalysis such as the

initial pollutant concentration, catalyst load, pH of the solution, and the intensity of light, which can affect the effectiveness of the photocatalytic process, and it's been discussed in detail by [42]–[45]. The effect of these factors on the photocatalytic degradation rate of most organic compounds is evident according to last works.

3.4.8. Proposed mechanism

A preliminary mechanism for the photocatalytic process is proposed based on the above results and illustrated in figure 3.10. Upon LED light excitation, electron-hole pairs generate within the semiconductor Fe_2TiO_5, these photogenerated electrons tend to be transferred to graphene sheets, graphene accepts the electrons generated during photocatalysis and has worked beneficially a the receiver, This extends the lifetime of the charge carrier and is then scavenged by dissolved oxygen, thus facilitating the separation of the hole-electron. Furthermore, the $O_2/\cdot O_2^-$ reduction potential is -0.16 V (vs. NHE), which is very near to the rGO Fermi level (~0 V vs. NHE) potential. Consequently, the electron on the rGO surface could be captured by O_2 to form $\cdot O2^-$ and further, generate H_2O_2. The rGO also played a role in scavenging the photoexcited electron from Fe_2TiO_5, resulting in the abundance of photoexcited electrons on the rGO surface to promote the formation of $\cdot O_2^-$ and H_2O_2 for MB degradation. Therefore, in the present nano-heterostructure of Fe_2TiO_5/rGO, the scavenged electrons on rGO as well as the radical anion process dominated the degradation mechanism of MB. In the meantime, the holes leaving the semiconductor Fe_2TiO_5 from the VB either react to form hydroxyl radicals with adsorbed water or directly oxidize MB.

The graphene in the composites facilitates the separation of charge, restrains the hole-electron recombination, and gives a large surface/interface for heterogeneous connection reactions. Furthermore, graphene oxide is a mixture of hybridized carbon atoms S*p2* and S*p3* with very high oxygen bonding on hybrid carbon S*p3*. Oxygen atoms have a higher electronegativity than carbon atoms and thus graphene oxide becomes a p-type semiconductor material where its conduction band is the orbital antibonding π^* and its valence band is basically the orbital O*p2*. By removing most of the oxygen-containing functional groups from the GO surface using the hydrothermal route, the reduced graphene oxide was obtained. However, the p-type behavior of the rGO was caused by oxygen remaining on the carbon surface. A p-n junction composite photocatalyst can be obtained when combining rGO sheets with n-type Fe_2TiO_5 semiconductors. There are some advantages of forming p-n heterostructures, such as (a) more effective charge separation; (b) fast charge transfer to the catalyst; (c) longer charge carrier life; and (d) separation of locally

incompatible nano-space reduction and oxidation reactions. As a result, the enhancement of the photocatalytic activity of Fe_2TiO_5/rGO composites under visible light could be ascribed to the formation of p-n heterojunctions between Fe_2TiO_5 and rGO sheets. It should be noted that the electronic interactions and charge balance between graphene and semiconductor result in a shift in the Fermi level and decrease the semiconductor's CB potential (Figure 3.10) E_{gap}= 2.06 eV to E_{gap}= 1.95 eV. Thus, the negative shift in Fe_2TiO_5/rGO Fermi level and the high migration of photoinduced electrons efficiency effectively suppress the recombination of the charge, resulting in increased photocatalytic activity.

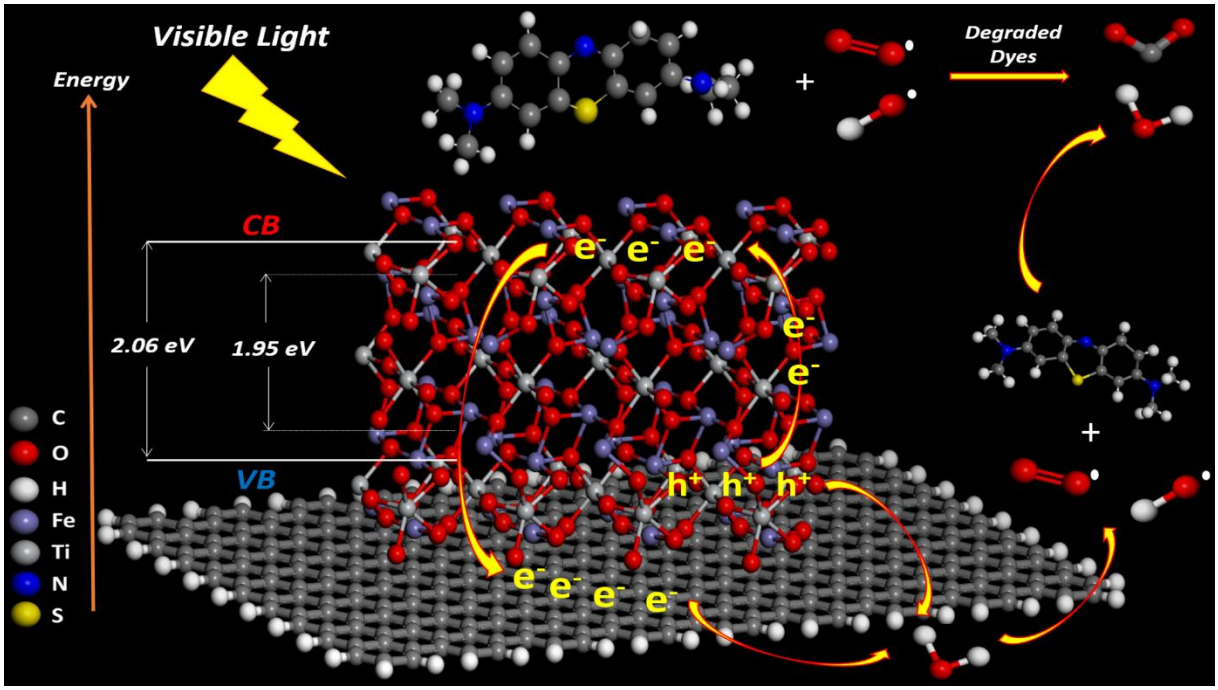

Figure 3.10: *Schematic illustration of the photocatalytic mechanism of Fe_2TiO_5/rGO_x composite.*

3.5. Conclusions

The Fe_2TiO_5 nanocrystals were successfully synthesized and were used with rGO to form heterojunction composites. The XRD analysis proved that the Fe_2TiO_5 nanocrystals have a pseudobrookite crystalline structure; this structure is conserved after the deposition of rGO, although the crystalline seize decreases. Furthermore, SEM images proved the formation of the heterojunction and the good mixing of rGO with Fe_2TiO_5. The experimental gap value was given by the UV-Vis-DRS spectroscopy and was found to be about 2.06 eV, while the gap value given by DFT

was about 1.81 eV and 1.88 using LSDA+U and GGA calculations respectively; the gap value was reduced when the quantity of rGO increased.

Moreover, the adsorption kinetic curves showed that the amount of MB adsorbed increased with the increase of the rGO amount. The fit of the kinetic curves proved that the pseudo n^{th} order model is adequate, and the modeling of the experimental results illustrated that the adsorption mechanism is guided by film-diffusion and/or chemical reaction. Furthermore, the photocatalytic study showed that all synthetized compounds have an impact on the degradation of the MB under visible light; the junction with rGO sheets improves considerably the photocatalytic performances and the best results were obtained using the $Fe_2TiO_5/rGO_{10\%}$ composite.

References

[1] S. Chen, M. Zhou, T. Li, and W. Cao, "Synthesis of Ag-loaded Sb2WO6 microsphere with enhanced photocatalytic ability for organic dyes degradations under different light irradiations," *Journal of Molecular Liquids*, vol. 272, pp. 27–36, 2018.

[2] R. D. Ambashta and M. Sillanpää, "Water purification using magnetic assistance: a review," *Journal of hazardous materials*, vol. 180, no. 1–3, pp. 38–49, 2010.

[3] T. Mekhalif, K. Guediri, A. Reffas, D. Chebli, A. Bouguettoucha, and A. Amrane, "Effect of acid and alkali treatments of a forest waste, Pinus brutia cones, on adsorption efficiency of methyl green," *Journal of Dispersion Science and Technology*, vol. 38, no. 4, pp. 463–471, 2017.

[4] A. Elhalil *et al.*, "Enhanced photocatalytic degradation of caffeine as a model pharmaceutical pollutant by Ag-ZnO-Al2O3 nanocomposite," *DESALINATION AND WATER TREATMENT*, vol. 94, pp. 254–262, 2017, doi: 10.5004/dwt.2017.21587.

[5] Inamuddin, M. I. Ahamed, A. M. Asiri, and E. Lichtfouse, *Nanophotocatalysis and environmental applications: energy conversion and chemical transformations*. 2019. Accessed: May 02, 2019. [Online]. Available: http://search.ebscohost.com/login.aspx?direct=true&scope=site&db=nlebk&db=nlabk&AN=2093394

[6] A. K. Alves, "Nanophotocatalysts for Fuel Production," in *Nanophotocatalysis and Environmental Applications : Energy Conversion and Chemical Transformations*, Inamuddin, M. I. Ahamed, A. M. Asiri, and E. Lichtfouse, Eds. Cham: Springer International Publishing, 2019, pp. 1–15. doi: 10.1007/978-3-030-04949-2_1.

[7] T. Tong, H. Zhang, J. Chen, D. Jin, and J. Cheng, "The photocatalysis of BiFeO3 disks under visible light irradiation," *Catalysis Communications*, vol. 87, pp. 23–26, 2016.

[8] X. Li, R. Shen, S. Ma, X. Chen, and J. Xie, "Graphene-based heterojunction photocatalysts," *Applied Surface Science*, vol. 430, pp. 53–107, 2018.

[9] P. S. Bassi, S. Y. Chiam, J. Barber, and L. H. Wong, "Hydrothermal grown nanoporous iron based titanate, Fe2TiO5 for light driven water splitting," *ACS applied materials & interfaces*, vol. 6, no. 24, pp. 22490–22495, 2014.

[10] M. Waqas, S. Iqbal, A. Bahadur, A. Saeed, M. Raheel, and M. Javed, "Designing of a spatially separated hetero-junction pseudobrookite (Fe2TiO5-TiO2) yolk-shell hollow spheres as efficient photocatalyst for water oxidation reaction," *Applied Catalysis B: Environmental*, vol. 219, pp. 30–35, 2017.

[11] X. Lv *et al.*, "Fe2TiO5-incorporated hematite with surface P-modification for high-efficiency solar water splitting," *Nano Energy*, vol. 32, pp. 526–532, Feb. 2017, doi: 10.1016/j.nanoen.2017.01.001.

[12] P. S. Bassi, R. P. Antony, P. P. Boix, Y. Fang, J. Barber, and L. H. Wong, "Crystalline Fe2O3/Fe2TiO5 heterojunction nanorods with efficient charge separation and hole injection as photoanode for solar water oxidation," *Nano Energy*, vol. 22, pp. 310–318, 2016.

[13] M. Waqas *et al.*, "Multi-shelled TiO2/Fe2TiO5 heterostructured hollow microspheres for enhanced solar water oxidation," *Nano Research*, vol. 10, no. 11, pp. 3920–3928, 2017.

[14] M. Enhessari, M. K. Razi, L. Etemad, A. Parviz, and M. Sakhaei, "Structural, optical and magnetic properties of the Fe2TiO5 nanopowders," *Journal of Experimental Nanoscience*, vol. 9, no. 2, pp. 167–176, Feb. 2014, doi: 10.1080/17458080.2011.649432.

[15] J. L. Tholence, Y. Yeshurun, J. K. Kjems, and B. Wanklyn, "Spin dynamics and low temperature properties of the anisotropic spin glass Fe2TiO5," *Journal of Magnetism and Magnetic Materials*, vol. 54–57, pp. 203–204, Feb. 1986, doi: 10.1016/0304-8853(86)90551-2.

[16] X. M. Gao, M. W. Li, Y. L. Hou, and C. Y. Wang, "Characterisation of Fe2TiO5 nanocrystallites synthesised via homogeneous precipitation," *Materials Research Innovations*, vol. 19, no. 1, pp. 1–6, 2015.

[17] Y.-G. Lin, Y.-K. Hsu, Y.-C. Lin, and Y.-C. Chen, "Electrodeposited Fe2TiO5 nanostructures for photoelectrochemical oxidation of water," *Electrochimica Acta*, vol. 213, pp. 898–903, 2016.

[18] J. Li, M. Han, Y. Guo, F. Wang, and C. Sun, "Fabrication of FeVO4/Fe2TiO5 composite catalyst and photocatalytic removal of norfloxacin," *Chemical Engineering Journal*, vol. 298, pp. 300–308, 2016.

[19] G. Xie, K. Zhang, B. Guo, Q. Liu, L. Fang, and J. R. Gong, "Graphene-Based Materials for Hydrogen Generation from Light-Driven Water Splitting," *Advanced Materials*, vol. 25, no. 28, pp. 3820–3839, Jul. 2013, doi: 10.1002/adma.201301207.

[20] J. Zhang, Z. Xiong, and X. S. Zhao, "Graphene–metal–oxide composites for the degradation of dyes under visible light irradiation," *Journal of Materials Chemistry*, vol. 21, no. 11, pp. 3634–3640, 2011.

[21] Y.-C. Pu, H.-Y. Chou, W.-S. Kuo, K.-H. Wei, and Y.-J. Hsu, "Interfacial charge carrier dynamics of cuprous oxide-reduced graphene oxide (Cu2O-rGO) nanoheterostructures and their related visible-light-driven photocatalysis," *Applied Catalysis B: Environmental*, vol. 204, pp. 21–32, 2017.

[22] B. Bajorowicz *et al.*, "Perovskite-type KTaO3–reduced graphene oxide hybrid with improved visible light photocatalytic activity," *RSC Adv.*, vol. 5, no. 111, pp. 91315–91325, Oct. 2015, doi: 10.1039/C5RA18124K.

[23] R. D. Kumar, R. Thangappan, and R. Jayavel, "Facile Preparation of LaFeO 3/rGO Nanocomposites with Enhanced Visible Light Photocatalytic Activity," *Journal of Inorganic and Organometallic Polymers and Materials*, vol. 27, no. 4, pp. 892–900, 2017.

[24] H. Atout *et al.*, "Enhanced photocatalytic degradation of methylene blue: Preparation of TiO2/reduced graphene oxide nanocomposites by direct sol-gel and hydrothermal methods," *Materials Research Bulletin*, vol. 95, pp. 578–587, Nov. 2017, doi: 10.1016/j.materresbull.2017.08.029.

[25] R. Dhinesh Kumar, R. Thangappan, and R. Jayavel, "Facile Preparation of LaFeO3/rGO Nanocomposites with Enhanced Visible Light Photocatalytic Activity," *Journal of Inorganic and Organometallic Polymers and Materials*, vol. 27, no. 4, pp. 892–900, Jul. 2017, doi: 10.1007/s10904-017-0534-8.

[26] T. F. Emiru and D. W. Ayele, "Controlled synthesis, characterization and reduction of graphene oxide: A convenient method for large scale production," *Egyptian Journal of Basic and Applied Sciences*, vol. 4, no. 1, pp. 74–79, Mar. 2017, doi: 10.1016/j.ejbas.2016.11.002.

[27] A. M. Huerta-Flores, L. M. Torres-Martínez, D. Sánchez-Martínez, and M. E. Zarazúa-Morín, "SrZrO3 powders: alternative synthesis, characterization and application as photocatalysts for hydrogen evolution from water splitting," *Fuel*, vol. 158, pp. 66–71, 2015.

[28] B. Bajorowicz *et al.*, "Perovskite-type KTaO3-reduced graphene oxide hybrid with improved visible light photocatalytic activity," p. 11.

[29] L. Jin and C. Zhou, "Electronic structures and optic properties of Fe2TiO5 using LSDA+ U approach," *Progress in Natural Science: Materials International*, vol. 23, no. 4, pp. 413–419, 2013.

[30] S. Sugapriya, R. Sriram, and S. Lakshmi, "Effect of annealing on TiO2 nanoparticles," *Optik - International Journal for Light and Electron Optics*, vol. 124, no. 21, pp. 4971–4975, Nov. 2013, doi: 10.1016/j.ijleo.2013.03.040.

[31] J. I. Langford and A. J. C. Wilson, "Scherrer after sixty years: A survey and some new results in the determination of crystallite size," *J Appl Cryst, J Appl Crystallogr*, vol. 11, no. 2, pp. 102–113, Apr. 1978, doi: 10.1107/S0021889878012844.

[32] S. Yousaf, T. Kousar, M. B. Taj, P. O. Agboola, I. Shakir, and M. F. Warsi, "Synthesis and characterization of double heterojunction-graphene nano-hybrids for photocatalytic applications," *Ceramics International*, 2019.

[33] D. Jassby, J. Farner Budarz, and M. Wiesner, "Impact of Aggregate Size and Structure on the Photocatalytic Properties of TiO2 and ZnO Nanoparticles," *Environmental Science & Technology*, vol. 46, no. 13, pp. 6934–6941, Jul. 2012, doi: 10.1021/es202009h.

[34] J. Melcher, N. Barth, C. Schilde, A. Kwade, and D. Bahnemann, "Influence of TiO2 agglomerate and aggregate sizes on photocatalytic activity," *J Mater Sci*, vol. 52, no. 2, pp. 1047–1056, Jan. 2017, doi: 10.1007/s10853-016-0400-z.

[35] D. M. Sherman and T. D. Waite, "Electronic spectra of Fe3+ oxides and oxide hydroxides in the near IR to near UV," *American Mineralogist*, vol. 70, no. 11–12, pp. 1262–1269, 1985.

[36] L. A. Marusak, R. Messier, and W. B. White, "Optical absorption spectrum of hematite, αFe2O3 near IR to UV," *Journal of Physics and Chemistry of Solids*, vol. 41, no. 9, pp. 981–984, 1980.

[37] G. Burgeth and H. Kisch, "Photocatalytic and photoelectrochemical properties of titania–chloroplatinate(IV)," *Coordination Chemistry Reviews*, vol. 230, no. 1–2, pp. 41–47, Aug. 2002, doi: 10.1016/S0010-8545(02)00095-4.

[38] E. L. Simmons, “Diffuse reflectance spectroscopy: a comparison of the theories,” *Appl Opt*, vol. 14, no. 6, pp. 1380–1386, Jun. 1975.

[39] G. Kortüm, *Reflectance Spectroscopy: Principles, Methods, Applications*. Springer Science & Business Media, 2012.

[40] *The Physics of Semiconductors - An Introduction Including | Marius Grundmann | Springer*. Accessed: Feb. 19, 2017. [Online]. Available: http://www.springer.com/fr/book/9783642138843

[41] B. Choudhury, M. Dey, and A. Choudhury, “Defect generation, d-d transition, and band gap reduction in Cu-doped TiO2 nanoparticles,” *Int Nano Lett*, vol. 3, no. 1, p. 25, Dec. 2013, doi: 10.1186/2228-5326-3-25.

[42] L. Favier, A. I. Simion, L. Rusu, M. L. Pacala, C. Grigoras, and A. Bouzaza, “REMOVAL OF AN ORGANIC REFRACTORY COMPOUND BY PHOTOCATALYSIS IN BATCH REACTOR - KINETIC STUDIES,” *Environmental Engineering and Management Journal*, vol. 14, no. 6, pp. 1327–1338, 2015, doi: 10.30638/eemj.2015.144.

[43] L. Favier *et al.*, “Advanced oxidation process for the removal of chlorinated phenols in aqueous suspensions,” *Journal of Environmental Protection and Ecology*, vol. 17, no. 3, pp. 1132–1141, 2016.

[44] A. Ounnar, L. Favier, A. Bouzaza, F. Bentahar, and M. Trari, “Kinetic study of spiramycin removal from aqueous solution using heterogeneous photocatalysis,” *Kinetics and Catalysis*, vol. 57, no. 2, pp. 200–206, Mar. 2016, doi: 10.1134/S0023158416020087.

[45] A. Ounnar, A. Bouzaza, L. Favier, and F. Bentahar, “Macrolide antibiotics removal using a circulating TiO2-coated paper photoreactor: parametric study and hydrodynamic flow characterization,” *Water Science and Technology*, vol. 73, no. 11, pp. 2627–2637, May 2016, doi: 10.2166/wst.2016.096.

Bottom-up construction of reduced-Graphene-Oxide-anchored spinel magnet $Fe_{2.02}Ni_{1.01}O_{3.22}$, anatase TiO_2 and metallic Ag nanoparticles and their synergy in photocatalytic water reduction

4. Bottom-up construction of reduced-Graphene-Oxide-anchored spinel magnet $Fe_{2.02}Ni_{1.01}O_{3.22}$, anatase TiO_2 and metallic Ag nanoparticles and their synergy in photocatalytic water reduction

4.1. Abstract

Paramagnet spinel $NiFe_2O_4$ nanocrystals were synthesized using the hydrothermal route and were put in contact with anatase TiO_2 PC500; the mixture of semi-conductors was employed as substrate to deposit reduced Graphene Oxide (rGO) sheets synthetised via Hummers modified method. Several rGO mass amounts 'x' were deposited (x = 0, 5, 10, 15% and 20%). These steps of synthesis were followed by surface decoration with Ag metallic particles using the photodeposition method, wich led to different heterojunction nanocomposite materials. The XRD analysis proved that the $NiFe_2O_4$ has a spinel crystalline structure and the anatase TiO_2 has a tetragonal system; these crystalline systems were conserved after the deposition of rGO. The electronic properties were studied experimentally using the UV-Vis DRS illustrating a hierarchical gap for the spinel $NiFe_2O_4$ and an indirect gap for TiO_2; these analyses revealed that the electronic and structural properties are affected when the rGO is deposited. The SEM images proved the formation of the heterojunction and the good mixing of $NiFe_2O_4$ and TiO_2 with the rGO. The EDX allowed attributing a chemical formula for the spinel structure, $Fe_{2.02}Ni_{1.01}O_{3.22}$. Furthermore, the photocatalytic properties are influenced by the specific area of the photocatalyst; for that the DLS analysis was carried out to estimate the average aggregated grain seize. At the end, the composites were evaluated for their enhanced adsorptive performance and photocatalytic activity under visible light irradiation to degrade Methylene Blue (MB). In addition, the deposit of metallic Ag showed greatly improvement in the photocatalytic performances over pristine composites.

4.2. Introduction

Non-biodegradable or recalcitrant organic pollution have today become crucial environmental problems because of their toxicities and persistence. Refractory organic products, mainly generated by industries are continuously discharged into waterways or the environment. A large quantity of wastewater from the textile industry contains dyes of various kinds whose elimination by conventional biological processes turns out to be ineffective. Thus, adsorption materials have found an importance in environmental processes [1]–[3], but with these materials, pollution is only transferred from the liquid phase to the solid phase [4]. Consequently, it is necessary to find a new material having high catalytic

power, which is not only capable to destroy pollutants into simpler and above all biodegradable compounds. In this way, many researchers have tried to synthesize new heterogeneous photocatalysts based on nanoparticles metallic oxides [5], [6].

As a new carbon material considered as an ideal support for nanoparticles [7], discovered in 2004, graphene has a two-dimensional (2D) structure and has a thickness of only one atom. It aroused extraordinary interest, thanks to its physical properties. Graphene has been widely used in several fields [8]–[10], owing to its high surface area, excellent electronic conductivity in storage and transport of electrons and high mechanical resistance [11], [12]. In addition, graphene oxide (GO) can be easily functionalized in order to modify its physical properties [7], rGO can be obtained by reduction of GO by electrical, chemical or thermal treatments [13], [14].

The fixation of metal oxide nanoparticles on graphene or its derivatives including graphene oxide and carbon nanotube have shown their effectiveness as adsorbent and in Photocatalysis [15]–[18]. It is noted that the carbonic materials prevent the aggregation of nanoparticles immobilized on their surface.

The metal oxides of structures AB_2O_4, A and B are divalent and trivalent metal cations respectively, are called spinel compounds and they can be indexed regarding the X-ray diffraction analysis as cubic face-centered with Fd3m space group [19]–[22], in which, 1/8 of tetrahedral sites and 1/2 of octahedral sites are occupied by A and B cations respectively. This family of compounds has attracted considerable attention in few recent years, owing to their narrow band gaps and their great visible-light responses in wastewater treatment.

Among the spinel composite oxide compounds, the spinel ferrite nanoparticles MFe_2O_4 (where M is divalent metal) have a vast potential for several technological applications [23], [24], because of their optical-electrical properties, magnetic properties and mechanical and chemical stabilities [25], [26]. They have been used in adsorption, photocatalysis, hydrogen in solar cells, magnetostrictive sensors, transducers, actuators, supercapacitors, Li-ion batteries, drug delivery, memory devices, microwave and spintronic devices, catalysis and gas sensor [27]–[30]. From that, several researchers have synthesized nanoparticles of MFe_2O_4 by different techniques, such as micro-emulsion method, co-precipitation method, sol-gel auto-combustion method, hydrothermal method, solvothermal method, etc. [31]–[34]. Among the spinel ferrite nanoparticles, the $NiFe_2O_4$ spinel has shown good magnetic properties, allowing an easy separation, and it also shows an interesting photocatalytic

activity [35]. In this context, only few researches on $NiFe_2O_4$ were developed in the fields of elimination of organic pollutant by photocatalytic processes [36], [37]. Other than that, $NiFe_2O_4$ nanoparticles were used for reduction of metals [38], hydrogen production, reduction of CO_2 and photoelectrochemical water splitting [39], [40]. Other researchers have synthesized spinel-LDH composites for the adsorption and Photocatalysis [41].

In order to increase the photocatalytic activity of spinels by separating the photogenerated e-hole couple [42], [43], some researchers have synthesized nanocomposites of $NiFe_2O_4$ deposited on two-dimensional structure materials, such as g-C_3N_4 as well as on other photocatalytic semiconductors such as ZnO and TiO_2 [44]–[46]. Other researchers have introduced other materials into the $NiFe_2O_4$-TiO_2 matrix, such as polypropylene, silica and ionic liquids [47].

This study focused therefore on the development of the photolytic properties of $NiFe_2O_4$, by adopting three strategies. The first one was the production of the junction $NiFe_2O_4$-TiO_2; the second one was the deposition of rGO on $NiFe_2O_4$-TiO_2 and the last one was the deposition of metallic Ag nanoparticules; synthesizing finally the $NiFe_2O_4$-TiO_2/rGO/Ag composite. The photocatalytic activities of $NiFe_2O_4$-TiO_2, $NiFe_2O_4$-TiO_2/rGO and $NiFe_2O_4$-TiO_2/rGO/Ag were compared; the systematic structural and electronic characterizations were also performed.

4.3. Experimental part

4.3.1. Preparation methods

4.3.1.1. Preparation of Graphene Oxide (GO)

GO was synthesized by the modified Hummers method [48]. In a typical synthesis, 5 g of powder graphite and 2.5 g of potassium nitrate $K(NO_3)$ were added to 115 mL of 98% sulfuric acid H_2SO_4 and mixed with constant stirring; the temperature of the mixture was kept below 10 °C using an ice bath. 15 g of potassium permanganate $KMnO_4$ was slowly added to the suspension and the stirring was continued for 2 h. Next, the temperature was increased to 35 °C and the mixture was kept at this temperature for another 45 min. Further, 230 mL of distilled water was added dropwise to the paste; the temperature was increased up to 98 °C and the reaction was maintained for 45 min. Finally, the resulted suspension was further diluted with addition of 350 mL of warm distilled water H_2O, and then treated with 15 mL of H_2O_2 (30%) solution to reduce the residual permanganate; the addition of H_2O_2 resulted in a yellow color, indicating high level of oxidation and the manganese dioxide swing to colorless soluble manganese sulfate. The suspension was washed with 5% HCl

aqueous solution using centrifuge until total removal of SO_4^{-2}. The removal of SO_4^{-2} was detected by addition of barium chloride, since the presence of sulfate ion induced a white precipitate when barium chloride was added to the supernatant [49]. Then, the mixture was repeatedly centrifuged and washed with de-ionized water until the pH of the supernatant was neutral. Finally, the material was dried at 40 °C for 72 h giving brown black sample.

4.3.1.2. Preparation of $NiFe_2O_4$

0.02 mol of $Ni(NO_3)2.6H_2O$, 0.04 mol of $Fe(NO_3)_3.9H_2O$ (the Ni^{2+}/Fe^{3+} molar ratio was 1/2) and 5 g of PEG (Poly Ethylene Glycol) in 20 ml of 50% aqueous alcohol were added in 100 ml water. PEG was added to obtain small homogeneous particle size; after 10 minutes of stirring, the aqueous NaOH solution was added successively dropwise with continuous stirring until the pH reached 11.

Then, the precursor solution was treated by sonication for 30 minutes and transferred to a hydrothermal stainless steel reactor for 12 h of hydrothermal treatment at 190 °C. It was then cooled to room temperature. The resulting product was collected by centrifugation, then washed with deionized water and ethanol several times, then dried under vacuum. The last step was calcination at 600 °C for 4 h.

4.3.1.3. Preparation of $NiFe_2O_4$-TiO_2

Commercial TiO_2 PC500, with an average particle size of 25 nm, was chosen as precursor in the preparation of $NiFe_2O_4$-TiO_2 junction. The composite consisted of a mass ratio of 5 % $NiFe_2O_4$ and 95 % TiO_2; this molar ratio corresponded to 0.08 g of $NiFe_2O_4$ and 1.52 g of TiO_2. For this purpose, they were suspended in 40 ml ethanol, with subsequent addition of 0.25 g of maleic acid; the mixture was maintained under stirring vigorously for 2 h. The suspension was collected by centrifugation and washed several times with water and ethanol and was dried overnight in air at 60 °C, and finally annealed at 230 °C for 3 h.

4.3.1.4. Preparation of $NiFe_2O_4$-TiO_2/rGO

The preparation of $NiFe_2O_4$-TiO_2/rGO photocatalysts with different weight ratios 5, 10, 15 and 20 wt.% of rGO to $NiFe_2O_4$-TiO_2 were prepared via the hydrothermal method. 200 mg of $NiFe_2O_4$-TiO_2 powder and appropriate mass percent of GO were dispersed in solution of H_2O (40 ml) and ethanol (20 ml); the mixture was treated by ultrasonic waves for 2 h and stirred for another 2 h to obtain homogenous suspension. The suspension was transferred to Teflon sealed autoclave and maintained at 120 °C for 12 h. The resulting compound was

washed several times by centrifugation in distilled water and ethanol and finally, dried in an oven at 60 °C for 24 h.

4.4. Results and discussion

4.4.1. Characterization

4.4.1.1. X-ray diffraction (XRD)

The Figure 4.1 shows the XRD patterns of TiO_2, $NiFe_2O_4$ and $NiFe_2O_4$-TiO_2/rGO_x (x = 0, 5, 10, 15 and 20%). Several diffraction peaks can be seen on the diffractograms for TiO_2 at the angular positions: 2θ = 25.24°, 37.87°, 47.98°, 54.54°, 62.57°, 69.70°, 75.21° and 82.78°. These peaks were attributed according to the reference pattern (96-900-8215) as respectively (1 0 1), (0 0 4), (2 0 0), (1 0 5), (2 0 4), (1 1 6), (2 1 5) and (2 2 4) Bragg's planes of anatase structure, which has a tetragonal system. For $NiFe_2O_4$ at the angular positions 2θ = 18.40°, 30.25°, 35.69°, 37.30°, 43.30°, 44.50°, 53.89°, 57.28°, 62.99°, 71.59° and 74.45°, the peaks were attributed according to the reference pattern (96-100-6117) as respectively (1 0 1), (0 0 4), (2 0 0), (1 0 5), (2 0 4), (1 1 6), (2 1 5) and (2 2 4) Bragg's planes of cubic system. No new peaks were observed for $NiFe_2O_4$–TiO_2 in comparison with those of $NiFe_2O_4$ and TiO_2, indicating the absence of any chemical reaction between the two pristine compounds.

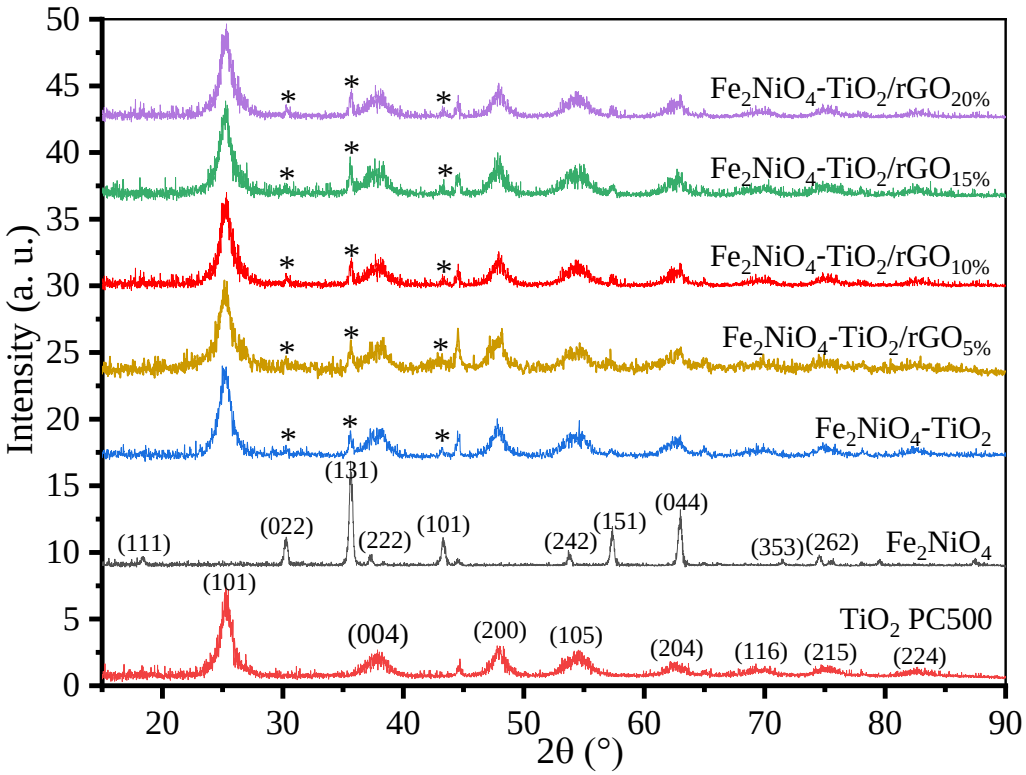

***Figure. 4.1**. Diffraction patterns of TiO_2, Fe_2NiO_4 and Fe_2NiO_4-TiO_2/rGOx (x = 0%, 5%, 10%, 15% and 20%).*

For the composites, the mass ratio of $NiFe_2O_4$ to TiO_2 was 5% to 95 %, leading to a weak apparition of the peaks relative to $NiFe_2O_4$ in the composite patterns, which are marked by only three first intense peaks (022), (131) and (101) (mentioned by a star *).

It can be seen also from the XRD-patterns that more the ratio of rGO sheets was high more the XRD-patterns appeared noisy, indicating the presence of amorphous phase of rGO.

Furthermore, the diffraction peaks of the composites shifted comparatively to the peaks of $NiFe_2O_4$-TiO_2, when mass ratio "x" of rGO increased toward the great angles, which indicates that the cell parameters were affected during the deposit, leading to the generation of a stress in the crystalline structure. The comparison of the cell parameter measures of $NiFe_2O_4$, TiO_2, and in their junction are summarized in the Table 1, and the variations of the cell parameters with the increase of rGO ratio are illustrated in the Figure 2.

Table 4.1. *Lattice parameters, grain sizes, microconstraints and dislocation densities of $NiFe_2O_4$, TiO_2 and $NiFe_2O_4$-TiO_2/rGO_x (x = 0. 5. 10. 15 and 20%).*

Single						
TiO_2	a (Å)			3.793		
	c (Å)			9.4929		
	D (Å)			99.57		
$NiFe_2O_4$	a (Å)			8.3471		
	D (Å)			192.59		
$NiFe_2O_4$-TiO_2/rGO_x		0%	5%	10%	15%	20%
TiO_2	a (Å)	3.8017	3.800	3.7955	3.7954	3.7918
	c (Å)	9.5512	9.5395	9.5317	9.5239	9.5200
	D (Å)	86.60	78.76	77.01	76.90	73.77
	ε %	0.940	1.021	1.052	1.059	1.100
	$\delta(nm)^{-2}.10^{-3}$	0.133	0.165	0.168	0.169	0.183
$NiFe_2O_4$	a (Å)	8.3518	8.3446	8.3373	8.339	8.3337

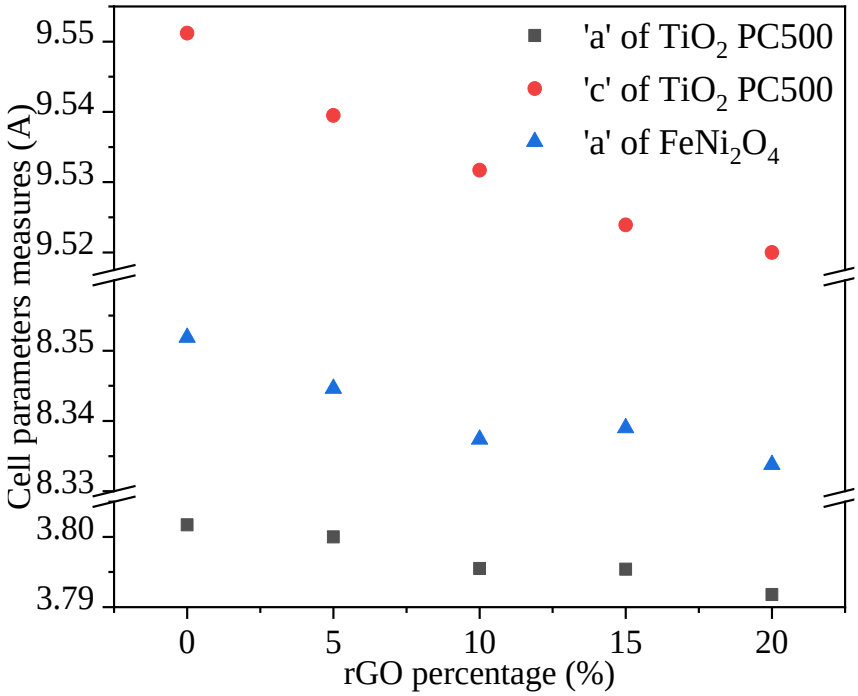

Figure. 4.2. *Cell parameter measures.*

It is seen from the values of the Table 1 that the cells of $NiFe_2O_4$ and TiO_2 were dilated when they were attached; the dilation rate $\frac{\Delta a}{a} = \frac{a-a_0}{a_0}$ was 0.056 % for cubic $NiFe_2O_4$ and the $\frac{\Delta a}{a}$ and $\frac{\Delta c}{c}$ values for TiO_2 were 0.229 % and 0.614 %. Those values indicate that the junction of the two semiconductors induced a significant dilation of the TiO_2 especially along the direction ‘c’, while the cell of $NiFe_2O_4$ was almost unchangeable.

The cell parameter measures were calculated for both crystalline phases of $NiFe_2O_4$ and TiO_2, but because the weak intensity of the peaks of $NiFe_2O_4$, the grain seize (D), microconstraint (ε%) and the density of the dislocations (δ) were estimated and discussed only for TiO_2. The results are summarized in the Table 1 and the variations of the grain seize (D), the microconstraint (ε%) with the ratio x are illustrated in the Figure 4.3:

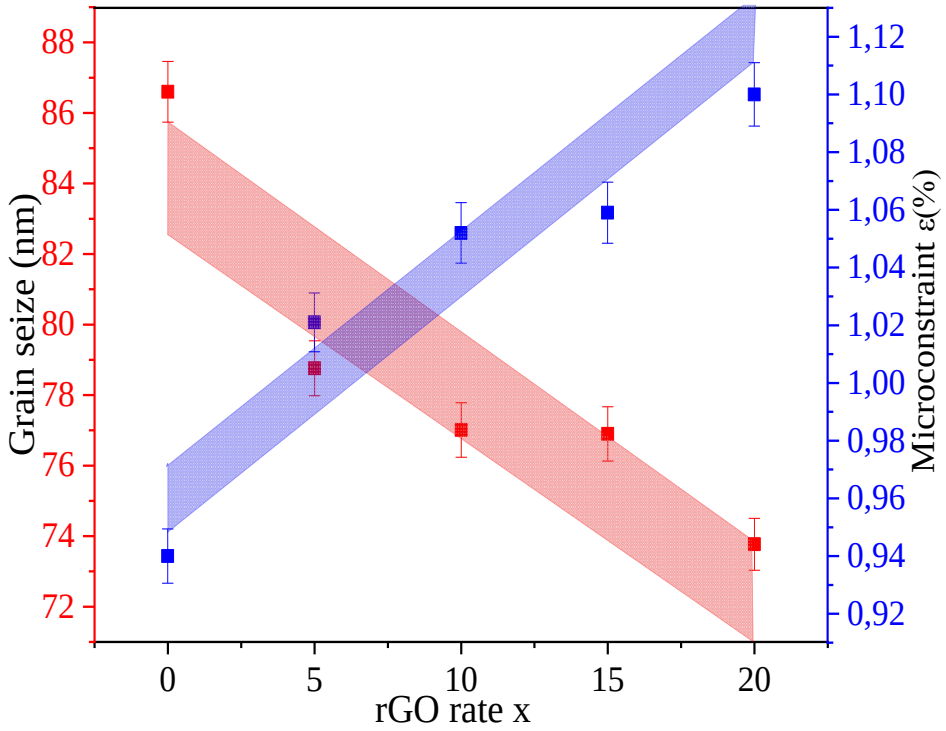

Figure. 4.3. *Variation of grain sizes and microconstraints vs rGO rate x.*

It is clearly observed from the Figure 4.2 and the Figure 4.3, that the fixation of graphene sheets on $NiFe_2O_4$-TiO_2 at the microscopic scale decreased the lattice parameter measures and increased the microconstraints; and at the macroscopic scale, it reduced the grain seize and induced strong structural defects estimated by a rise of the density of the dislocation.

4.4.1.2. Energy dispersive X-ray spectrometry (EDX)

In the focus to know the chemical formula of the synthetized $NiFe_2O_4$ compound, EDX analysis was exploited. The EDX spectrum (Figure 4.4) illustrated the presence of only O, Fe and Ni elements, which confirmed the purity of the compound, with the weight percent of 23.42 %, 49.97 % and 26.61 % (wt. %) respectively. Those values corresponded to atomic fractions, 51.54 %, 32.31 % and 16.15 % and the empiric formula can be written as $Ni_{1.01}Fe_{2.02}O_{3.22}$.

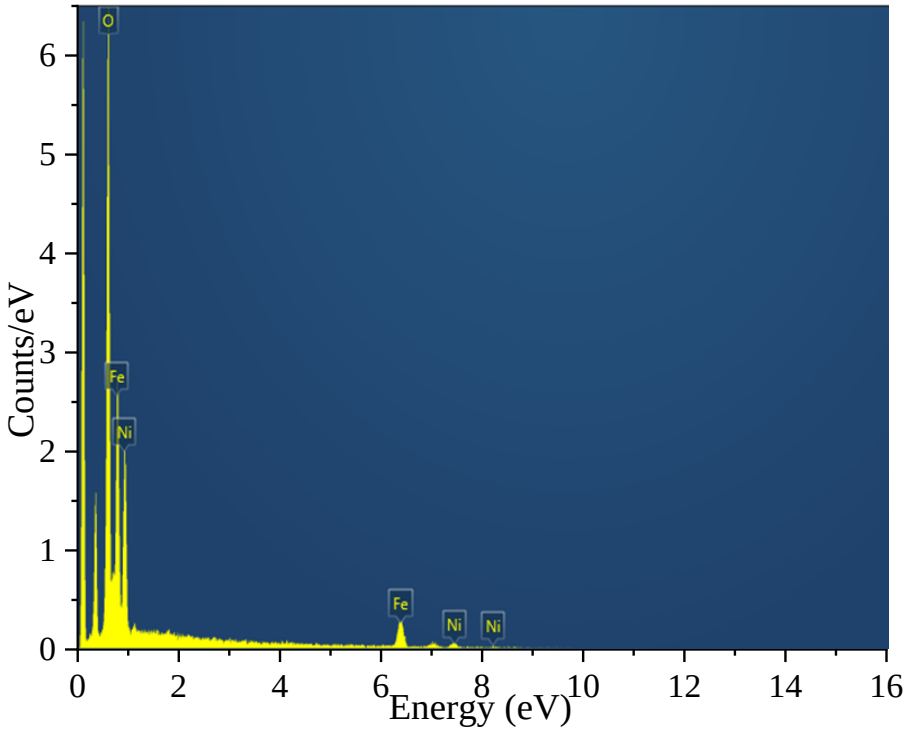

Figure. 4.4. *EDX spectrum of $NiFe_2O_4$.*

4.4.1.3. Scanning Electron Microscopy (SEM)

The Figure 4.5 shows the SEM images of $NiFe_2O_4$-TiO_2/rGO_x. The images of the first line of the table were captured at weak zoom (x100); they illustrate that the particles of $NiFe_2O_4$ had a strong tendency to form aggregated clusters, which were destroyed when the $FeNi_2O_4$ was joined to TiO_2. Regarding the composites $NiFe_2O_4$-TiO_2/rGO_x (x = 0, 5, 10, 15 and 20%), the images at weak zoom showed a homogenous distribution of $NiFe_2O_4$-TiO_2 particles on the graphene sheets, with a considerable diminution of the aggregation.

The second line of the table shows images captured with the zoom of (x10000); they focalized on the particles of $NiFe_2O_4$-TiO_2, illustrating that the particles had an intermediate shape between spherical and cubic forms. The images of the third line proved the existence of a contact at the microscopic scale between $NiFe_2O_4$-TiO_2 and graphene sheets, confirming the formation of the heterojunction. Otherwise, the fourth line proves the formation of the junction between $NiFe_2O_4$ and TiO_2 with related focalized EDX spectra.

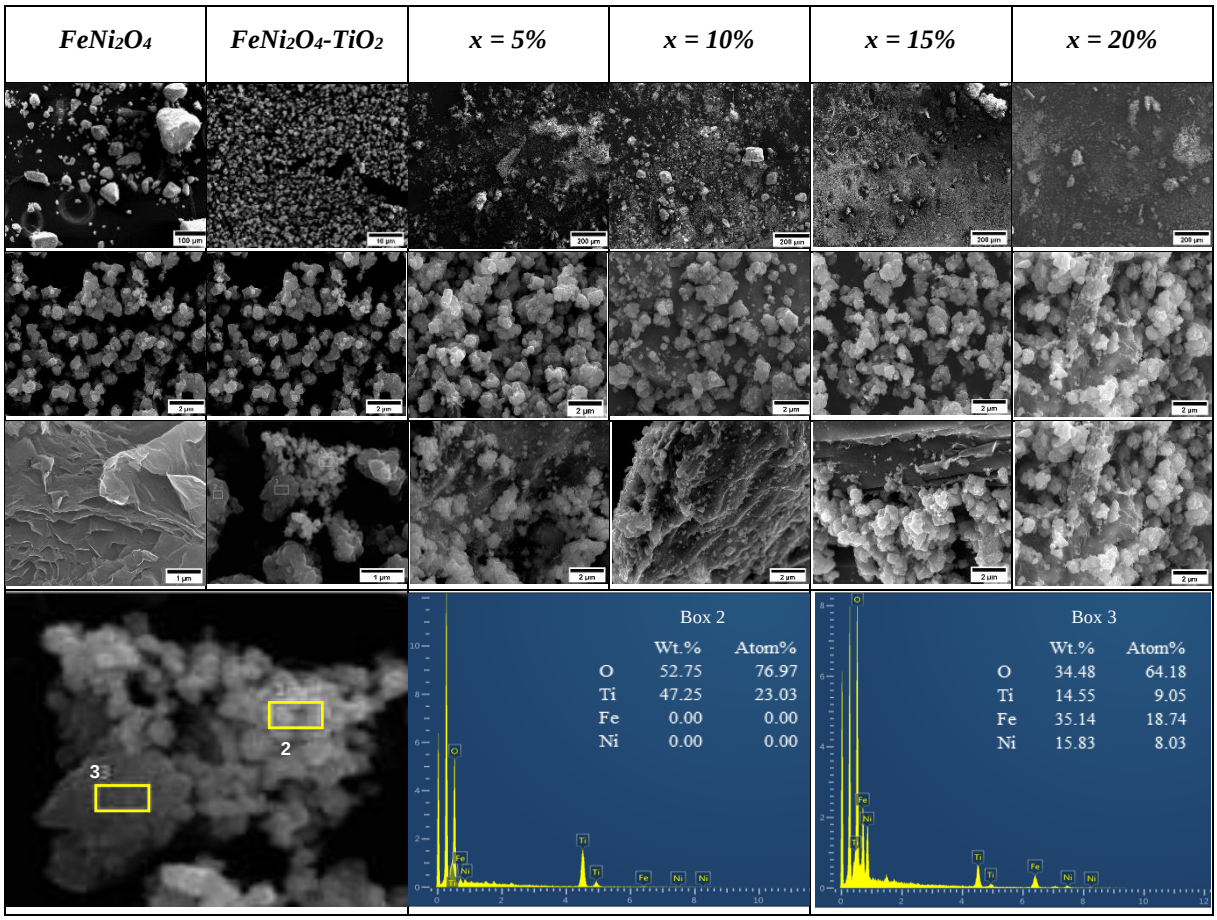

Figure. 4.5. *SEM images, first line: weak zoom x100, middle and third-line strong zoom x10000 for NiFe2O4 and NiFe2O4-TiO2/rGOx (x = 0%, 5%, 10%, 15% and 20%).*

4.4.1.4. Dynamic light scattering (DLS)

The photocatalytic reactivity is controlled by the external surface state of the particles. Indeed, the surface exposed to the external media is the surface of the aggregated particles; the aggregation of transition metal oxides in aqueous solution is well known [54], [55]. For this reason, the semiconductor particle of $NiFe_2O_4$ and $NiFe_2O_4$-TiO_2 were characterized by DLS.

The Figure 4.6 shows the distributions of the hydrodynamic diameter of aggregated nanoparticles in distilled water suspension, showing the formation of various sizes of aggregated particles; the experimental data were fitted with a Gaussian function.

The fitted curve shows that the average seize value of hydrodynamic diameter were 839.29 ± 1.67 nm and 1847.39 ± 4.96 nm and the width at half height of the fitted curve were 251.89 ± 3.39 nm and 631.65 ± 9.79, for $NiFe_2O_4$ and $NiFe_2O_4$-TiO_2 respectively. Those results indicate that both compounds had a great tendency to form aggregated particles; this tendency was more considerable for Fe_2NiO_5 than for the junction $NiFe_2O_4$-TiO_2.

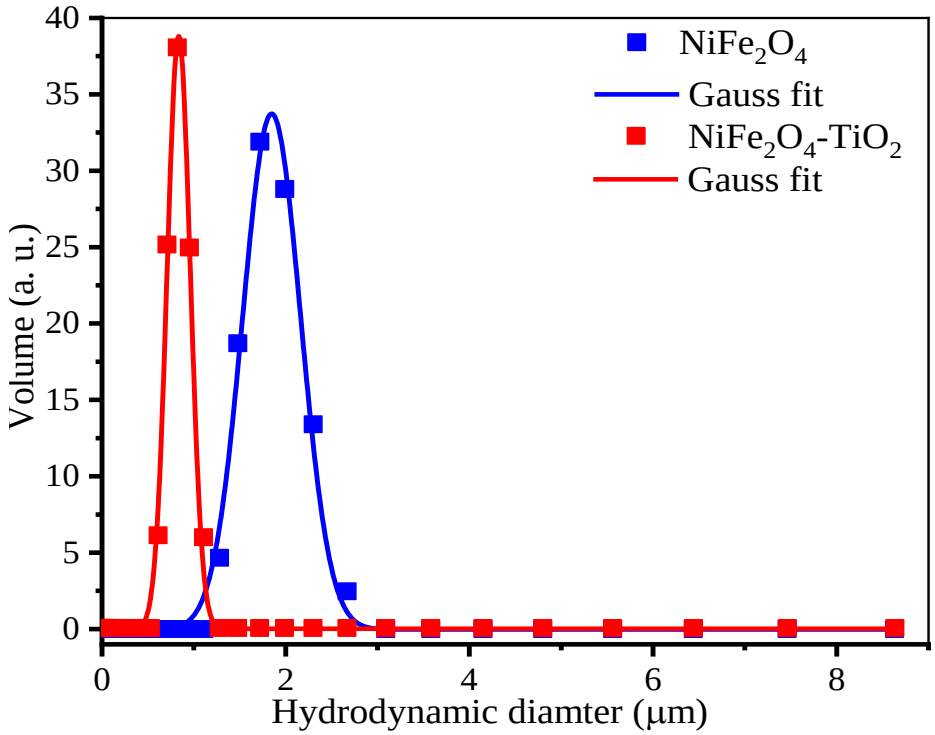

Figure. 4.6. *Hydrodynamic diameter of $NiFe_2O_4$ and $NiFe_2O_4$-TiO_2 in H_2O suspension (experimental results: independent points, fit curves: continuous lines).*

4.4.1.5. Diffuse Reflectance Spectroscopy (DRS)

The catalysis is influenced by the structural and electronic properties of the external surfaces and the interfaces of the compounds. Consequently, strong correlation is obvious between structure, charge-carrier lifetimes and interfacial charge transfer with the adsorption and the photocatalytic activities. More precisely, the light absorption characteristics (i.e., absorption coefficient, band gap energy and Urbach energy) of $NiFe_2O_4$ and $NiFe_2O_4$-TiO_2/rGO_x (x = 0, 5, 10, 15 and 20 %) are critical factors affecting the photocatalytic activity; the UV-Vis-DRS spectroscopy is a suitable tool for studying these properties. The corresponding spectra are shown in the Figure 4.7.

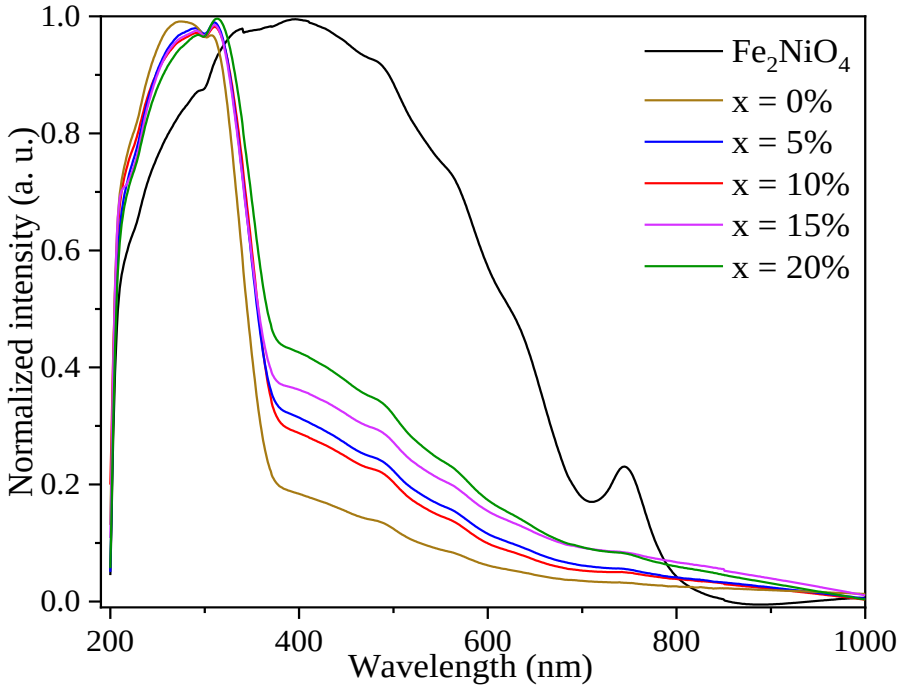

Figure. 4.7. *UV-Visible spectra of $NiFe_2O_4$ and $NiFe_2O_4$-TiO_2/rGOx (x = 0%, 5%, 10%, 15% and 20%). All spectra are normalized to 1 by the maximum of absorbance.*

The line of $NiFe_2O_4$ exhibited a large adsorption band in the visible domain overlapped by many small bumps, interpreting thereby a complicate electronic character. In addition, spectroscopic studies revealed a hierarchy of band gaps in both spin up and down channels. The band hierarchical gap refers to the presence of multiple charge gaps in the optical absorption spectrum [56], [57]; its large absorption band can be attributed to the transition from the highest occupied bands formed by both Ni3d and O2p to the lowest unoccupied band formed principally by Fe states. The small bumps can be analyzed in the optical data in terms of metal-to-metal intersite d-d and p-d charge-transfer-like excitations [58].

The choice of the $NiFe_2O_4$ was essential, if we take into consideration its hierarchical gap in both up and down channel; in such case, the electron transfer can occur in many ways between the $NiFe_2O_4$, TiO_2 and rGO.

Moreover, the spectra of the composites were mostly dominated by the adsorption of the TiO_2 anatase [59], [60], showing an adsorption band in the UV domain. This adsorption band was due to the electronic transition from the valence band related to the O2p orbitals, followed by Ti4s orbitals, to the conduction band related to the Ti3d, followed by the O2p orbitals [61]. It is seen also from the spectra of the composites that the intensity of the large

band in the visible domain increased with the increase of rGO ratio 'x', this band was due to the adsorption of the graphene, which was superimposed with the adsorption of the small amount of $NiFe_2O_4$. The adsorption of the composites in the visible light overlapped well with the solar spectrum; an interesting photocatalytic activity can be therefore predicted.

The band gap 'E_g' was evaluated through the 'Tauc plot' on linear part of $(\alpha.h\gamma)^n \propto (h\gamma\text{-}E_g)$, where n = 2 for the direct gap (Figure 4.8 (b)) and n = 1/2 for the indirect gap (Figure 4.8 (a)). The synthetized $NiFe_2O_4$ had energy values of 2.9 and 2.5 eV for n = 2 and n = 1/2 respectively, which were in good agreement with those found in literature [58], [63]. For the studied composites, the decrease of the gap was not well defined with the increase of the ratio 'x'; it was found 3.59 to 3.68 eV and from 3.87 to 3.90 eV, for the indirect and direct gap energy respectively.

Another characteristic parameters, which can be evaluated and discussed through the UV-Vis-DRS is the Urbach energy 'E_U'. This energy characterizes the variation in the electronic band structure caused by different origins (vacant or interstitial sites, lattice strain, dislocation…); it characterizes additional states within the band gap near HOMO and LUMO levels, and can be seen as tails of conduction and valence bands. E_U is roughly equal to the average width of tails [64].

'E_U' was estimated through the plot of $(\ln\alpha)$ vs $(h\upsilon)$ and it was evaluated from the slope of the linear part: $(\ln\alpha) \propto (h\alpha\text{-}E_0)$ (Figure 4.8 (c)). Contrarily to the gap values, the increase of the values of the Urbach energy was well observed; it increased with the increase of the ratio 'x' from 216 to 386 meV. This increase indicated that the deposit of rGO_x sheets on $NiFe_2O_4$-TiO_2 induced an increase of defects in the crystalline structure, in good agreement with the XRD results that showed an increase of the dislocation density 'δ'. The tails of Urbach shifts the Fermi level; this shift may strengthens the migration of photogenerated electrons and represses the recombination electron-hole, which let expect an improvement of the photocatalytic activity.

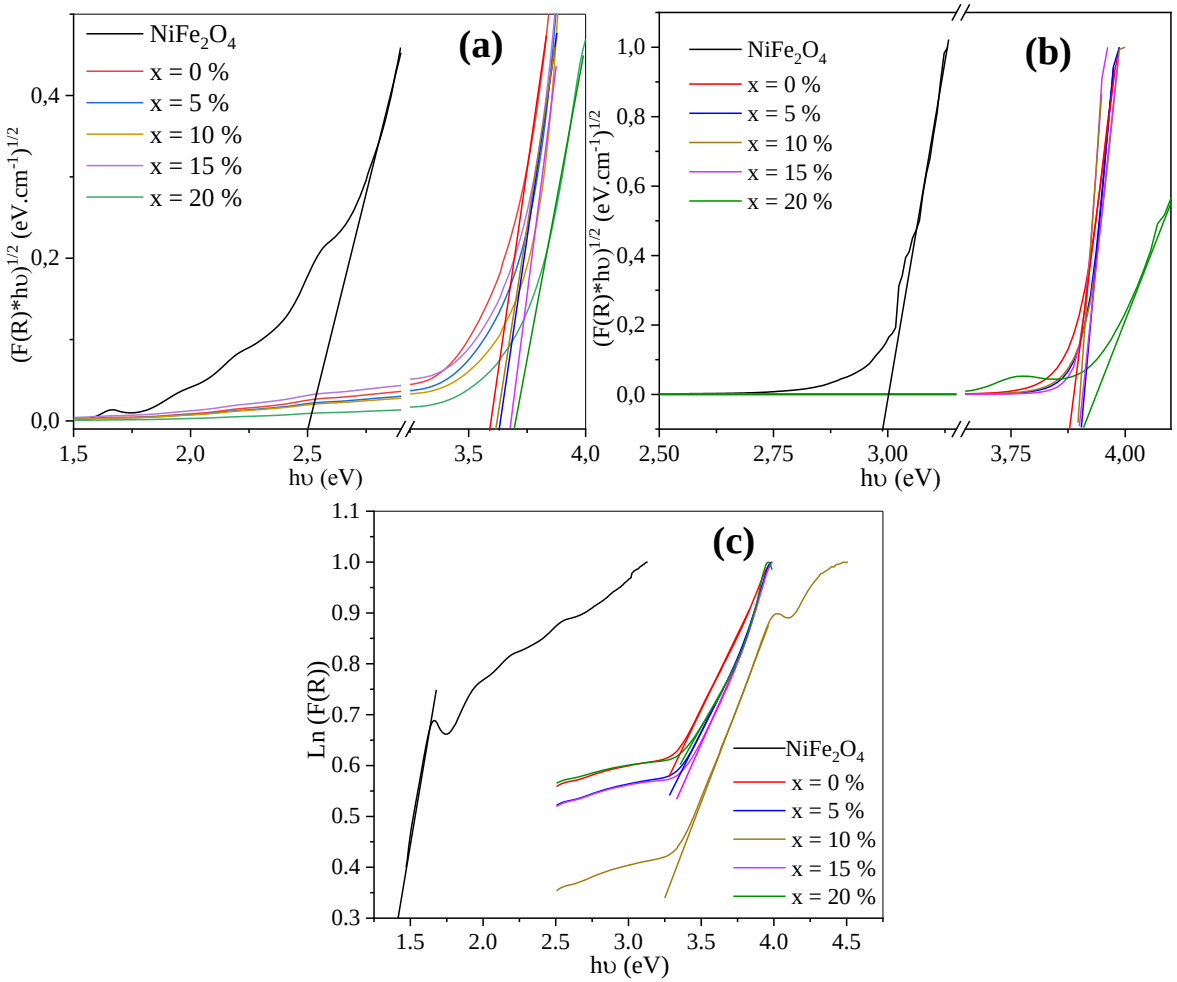

Figure. 4.8. *Variation of the band gap Eg (a) indirect, (b) direct and (c) variation of Urbach energy EU.*

4.4.2. Adsorption activity

The study of adsorption dynamics describes solute adsorption rate. This rate controls the residence time of adsorbed molecules on the solid–solution interface. The Figure 4.9 shows the experimental points of the adsorption of MB as a function of time and the corresponding fitted curves with PFO, PSO and PNO models. The experimental values of the adsorption quantities and the results of the fits are summarized in the Table 2. It can be concluded from the fit curves that the saturation of adsorption was obtained after 40 min; to ensure saturation, 70 min equilibrium time was therefore considered. In addition, the adsorbed quantity at saturation increased significantly with the increase of rGO rate 'x' (from Q_{ads} = 14.59 mg/g to Q_{ads} = 25.40 mg/g), due to the high specific area of the graphene.

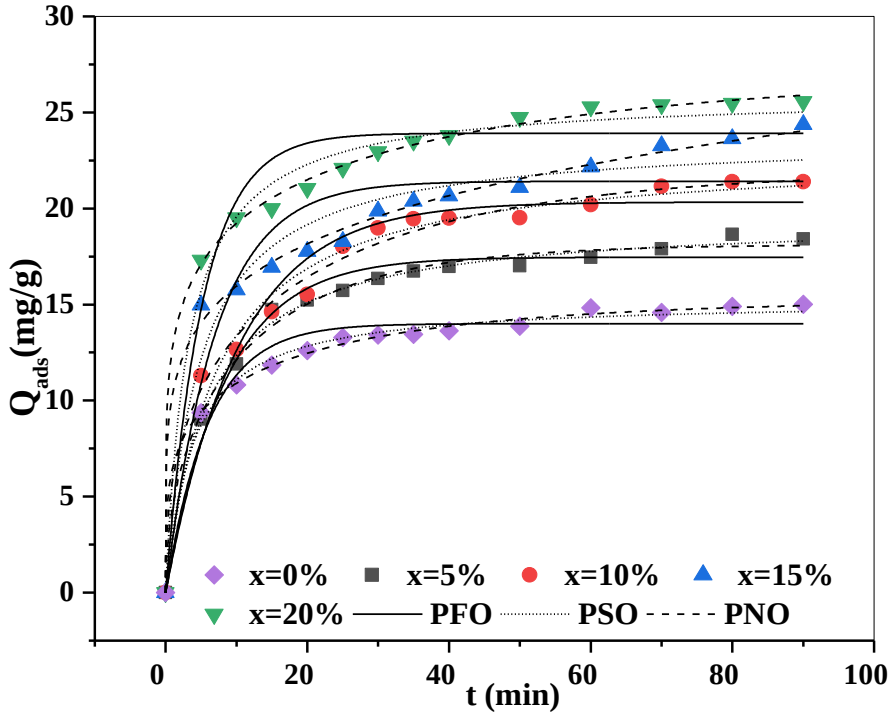

Figure. 4.9. *Adsorption of MB on $NiFe_2O_4$-TiO_2/rGOx, experimental points and their fitting curves.*

Table 4.2. *Experimental maxima of the adsorbed quantities and modeling results of MB onto $NiFe_2O_4$-TiO_2/rGO$_x$.*

	Q_{exp}	PFO			PSO			$Pn^{th}O$			
	(mg/g)	Q_e (mg/g)	R^2	K_1	Q_e (mg/g)	R^2	K_2	Q_e (mg/g)	R^2	n	K_n
x=0%	14.89	14.12	0.927	0.165	15.24	0.997	0.0177	15.96	0.994	2.40	0.006
x=5%	18.65	17.46	0.981	0.118	19.48	0.996	0.0087	19.45	0.996	2.00	0.009
x=10%	21.39	20.33	0.953	0.096	22.85	0.982	0.0062	23.00	0.983	2.12	0.005
x=15%	23.63	21.41	0.888	0.141	23.71	0.956	0.0089	25.01	0.966	2.63	0.001
x=20%	25.46	23.92	0.942	0.191	25.92	0.985	0.0118	28.02	0.992	2.85	0.009

According to the Table 4.2, the adsorbed quantities Q_{ads} calculated with the PFO model were not close to the experimental values; while those given by the PSO model were much closer. In addition, the precision of the adjustment was generally better seen through the correlation coefficients R^2. R^2 values were between 0.888-0.981, 0.956-0.997 and 0.983-0.994 for the

PFO, PSO and PNO models, respectively. According to the results obtained concerning the correlation coefficients R^2, we can rule out the PFO model, which led to the lowest correlation coefficients.

A statistical factor has been recently introduced to choose the most suitable correlation model; it is the Akaike Information Criterion (AIC). A comparison of the kinetic models was also carried out considering the AIC and the results are summarized in the Table 4.3.

Table 4.3. *Comparison of AIC and R^2 of the models used in this work (adsorption kinetics of MB on $NiFe_2O_4$-TiO_2/rGO_x).*

	PFO		PSO		PNO	
	R^2	AIC	R^2	AIC	R^2	AIC
x=0%	0.927	00.55	0.997	-22.950	0.994	-23.38
x=5%	0.981	-03.40	0.996	-25.780	0.996	-21.73
x=10%	0.953	13.81	0.982	00.075	0.983	03.56
x=15%	0.888	27.11	0.956	14.170	0.966	14.30
x=20%	0.942	20.44	0.985	01.470	0.992	-03.46

The AIC measures the quality of statistical models; it was proposed in 1973 by Hirotugu Akaike. Thus, the AIC must be minimal to minimize the loss of information. The model proposed was implemented for the description of the experimental data points of the dye adsorption. The ideal adjustment is obtained when the R^2 are high and the AIC values are low. The general form for calculating the AIC is given by the formula (13) [66], [67].

$$AIC = 2K - Ln\left(\frac{SSR}{n-k}\right) \quad (13)$$

Where: k is the number of data points, RSS is the residual sums of squares and n is number of parameters.

Also, the AIC can be deduced by introducing the chi-square of fitting [68] by the expression (14):

$$AIC = x^2 + 2p \quad (14)$$

Where p is the number of parameters of the fitted model, x^2 is the chi-square.

According to the results summarized in the Table 4.3, it seems that the PSO model gave the best results concerning the AIC (lowest values) for $NiFe_2O_4$-TiO_2/rGO_x (x = 5%, x = 10%, x = 15% and x = 20%), although the R^2 values were comparable to those obtained by the

PNO model. It can also be pointed out that the AIC for $NiFe_2O_4$-TiO_2/rGO_x (x = 0% and x = 20%) showed that the PNO model was more suited to represent the absorption of MB on semiconductor composites ($NiFe_2O_4$-TiO_2/rGO_x). It can also be noted that the AIC values for the $NiFe_2O_4$-TiO_2/$rGO_{0\%}$ were very close, AIC = -22.95 and AIC = -23.38 for PSO and PNO models, respectively. The PFO model was therefore discarded because it gave low R^2 and large AIC compared to the PSO and PNO models. Overall, the PSO model can be considered as the most appropriate to represent the MB adsorption mechanism on the different composites.

To identify the adsorption mechanism, the effect of resistance to intra-particulate scattering on adsorption was evaluated by the intra-particulate scattering model expressed by the mathematic relation (15):

$$Q = k_{id} * t^{0.5} + C \quad (15)$$

The values of the external diffusion constant k_{id} obtained after the first 5 minutes, as well as R^2 are given in the Table 4.4. From the Figure 4.10, it is easy to see that the intra-particle diffusion is an important step in the process of adsorption of MB on the various composites used in this work.

Table 4.4. *Intraparticle diffusion model of adsorption of methylene blue MB, on the various composites.*

Parameters	Intraparticle diffusion				
C (mg/g)	6.68	4.75	5.33	11.42	13.79
K_{id} (mg/gmin$^{0.5}$)	1.29	2.25	2.44	1.45	1.66
R^2	0.981	0.926	0.971	0.963	0.983

The plot of Q(t) as a function of the square root of time $t^{0.5}$, in the time interval ranging from 5 to 30 min of contact between the MB and the different composites, is displayed in Figure 4.10. In this time interval, the straight lines showed that the adsorption process of MB on the composites was in the zone, which corresponds to the diffusion in the macropores and the transport of the dye molecules from the solution to the surface of the adsorbent. This lag time in adsorption can be explained by the displacement of the dye molecules in the channels of the $NiFe_2O_4$-TiO_2 particles, before reaching the surface.

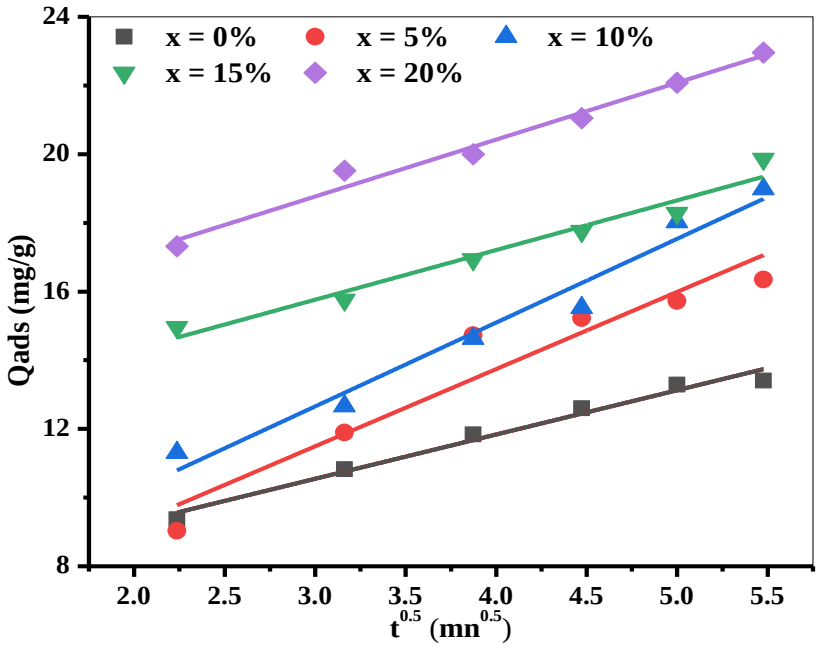

Figure. 4.10. *Experimental (symbols) and calculated data (continuous lines) by means of intraparticle diffusion model for MB adsorption onto $NiFe_2O_4$- TiO_2/rGOx.*

However, the surface adsorption process, which begins from the first minutes of contact and whose experimental points were well represented by the PSO model with very good regression coefficients R^2, indicates that the intraparticle diffusion step was limiting, and hence controlled the transfer rate of MB at each instant t. The results obtained for the K_{id} showed a maximal value of this constant for the $NiFe_2O_4$-TiO_2/$rGO_{10\%}$ composite.

4.4.3. Photocatalytic activity

The photo-degradation of the MB by $NiFe_2O_4$-TiO_2/rGO_x (x = 0, 5, 10, 15 and 20 %) composites was followed by UV-Visible spectroscopy. The Figure 4.11 shows the decay of normalized concentration ($C(t)/C_0$) recorded at λ = 664 nm, and the kinetic points are fitted by an exponential fuction according to the relation (16):

$$\frac{C(t)}{C_0} = A_0 + B_0 e^{-k_{ap}t} \qquad (16)$$

Where: A_0 is undegraded rest, A_0+B_0 gives the initial point at t = 0 and k_{ap} is the apparent rate constant of photocatalysis, the fit curves are superimposed on the Figure 4.11, and the constant rates calculated considering the linear regression are summarized in the Table 4.5.

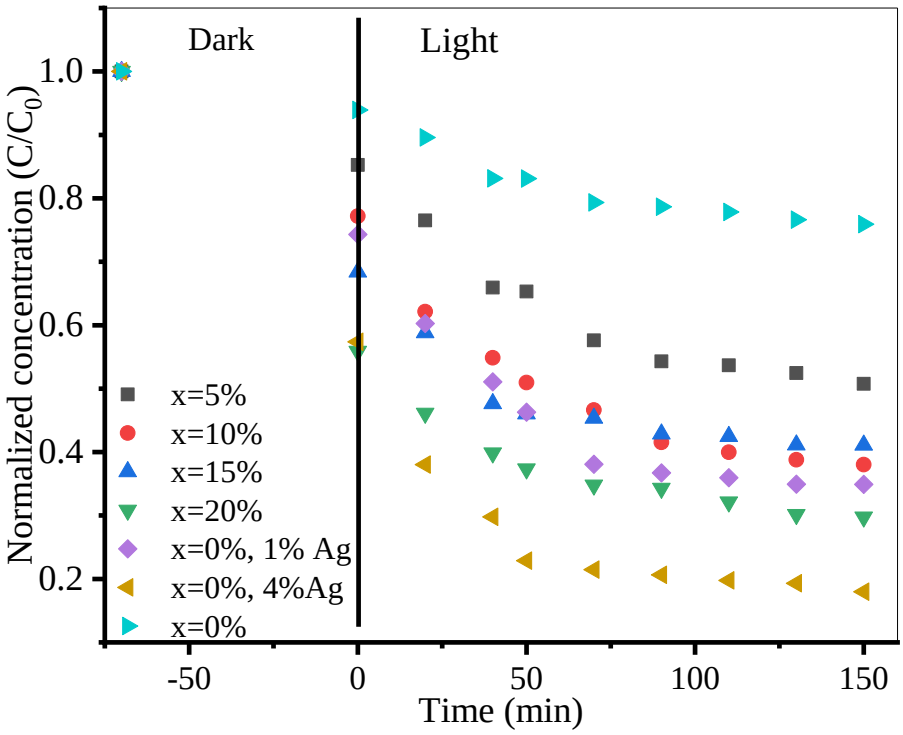

Figure. 4.11. *Photodegradation of MB under visible light, experimental and fitted curves.*

Table 4.5. *Apparent rate constants of photocatalysis.*

x	0%	5%	10%	15%	20%	1%Ag	4%Ag
$K_{ap}10^{-3}$ (min^{-1})	2.66	5.73	8.62	8.28	8.34	9.52	17.88
R^2	0.988	0.992	0.993	0.996	0.996	0.999	0.995

To better compare the effect of adsorption and photocatalysis, the histograms displayed in Figure 4.12 show their yields of elimination. Comparatively to the others, the composite x = 10% gave a high constant rate, 8.62 mn^{-1}, as well as a high removal yield by photocatalysis, 36.19%. Owing to the good yields of elimination by adsorption and photocatalysis, the composite x = 10% was chosen as substrate for the decoration by metallic Ag nanoparticles, in order to improve the elimination of MB. Two amounts of metallic Ag were considered, 1% and 4%. Comparatively to $NiFe_2O_4$-TiO_2/$rGO_{10\%}$, the deposit of metallic Ag enhanced well the photocatalytic activity; the constant rates were 9.52 and 17.88 mn^{-1} and the elimination yields were improved by 21% and 26% for $Ag_{1\%}$ and $Ag_{4\%}$ respectively. Otherwise, the synthetized composites have a good yield of elimination, and can be considered as a good photocatalysts compared to other photocatalytic systems based on

metal-oxyde/graphen composites [69], for example, M. K. Guediri and al. found a total yield of elimination about 45 % for $FeTiO_3/rGO_{10\%}$ [70].

However, the UV-Visible spectroscopy proves the good photocatalytic performance of the synthetized composites, but, it cannot prove the complete mineralization of the MB molecules, this is related to the fact that, the photodegradation of the dyes may induce the formation of colorless unstable transition products, especially in the presence of dissolved molecular oxygen [69].

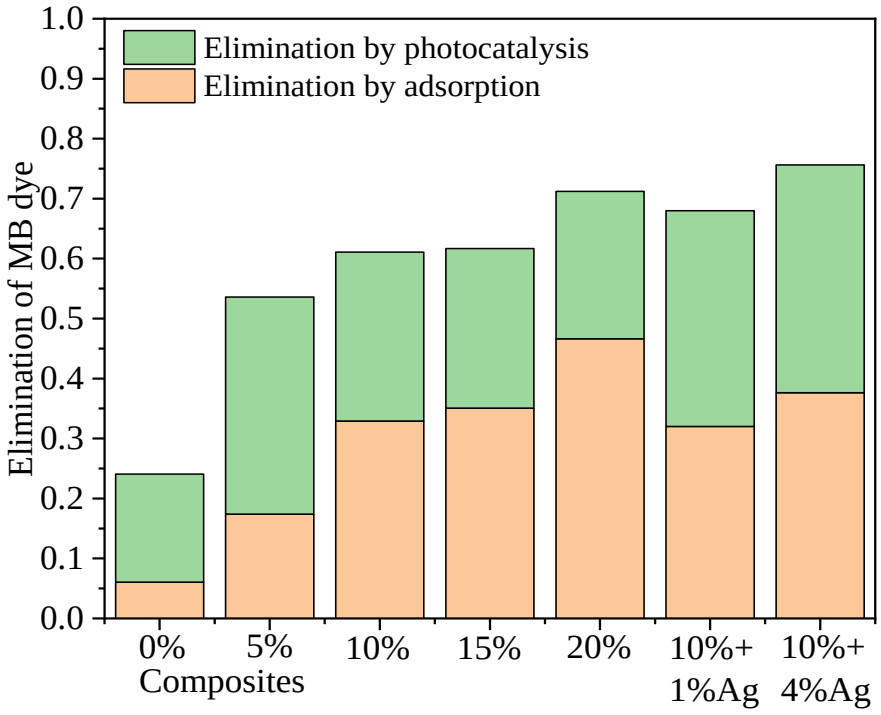

Figure. 4.12. *Yield of elimination of MB by adsorption and photocatalysis.*

4.4.4. Proposed mechanism

The histograms (Figure 4.12) illustrate that the yield of the photocatalytic process was influenced by the addition of graphene. In other words, the graphene not only increased the adsorption but is also involved in the electronic transfer during photocatalysis. This latter can act through different ways:

(i) The rGO π-conjugated electrons system favors thermodynamically the generation of ROS (Reactive Oxygen Species), and can oxidizes directly MB, and creates additional photocatalytic active sites in the composites [71], [72]; (ii) thanks to its gap null, rGO shifts the adsorption to the high wavelength and increases the absorption in the visible region, increasing the photogenerated carriers quantity; and (iii) rGO works as 'p' part (receiver) in the p-n junction ($NiFe_2O_4$-TiO_2 as donor), the electrons photogenerated on $NiFe_2O_4$-TiO_2

surfaces tend to be transferred to rGO sheets, which enhances the lifetime of the photogenerated charge carrier.

The choice of the $NiFe_2O_4$ is essential if we take into consideration its hierarchical gap in both the up and down channels; in such case, the electron transfer can occur in many electronic ways between the $NiFe_2O_4$, TiO_2 and rGO.

The addition of metallic Ag increased considerably the elimination yield. This can be explained by the extension of the lifetime of photogenerated carriers; when Ag is deposited on the surface of the semiconductor ($NiFe_2O_4$-TiO_2/$rGO_{10\%}$) (Schottky junction), at the interface, the band states of the metallic Ag are deeply buried into the band states of semiconductors [73]. In such situation, two parameters of the semiconductor must raise the work function of the electrons in the semiconductors and the Fermi level [62]. Furthermore, when the semiconductor is excited, the electrons of the CB flow into the Ag metal until equilibrium that is achieved when the Fermi energies are the same for both the metal and the semiconductor. The electron transfer to the metal delays the recombination electron-hole and increases the reactivity of electrons with the external media, enhancing thereby the photocatalytic performances. The Figure 4.13 summarizes the different proposed ways of the electron transfer in the composites.

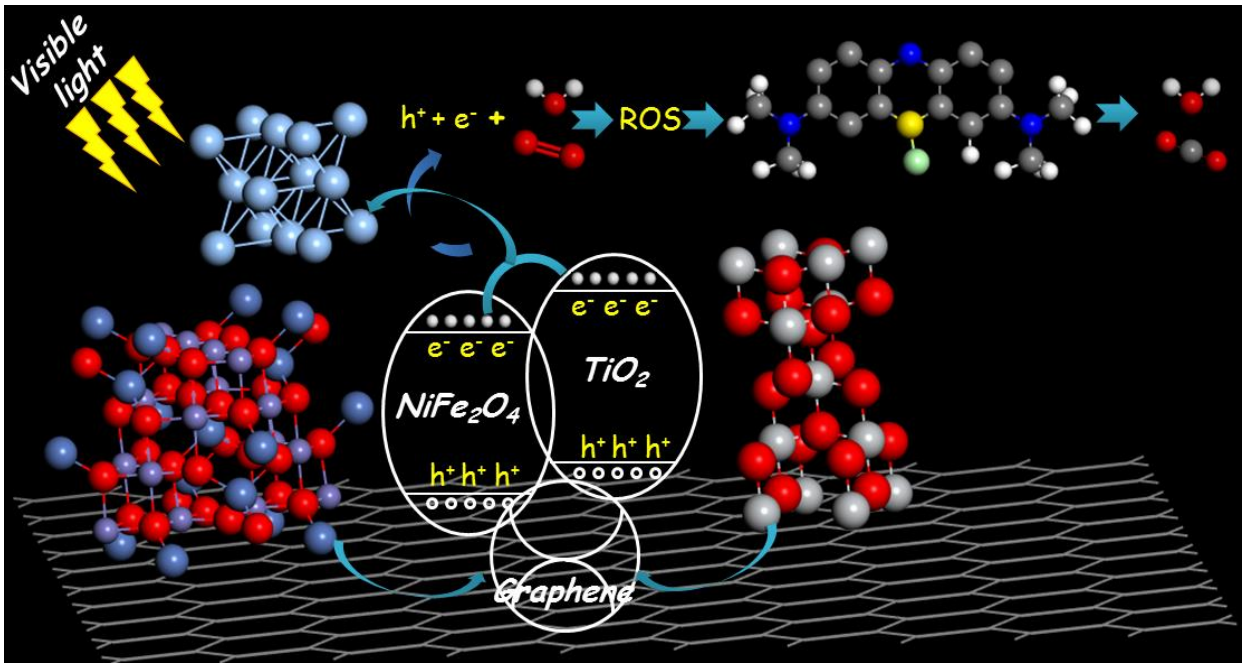

Figure. 4.13. *Schematic illustration of the photocatalytic mechanism of $NiFe_2O_4$/TiO_2@Ag composite.*

4.5. Conclusion

A series of $NiFe_2O_4$-TiO_2/rGO_x nanocomposites with various graphene amounts were successfully synthesized using a facile hydrothermal method to form heterojunction composites.

The XRD analysis proved that the $NiFe_2O_4$ had a spinel crystalline structure and the anatase TiO_2 had a tetragonal system. These structures are conserved after the deposition of rGO, although the crystalline size and the cell parameters decreased, evidently accompanied by an increase of the microconstraints (ξ%); this induced strong structural defects estimated by an increase of the dislocation density (δ). Furthermore, SEM images proved the formation of the heterojunction and the good mixing of $NiFe_2O_4$ and TiO_2 with the rGO.

The gap of pristine $NiFe_2O_4$ is hierarchical; this property offers to the composites many channels for the electron transfer. The UV-Vis-DRS spectroscopy revealed, though the Tauc formula, a direct gap of 2.9 eV and an indirect gap value of 2.2 eV. Owing to the presence of the anatase TiO_2, the composites had a strong absorption in the UV domain, and the graphene extended the absorption in the visible giving a good absorption in all the electromagnetic spectrum. This characteristic offered to the composites good photosensing ability. The gap values given by the Tauc formula was similar to the gap of anatase TiO_2; its change was not well defined, while the increase of the Urbach energy with the increase of the ratio x was well observed from 216 to 386 meV.

Moreover, the adsorption kinetic curves showed that the amount of MB adsorbed increased with the increase of the rGO amount, with an equilibrium time of approximately 40 minutes. The fit of the kinetic curves proved that the pseudo second order model was adequate. The photocatalytic study showed that all synthetized compounds had an impact on the degradation of the MB under visible light; the junction with rGO sheets improved considerably the adsorptive and photocatalytic performances and the best synergy between the two ways of elimination was obtained for the $NiFe_2O_4$/$rGO_{10\%}$ composite. The results indicated that deposit of graphene and decoration with Ag metallic particles enhanced visible light absorption and greatly improved separation of photogenerated carriers; the sample $NiFe_2O_4$-TiO_2/$rGO_{10\%}$@$Ag_{4\%}$ exhibited the best photocatalytic performances. At the end, a mechanism of photocatalysis was proposed.

References

[1] S. Farhadi and F. Siadatnasab, "CoFe2O4/CdS nanocomposite: Preparation, characterisation, and application in sonocatalytic degradation of organic dye pollutants," *Chinese Journal of Catalysis*, vol. 37, no. 9, pp. 1487–1495, 2016.

[2] S. Karthikeyan, V. K. Gupta, R. Boopathy, A. Titus, and G. Sekaran, "A new approach for the degradation of high concentration of aromatic amine by heterocatalytic Fenton oxidation: kinetic and spectroscopic studies," *Journal of Molecular Liquids*, vol. 173, pp. 153–163, 2012.

[3] Y. Liu, C. Luo, J. Sun, H. Li, Z. Sun, and S. Yan, "Enhanced adsorption removal of methyl orange from aqueous solution by nanostructured proton-containing δ-MnO 2," *Journal of Materials Chemistry A*, vol. 3, no. 10, pp. 5674–5682, 2015.

[4] D. Chebli, F. Fourcade, S. Brosillon, S. Nacef, and A. Amrane, "Supported photocatalysis as a pre-treatment prior to biological degradation for the removal of some dyes from aqueous solutions; Acid Red 183, Biebrich Scarlet, Methyl Red Sodium Salt, Orange II," *Journal of Chemical Technology & Biotechnology*, vol. 85, no. 4, pp. 555–563, 2010.

[5] L. Xia *et al.*, "Cr2O3 nanoparticle-reduced graphene oxide hybrid: A highly active electrocatalyst for N2 reduction at ambient conditions," *Inorganic chemistry*, vol. 58, no. 4, pp. 2257–2260, 2019.

[6] J. Qian *et al.*, "Exploration of CeO2–CuO quantum dots in situ grown on graphene under hypha assistance for highly efficient solar-driven hydrogen production," *Inorganic Chemistry*, vol. 57, no. 23, pp. 14532–14541, 2018.

[7] Y. Zhu *et al.*, "Graphene and graphene oxide: synthesis, properties, and applications," *Advanced materials*, vol. 22, no. 35, pp. 3906–3924, 2010.

[8] K. S. Novoselov *et al.*, "Electric field effect in atomically thin carbon films," *science*, vol. 306, no. 5696, pp. 666–669, 2004.

[9] S. Chen, J. Zhu, and X. Wang, "From graphene to metal oxide nanolamellas: a phenomenon of morphology transmission," *Acs Nano*, vol. 4, no. 10, pp. 6212–6218, 2010.

[10] A. Khort *et al.*, "Graphene@ metal nanocomposites by solution combustion synthesis," *Inorganic chemistry*, vol. 59, no. 9, pp. 6550–6565, 2020.

[11] A. K. Geim and K. S. Novoselov, "The rise of graphene," in *Nanoscience and Technology*, Co-Published with Macmillan Publishers Ltd, UK, 2009, pp. 11–19. doi: 10.1142/9789814287005_0002.

[12] L. Tang *et al.*, "Ultrahigh-rate behavior anode materials of MoSe2 nanosheets anchored on dual-heteroatoms functionalized graphene for sodium-ion batteries," *Inorganic chemistry*, vol. 58, no. 12, pp. 8169–8178, 2019.

[13] Y. Wang, H. Wu, Z. Liu, H. Zhao, H. Liu, and Y. Zhang, "Bottom-up construction of reduced-graphene-oxide-anchored MnO with an nitrogen-doped carbon coating for synergistically improving lithium-ion storage," *Inorganic chemistry*, vol. 57, no. 21, pp. 13693–13701, 2018.

[14] A. T. Habte and D. W. Ayele, "Synthesis and characterization of reduced graphene oxide (rGO) started from graphene oxide (GO) using the tour method with different parameters," *Advances in Materials Science and Engineering*, vol. 2019, 2019.

[15] Y. Fu, H. Chen, X. Sun, and X. Wang, "Graphene-supported nickel ferrite: A magnetically separable photocatalyst with high activity under visible light," *AIChE Journal*, vol. 58, no. 11, pp. 3298–3305, 2012.

[16] Y. Men, X. Liu, F. Yang, F. Ke, G. Cheng, and W. Luo, "Carbon encapsulated hollow Co3O4 composites derived from reduced graphene oxide wrapped metal–organic frameworks with enhanced lithium storage and water oxidation properties," *Inorganic Chemistry*, vol. 57, no. 17, pp. 10649–10655, 2018.

[17] J. Zhang, X. Wang, Y. Xue, Z. Xu, J. Pei, and Z. Zhuang, "Self-assembly precursor-derived MoP supported on N, P-codoped reduced graphene oxides as efficient catalysts for hydrogen evolution reaction," *Inorganic Chemistry*, vol. 57, no. 21, pp. 13859–13865, 2018.

[18] M. Feliz *et al.*, "Supramolecular anchoring of octahedral molybdenum clusters onto graphene and their synergies in photocatalytic water reduction," *Inorganic Chemistry*, vol. 58, no. 22, pp. 15443–15454, 2019.

[19] T. Tatarchuk, B. Al-Najar, M. Bououdina, and M. A. Ahmed, "Catalytic and photocatalytic properties of oxide spinels," *Handbook of ecomaterials*, vol. 3, pp. 1701–1750, 2019.

[20] R. Boulkroune *et al.*, "Hydrothermal synthesis of strontium-doped ZnS nanoparticles: structural, electronic and photocatalytic investigations," *Bulletin of Materials Science*, vol. 42, no. 5, pp. 1–8, 2019.

[21] S. Joshi, M. Kumar, S. Chhoker, G. Srivastava, M. Jewariya, and V. N. Singh, "Structural, magnetic, dielectric and optical properties of nickel ferrite nanoparticles synthesized by co-precipitation method," *Journal of Molecular structure*, vol. 1076, pp. 55–62, 2014.

[22] H. Bi *et al.*, "Quad-model imaging-guided high-efficiency phototherapy based on upconversion nanoparticles and ZnFe2O4 integrated graphene oxide," *Inorganic Chemistry*, vol. 57, no. 16, pp. 9988–9998, 2018.

[23] S. Kamali, "Spin structure, magnetism, and cation distributions of NiFe2- xAlxO4 solid solutions," *Journal of Magnetism and Magnetic Materials*, vol. 433, pp. 155–161, 2017.

[24] R. Zhang *et al.*, "Tuning conductivity and magnetism of CuFe 2 O 4 via cation redistribution," *RSC advances*, vol. 7, no. 35, pp. 21926–21932, 2017.

[25] S. M. Ismail, M. Yehia, and S. S. Ata-Allah, "Influence of zinc doping on the structural and magnetic properties of Ni-Ga-Sm polycrystalline ferrites," *Journal of Superconductivity and Novel Magnetism*, vol. 28, no. 9, pp. 2875–2880, 2015.

[26] B. Vara Prasad, K. V. Ramesh, and A. Srinivas, "Structural and magnetic studies of nano-crystalline ferrites MFe2O4 (M= Zn, Ni, Cu, and Co) synthesized via citrate gel autocombustion method," *Journal of superconductivity and Novel magnetism*, vol. 30, no. 12, pp. 3523–3535, 2017.

[27] A. Kovalenko *et al.*, "Towards improved efficiency of bulk-heterojunction solar cells using various spinel ferrite magnetic nanoparticles," *Organic Electronics*, vol. 39, pp. 118–126, 2016.

[28] P. N. Anantharamaiah and P. A. Joy, "Tuning of the magnetostrictive properties of cobalt ferrite by forced distribution of substituted divalent metal ions at different crystallographic sites," *Journal of Applied Physics*, vol. 121, no. 9, p. 093904, 2017.

[29] R. S. Yadav *et al.*, "Magnetic properties of Co1- xZnxFe2O4 spinel ferrite nanoparticles synthesized by starch-assisted sol–gel autocombustion method and its ball milling," *Journal of Magnetism and Magnetic Materials*, vol. 378, pp. 190–199, 2015.

[30] R. S. Yadav *et al.*, "Structural, cation distribution, and magnetic properties of CoFe2O4 spinel ferrite nanoparticles synthesized using a starch-assisted sol–gel auto-combustion method," *Journal of Superconductivity and Novel Magnetism*, vol. 28, no. 6, pp. 1851–1861, 2015.

[31] P. Guo, L. Cui, Y. Wang, M. Lv, B. Wang, and X. S. Zhao, "Facile Synthesis of ZnFe2O4 Nanoparticles with Tunable Magnetic and Sensing Properties," *Langmuir*, vol. 29, no. 28, pp. 8997–9003, Jul. 2013, doi: 10.1021/la401627x.

[32] J. L. Gunjakar, A. M. More, K. V. Gurav, and C. D. Lokhande, "Chemical synthesis of spinel nickel ferrite (NiFe2O4) nano-sheets," *Applied Surface Science*, vol. 254, no. 18, pp. 5844–5848, Jul. 2008, doi: 10.1016/j.apsusc.2008.03.065.

[33] "SciELO - Brazil - Facile synthesis of inverse spinel NiFe2O4 nanocrystals and their superparamagnetic properties Facile synthesis of inverse spinel NiFe2O4 nanocrystals and their superparamagnetic properties." https://www.scielo.br/j/mr/a/FFkKfZqgybscFKtVNwnsW8H/abstract/?lang=en (accessed Feb. 04, 2022).

[34] "The Magnetic Structure of NiFe2O4 Nanoparticles | SpringerLink." https://link.springer.com/article/10.1134/S1063785019100092 (accessed Feb. 04, 2022).

[35] K. Raj and R. Moskowitz, "Commercial applications of ferrofluids," *Journal of Magnetism and Magnetic Materials*, vol. 85, no. 1, pp. 233–245, Apr. 1990, doi: 10.1016/0304-8853(90)90058-X.

[36] A. Ren, C. Liu, Y. Hong, W. Shi, S. Lin, and P. Li, "Enhanced visible-light-driven photocatalytic activity for antibiotic degradation using magnetic NiFe2O4/Bi2O3 heterostructures," *Chemical Engineering Journal*, vol. 258, pp. 301–308, Dec. 2014, doi: 10.1016/j.cej.2014.07.071.

[37] "Solar photocatalytic mineralization of antibiotics using magnetically separable NiFe2O4 supported onto graphene sand composite and bentonite - ScienceDirect." https://www.sciencedirect.com/science/article/abs/pii/S2214714416303762 (accessed Feb. 04, 2022).

[38] M. O. Ojemaye, O. O. Okoh, and A. I. Okoh, "Uptake of Zn2+ and As3+ from Wastewater by Adsorption onto Imine Functionalized Magnetic Nanoparticles," *Water*, vol. 10, no. 1, Art. no. 1, Jan. 2018, doi: 10.3390/w10010036.

[39] "Research Update: Photoelectrochemical water splitting and photocatalytic hydrogen production using ferrites (MFe2O4) under visible light irradiation: APL Materials: Vol 3, No 10." https://aip.scitation.org/doi/full/10.1063/1.4931763 (accessed Feb. 04, 2022).

[40] "Spinel photocatalysts for environmental remediation, hydrogen generation, CO2 reduction and photoelectrochemical water splitting - Journal of Materials Chemistry A (RSC Publishing)." https://pubs.rsc.org/en/content/articlelanding/2018/ta/c8ta03669a/unauth (accessed Feb. 04, 2022).

[41] C. D. Valencia-Lopez *et al.*, "Synthesis of NiFe2O4-LDH Composites with High Adsorption and Photocatalytic Activity for Methyl Orange Degradation," *Inorganics*, vol. 6, no. 3, Art. no. 3, Sep. 2018, doi: 10.3390/inorganics6030098.

[42] "One-step combustion synthesis of CoFe2O4–graphene hybrid materialsfor photodegradation of methylene blue - ScienceDirect." https://www.sciencedirect.com/science/article/abs/pii/S0167577X13013323 (accessed Feb. 04, 2022).

[43] "Combustion synthesis and characterization of Sn4+ substituted nanocrystalline NiFe2O4 - ScienceDirect." https://www.sciencedirect.com/science/article/abs/pii/S0921510705001285 (accessed Feb. 04, 2022).

[44] "Inverse spinel NiFe2O4 deposited g-C3N4 nanosheet for enhanced visible light photocatalytic activity - ScienceDirect." https://www.sciencedirect.com/science/article/abs/pii/S1369800119301933 (accessed Feb. 04, 2022).

[45] "Preparation of NiFe2O4 - TiO2 nanoparticles and study of their photocatalytic activity | VNU Journal of Science: Mathematics - Physics." https://js.vnu.edu.vn/MaP/article/view/1531 (accessed Feb. 04, 2022).

[46] "SYNTHESIS OF MAGNETIC NANOPARTICLES OF TiO2-NiFe2O4: CHARACTERIZATION AND PHOTOCATALYTIC ACTIVITY ON DEGRADATION OF RHODAMINE B | Rahmayeni | Indonesian Journal of Chemistry." https://journal.ugm.ac.id/ijc/article/view/21335 (accessed Feb. 04, 2022).

[47] A. Vasanthakumar, G. G. Redhi, and R. M. Gengan, "Efficient catalytic activity of ionic liquid-supported NiFe2O4 magnetic nanoparticle doped Titanium Dioxide nano-composite," Dec. 2016, doi: 10.18178/ijcea.2016.7.6.618.

[48] "Facile Preparation of LaFeO3/rGO Nanocomposites with Enhanced Visible Light Photocatalytic Activity | SpringerLink." https://link.springer.com/article/10.1007/s10904-017-0534-8 (accessed Feb. 04, 2022).

[49] "Controlled synthesis, characterization and reduction of graphene oxide: A convenient method for large scale production - ScienceDirect." https://www.sciencedirect.com/science/article/pii/S2314808X16301762 (accessed Feb. 04, 2022).

[50] "Valorization of an agricultural waste, Stipa tenassicima fibers, by biosorption of an anionic azo dye, Congo red: Desalination and Water Treatment: Vol 54, No 1." https://www.tandfonline.com/doi/abs/10.1080/19443994.2014.880154 (accessed Feb. 04, 2022).

[51] "Novel activated carbon prepared from an agricultural waste, Stipa tenacissima, based on ZnCl2 activation—characterization and application to the removal of methylene blue: Desalination and Water Treatment: Vol 57, No 50." https://www.tandfonline.com/doi/abs/10.1080/19443994.2015.1137231 (accessed Feb. 04, 2022).

[52] "Impact of the annealing temperature on perovskite strontium doped neodymium manganites nanocomposites and their photocatalytic performances - ScienceDirect." https://www.sciencedirect.com/science/article/abs/pii/S1876107017301335 (accessed Feb. 04, 2022).

[53] "Simultaneous and efficient photocatalytic reduction of Cr(VI) and oxidation of trace sulfamethoxazole under LED light by rGO@Cu2O/BiVO4 p-n heterojunction composite - ScienceDirect."

https://www.sciencedirect.com/science/article/abs/pii/S0045653519300931 (accessed Feb. 04, 2022).

[54] "Impact of Aggregate Size and Structure on the Photocatalytic Properties of TiO2 and ZnO Nanoparticles | Environmental Science & Technology." https://pubs.acs.org/doi/abs/10.1021/es202009h (accessed Feb. 04, 2022).

[55] "Influence of TiO2 agglomerate and aggregate sizes on photocatalytic activity | SpringerLink." https://link.springer.com/article/10.1007/s10853-016-0400-z (accessed Feb. 04, 2022).

[56] "First-principles investigations of the magnetocrystalline anisotropy in strained Ni-substituted magnetite (NiFe2O4) - ScienceDirect." https://www.sciencedirect.com/science/article/abs/pii/S0304885301008861 (accessed Feb. 04, 2022).

[57] Q.-C. Sun *et al.*, "Optical band gap hierarchy in a magnetic oxide: Electronic structure of NiFe${}_{2}$O${}_{4}$," *Phys. Rev. B*, vol. 86, no. 20, p. 205106, Nov. 2012, doi: 10.1103/PhysRevB.86.205106.

[58] "Solution quenched in-situ growth of hierarchical flower-like NiFe2O4/Fe2O3 heterojunction for wide-range light absorption - ScienceDirect." https://www.sciencedirect.com/science/article/abs/pii/S0378775319311139 (accessed Feb. 04, 2022).

[59] "Milling effect on the photo-activated properties of $$\hbox {TiO}_{2}$$ TiO 2 nanoparticles: electronic and structural investigations | SpringerLink." https://link.springer.com/article/10.1007/s12034-018-1572-8 (accessed Feb. 04, 2022).

[60] "Iron-doped Pt–TiO2 nanotubes for photo-catalytic water splitting - IOPscience." https://iopscience.iop.org/article/10.1088/0957-4484/20/5/055602/meta (accessed Feb. 04, 2022).

[61] "TiO2 anatase's bulk and (001) surface, structural and electronic properties: A DFT study on the importance of Hubbard and van der Waals contributions - ScienceDirect." https://www.sciencedirect.com/science/article/abs/pii/S0039602816303004 (accessed Feb. 04, 2022).

[62] "Effect of surface Ag metallization on the photocatalytic properties of BaTiO3: Surface plasmon effect and variation in the Schottky barrier height - ScienceDirect." https://www.sciencedirect.com/science/article/abs/pii/S2468023018305510 (accessed Feb. 04, 2022).

[63] S. N. Dolia, R. Sharma, M. P. Sharma, and N. S. Saxena, "Synthesis, X-ray diffraction and optical band gap study of nanoparticles of $NiFe_2O_4$," *IJPAP Vol.44(10) [October 2006]*, Oct. 2006, Accessed: Feb. 04, 2022. [Online]. Available: http://nopr.niscair.res.in/handle/123456789/8367

[64] "Defect generation, d-d transition, and band gap reduction in Cu-doped TiO2 nanoparticles | SpringerLink." https://link.springer.com/article/10.1186/2228-5326-3-25 (accessed Feb. 04, 2022).

[65] M. Grundmann, *The Physics of Semiconductors: An Introduction Including Nanophysics and Applications*. Cham: Springer International Publishing, 2016. doi: 10.1007/978-3-319-23880-7.

[66] "Small-Sample Corrected Akaike Information Criterion: An appropriate statistical tool for ranking of adsorption isotherm models - ScienceDirect."

https://www.sciencedirect.com/science/article/abs/pii/S0011916411000142 (accessed Feb. 04, 2022).

[67] "Evaluation of an activated carbon packed bed for the adsorption of phenols from petroleum refinery wastewater | SpringerLink." https://link.springer.com/article/10.1007/s11356-017-8469-8 (accessed Feb. 04, 2022).

[68] M. B. Yahia, S. Knani, L. B. H. Hsan, M. B. Yahia, H. Nasri, and A. Ben Lamine, "Statistical studies of adsorption isotherms of iron nitrate and iron chloride on a thin layer of porphyrin," *Journal of Molecular Liquids*, vol. 248, pp. 235–245, Dec. 2017, doi: 10.1016/j.molliq.2017.10.073.

[69] "Catalysts | Free Full-Text | Mechanistic Insights into Photodegradation of Organic Dyes Using Heterostructure Photocatalysts." https://www.mdpi.com/2073-4344/9/5/430 (accessed Feb. 04, 2022).

[70] "Novel Fe2TiO5/reduced graphene oxide heterojunction photocatalyst with improved adsorption capacity and visible light photoactivity: experimental and DFT approach | SpringerLink." https://link.springer.com/article/10.1007/s11356-020-11221-0 (accessed Feb. 04, 2022).

[71] "Graphene oxide as a chemically tunable 2-D material for visible-light photocatalyst applications - ScienceDirect." https://www.sciencedirect.com/science/article/abs/pii/S0021951712004150 (accessed Feb. 04, 2022).

[72] Y. Li *et al.*, "Graphene-induced formation of visible-light-responsive SnO2-Zn2SnO4 Z-scheme photocatalyst with surface vacancy for the enhanced photoreactivity towards NO and acetone oxidation," *Chemical Engineering Journal*, vol. 336, pp. 200–210, Mar. 2018, doi: 10.1016/j.cej.2017.11.045.

[73] "Plasmonic Ag nanoparticles decorated SrTiO3 nanocubes for enhanced photocatalytic CO2 reduction and H2 evolution under visible light irradiation - ScienceDirect."
https://www.sciencedirect.com/science/article/abs/pii/S221298201930486X (accessed Feb. 04, 2022).

Interfacial coupling effects on adsorptive and photocatalytic performances for photoresponsive graphene wrapped-$SrTiO_3$@Ag under UV-visible light: experimental and DFT approach

5. Interfacial coupling effects on adsorptive and photocatalytic performances for photoresponsive graphene wrapped- $SrTiO_3$@Ag under UV-visible light: experimental and DFT approach

5.1. Abstract

Understanding the graphene/semiconductor/metal interactions is crucial to design innovative photocatalytic materials with efficient photocatalytic activity for environmental cleanup applications. $SrTiO_3$ on reduced graphene oxide (rGO) with various graphene contents was successfully synthesized in this study utilizing a simple hydrothermal method, followed by decorating the surface with Ag particles by using the photodeposition process. Under UV-visible light irradiation, the resulting composites were tested for their improved photocatalytic activity to decompose methylene blue (MB). The prepared photocatalysts were characterized by XRD, SEM, EDX, DLS, FT-IR, Raman spectroscopy, and DRS. First-principles density functional theory calculations (DFT) were also carried out by using the generalized gradient approximation (GGA) and PBE functional with the addition of on-site Coulomb correction (GGA + U). The obtained $SrTiO_3$/rGO@Ag composites showed great improvement in the photocatalytic performances over pristine $SrTiO_3$. For the degradation reaction of MB, $SrTiO_3/rGO_{20\%}@Ag_{4\%}$ composites yielded the best photocatalytic activity with efficacy reach 94 %, which was also shown that it could be recycled up to four times with nearly unchanged photocatalytic activity.

5.2. Introduction

Research in photocatalysis has much increased in the last years due to its potential use in environmental applications such as hydrogen generation, organic synthesis and water treatment technologies [1], [2]. Due to its environmental friendliness and energy sustainability, semiconductor photocatalysis has gained a lot of attention as one of the most important solar energy technologies [3]. The charge carriers on the semiconductor surface can be generated under light radiation and then accelerate the thermodynamic reaction upward to breakdown organic contaminants or produce chemical fuels with high energy density. They are principally caused by the generation of reactive oxygen-containing radicals with a short-lived (e.g., $OH^{\bullet}$, $HOO^{\bullet}$, and $O_2^{\bullet-}$) [4]. Because the photocatalyst is such an important component of semiconductor photocatalysis, synthesizing nanomaterials with a unique hierarchical structure and excellent photocatalytic activity has become a hot topic. The research work in the area of photocatalytic water splitting into hydrogen and oxygen has led to the development of many photocatalytic systems [5]–[7]. Heterogeneously dispersed

photocatalysts, such as TiO_2, $SrTiO_3$, ZnO, CdS and Fe_2O_3 have been extensively studied [8]–[11]. Perovskite materials are a diverse group of promising semiconductor photocatalysts that have been extensively investigated for use in Photocatalysis due to their structural, cost-effectiveness, tenability, excellent stability, and photocatalytic efficiency [12]–[14]. The strontium titanate ($SrTiO_3$) is a cubic ternary perovskite-type oxide with a significant nonlinear optical coefficient; it is considered one of the best n-type semiconductor photocatalysts known due to durable photostability, corrosion resistance and low cost, which exhibits great potential in splitting water into hydrogen and oxygen, as well as degrading organic compounds [15], [16]. $SrTiO_3$ has a comparable electronic structure with TiO_2 but with a more negative conduction band edge, making it more suitable for photocatalytic reduction. Furthermore, in regard of crystallographic texture, $SrTiO_3$'s cubic perovskite structure is more stable than TiO_2. [17]. It has been reported that pure $SrTiO_3$ [16], [18], [19] or ions doped $SrTiO_3$ [20]–[22] can show effective photocatalysis of organic pollutants under UV or Visible light irradiation.

The high performance of $SrTiO_3$ in reaction to heterogeneous photocatalysis requires an effective architecture that maximizes the absorption of photons and reduces electron losses during excitation state [23], [24]. Major efforts are required to further develop heterogeneous photocatalysis of $SrTiO_3$ under Ultraviolet, visible and solar illumination, in order to further improvement the transfer of charge carriers during excitation state. Actually, interesting and unique features of the binary photocatalyst mechanism have drawn more attention from researchers and have become a favorite subject of research among different groups of scientists across the globe [25]–[28]. It was reported that the properties of the photocatalyst system depend primarily on the nature of the surface properties, the surface morphologies and the role of the optimum amount of doping incorporated in the $SrTiO_3$ [14].

Graphene, with its exceptional properties have established itself as a promising supporting material for the manufacture of such hybrid material [29]. The conduction band contacts with the valence band at two points in the Brillouin zone makes graphene having high carrier mobility. In the visible light spectrum, graphene shows excellent optical transparency (97%) and refractive index (2.6-3.0). Its high extinction coefficient in the near IR range also provides graphene with a high photothermal conversion ability [30], graphene also have an excellent specific surface area (2630 $m^2.g^{-1}$) and unique structural features [31], [32]. These unique properties allow the use of graphene to produce hybrid materials with superior photo-responsive properties. These properties could be used to enhance the performance of

conventional organic and inorganic polymers for enhanced optical performance [33]. A major problem is the solubility and the processability of graphene-based materials, but it can be reduced by using GO (Graphene Oxide) [34]. Further chemical modification is also possible for GO as it has hydrophilic functional groups such as epoxide, carboxyl and hydroxyl groups on both edge and surface.

A semiconductor irradiated with photons containing energy equal to band gap energy contributes to the creation of electron hole (e^-, h^+) pairs during photocatalysis. The quick recombination of photogenerated electron-hole pairs limits the applicability of photocatalysis technologies in the industry, the substantial amount of scientific research is to extend life time [35]. The electron-hole recombination can be suppressed using a variety of strategies, this entails lowering the diffusion length by shrinking the size and creating various nanostructures interaction with other semiconductor materials that have a band location, which is appropriate for a smooth charge transfer, and connection with a conductor such as graphene [32], [36], [37]. Conducting materials such as graphene furnished support for catalytic particles and operate as an acceptor of electrons provided the photocatalyst conduction band must be more negative than the graphene band [38]. Graphene's new role as a photosensitizer macromolecular has been investigated where graphene interacts as an organic dye-like photosensitizer for wide band gap semiconductors [39]. The semiconductor cannot form an electron and a hole in this mechanism, but it is theoretically possible to photoexcite graphene under visible light. To put it another way, graphene becomes a semiconductor. The photoexcited electrons are moved from the CB of Graphene to the CB of the semiconductor, resulting in the separation of electrons and holes and resulting in visible-light photo-responsive [40]. A good photosensitizer might exhibit high optical absorption at a large range of wavelengths, especially in the visible region, and a sufficiently long life of the excited state to react with the semiconductors. In addition, the construction of metal semiconductor composites by the introduction of noble metal nanoparticles is also a promising method [21], [22]. For instance, Attout and colleagues created a bimetallic complex Au-Ag, which they grafted on the surface of P25-TiO_2 NPs and then incorporated into rGO sheets, resulting in an increase in visible light absorption and a reduction in the bandgap, which improved charge carrier separation and thus improved photocatalytic activity. The primary function of noble metal is illustrated as follows: used as electrons sink to facilitate the transfer of the interfacial electron to the composites; and the Surface Plasmon Resonance (SPR) of the noble metal enhances the light absorbance of the composite [41].

Herein, $SrTiO_3$ on reduced graphene oxide (rGO) with various graphene contents was successfully synthesized in this study utilizing a simple hydrothermal method. Then, the surface coated with Ag particles by using the photodeposition process; the synthesized sample's photocatalytic properties were examined in the degradation of methylene blue (MB) as a typical organic contaminant. As far as we know, the majority of the literature only focusses on charge migration in the system graphene/semiconductor and/or metal/semiconductor nanocomposite. Hence, certain parts of reaction mechanisms are still unknown. Therefore, the goal of this study was to look into the involvement of rGO and Ag metal in the UV-visible light photocatalytic activity of $SrTiO_3$/rGO@Ag nanocomposite. Moreover, the composite structure, morphological, electronic, and absorption properties were examined in detail and correlated to photocatalytic experiments. For this, several experimental characterizations and theoretical computational based on density functional theory (DFT) were employed by using the generalized gradient approximation (GGA) and PBE functional with the addition of on-site coulomb correction (GGA + U).

5.3. Experimental

5.3.1. Preparation methods

5.3.1.1. Synthesis of graphene oxide (GO) and cubic $SrTiO_3$

The modified Hummers method was used to prepare graphene oxide (GO), which is discussed in detail in our previous paper [42]. Strontium titanate $SrTiO_3$ was synthesized adopting the hydrothermal method [18], [43]. An amount of titanium (IV) isopropoxide was mixed with a stoichiometric amount of $Sr(NO_3)_2$ powders to obtain mixed phases, a solution of acetic acid as a lubricant were separately dissolved in minimum volume of distilled water; to obtain a homogeneous metal ion distribution, stoichiometric proportions of the required metal and acetic acid were utilized. Following total dissolution, acetic acid solution was poured onto the metal precursors followed by Polyethylene Glycol (PEG, 2 g/90 mL) addition. The addition of PEG controls the nanoparticle’s growth, leads to the prevention of agglomeration and the production of nanoparticles of uniform size. After one hour stirring, and under continuous stirring, the NaOH aqueous solution was added drop by drop until the pH value reached 13. Indeed, the suspension was transferred to Teflon sealed autoclave and maintained at 180°C for 24 hours. Finally, it was washed in ethanol and distilled water multiple times before being dried in a 60°C oven for 24 hours.

5.3.1.2. Preparation of $SrTiO_3/rGO_{20}$@Ag photocatalysts

The Preparation of $SrTiO_3$/rGO photocatalysts with different weight ratios of rGO were obtained via the hydrothermal method, Figure 5.1 [40]. Firstly, 200 mg of $SrTiO_3$ powder and appropriate weight ratios of GO to $SrTiO_3$ (x = 0, 5, 10, 15 and 20 wt.%) was dispersed in a mixing solution of ethanol and water (2:1) by ultrasonic treatment for 1 hour. Then, the mixing solution was agitated for additional 30 minutes to get homogenous suspension. The suspension was placed in Teflon-sealed autoclave at 120°C for 12 hours. The obtained photocatalyst was centrifuged three times with distilled water before being dried in a 60°C oven for 24 hours. A simple photo-deposition method was used to prepare the $SrTiO_3$/ rGO_{20}@Ag_x photocatalyst with 1, 2, 3 and 4 wt.% of metallic Ag [44]. For this purpose, an amount of synthesized $SrTiO_3/rGO_{20}$ nanocomposite powder was dispersed into 100 mL of deionized water, then 9.27 $x10^{-5}$ M of $AgNO_3$ solution was suspended in the mixture solution and diluted to 0.5 L with distilled water accompanied by 30 minutes of ultrasound treatment and 2 hours magnetic stirring under 300 W Xenon lamp for the photoreduction of Ag^+ to Ag^0. The powder was then collected and dried under vacuum.

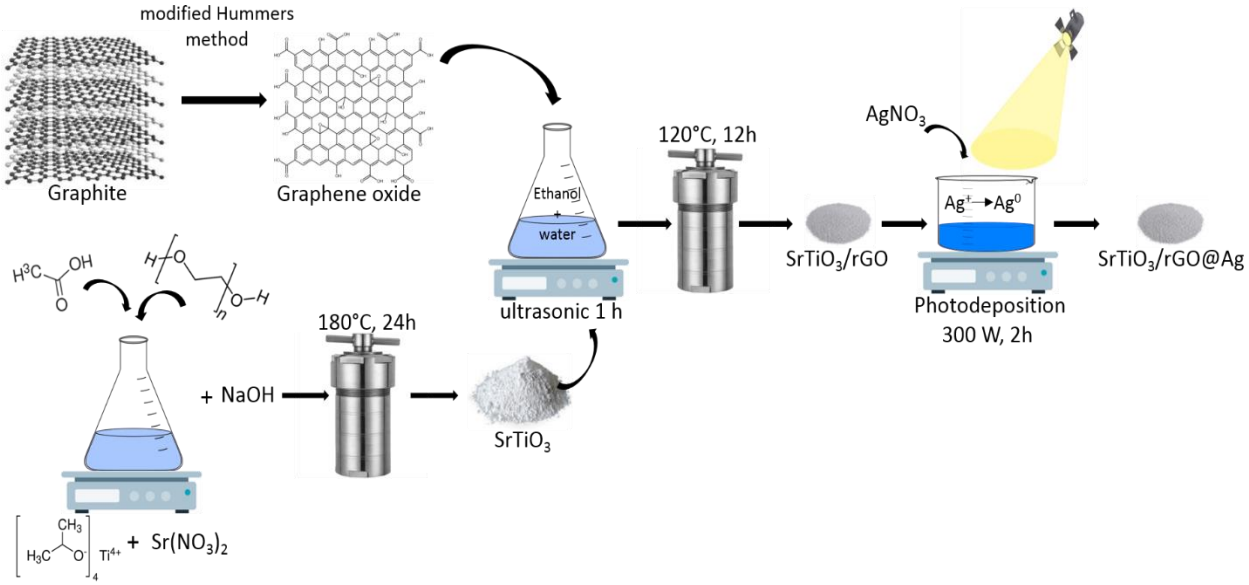

***Figure 5.1**: Schematic diagram for preparing the $SrTiO_3$/rGO@Ag nanocomposites.*

5.3.2. Computational Details

The electronic and structural properties of $SrTiO_3$ bulk, density functional theory (DFT) computations was used to examine pristine $SrTiO_3$, graphene and hybrid $SrTiO_3$/rGO@Ag composite to comprehend the mechanisms of its enhanced photocatalytic activity under visible light irradiation. The use of DFT calculations to decipher the nature of electronic interactions at composite interfaces is pretty helpful. [45]. Exchange and correction energies

were described by using the Generalized Gradient Approximation (GGA) and PBE functional with the addition of on-site coulomb correction (GGA + U), by employing the Cambridge Serial Total Energy Package (CASTEP), which is based on plane-wave pseudopotential DFT methods [46]. It has been reported that GGA methods provide a better prediction of lattice constants and electron structure than LDA, especially for surface layers [47]. However, (GGA+U) has been known generally to prevent the unwanted delocalization of the *d* or *f* electrons and to underestimate the energy gap of semiconductor [48], resulting into an overestimate for photoinduced electrons transfer in photocatalytic processes. The required Hubbard U values for Ti 3*d*, Sr 4*d*, and O 2*p* were 5.0, 5.0, and 5.0 eV [49], respectively, to correct the $SrTiO_3$ band gap problem.

The $SrTiO_3$ bulk, pristine rGO, and $SrTiO_3$/rGO@Ag composite structures were constructed using Material Studio software, by choosing a cubic $SrTiO_3$ (100) surface: in a supercell ($8.16 \times 7.59 \times 25$ $Å^3$), a 5×3 single layer of rGO containing 60 carbon atoms sits on a 3×2 five atomic layer STO (100) and 5×5 tow layer Ag metal (200) surface slab. A Morkhost-Pack mesh of k points, 4×4×1, 8×8×1 and 2×2×1 point, was used to sample the two-dimensional Brillouin zone for geometry optimization and for calculating the density of states of $SrTiO_3$, rGO and $SrTiO_3$/rGO@Ag composite, respectively. The plane wave cutoff energy was set at 571 eV. All geometrical structures were totally relaxed until the convergence criteria of force and energy were less than 0.03 eV/Å and 10^{-6} eV/atom, respectively. Total energy tolerance at 105 eV/atom for convergence parameters, maximum force tolerance was chosen at 0.03 eV/nm, and maximum stress component at 0.05 GPa.

5.4. Results and discussion

5.4.1. Structural analysis

The XRD pattern of $SrTiO_3/rGO_x$ (x = 0, 5, 10, 15 and 20 %) composites are shown in the Figure 5.2(a). The composites presented almost the same profiles and the peaks were localized at the angular positions: 2θ = 22.74, 32.38, 39.95, 46.47, 52.36, 57.79, 67.83, 77.21, 81.76 and 86.22 °; these peaks were identified according to (JCPDS card No. 35-0734) as respectively (1 0 0), (1 1 0), (1 1 1), (2 0 0), (2 1 0), (2 1 1), (2 2 0), (3 1 0), (3 1 1) and (2 2 2) Bragg's planes of the cubic perovskite $SrTiO_3$ structure [16]. The Figure 5.2(a) also shows the XRD patterns of $SrTiO_3/rGO_{20}@Ag_x$ composites for 2 and 4 % weight ratio of Ag; the most significant peaks appeared at the angular positions 2θ = 38.12º and 44.28º, which corresponded to the (111) and (200) Bragg's planes of cubic Ag phase (JCPDs No. 04-0783) [20]. The development of metallic Ag^0 particles adhered to the surface of the

composites was evidenced by the extra diffraction peaks detected in Ag deposited samples. Furthermore, metallic Ag had an atomic radius of 1.44 Å, which was significantly more than the ionic radius of Ti^{4+} (0.68 Å) [50]. Consequently, without causing crystal structural distortion, Ag cannot easily diffuse into the $SrTiO_3$ lattice. No diffraction peaks related to other impurities were detected on the XRD patterns, suggesting a high purity of the crystalline phases.

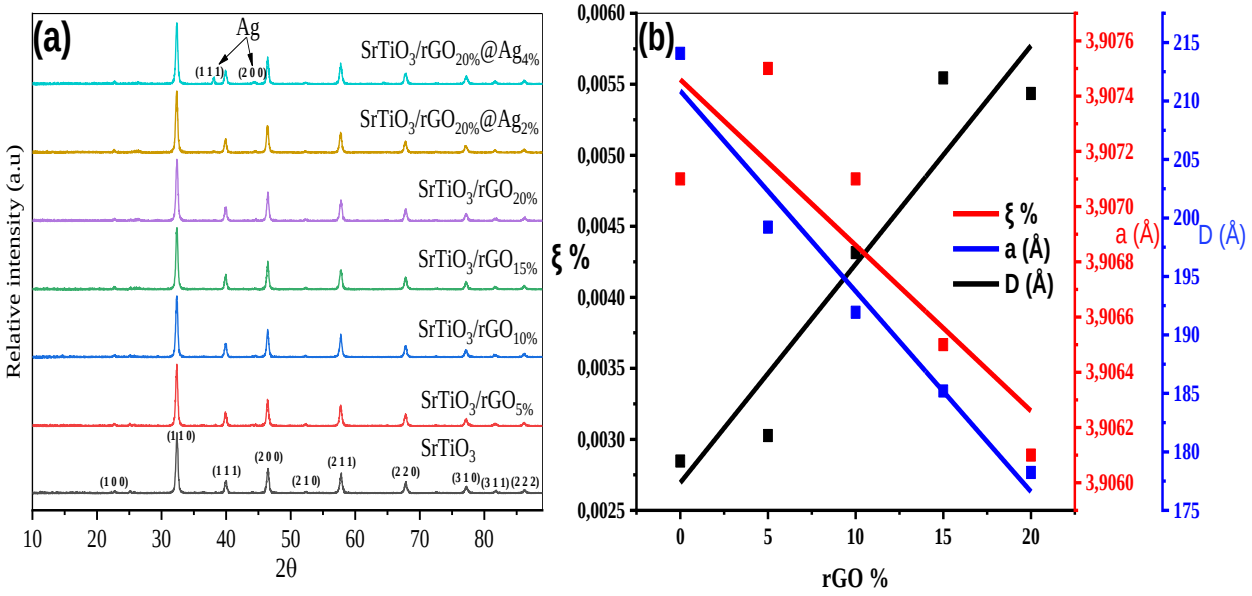

Figure 5.2: (a) *XRD patterns of $SrTiO_3/rGO_x$ (x = 0, 5, 10, 15 and 20%) and $SrTiO_3/rGO_{20}@Ag_x$ (x = 2 and 4%), normalized by the highest intensity to one.* ***(b)*** *The characteristic crystalline parameter (a), the average grain seizes (D), microconstraint (ξ%) for the composites $SrTiO_3/rGO_x$ (x=0, 5, 10, 15 and 20%).*

Moreover, the characteristic crystalline parameter (a), the average grain seizes (D), microconstraint (ξ%) and dislocation density (δ) are illustrated in Table 5.1.

The largest lattice parameter was estimated for pristine $SrTiO_3$. Subsequently, the deposit of rGO on $SrTiO_3$ caused a shrinkage of the unit cell; small but noticeable, a decrease in the lattice parameter (a) was observed with increasing the rGO weight ratio. It is seen from both the Figure 5.2(b) and the Table 5.1 that the fixation of rGO sheets on $SrTiO_3$ decreased the average grain seize (D), obviously accompanied by a rise in microconstraints (ξ%) and caused significant structural defects as measured by an increase in dislocation density (δ); this indicates that the rGO induced stress in the $SrTiO_3$ crystal structure. On another hand, the lattice strain values and the grain size were affected by the Ag decoration.

Table 5.1: *Lattice parameters, grain seizes, microconstraints and dislocation densities of $SrTiO_3/rGO_x$ (x = 0, 5, 10, 15 and 20%) and $SrTiO_3/rGO_{20}@Ag_x$ (x = 2 and 4%)*

	$SrTiO_3/rGO_x$	0%	5%	10%	15%	20%	@Ag 2%	@Ag 4%
a (Å)	experimental	3,9073	3,9074	3,9071	3,9065	3,9061	3,9070	3,9081
	theoretical GGA	3,9053						
	D (Å)	214,07	199,21	191,93	185,20	178,24	189,93	199,25
	ξ %.10^{-2}	0,285	0,303	0,431	0,554	0,543	0,671	0,701
	δ $(nm)^{-2}.10^{-3}$	2,182	2,520	2,715	2,915	3,148	2,772	2,519

5.4.2. Scanning Electron Microscopy (SEM)

The shape of $SrTiO_3$ and the formation of the junction between $SrTiO_3$ and rGO were studied by SEM analysis.

As shown in the Figure 5.3 (a and b), the $SrTiO_3$ had a cubic form and the sizes distribution was fitted with Gaussian function which is shown in the Figure 5.3 (x); this latter proved that the average size of $SrTiO_3$ nanocubes was about 51 nm, with a width at half height of about 12 nm, this value was compatible with the result found by XRD analysis [19], [54]. In addition, a perfect cubic particle can only be formed with six equivalent {100} facets of a crystal with a cubic structure [55], [56]. The Figure 5.3 (c−h) shows SEM images of $SrTiO_3/rGO_x$; it can be seen that the cubic structure of $SrTiO_3$ was retained and the $SrTiO_3$ particles were well dispersed on the overall surface of the graphene sheets. These results revealed that $SrTiO_3/rGO_x$ heterojunction was successfully prepared.

Otherwise, the composition of $SrTiO_3$ obtained by EDX analysis, the Figure 5.3 (y) illustrates the presence of the Ti, Sr and O elements, which confirmed the product's purity. The chemical formula can be writing as $Sr_{0,93}Ti_{1,08}O_{2,99}$; this formula was in good agreement with what can be expected for a perovskite structure.

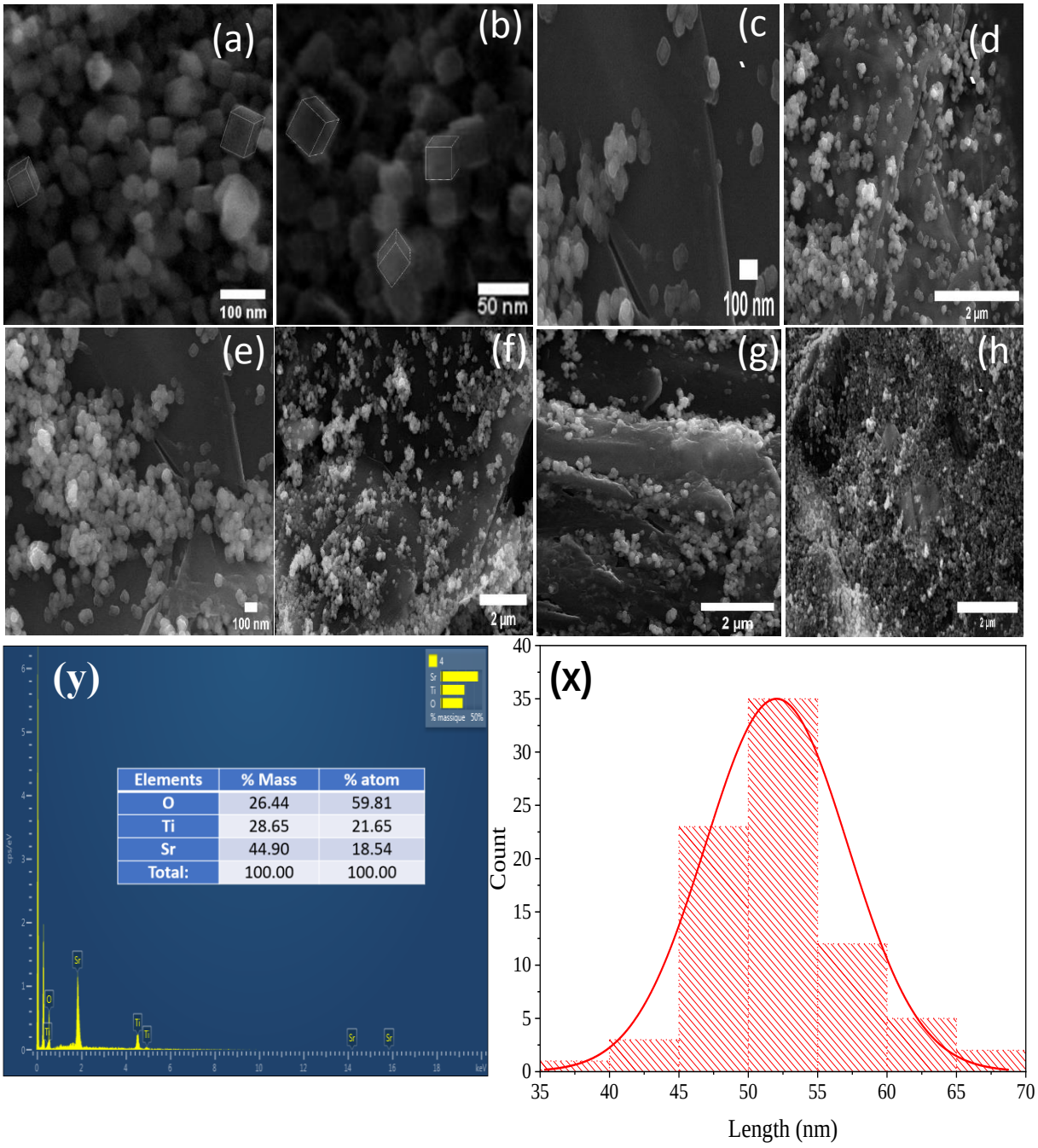

Figure 5.3: *In top SEM images of $SrTiO_3$ (a and b) and $SrTiO_3$/rGO_x composites (c−h) with different amount of rGO. In bottom* ***(a)*** *the widths of $SrTiO_3$ nanocubes is in the range 51 nm,* ***(b)*** *the composition of $SrTiO_3$ were obtained by EDX analysis.*

5.4.3. Dynamic light scattering (DLS)

The external surface of nanoparticles, as well as their surface state, have a significant impact on their adsorption and photocatalytic activities; the aggregated particles' surface is the effective surface exposed to the external medium. Furthermore, the aqueous solution aggregation of metal oxides is well-known and well-studied [57], [58]. For this basis, DLS

was used to characterize the $SrTiO_3$ samples, Figure 5.4 depicts the hydrodynamic diameter of aggregated nanoparticles suspended in distilled water and the Gaussian function was used to fit the experimental data. The fitted curve demonstrated the growth of aggregated particles of various sizes, the average hydrodynamic diameter seize value was around 199 nm, with a width at half height of about 147 nm and the experimental standard deviation was about 14 nm (the measurement was performed three times), comparatively to the grain seizes estimated by XRD and SEM analysis (D = 21.4 and 51 nm respectively). The $SrTiO_3$ had a weak tendency to aggregate; this result was due to the use of PEG in the synthesis which prevent from agglomeration and leads to the production of nanoparticles of uniform shapes.

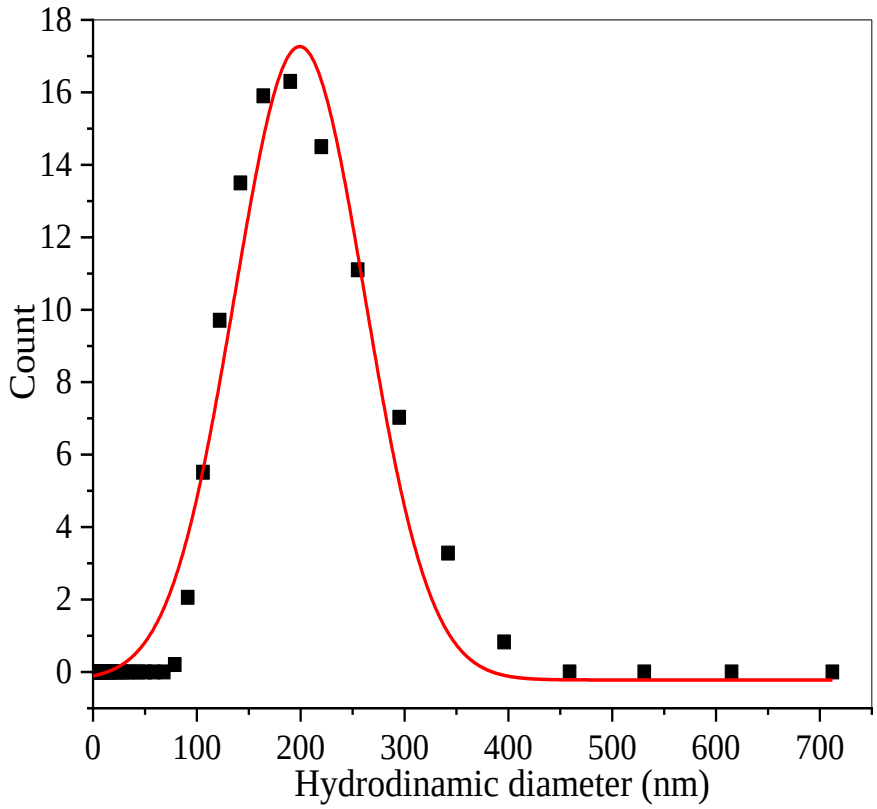

Figure 5.4: *Hydrodynamic diameter of $SrTiO_3$ in H_2O suspension.*

5.4.4. Fourier-Transform Infrared Spectroscopy (FT-IR)

The FT-IR spectra obtained for GO (Graphene Oxide), $SrTiO_3$/rGO_x and $SrTiO_3$/rGO_x@Ag nanocomposites are shown in the Figure 5.5. The spectra of GO clearly showed numerous absorption peaks that related to distinct functional groups. C−H bending vibration was attributed for the band at 934 cm^{-1}, the peak at 1713 cm^{-1} was assigned to C=O stretching vibration of the COOH group. The band at 1632 cm^{-1} was due to C=C stretching vibration

and the absorption peak at 1397 cm^{-1} corresponded to C−OH bending vibration [40], [59]. The absorption peak at 1249 cm^{-1} was due to C−O−C asymmetric stretching vibration, the peak at 1041 cm^{-1} was attributed to C−O stretching vibration [60]. From the comparison between the spectra of the composites and the GO spectrum, the reduction of the C=O band intensity at 1713 cm^{-1} indicated that GO was reduced to rGO after the hydrothermal treatment.

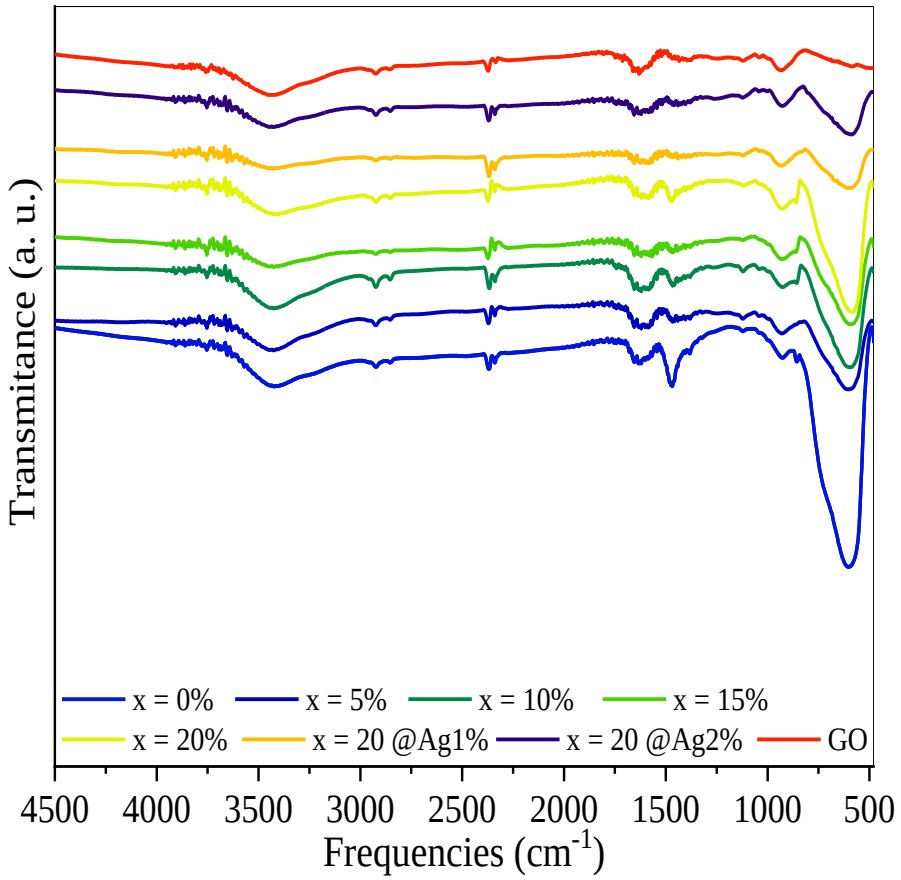

Figure 5.5: *FT-IR spectra of GO, $SrTiO_3$/rGO_x (x = 0, 5, 10, 15 and 20%) and $SrTiO_3$/rGO_{20}@Ag_x (x = 1 and 2%) nanocomposites.*

On the spectra of the $SrTiO_3$/rGO_x composites, compared to pristine $SrTiO_3$, the Ti–O–Ti bands at 602 cm^{-1} shifted to 545 cm^{-1} at lower wavenumber and exhibited weaker peak intensity; the absorption of the TiO_6 group in the octahedral structure was attributed to this band. [61], [62]. It may be attributed to the incorporation of C atoms into the $SrTiO_3$ and the formation of the Ti–C bond [63]. In addition, a new band at 928 cm^{-1} can be observed, confirming the formation of Ti–C bond; the presence of this bond indicates that during the reduction of GO, the residual carboxylic acid functional groups interact with the surface of

$SrTiO_3$ nanoparticles, and form a bonded $SrTiO_3/rGO_x$ composite. The C=C bands at 1632 cm^{-1} shifted gradually to 1620 cm^{-1} with increasing ratio of rGO, indicating that the skeletal of the graphene sheets was influenced. Finally, the IR spectrum of $SrTiO_3/rGO_x$@Ag was comparable to that of $SrTiO_3/rGO_x$ composites.

5.4.5. Raman spectroscopy

For the characterization of graphitic materials, Raman spectroscopy is widely employed [64], [65]. The distinctive bands of graphene, such as D, G, and 2D, provide relevant information regarding defects, sp^2 carbon atom in-plane vibrations, and stacking orders, respectively. In addition, the G band (1582 cm^{-1}) was formed by first-order scattering of E_2g phonons of the sp^2-hybridized carbon atoms. While the D band (1350 cm^{-1}) was formed by a breathing mode of *K*-point phonons of A_1g symmetry of the defects involved in sp^3-hybridized carbon bonds such as epoxide and/or hydroxyl bonds, and the 2D band (2679 cm^{-1}), which is quite sensitive to graphene sheet stacking [66]. Figure 5.6 (a) illustrate the Raman spectroscopy of $SrTiO_3$/rGO nanocomposites. All the composites $SrTiO_3$/rGO exhibits the appearance of G peak around (1584 cm^{-1}). The D peak appear from the ratio 15% of rGO in $SrTiO_3$/rGO nanocomposites at (1352 cm^{-1}), and the 2D peak is not observed so far, which might have been due to substrate screening effect and the small quantity of rGO in the composites. The repression of 2D peak is observed at (2697 cm^{-1}) in the composite $SrTiO_3$/rGO (20% of rGO).

The D to G peak intensity ratio is commonly used to evaluate graphene disorder, which is an indirect indication of the material's quality (Figure 5.6 (b)). The D/G ratio was determined to be 0.34 in this study, which is lower than the value reported in prior research [66]. This higher ratio can be attributable to the existence of more disordered nano-graphene. The bilayer sheets' 2D/G ratios were found to be in the range of 0.26, confirming the deposition of triple- and multi-layer (>4) graphene sheets on $SrTiO_3$ nanocubes based on the same earlier study.

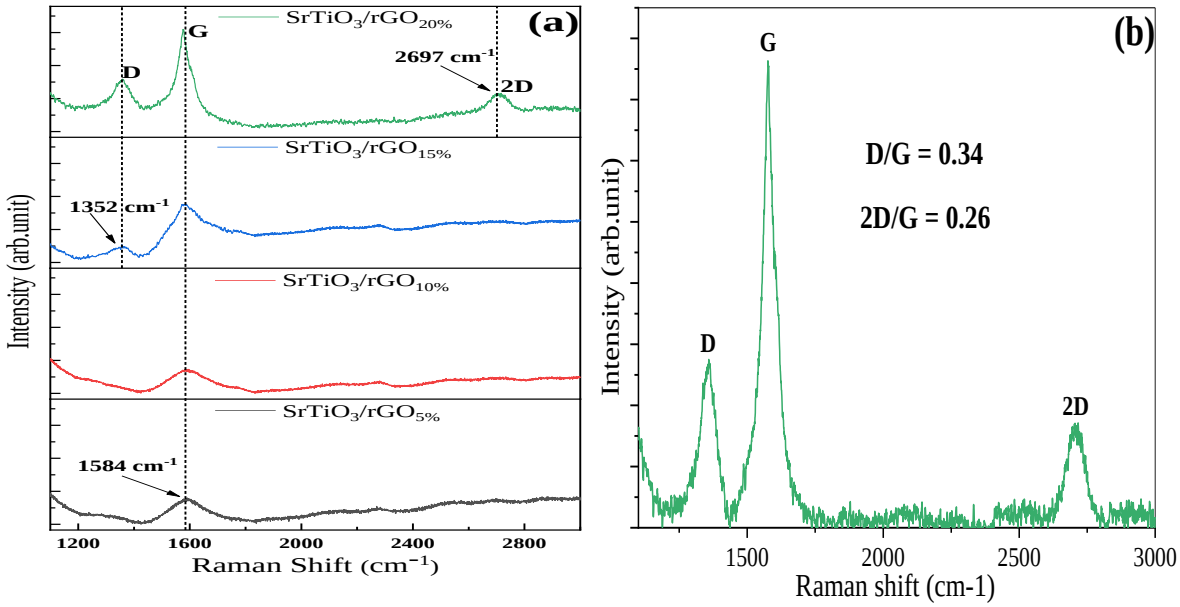

Figure 5.6: *(a) Raw Raman spectra of $SrTiO_3/rGO_x$ (x = 5, 10, 15 and 20%) nanocomposites, (b) subtract straight line Raman spectra of $SrTiO_3/rGO_x$ (x = 20%) present D/G and 2D/G ratios.*

5.4.6. Electronic structure and optical properties

5.4.6.1. First Principle Study of the $SrTiO_3$/rGO@Ag Heterojunction

In order to understand the structure well, the binding and the electronic properties of $SrTiO_3$/rGO@Ag composite were studied by DFT simulations. The optimized relaxed geometries of $SrTiO_3$/rGO and $SrTiO_3$/rGO@Ag are shown in the Figure 5.7. The electronic structure of nanocomposites is mostly defined by the components' interfacial interactions; their total (DOS) and Partial (PDOS) Density of States can evidence the variation of electronic properties of the $SrTiO_3$/rGO@Ag composites. The band structure and PDOS plots of $SrTiO_3$ are given in the Figures 5.8 and 5.9, respectively. It can be seen that the maximum of the valence band (VBM) and the minimum of the conduction band (CBM) of $SrTiO_3$ were located at 0.00 eV and +2.98 eV respectively (Figure 5.8), so the band gap was about 2.98 eV. In addition, the VBM was mainly dominated by the Sr *4p* and O *2p* states; while, the main contribution in the CBM was the Ti *3d* state (Figure 5.9). Moreover, the band structure of rGO is shown in the Figure 5.8. For the rGO, its antibonding π* orbitals (which makes up its conduction band) and bonding π orbitals (which makes up its valence band) degenerated and touch at Brillouin zone corners, making graphene a zero-band gap semi-conductor material.

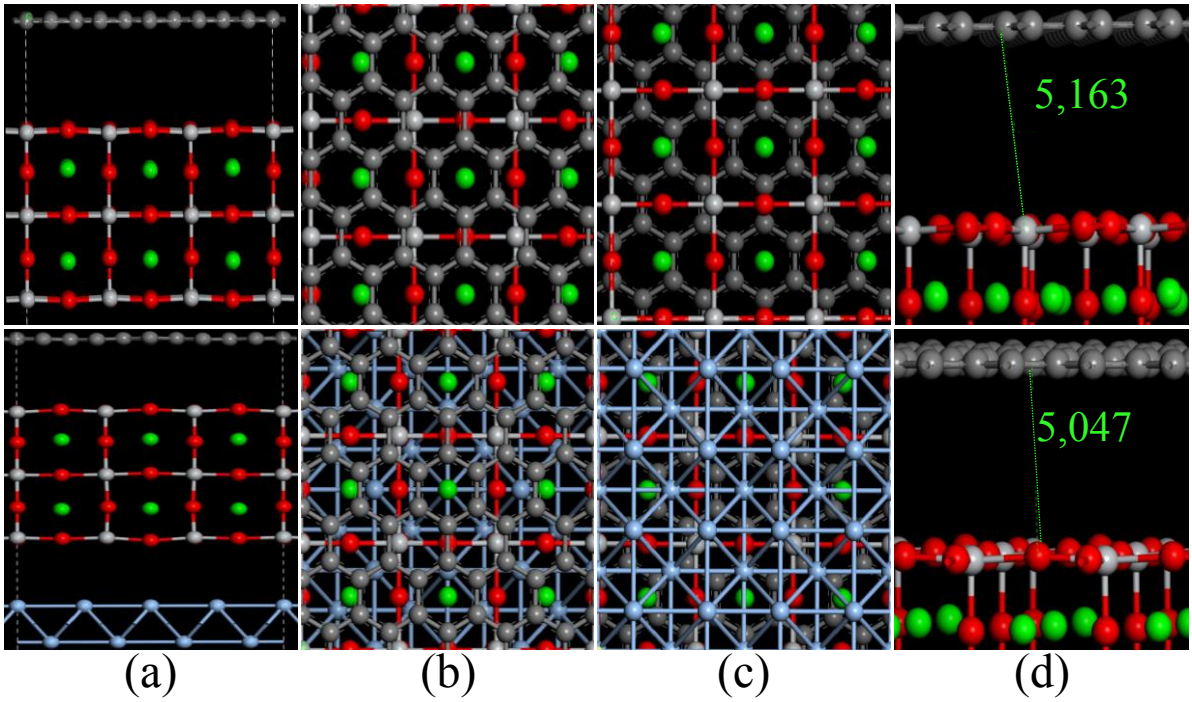

Figure 5.7: *the columns (a) side, (b) bottom, and (c) top views of $SrTiO_3$/rGO on top, and $SrTiO_3$/rGO@Ag in bottom. The column (d): on top the distance (Å) of C–Ti, and the bottom C–O.*

When contacting the $SrTiO_3$ surface with rGO sheets, the difference in the work function of the graphene and the $SrTiO_3$ leads to electrons transfer between them to equilibrate their Fermi levels [67]–[69]. Compared to the gap of pristine $SrTiO_3$, the band gap was substantially reduced and decreased from 2.98 to 0.06 eV. The contact of $SrTiO_3$ with rGO produced some inter-levels in the band gaps of $SrTiO_3$; these levels belonged to the C of rGO as can be seen in the Figure 5.8. These inter-levels (also called trap centers) can trap the electron–hole recombination which may consequently enhance the photocatalytic activity, the photogenerated electrons transfer from the VB to the CB of the $SrTiO_3$/rGO composites become easier, which lead to red shift of the optical absorption edge. These statements can explain our experimental results.

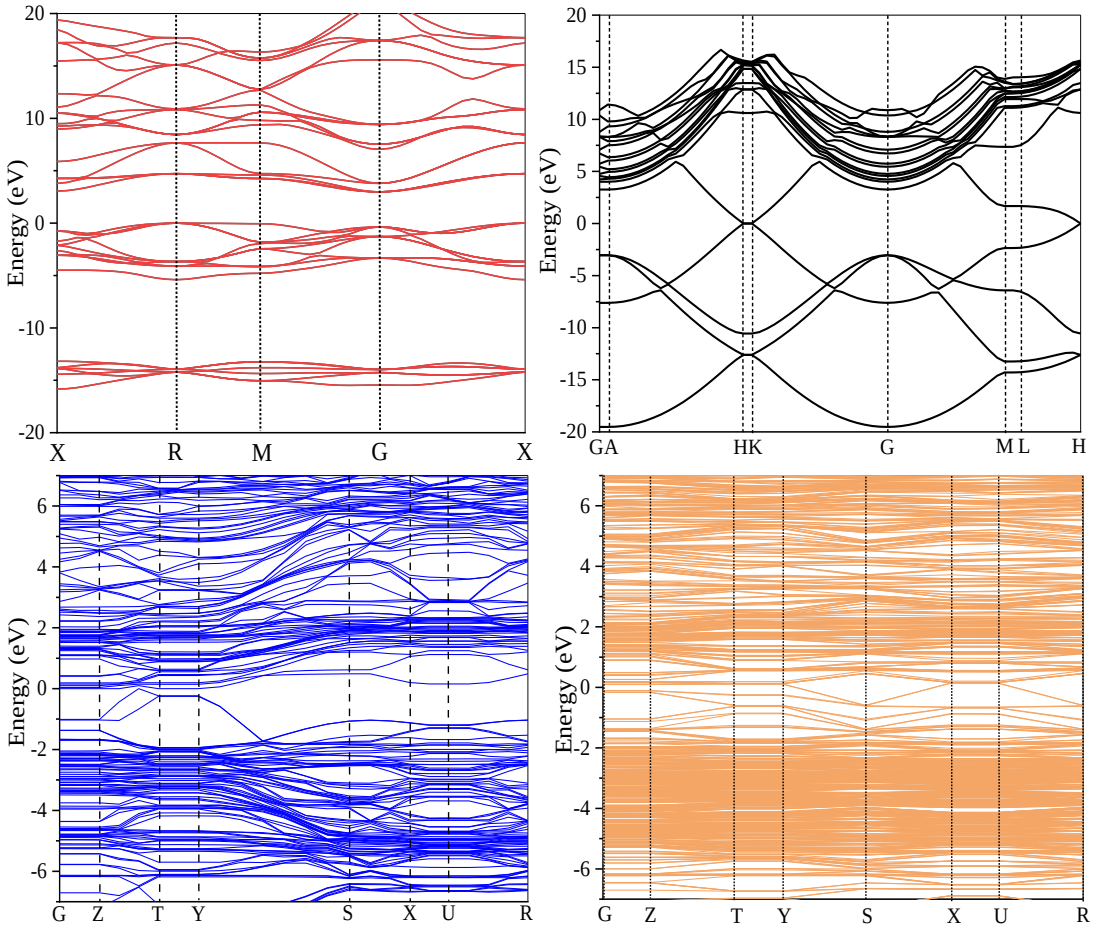

Figure 5.8: *Band structure of $SrTiO_3$ (red), rGO (black), $SrTiO_3$/rGO (blue), and $SrTiO_3$/rGO@Ag (orange).*

Another important feature in the Figure 5.10 was the band alignment between the $SrTiO_3$ surface and rGO sheet. One can find that the main shapes of the calculated PDOS projected on the composite can be seen as a superposition of the total DOS of the $SrTiO_3$ and rGO; this can be due to the large geometrical separation space between the $SrTiO_3$ and rGO layers. On the other hand, we find that the theoretical bond lengths C–O and C–Ti are about 1.42 and 2.27 Å [70], [71], respectively; in return, the separation of oxygen and titanium from carbon in the optimized structure was about 5.05 and 5.16 Å; these large values suggested a weak interaction and an absence of covalent bonding. This leads us to conclude that the van der Waals interaction is expected to be significant in these composites [49]. Figure 5.10 displays that the VBM of the $SrTiO_3$/rGO composite only consisted of O *2p* states, while the CBM was formed from C *2p* and Ti 3*d* orbitals.

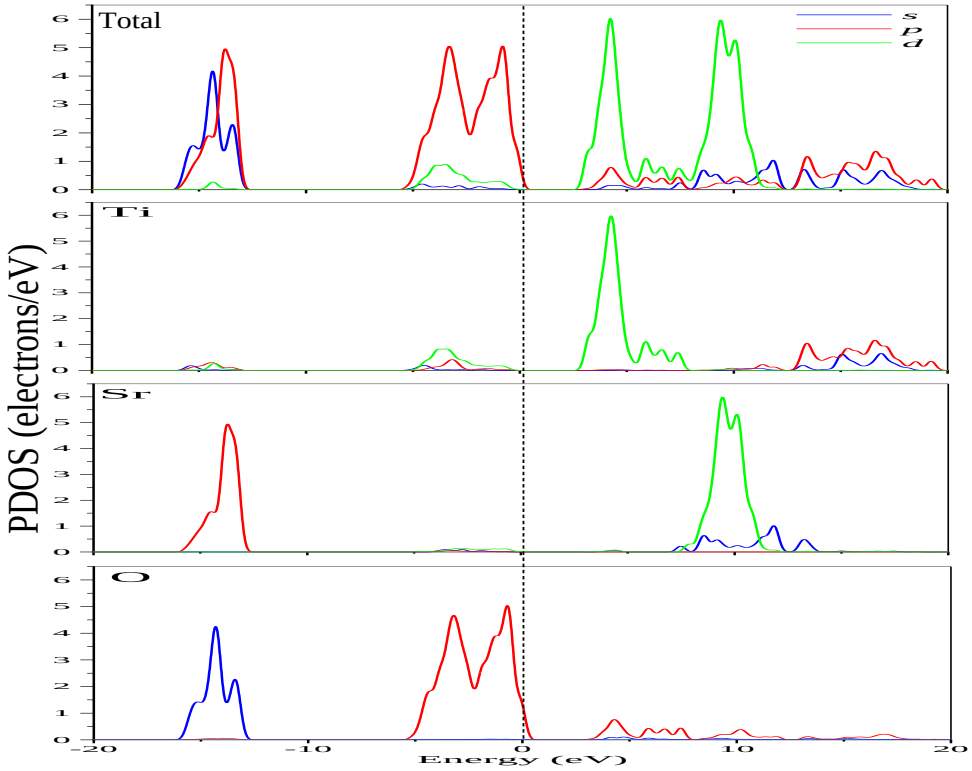

***Figure 5.9**: PDOS for the $SrTiO_3$ composite. The Fermi level is set to zero.*

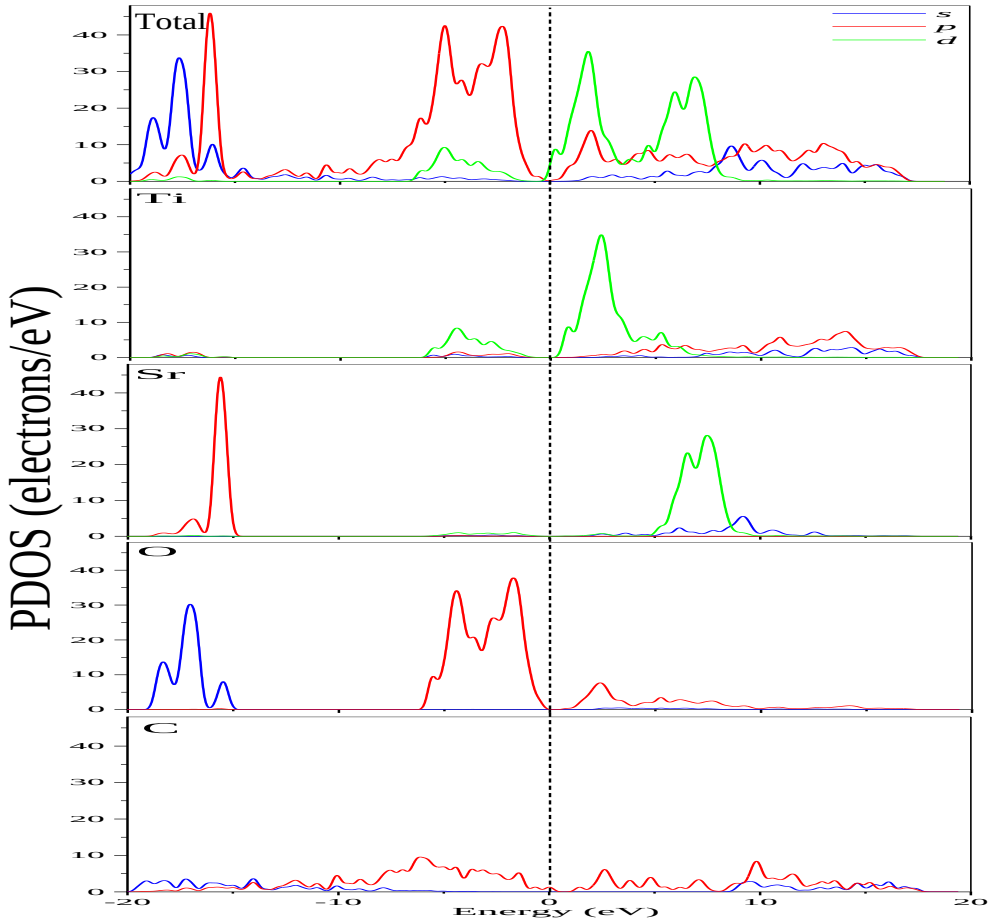

***Figure 5.10:** PDOS for the $SrTiO_3$/rGO composite. The Fermi level is set to zero.*

The transformation of band gap upon deposit of Ag nanoparticles suggests an important fact, it enhances the photocatalytic activity under light illumination due to slow electron-hole recombination process, as compared to those of $SrTiO_3$/rGO where the recombination happens more quickly [72]. For the sake of comparison between the $SrTiO_3$/rGO and decorated systems ($SrTiO_3$/rGO@Ag), the PDOS were plotted in the Figure 5.11, showing significant differences in valance and conduction band states before and after deposit of Ag (the VBM and CBM of the composites $SrTiO_3$/rGO@Ag were moved toward more positive potentials). The deposition of Ag nanoparticles on $SrTiO_3$/rGO showed that the valence band was shifted upward and was mainly formed by Ag *5s* and O *2p* states, while the bottom of CB was formed from Ti *3d* orbitals. Furthermore, the work function of Ag was slightly higher than that of $SrTiO_3$/rGO composite. Therefore, in this case, the photo-generated electrons (CB) of $SrTiO_3$/rGO are transferred to the surface of Ag nanoparticles, until the equilibrium of the Fermi level, and consequently the lifetime of photo-generated carriers increases.

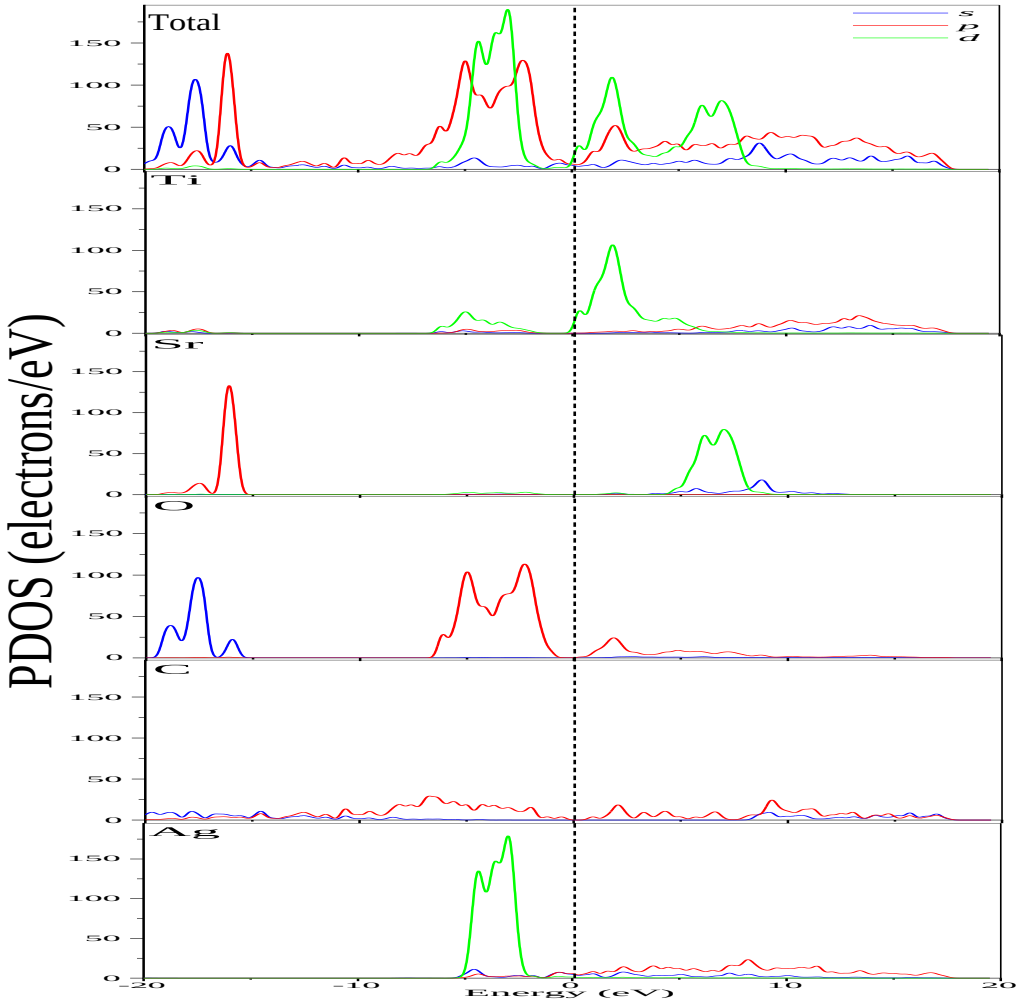

Figure 5.11: *PDOS for the $SrTiO_3$/rGO@Ag composite. The Fermi level is set to zero.*

5.4.6.2. Diffuse reflection spectroscopy (DRS)

UV-Vis-DRS spectroscopy is a proven tool for experimentally quantifying electronic characteristics [73]. The spectra shown in the Figure 5.12 correspond to $SrTiO_3/rGO_x$ (x = 0, 10, and 20%) and $SrTiO_3/rGO_{20}@Ag_x$ (x= 2 and 4%), the lines demonstrated that the composites had a robust and wide UV absorption band and that they are transparent in the visible range, due to the transitions from the VB to the CB.

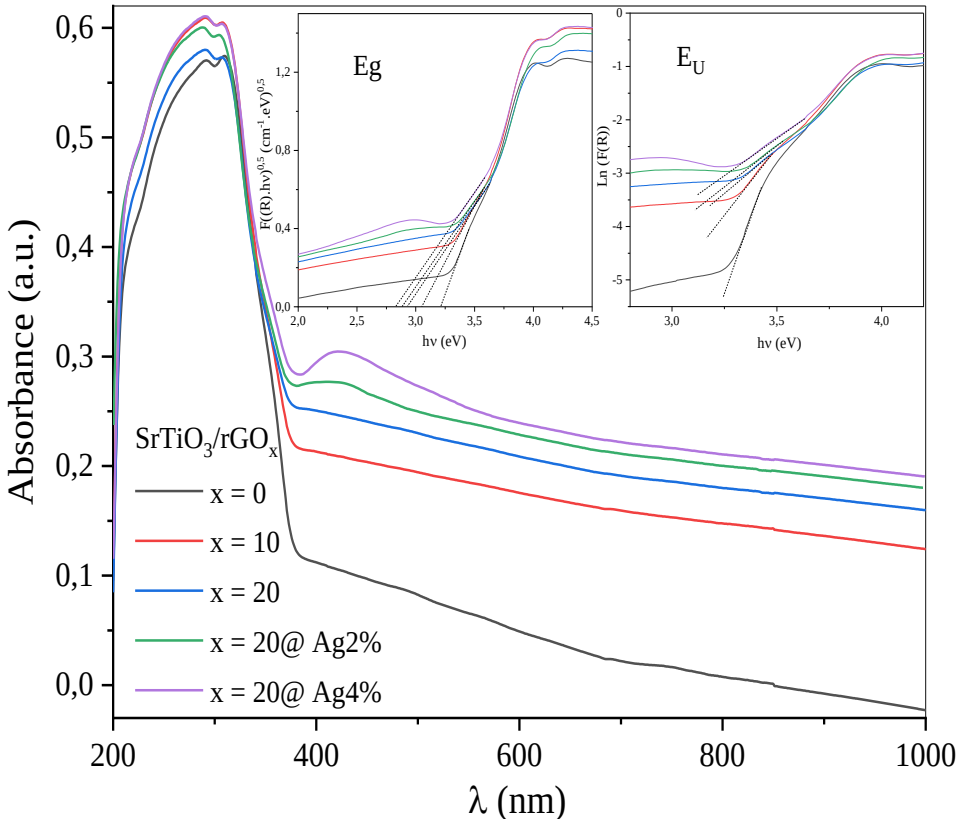

Figure 5.12: *UV-Visible spectra of $SrTiO_3/rGO_x$ (x=0, 5, 10, 15 and 20%) and $SrTiO_3/rGO_{20}@Ag_x$ (x = 2 and 4%) nanocomposites. The insert figure: variation of the band gap E_g according to Kubelka-Munk method and variation of Urbach energy E_U. All spectra are normalized to one by the maximum of absorbance.*

Figure 5.12 shows the variation of Urbach energy 'E_U' and the band gap 'E_g' according to the Kubelka-Munk method as an insert. The maximum absorbance has been used to normalize all spectra to one.

The band gap 'E_g' was estimated using a Tauc plot on linear part of $(\alpha.h\nu)^n \propto (h\nu\text{-}E_g)$, where n = 1/2 for indirect band gap, and n = 2 for direct gap (insert of Figure 5.12); Table 5.2 represents the calculated band gap energies.

The value of 'E_U' is calculated from the slope of the linear part [$\ln(F(R)) \propto (h\nu - E_0)$] of the plot [$\ln(F(R))$ vs $h\nu$] (insert of Figure 5.12); Table 5.2 summarizes the results.

Table 5.2: *Indirect and direct band gap energies and Urbach energy of $SrTiO_3/rGO_x$ (x = 0, 10 and 20%) and and $SrTiO_3/rGO_{20}@Ag_x$ (x = 2 and 4%) nanocomposites.*

$SrTiO_3/rGO_x$	x = 0%		x = 10%	x = 20%	Ag 2%	Ag 4%
	Exp	GGA+U				
Indirect band gap energy (eV)	3,21	2.98	3,05	2,93	2,88	2,82
Urbach energy (meV)	89		198	304	326	359

'E_U' characterizes the shift in the electronic band structure generated by several sources. (dislocation, lattice strain, vacant or interstitial sites…). These sources produce extra states in the band gap near HOMO and LUMO levels, which can be seen as CB and VB tails; 'E_U' is approximately equivalent to the average tail width [42]. Table 5.2 shows that depositing rGO sheets and Ag particles over $SrTiO_3$ increased the Urbach energy, in good agreement with theoretical calculation, which were observed inter-levels. In the band gap caused by the deposit of rGO and metallic Ag, UV-Vis-DRS and XRD analyses confirmed that the deposit of rGO sheets and Ag particles induces stress and defects within $SrTiO_3$ nanocrystals. Furthermore, decreasing 'E_g' by adding rGO sheets changed the Fermi level, which boosts photogenerated electron migration while suppressing the recombination electron hole, implying an improvement in photocatalytic activity.

5.4.7. Adsorption kinetic and modeling

According to the adsorption curves shown in the Figure 5.13, the equilibrium time for the five samples was about 40 minutes. The adsorbed quantities (Q_{ads}) increased for increasing rGO content in the composites $SrTiO_3/rGO_x$ and varied from Q_{ads} = 5.15 mg/g to Q_{ads} = 12.57 mg/g for x = 0 to x = 20% respectively, which means that the rGO was responsible for MB adsorption due to its high speciic surface area.

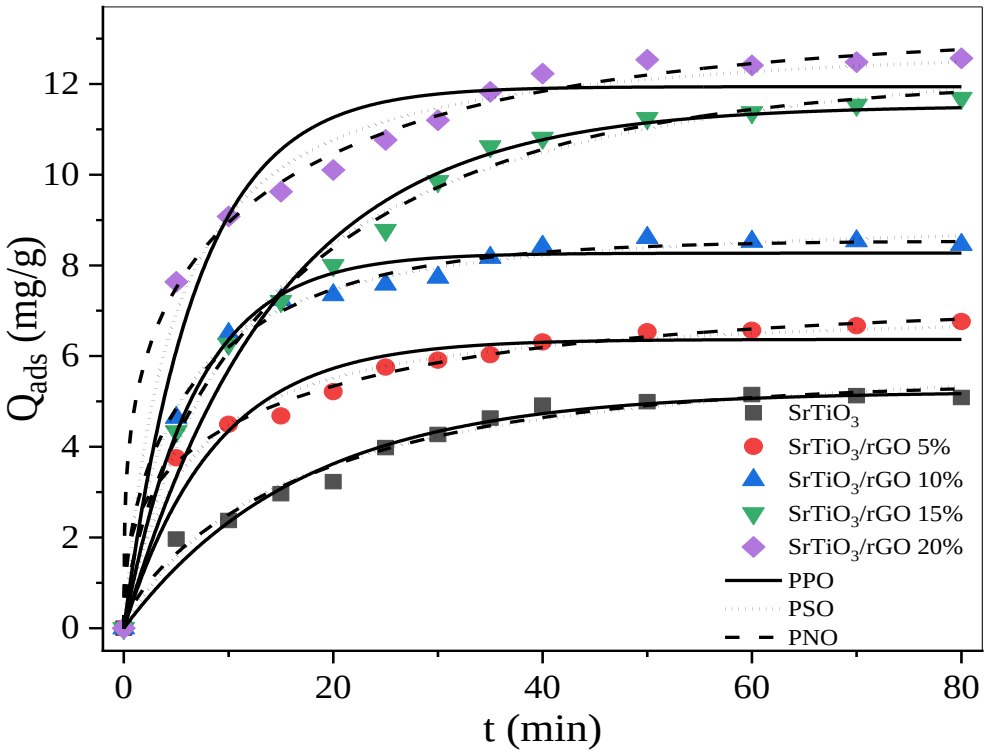

Figure 5.13: *Adsorption kinetic curves of MB on $SrTiO_3/rGO_x$ (x= 0, 5, 10, 15 and 20%) nanocomposites.*

The modeling results are shown in the Figure 5.13. The constants obtained from the adsorption models, namely the rate constants K, Table 5.3 lists the R^2 correlation coefficients and the maximum theoretical amount adsorbed Q_{ads}. The best-established model for the kinetic study was chosen according to the highest correlation factor R^2.

Table 5.3: *Modeling results of adsorption kinetics of BM on $SrTiO_3/rGO_x$ (x=0, 5, 10, 15 and 20%).*

$SrTiO_3$ /rGO_x	Q_e experimental (mg/g)	Model									
		PFO			PSO			$Pn^{th}O$			
		K_1 (mn^{-1})	Q_e (mg/g)	R^2	K_2 (mn^{-1})	Q_e (mg/g)	R^2	K_n (mn^{-1})	Q_e (mg/g)	n	R^2
0	5.15	0.059	5.22	0.979	0.010	6.34	0.979	0.040	5.43	0.702	0.985
5	6.67	0.115	6.37	0.950	0.023	7.14	0.985	0.026	7.10	0.318	0.996
10	8.53	0.146	8.27	0.983	0.024	9.14	0.995	0.069	8.54	0.461	0.994
15	11.69	0.068	11.53	0.984	0.006	13.73	0.992	0.040	12.12	0.625	0.995
20	12.57	0.143	11.94	0.951	0.017	13.20	0.987	0.030	13.11	0.282	0.997

The adsorbed quantities Q_{ads} derived by the pseudo-first-order model were not comparable to those obtained experimentally, and the correlation coefficients R^2 for all composites were between 0.949 and 0.984, according to the values quoted in Table 5.3. . On another hand, the adsorbed quantities calculated Q_{ads} by the pseudo-second-order model were close to the experimental results with correlation coefficients R^2 between 0.979 and 0.995. For the pseudo-n^{th} order model, the correlation coefficients R^2 were between 0.986 to 0.996 with adsorbed quantities Q_{ads} determined experimentally close to those calculated. In conclusion, and according to the fits carried out, the pseudo n^{th} order model was the most suitable for describing the adsorption kinetics of MB on $SrTiO_3$/rGO.

5.4.8. Photocatalytic activity under UV-visible light illumination

The overall elimination curves of MB by adsorption and photocatalysis are shown in the Figure 5.14. For $SrTiO_3$/rGO_x composites, it was found that the elimination of MB increased as the rGO content rose; the obtained yields were R = 6, 31, 53, 63 and 67 % for x = 0, 5, 10, 15 and 20% respectively. This was owing to rGO's large specific surface area, which enhanced the interface (solid solution) and thus improved photocatalytic activity.

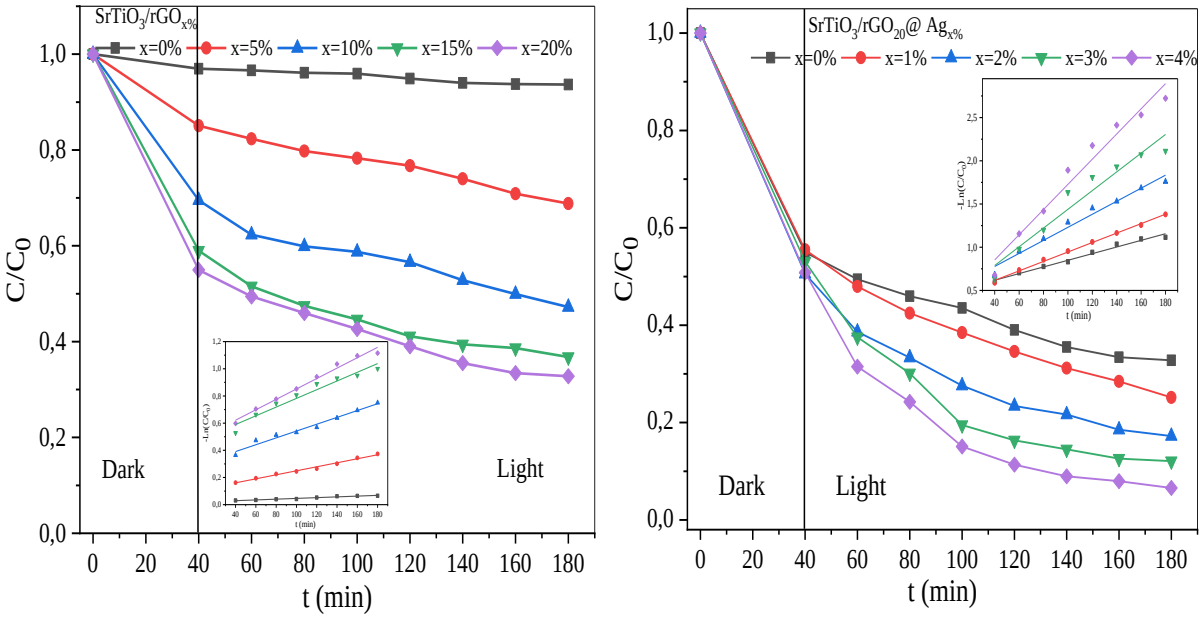

***Figure 5.14**: Photodegradation of MB dye by $SrTiO_3$/rGO_x (x= 0, 5, 10, 15 and 20%) (Left) and $SrTiO_3$/rGO_{20}@Ag_x (x = 1, 2, 3 and 4%) (Right) nanocomposites.*

In other words, Graphene used kinetically to enhance the efficiency of photocatalysis owing to the high adsorption capacity of organic/inorganic contaminants by facilitating the access to the active sites [42]. This occurred in two stages: (i) in the dark, mostly by MB adsorption on rGO sheets due to its height specific surface, and (ii) Electron-hole pairs produced within

$SrTiO_3/rGO_x$ can oxidize MB via photocatalysis after adsorption saturation and under UV-visible light. An exponential function was used to fit the rate constants of the photocatalytic kinetic curves. (Insert of Figure 5.14 (*a*)), and were $K*10^{-4}$ = 2.81, 15.8, 24.7, 32.3 and 38.4 mn^{-1} for the composites $SrTiO_3/rGO_x$ (with x = 0, 5, 10, 15 and 20%) respectively. It is worth mentioning that in the absence of the photocatalyst (SrTiO3/rGOx); the concentration of MB did not change significantly, demonstrating that MB cannot be decomposed by photolysis. The removal yields for the composites $SrTiO_3/rGO_{20}@Ag_{x\%}$ increased with increasing Ag weight ratio and were about R = 67, 75, 83, 88 and 94 % for x = 0, 1, 2, 3 and 4 %, respectively. Moreover, the rate constants of the kinetics (insert of Figure 5.14 (*b*)) were $K*10^{-4}$ = 38.4, 54.6, 80.0, 108.3 and 145.7 mn^{-1} for x = 0, 1, 2, 3 and 4 % respectively. The obtained $SrTiO_3$/rGO@Ag composites showed high improvement in the photocatalytic performance over pristine $SrTiO_3$ and $SrTiO_3$/rGO, which could be linked to graphene's function as a photosensitizer in p-n heterojunctions $SrTiO_3$/rGO composites, as well as the benefit from the localized surface plasmon resonance caused by Ag nanoparticles in $SrTiO_3$/rGO@Ag composites. For the commercial application of the photocatalyst, it is necessary to test the photocatalyst across numerous cycles. Figure 5.15 illustrates the recycled $SrTiO_3/rGO_{20}@Ag_2$ photocatalyst four times, for each cycle three hours (4*3h =12h) of irradiation, which photocatalytic activity remained almost unaltered.

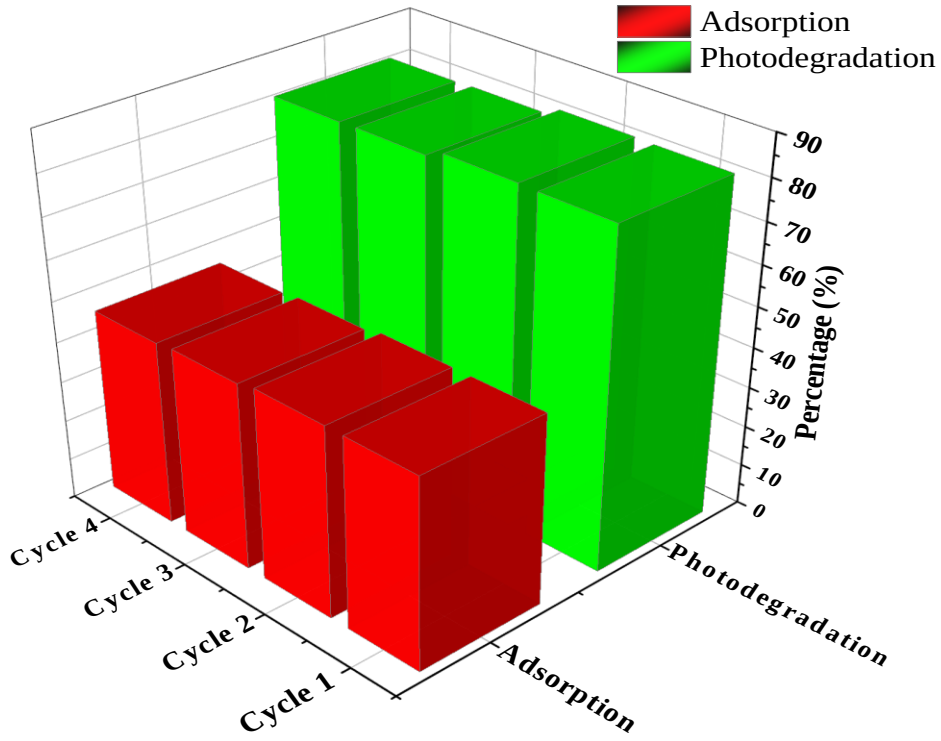

Figure 5.15: *Recycled $SrTiO_3/rGO_{20}@Ag_2$ photocatalyst for four times*

5.4.9. Proposed mechanism

A putative mechanism for the photocatalytic process is given based on the previous findings and depicted by a scheme in Figure 5.16. In the $SrTiO_3$/rGO@Ag system, the wide bandgap of $SrTiO_3$ prevents it from being photoexcited by visible light (3.19 eV §3.5.2). However, in the pristine graphene, its antibonding π* orbitals and bonding π orbitals degenerated and reaching Brillouin zone corners [75], rendering graphene a zero bandgap semi-metallic material and hence it can behave as a photosensitizing compound under visible light irradiation. In addition, the junction with $SrTiO_3$ broke the lattice symmetry and open the bandgap, thus converting semi-metallic character of graphene into a pure semiconductor character due to the formation of gap between π and π* bands; it has been demonstrated previously theoretically and experimentally that rGO semiconductor can directly act as photocatalysts for water splitting [34], [39], [60], [76]–[78]. Therefore, when exposed to UV-visible light, rGO in $SrTiO_3$/rGO_x composites is photoexcited from the ground state (rGO) to the excited state (rGO*), during which electrons are photogenerated. The excited state of rGO* injects electrons into $SrTiO_3$'s conduction band (CB); the photoexcited electrons react with dissolved oxygen and water molecules to produce oxidative species such as hydroxyl radicals ($OH^{\bullet}$) and peroxide radical anions ($O^{2\bullet-}$); the Reactive Oxygen Species (ROS) can drive mineralization and oxidize totally MB into CO_2 and H_2O. Otherwise, $SrTiO_3$/rGO_x composites are also expected to be efficient photocatalysts excited by UV light irradiation, with rGO acting as an electron acceptor rather than a photosensitizer.

When an Ag metal is coated on a semiconductor ($SrTiO_3$/rGO@Ag), the semiconductor electrons' work function must match that of the metal electrons at the interface, as well as the Fermi levels for the two materials [79]. In this case, there is a state in the energy gap that penetrates deeper into the semiconductor; it is actually the metal's band states that are deeply buried into the semiconductor's states [80].

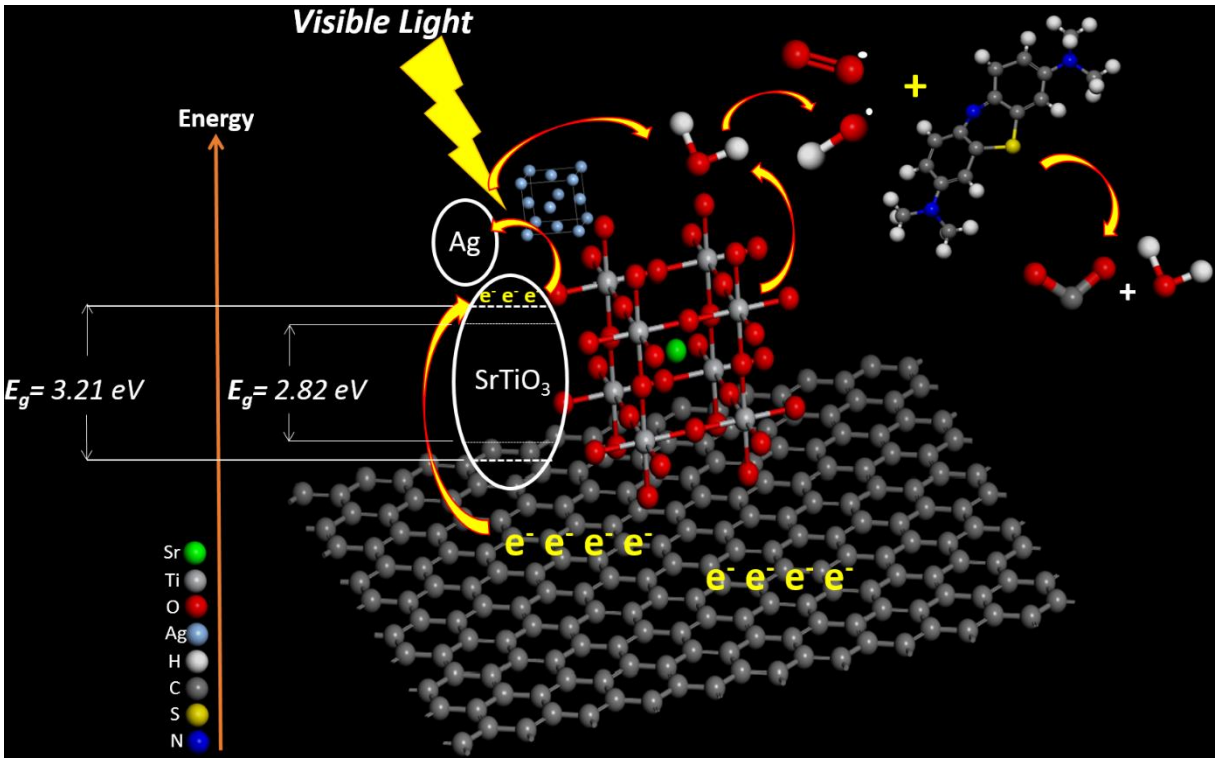

Figure 5.16: *Schematic illustration of the photocatalytic mechanism of $SrTiO_3$/rGO@Ag nanocomposite.*

In the present case, the work function of the Ag metal was near to the CB and acted as an electron acceptor from the $SrTiO_3$/rGO. The semiconductor's work function can be divided into two parts [22], [50]: first, the internal work function (W_I) is defined as the energy difference between Fermi energy and the CB's bottom; and second, external work function (W_E) refers to the amount of work required to extract a free electron from $SrTiO_3$/rGO. As a result, the total work function of the $SrTiO_3$/rGO (W_S) can be written as (W_S) = (W_I) + (W_E). Let (W_M) be the deposited Ag's work function, the donor levels in the $SrTiO_3$/rGO are totally ionized when the $SrTiO_3$/rGO and the Ag metal come into contact, the electrons in these states ($W_M > W_S$) should flow into the Ag metal in the CB of $SrTiO_3$/rGO until the Fermi energies of the metal and the semiconductor approach equilibrium. At equilibrium, the energy levels of the $SrTiO_3$/rGO are dropped by the amount (W_M-W_S) since the Fermi energies are at the same level, and Schottky barrier (W_{SK}) formed at the $SrTiO_3$/rGO@Ag interface.

5.5. Conclusions

In conclusion, by using a simple hydrothermal technique, a series of $SrTiO_3$/rGO nanocomposites with varied graphene weight ratios were successfully synthesized, followed by decorating the surface with Ag nanoparticles by using the photodeposition process, and tested for the photocatalytic degradation and adsorption of MB dye under irradiation of UV-visible light. The XRD analysis proved that the $SrTiO_3$ nanocrystals have a cubic crystalline structure. The rGO and the Ag^0 particles caused stress on the crystal structure of $SrTiO_3$ that confirmed by a notifiable decrease of the average grain seizes (D) obviously accompanied by a rise in microconstraints (ξ%) and caused significant structural defects as measured by an increase in dislocation density (δ). Furthermore, SEM images also confirmed the establishment of the heterojunction and the superior intimate interaction between rGO sheets and $SrTiO_3$ nanocubes. The experimental gap values was about 3.21 eV and 2.82 eV for $SrTiO_3$ and $SrTiO_3/rGO_{20\%}@Ag_{4\%}$, respectively, as determined by UV-Vis-DRS spectroscopy; whereas, the gap value of $SrTiO_3$ determined by DFT was about 2.98 eV using GGA +U computations. Due to the introduction of hybridized states, increasing the rGO and Ag metal quantities positively tuned the electronic structure with a lowered band gap, expanding the absorption to the visible region of the electromagnetic spectrum. Moreover, the adsorption kinetic curves showed that the equilibrium time was about 40 minutes and the quantity of MB adsorbed rose as the amount of rGO increased. The fit of kinetic curves showed that the pseudo n^{th} order model was adequate to model the experimental results. Furthermore, compared to pristine $SrTiO_3$, all of the prepared $SrTiO_3$/rGO nanocomposites had higher photocatalytic activity under UV-visible light irradiation, which could be attributed to graphene's photosensitizer role in the $SrTiO_3$/rGO composites and the formation of p-n heterojunctions between p-type rGO and n-type $SrTiO_3$ nanocubes, as well as the localized surface plasmon resonance caused by Ag nanoparticles. The findings show that incorporation of graphene into $SrTiO_3$/rGO nanocubes and their decoration Ag particles increased visible light absorption and considerably improved photogenerated carrier separation. The photocatalytic performance of the sample $SrTiO_3/rGO_{20\%}$ @$Ag_{4\%}$ in the MB degradation was the best of all the photocatalysts tested, with activity reaching 94% under UV-visible light after 40 minutes of irradiation. On the basis of these findings, a photocatalytic reaction mechanism can be proposed. In this mechanism, the rGO acts as photosensitizer for wide band gap of $SrTiO_3$ semiconductor and the metal band states that are firmly buried into the states of the semiconductor forms Schottky barrier at the metal–semiconductor interface.

References

[1] M. I. Fadlalla, P. Senthil Kumar, V. Selvam, and S. Ganesh Babu, "Recent Advances in Nanomaterials for Wastewater Treatment," in *Advanced Nanostructured Materials for Environmental Remediation*, vol. 25, Mu. Naushad, S. Rajendran, and F. Gracia, Eds. Cham: Springer International Publishing, 2019, pp. 21–58. doi: 10.1007/978-3-030-04477-0_2.

[2] B. L. Phoon, C. W. Lai, J. C. Juan, P.-L. Show, and G.-T. Pan, "Recent developments of strontium titanate for photocatalytic water splitting application," *International Journal of Hydrogen Energy*, Feb. 2019, doi: 10.1016/j.ijhydene.2019.01.166.

[3] H. Wang *et al.*, "Semiconductor heterojunction photocatalysts: design, construction, and photocatalytic performances," *Chemical Society Reviews*, vol. 43, no. 15, p. 5234, Jul. 2014, doi: 10.1039/C4CS00126E.

[4] T. S. Natarajan, K. R. Thampi, and R. J. Tayade, "Visible light driven redox-mediator-free dual semiconductor photocatalytic systems for pollutant degradation and the ambiguity in applying Z-scheme concept," *Applied Catalysis B: Environmental*, vol. 227, pp. 296–311, Jul. 2018, doi: 10.1016/j.apcatb.2018.01.015.

[5] X. Zuo *et al.*, "Bubble-template-assisted synthesis of hollow fullerene-like MoS_2 nanocages as a lithium ion battery anode material," *Journal of Materials Chemistry A*, vol. 4, no. 1, pp. 51–58, 2016, doi: 10.1039/C5TA06869J.

[6] P. Li *et al.*, "An overview and recent progress in the heterogeneous photocatalytic reduction of U(VI)," *Journal of Photochemistry and Photobiology C: Photochemistry Reviews*, vol. 41, p. 100320, Dec. 2019, doi: 10.1016/j.jphotochemrev.2019.100320.

[7] J. N. Jebaranjitham and B. G. Kumar, "Heterogeneous Type-I and Type-II Catalysts for the Degradation of Pollutants," in *Green Photocatalysts*, vol. 34, Mu. Naushad, S. Rajendran, and E. Lichtfouse, Eds. Cham: Springer International Publishing, 2020, pp. 209–234. doi: 10.1007/978-3-030-15608-4_9.

[8] K. Qi, B. Cheng, J. Yu, and W. Ho, "Review on the improvement of the photocatalytic and antibacterial activities of ZnO," *Journal of Alloys and Compounds*, vol. 727, pp. 792–820, Dec. 2017, doi: 10.1016/j.jallcom.2017.08.142.

[9] J. Xie *et al.*, "Strontium titanate with inverse opal structure as the photocatalysts," *Journal of Materials Science: Materials in Electronics*, vol. 31, no. 3, pp. 2691–2698, Feb. 2020, doi: 10.1007/s10854-019-02809-5.

[10] Inamuddin, M. I. Ahamed, A. M. Asiri, and E. Lichtfouse, *Nanophotocatalysis and environmental applications: energy conversion and chemical transformations*. 2019. Accessed: May 02, 2019. [Online]. Available: http://search.ebscohost.com/login.aspx?direct=true&scope=site&db=nlebk&db=nlabk&AN=2093394

[11] S. Ali *et al.*, "Synthesis of activated carbon-supported TiO2-based nano-photocatalysts with well recycling for efficiently degrading high-concentration pollutants," *Catalysis Today*, vol. 335, pp. 557–564, Sep. 2019, doi: 10.1016/j.cattod.2019.03.044.

[12] P. Kanhere and Z. Chen, "A Review on Visible Light Active Perovskite-Based Photocatalysts," *Molecules*, vol. 19, no. 12, pp. 19995–20022, Dec. 2014, doi: 10.3390/molecules191219995.

[13] S. Bhattacharjee, S. P. Chaudhary, and S. Bhattacharyya, “Lead-Free Metal Halide Perovskite Nanocrystals for Photocatalysis in Water,” 2019.

[14] Y. Hu *et al.*, “Layered perovskite oxides and their derivative nanosheets adopting different modification strategies towards better photocatalytic performance of water splitting,” *Renewable and Sustainable Energy Reviews*, vol. 119, p. 109527, Mar. 2020, doi: 10.1016/j.rser.2019.109527.

[15] B. Kayaalp, “Design strategies towards SrTiO3 based perovskite nanostructures for environmental catalysis,” 2019.

[16] S.-T. Huang, W. W. Lee, J.-L. Chang, W.-S. Huang, S.-Y. Chou, and C.-C. Chen, “Hydrothermal synthesis of SrTiO3 nanocubes: Characterization, photocatalytic activities, and degradation pathway,” *Journal of the Taiwan Institute of Chemical Engineers*, vol. 45, no. 4, pp. 1927–1936, Jul. 2014, doi: 10.1016/j.jtice.2014.02.003.

[17] I. A. Abdel-Latif, “Perovskite Strontium Doped Rare Earth Manganites Nanocomposites and Their Photocatalytic Performances,” in *Nanocomposites - Recent Evolutions*, S. Sivasankaran, Ed. IntechOpen, 2019. doi: 10.5772/intechopen.79479.

[18] J. Xie, C. Yang, Y. He, and H. Wang, “Effect of pH on the phase transformation of strontium titanium materials and their photocatalytic property,” *Journal of Materials Science: Materials in Electronics*, vol. 29, no. 22, pp. 19344–19352, Nov. 2018, doi: 10.1007/s10854-018-0061-6.

[19] H. Gao, H. Yang, and S. Wang, “Hydrothermal synthesis, growth mechanism, optical properties and photocatalytic activity of cubic SrTiO3 particles for the degradation of cationic and anionic dyes,” *Optik*, vol. 175, pp. 237–249, Dec. 2018, doi: 10.1016/j.ijleo.2018.09.027.

[20] Y. Wu and T. He, “Ag loading induced visible light photocatalytic activity for pervoskite SrTiO 3 nanofibers,” *Spectrochimica Acta Part A: Molecular and Biomolecular Spectroscopy*, vol. 199, pp. 283–289, Jun. 2018, doi: 10.1016/j.saa.2018.03.078.

[21] R. Konta, T. Ishii, H. Kato, and A. Kudo, “Photocatalytic Activities of Noble Metal Ion Doped $SrTiO_3$ under Visible Light Irradiation,” *The Journal of Physical Chemistry B*, vol. 108, no. 26, pp. 8992–8995, Jul. 2004, doi: 10.1021/jp049556p.

[22] X. Li, Z. Ge, F. Xue, H. Liu, B. Lyu, and M. Liu, “Lattice-oriented contact in Pd/SrTiO3 heterojunction for rapid electron transfer during photocatalytic H2 production,” *Materials Research Bulletin*, vol. 123, p. 110722, Mar. 2020, doi: 10.1016/j.materresbull.2019.110722.

[23] M. A. Ferreira *et al.*, “Fabrication of SrTiO3/g-C3N4 heterostructures for visible light-induced photocatalysis,” *Materials Science in Semiconductor Processing*, vol. 108, p. 104887, Mar. 2020, doi: 10.1016/j.mssp.2019.104887.

[24] U. Coleto *et al.*, “Influence of defects on photoluminescent and photocatalytic behavior of CaO/SrTiO3 heterojunctions,” *Ceramics International*, vol. 45, no. 12, pp. 15244–15251, Aug. 2019, doi: 10.1016/j.ceramint.2019.05.013.

[25] K. Ahlem, S. Boudjadar, R. Bourzami, and B. Allouche, “Eco-friendly synthesis of cuprous oxide (Cu 2 O) nanoparticles and improvement of their solar photocatalytic activities,” *Journal of Solid State Chemistry*, vol. 263, Apr. 2018, doi: 10.1016/j.jssc.2018.04.010.

[26] R. Boulkroune *et al.*, "Hydrothermal synthesis of strontium-doped ZnS nanoparticles: structural, electronic and photocatalytic investigations," *Bulletin of Materials Science*, vol. 42, no. 5, Oct. 2019, doi: 10.1007/s12034-019-1905-2.

[27] C. Du *et al.*, "A review of metal organic framework (MOFs)-based materials for antibiotics removal via adsorption and photocatalysis," *Chemosphere*, vol. 272, p. 129501, Jun. 2021, doi: 10.1016/j.chemosphere.2020.129501.

[28] C. Du *et al.*, "Construction of Z-scheme g-C3N4 / MnO2 /GO ternary photocatalyst with enhanced photodegradation ability of tetracycline hydrochloride under visible light radiation," *Environmental Research*, vol. 200, p. 111427, Sep. 2021, doi: 10.1016/j.envres.2021.111427.

[29] Y. Zhu *et al.*, "Graphene and Graphene Oxide: Synthesis, Properties, and Applications," *Advanced Materials*, vol. 22, no. 35, pp. 3906–3924, Sep. 2010, doi: 10.1002/adma.201001068.

[30] M. Yu *et al.*, "Selective graphene-like metal-free 2D nanomaterials and their composites for photocatalysis," *Chemosphere*, vol. 284, p. 131254, Dec. 2021, doi: 10.1016/j.chemosphere.2021.131254.

[31] Y. Zhu *et al.*, "Graphene and Graphene Oxide: Synthesis, Properties, and Applications," *Advanced Materials*, vol. 22, no. 35, pp. 3906–3924, Sep. 2010, doi: 10.1002/adma.201001068.

[32] X. Li, R. Shen, S. Ma, X. Chen, and J. Xie, "Graphene-based heterojunction photocatalysts," *Applied Surface Science*, vol. 430, pp. 53–107, Feb. 2018, doi: 10.1016/j.apsusc.2017.08.194.

[33] J. Zhang, Z. Xiong, and X. S. Zhao, "Graphene–metal–oxide composites for the degradation of dyes under visible light irradiation," *Journal of Materials Chemistry*, vol. 21, no. 11, p. 3634, 2011, doi: 10.1039/c0jm03827j.

[34] X. Jiang, J. Nisar, B. Pathak, J. Zhao, and R. Ahuja, "Graphene oxide as a chemically tunable 2-D material for visible-light photocatalyst applications," *Journal of Catalysis*, vol. 299, pp. 204–209, Mar. 2013, doi: 10.1016/j.jcat.2012.12.022.

[35] L. Zhang, H. H. Mohamed, R. Dillert, and D. Bahnemann, "Kinetics and mechanisms of charge transfer processes in photocatalytic systems: A review," *Journal of Photochemistry and Photobiology C: Photochemistry Reviews*, vol. 13, no. 4, pp. 263–276, Dec. 2012, doi: 10.1016/j.jphotochemrev.2012.07.002.

[36] J. Zhang, Z. Xiong, and X. S. Zhao, "Graphene–metal–oxide composites for the degradation of dyes under visible light irradiation," *Journal of Materials Chemistry*, vol. 21, no. 11, p. 3634, 2011, doi: 10.1039/c0jm03827j.

[37] C. Du *et al.*, "Reduced graphene oxide modified Z-scheme AgI/Bi2MoO6 heterojunctions with boosted photocatalytic activity for water treatment originated from the efficient charge pairs partition and migration," *Environ Sci Pollut Res*, Jul. 2021, doi: 10.1007/s11356-021-15180-y.

[38] H. Atout *et al.*, "Enhanced photocatalytic degradation of methylene blue: Preparation of TiO2/reduced graphene oxide nanocomposites by direct sol-gel and hydrothermal methods," *Materials Research Bulletin*, vol. 95, pp. 578–587, Nov. 2017, doi: 10.1016/j.materresbull.2017.08.029.

[39] H. Chi, K. Murali, T. Li, and S. Thomas, "Recent advances in graphene based photoresponsive materials," *Progress in Natural Science: Materials International*, Dec. 2019, doi: 10.1016/j.pnsc.2019.11.002.

[40] B. Bajorowicz *et al.*, "Perovskite-type KTaO3–reduced graphene oxide hybrid with improved visible light photocatalytic activity," *RSC Adv.*, vol. 5, no. 111, pp. 91315–91325, Oct. 2015, doi: 10.1039/C5RA18124K.

[41] A. Zada *et al.*, "Surface Plasmonic-Assisted Photocatalysis and Optoelectronic Devices with Noble Metal Nanocrystals: Design, Synthesis, and Applications," *Advanced Functional Materials*, p. 1906744, Dec. 2019, doi: 10.1002/adfm.201906744.

[42] M. K. Guediri, D. Chebli, A. Bouguettoucha, R. Bourzami, and A. Amrane, "Novel Fe2TiO5/reduced graphene oxide heterojunction photocatalyst with improved adsorption capacity and visible light photoactivity: experimental and DFT approach," *Environmental Science and Pollution Research*, Oct. 2020, doi: 10.1007/s11356-020-11221-0.

[43] M. Zhou *et al.*, "Shape-controlled synthesis of golf-like, star-like, urchin-like and flower-like SrTiO3 for highly efficient photocatalytic degradation and H2 production," *Journal of Alloys and Compounds*, vol. 817, p. 152796, Mar. 2020, doi: 10.1016/j.jallcom.2019.152796.

[44] Y. Tang *et al.*, "Fabrication of magnetically recoverable Ag/CuNb2O6/CuFe2O4 ternary heterojunction composite for highly efficient photocatalytic degradation of pollutants," *Separation and Purification Technology*, vol. 220, pp. 78–88, Aug. 2019, doi: 10.1016/j.seppur.2019.03.049.

[45] X.-F. Diao, Y. Tang, Q. Xie, D.-L. Chen, S. Li, and G.-F. Liu, "Study on the Property of Electron-Transport Layer in the Doped Formamidinium Lead Iodide Perovskite Based on DFT," *ACS Omega*, vol. 4, no. 22, pp. 20024–20035, Nov. 2019, doi: 10.1021/acsomega.9b03015.

[46] T. Mahmood, C. Cao, R. Ahmed, M. A. Saeed, and M. Ahmed, "Comparative study of structural and electronic properties of TiO2 at GGA and GGA+ U level," *Journal of Optoelectronics and Advanced Materials*, vol. 16, no. January-February 2014, pp. 117–122, 2014.

[47] A. Chen, S. V. Nair, B. Miljkovic, C. Souza, H. E. Ruda, and Z. Ji, "Electronic structure of bulk and two-dimensional SrTiO3: DFT calculation with GGA + U methods," *Journal of Nanoparticle Research*, vol. 22, no. 9, Sep. 2020, doi: 10.1007/s11051-020-04994-5.

[48] Z. Hu and H. Metiu, "Choice of *U* for DFT+ *U* Calculations for Titanium Oxides," *The Journal of Physical Chemistry C*, vol. 115, no. 13, pp. 5841–5845, Apr. 2011, doi: 10.1021/jp111350u.

[49] Y.-C. Yang, L. Xu, W.-Q. Huang, C.-Y. Luo, G.-F. Huang, and P. Peng, "Electronic structures and photocatalytic responses of SrTiO3 (100) surface interfaced with graphene, reduced graphene oxide, and graphane: surface termination effect," *The Journal of Physical Chemistry C*, vol. 119, no. 33, pp. 19095–19104, 2015.

[50] P. M. Nithya and L. G. Devi, "Effect of surface Ag metallization on the photocatalytic properties of BaTiO3: Surface plasmon effect and variation in the Schottky barrier height," *Surfaces and Interfaces*, vol. 15, pp. 205–215, Jun. 2019, doi: 10.1016/j.surfin.2019.03.005.

[51] Z. Huang *et al.*, "Simultaneous and efficient photocatalytic reduction of Cr(VI) and oxidation of trace sulfamethoxazole under LED light by rGO@Cu2O/BiVO4 p-n heterojunction composite," *Chemosphere*, vol. 221, pp. 824–833, Apr. 2019, doi: 10.1016/j.chemosphere.2019.01.087.

[52] I. A. Abdel-Latif, A. A. Ismail, M. Faisal, A. M. Ali, A. E. Al-Salmi, and A. Al-Hajry, "Impact of the annealing temperature on perovskite strontium doped neodymium manganites nanocomposites and their photocatalytic performances," *Journal of the Taiwan Institute of Chemical Engineers*, vol. 75, pp. 174–182, Jun. 2017, doi: 10.1016/j.jtice.2017.03.030.

[53] S. Yousaf, T. Kousar, M. B. Taj, P. O. Agboola, I. Shakir, and M. F. Warsi, "Synthesis and characterization of double heterojunction-graphene nano-hybrids for photocatalytic applications," *Ceramics International*, 2019.

[54] B. L. Phoon, C. W. Lai, J. C. Juan, P. Show, and W. Chen, "A review of synthesis and morphology of $SrTiO_3$ for energy and other applications," *International Journal of Energy Research*, vol. 43, no. 10, pp. 5151–5174, Aug. 2019, doi: 10.1002/er.4505.

[55] R. F. P. Grimbergen, H. Meekes, P. Bennema, C. S. Strom, and L. J. P. Vogels, "On the Prediction of Crystal Morphology. I. The Hartman–Perdok Theory Revisited," *Acta Cryst A*, vol. 54, no. 4, Art. no. 4, Jul. 1998, doi: 10.1107/S0108767397019806.

[56] W. Zhou and H. F. Greer, "What Can Electron Microscopy Tell Us Beyond Crystal Structures?," *European Journal of Inorganic Chemistry*, vol. 2016, no. 7, pp. 941–950, 2016, doi: 10.1002/ejic.201501342.

[57] W. S. Nam and G. Y. Han, "A photocatalytic performance of TiO2 photocatalyst prepared by the hydrothermal method," *Korean Journal of Chemical Engineering*, vol. 20, no. 1, pp. 180–184, Jan. 2003, doi: 10.1007/BF02697206.

[58] M. E. Simonsen, H. Jensen, Z. Li, and E. G. Søgaard, "Surface properties and photocatalytic activity of nanocrystalline titania films," *Journal of Photochemistry and Photobiology A: Chemistry*, vol. 200, no. 2–3, pp. 192–200, Dec. 2008, doi: 10.1016/j.jphotochem.2008.07.013.

[59] T. Xian, H. Yang, L. Di, J. Ma, H. Zhang, and J. Dai, "Photocatalytic reduction synthesis of SrTiO3-graphene nanocomposites and their enhanced photocatalytic activity," *Nanoscale Res Lett*, vol. 9, no. 1, p. 327, Dec. 2014, doi: 10.1186/1556-276X-9-327.

[60] M. Ahmadi, M. S. Seyed Dorraji, M. H. Rasoulifard, and A. R. Amani-Ghadim, "The effective role of reduced-graphene oxide in visible light photocatalytic activity of wide band gap SrTiO3 semiconductor," *Separation and Purification Technology*, vol. 228, p. 115771, Dec. 2019, doi: 10.1016/j.seppur.2019.115771.

[61] Y. Wu and T. He, "Ag loading induced visible light photocatalytic activity for pervoskite SrTiO3 nanofibers," *Spectrochimica Acta Part A: Molecular and Biomolecular Spectroscopy*, vol. 199, pp. 283–289, Jun. 2018, doi: 10.1016/j.saa.2018.03.078.

[62] D. Yang, X. Zou, Z. Tong, Y. Nan, F. Ding, and Z. Jiang, "Fabrication of SrTiO3 nanotubes via an isomorphic conversion strategy," *Journal of Nanoparticle Research*, vol. 20, no. 2, Feb. 2018, doi: 10.1007/s11051-018-4142-5.

[63] M. Guo, Q. Liu, M. Wu, T. Lv, and L. Jia, "Novel reduced graphene oxide wrapped-SrTiO3 flower-like nanostructure with Ti–C bond for free noble metal decomposition of

formic acid to hydrogen," *Chemical Engineering Journal*, vol. 334, pp. 1886–1896, Feb. 2018, doi: 10.1016/j.cej.2017.11.120.

[64] B. K. Bußmann, O. Ochedowski, and M. Schleberger, "Doping of graphene exfoliated on $SrTiO_3$," *Nanotechnology*, vol. 22, no. 26, p. 265703, Jul. 2011, doi: 10.1088/0957-4484/22/26/265703.

[65] S. Karamat *et al.*, "Graphene/SrTiO3 hetero interface studied by X-ray photoelectron spectroscopy," *Progress in Natural Science: Materials International*, vol. 26, no. 4, pp. 422–426, Aug. 2016, doi: 10.1016/j.pnsc.2016.06.010.

[66] O. Akhavan, "Bacteriorhodopsin as a superior substitute for hydrazine in chemical reduction of single-layer graphene oxide sheets," *Carbon*, vol. 81, pp. 158–166, Jan. 2015, doi: 10.1016/j.carbon.2014.09.044.

[67] J. D. Baran, C. Eames, K. Takahashi, M. Molinari, M. S. Islam, and S. C. Parker, "Structural, Electronic, and Transport Properties of Hybrid $SrTiO_3$ -Graphene and Carbon Nanoribbon Interfaces," *Chemistry of Materials*, vol. 29, no. 17, pp. 7364–7370, Sep. 2017, doi: 10.1021/acs.chemmater.7b02253.

[68] P. K. Gogoi *et al.*, "Optical conductivity renormalization of graphene on SrTiO 3 due to resonant excitonic effects mediated by Ti 3 d orbitals," *Physical Review B*, vol. 91, no. 3, Jan. 2015, doi: 10.1103/PhysRevB.91.035424.

[69] G. Schusteritsch and C. J. Pickard, "Predicting interface structures: From SrTiO 3 to graphene," *Physical Review B*, vol. 90, no. 3, Jul. 2014, doi: 10.1103/PhysRevB.90.035424.

[70] P. F. Lang and B. C. Smith, "Electronegativity effects and single covalent bond lengths of molecules in the gas phase," *Dalton Trans.*, vol. 43, no. 21, pp. 8016–8025, 2014, doi: 10.1039/C4DT00807C.

[71] J. Y. Wang and Y. C. Zhou, "First-principles study of equilibrium properties and electronic structure of $Ti_3Si_{0.75}Al_{0.25}C_2$ solid solution," *Journal of Physics: Condensed Matter*, vol. 15, no. 35, pp. 5959–5968, Sep. 2003, doi: 10.1088/0953-8984/15/35/305.

[72] M. Humayun *et al.*, "Experimental and DFT Studies of Au Deposition Over WO3/g-C3N4 Z-Scheme Heterojunction," *Nano-Micro Letters*, vol. 12, no. 1, Jan. 2020, doi: 10.1007/s40820-019-0345-2.

[73] V. Nadtochenko *et al.*, "Correlations for photocatalytic activity and spectral features of the absorption band edge of TiO2 modified by thiourea," *Applied Catalysis B: Environmental*, vol. 91, no. 1–2, pp. 460–469, Sep. 2009, doi: 10.1016/j.apcatb.2009.06.015.

[74] T. Entradas, J. F. Cabrita, S. Dalui, M. R. Nunes, O. C. Monteiro, and A. J. Silvestre, "Synthesis of sub-5 nm Co-doped SnO2 nanoparticles and their structural, microstructural, optical and photocatalytic properties," *Materials Chemistry and Physics*, vol. 147, no. 3, pp. 563–571, Oct. 2014, doi: 10.1016/j.matchemphys.2014.05.032.

[75] X. Li, R. Shen, S. Ma, X. Chen, and J. Xie, "Graphene-based heterojunction photocatalysts," *Applied Surface Science*, vol. 430, pp. 53–107, Feb. 2018, doi: 10.1016/j.apsusc.2017.08.194.

[76] B. Bajorowicz *et al.*, "Perovskite-type KTaO3-reduced graphene oxide hybrid with improved visible light photocatalytic activity," p. 11.

[77] C.-W. Chang and C. Hu, "Graphene oxide-derived carbon-doped SrTiO3 for highly efficient photocatalytic degradation of organic pollutants under visible light irradiation," *Chemical Engineering Journal*, vol. 383, p. 123116, Mar. 2020, doi: 10.1016/j.cej.2019.123116.

[78] H. Bantawal, M. Sethi, U. S. Shenoy, and D. K. Bhat, "Porous Graphene Wrapped $SrTiO_3$ Nanocomposite: Sr–C Bond as an Effective Coadjutant for High Performance Photocatalytic Degradation of Methylene Blue," *ACS Applied Nano Materials*, vol. 2, no. 10, pp. 6629–6636, Oct. 2019, doi: 10.1021/acsanm.9b01513.

[79] P. M. Nithya and L. G. Devi, "Effect of surface Ag metallization on the photocatalytic properties of BaTiO3: Surface plasmon effect and variation in the Schottky barrier height," *Surfaces and Interfaces*, Mar. 2019, doi: 10.1016/j.surfin.2019.03.005.

[80] S. Wan, M. Chen, M. Ou, and Q. Zhong, "Plasmonic Ag nanoparticles decorated SrTiO3 nanocubes for enhanced photocatalytic CO2 reduction and H2 evolution under visible light irradiation," *Journal of CO2 Utilization*, vol. 33, pp. 357–364, Oct. 2019, doi: 10.1016/j.jcou.2019.06.024.

General conclusion and recommendations for future work

6. General conclusion and recommendations for future work

This work is an exploration of a new hybrid material system, for the purpose of creating a visible-light photoactive material for the degradation of MB. The work extends to developing an understanding of new material properties that arise from the mixing of two or three materials (semiconductor, graphene, and metal), with reliance on numerical simulations of hybrid nanostructures using the DFT method approach, in order to determine the mechanisms of physical phenomena responsible for photocatalytic effects occurring in these hybrid materials.

First, all the semiconductors oxides were successfully synthesized using a solid-state reaction for Fe_2TiO_5, and a facile hydrothermal method for $NiFe_2O_4$-TiO_2, and $SrTiO_3$. Each semiconductor was employed as a substrate to deposit reduced Graphene Oxide (rGO) sheets with various contents, which were synthesized via Hummers modified method. In order to construct powerful heterojunctions photocatalysts and more efficient to degrade Methylene Blue (MB), through the exceptional properties of graphene. Graphene plays a key role in the advancements of heterojunction photocatalysts in enhanced photocatalytic activity, can be summarized thus:

- The graphene in the composites facilitates the separation of charge, restrains the hole-electron recombination, and gives a large surface/interface for heterogeneous connection reactions.

- Thanks to its gap null, rGO shifts the adsorption to the high wavelength and increases the absorption in the visible region, increasing the photogenerated carrier's quantity

- The rGO π-conjugated electrons system favors thermodynamically the generation of ROS (Reactive Oxygen Species), and can oxidize directly MB, and creates additional photocatalytic active sites in the composites.

In general, the structures of all the Semiconductor oxides are conserved after the deposition of rGO, although the crystalline size and the cell parameters changed, evidently accompanied by an increase of the microconstraints (ξ%); this induced strong structural defects estimated by an increase of the dislocation density (δ). On another hand, the lattice strain values and the grain size were affected by the Ag decoration in the case of $SrTiO_3$.

The gap values was reduced in all composites, due to the introduction of hybridized states. Increasing the rGO and Ag metal quantities positively tuned the electronic structure with a

lowered band gap, expanding the absorption to the visible region of the electromagnetic spectrum. The gap values given by DFT using LSDA+U, GGA, and GGA +U was compatible with what was obtained experimentally.

Moreover, the adsorption kinetic curves showed that the quantity of MB adsorbed rose as the amount of rGO increased. The fit of the kinetic curves proved that the pseudo nth order is the adequate model for the Fe_2TiO_5/rGO and $SrTiO_3$/rGO nanocomposites, and the pseudo-second-order is the adequate model for the $NiFe_2O_4$-TiO_2/rGO composites. Furthermore, the photocatalytic study showed that all synthesized compounds have an impact on the degradation of the MB under visible light, these results indicated that deposit of graphene and decoration with Ag metallic particles enhanced visible light absorption and greatly improved separation of photogenerated carriers thus could be attributed to graphene's receiver and photosensitizer role in the composites, as well as the localized surface plasmon resonance caused by Ag nanoparticles.

Perspectives and recommendations

In the near future, investigations can be devoted to the photo-efficiency of the new functionalized hybrid materials. This approach will allow potential applications of these systems in environmental preservation, such as for water depollution or for new sources of energy through photocatalytic production of hydrogen.

Following the results obtained for the different nanocomposites, several perspectives and recommendations are identified for the overall photocatalytic degradation of organic dyes:

- The photodegradation of all photocatalysts was a success with respect to the UV-Vis analysis. However, it is recommended that TOC or chromatography techniques be used after degradation of the samples to determine the total organic carbon of the pollutants and the extent of the total degradation.

- Other pollutants can be utilized to assess the photocatalysts' viability for photodegradation.

- It is also recommended to test the photocatalytic efficacy of the materials for the photo-degradation of real urban wastewater.

- It is recommended to construct a multi-semiconductor hybrid Z-scheme system, which has gradually become a focus of research due to its unique charge transfer pathway different from traditional charge transfer.